October 2018

Collider tests of fundamental symmetries and neutrino properties

Haolin Li

COLLIDER TESTS OF FUNDAMENTAL SYMMETRIES AND NEUTRINO PROPERTIES

A Dissertation Presented

by

HAO-LIN LI

Submitted to the Graduate School of the
University of Massachusetts Amherst in partial fulfillment
of the requirements for the degree of

DOCTOR OF PHILOSOPHY

September 2018

Department of Physics

COLLIDER TESTS OF FUNDAMENTAL SYMMETRIES AND NEUTRINO PROPERTIES

A Dissertation Presented

by

HAO-LIN LI

Approved as to style and content by:

Michael J. Ramsey-Musolf, Chair

Stephane Willocq, Member

Patrick I. Draper, Member

Daniel Q. Wang, Member

Menon Narayanan, Department Chair
Department of Physics

DEDICATION

This thesis is dedicated to my parents.

ACKNOWLEDGMENTS

I would thank my advisor Professor Michael Ramsey-Musolf for giving me opportunities to work on various projects and enlightening me when I was in trouble and teaching me the philosophy to do physics. I would thank the committee member, Professor Stephane Willocq, for help me a lot when I had questions in the experiment aspect. I would thank the Professor Patrick Draper and Professor Daniel Wang for giving me valuable advise on my talk and thesis. I would thank Jiang-Hao Yu, Hiren Patel, Kaori Fuyuto, Aniket Joglekar, who are always patient for my questions. I would thank Huai-Ke Guo who support me through the hard time. I would thank Joseph Babcock, Ben Brau and Peter Winslow helping me on using titan cluster. Finally, I would thank my parents for supporting me since I was born.

ABSTRACT

COLLIDER TESTS OF FUNDAMENTAL SYMMETRIES AND NEUTRINO PROPERTIES

SEPTEMBER 2018

HAO-LIN LI

B.S., NANKAI UNIVERSITY

Ph.D., UNIVERSITY OF MASSACHUSETTS AMHERST

Directed by: Professor Michael J. Ramsey-Musolf

The CP parity of the Higgs boson and the details of the electroweak symmetry breaking are the two crucial ingredients to understand the matter-antimatter asymmetry in our universe. Electroweak baryogenesis is an intriguing solution to the puzzle of this unexplained observed asymmetry because of its testability at present and near future collider experiments. The possibilities of testing CP phase in the Two-Higgs-Doublets Models (2HDMs) and the generation of a strong first-order electroweak phase transition (SFOEWPT) in the real singlet model at the future high luminosity LHC are studied. In addition to the specific extensions to the Standard Model (SM), I also study the sensitivity of the future 100 TeV collider in probing the Wilson coefficients of the dimension 6 operators related to the Higgs sector using the effective field theory (EFT) approach. The observed non-zero neutrino mass is another phenomenon that the SM fails to explain. The Left-Right Symmetric Model (LRSM) proposes a natural explanation of the smallness of the neutrino mass and its

connection to the high scale spontaneous parity violation. I study the prospects of searching the heavy right-handed neutrinos and measuring the mixing between the light and heavy neutrinos in the framework of the minimal LRSM at the future 100 TeV hadron collider.

TABLE OF CONTENTS

LIST OF TABLES

Table **Page**

LIST OF FIGURES

Figure **Page**

INTRODUCTION

The discovery of the new Higgs-like particle at the LHC [8, 58] leads us to a new era of particle physics. The standard model (SM) physics is extremely successful in explaining the relation between the electromagnetic and weak interactions, the property of asymptotic freedom in the QCD, the CP violation in the meson system, etc. Nevertheless, there are still many phenomena that the SM fails to explain. Why are there dark matter and dark energy in our universe? Why is matter more than antimatter in our universe? Why do neutrinos have masses? All these evidences indicate the existence of new physics beyond the SM.

The present measurement of the baryon asymmetry of the universe (BAU) is given by the results of the Planck experiments [16] and the Big-Ban Nucleosynthesis (BBN) [213]:

$$Y_B = \frac{n_B}{s} = (8.59 \pm 0.11) \times 10^{-11} \tag{1}$$

where n_B and s are the baryon number and entropy density respectively. The electroweak baryogenesis (EWBG) is one of the appealing solutions to this problem because of its testability at TeV collider experiment. The Sakharov conditions [228] demonstrate three requirements for a successful electroweak baryogenesis: baryon number violation, C and CP violation and the departure from the thermal equilibrium which may processes through a strong first order electroweak phase transition (SFOEWPT). It is well known that the first requirement is satisfied by the electroweak sphaleron process in the SM [195, 179]. However, the CP violation effect in the SM is too feeble [132, 161, 133]and the Higgs mass is too heavy to produce a SFOWEPT [47, 170]. Due to these shortcomings of the SM, new physics models

are proposed to compensate for the insufficient CP violation effect in the SM and to make the electroweak phase transition first-order and strong. These new physics model usually predict new particles with certain interactions with SM particles. In this case, the LHC becomes an excellent machine to test these new physics models by searching for new particles predicted in those models. In the meantime, one can also combine the experimental results from both the high energy searches and the low energy precision measurements to constrain a specific new physics model. Two of my projects related to this topic are: studying the prospective sensitivity of the future high luminosity LHC in constraining the CP violation in the scalar sector in Two-Higgs-Doublet Models (2HDMs) by searching a heavy Higgs decaying to the SM-like Higgs and a Z boson and testing the parameter space that gives the SFOEWPT in the singlet extended SM (xSM) through searching a resonant di-Higgs signal with 4 b quark final state.

Current measurements of the newly discovered scalar particle reveal that it closely resembles the SM Higgs boson and no significant deviation has been found [13]. Therefore, one should try to classify the small deviations from the SM predictions in a systematic way. The standard model effective field theory (SMEFT) provides a general way to write down the higher dimensional non-renormalizable operators that are consistent with the SM symmetries, which translate the small deviations from the SM predictions into the constraints on the Wilson coefficients of those non-renormalizable operators. In this thesis, I study the prospective constraints on the Wilson coefficients of the dimension 6 operators that related to the modification of the di-Higgs production rate relative to the SM by searching a non-resonant di-Higgs signal with the $bb\gamma\gamma$ final state in the future 100 TeV collider.

Neutrino oscillation experiments have confirmed that neutrinos have masses. The origin and the smallness of neutrino masses remain as a mystery that cannot be explained by the SM. Several mechanisms have been proposed to solve this problem,

among which the seesaw mechanisms are popular candidates as it simultaneously explain the origin and smallness of neutrino masses. In different types of seesaw models, the neutrino could be a Majorana fermion, which is closely related to the lepton number violation and can be tested by neutrinoless double-beta decay experiments ($0\nu\beta\beta$). On the other hand, in a certain model, one is also possible to constrain or measure neutrino masses at collider experiments. The Left-Right Symmetric Model is such a model that relates the smallness of neutrino masses to the high-scale restoration of the parity symmetry. It enables us to take advantage of highly boosted decay products of the heavy right-handed W_R boson in the model to scrutinize the the origin of neutrino masses in the future 100TeV collider.

Now I will briefly summarize the results of these four projects.

In the CPV 2HDMs project discussed in Chapter 5, we base on the previous works Ref. [163] and Ref. [61] to study the prospects of testing the CP violation in 2HDMs with the future High-Luminosity (HL) LHC and electric dipole moment (EDM) experiments. We point out that in the zero or small deviation from the alignment limit, the search for a most CP even Higgs h_2 decaying to a Z boson and a SM-like Higgs is directly sensitive to the magnitude of the CP violation effect in the scalar potential. In addition, a positive result from the future collider experiments will indicate an observation of non-zero EDMs. A positive result from EDM experiments with a null result from the future collider will immediately falsify the CPV 2HDMs. On the other hand, if the deviation from the alignment limit is large, then one may not directly draw a conclusion on the CP violation from a positive collider result, because in this case the most CP odd Higgs h_3 will decay to the Zh final state even if CP is conserved. Therefore, additional CP properties of the discovered particle need to be investigated.

In the xSM project discussed in Chapter 6, we estimate the future sensitivity of the HL LHC in searching a resonant heavy scalar S decaying to a pair of SM-like Higgs

with the $4b$ final state. Eleven benchmark points with the largest di-Higgs signal rate and simultaneously giving a SFOEWPT are studied. We found that, comparing with previous studies of $bb\tau\tau$ [208], $bb\gamma\gamma$ [181], 4τ [181] and $bbWW$ [160] final states at HL LHC, the $4b$ final state gives comparable sensitivities with the $bb\gamma\gamma$ and 4τ channel and better signal significance than $bbWW$ channel for a mass of the heavy scalar less than 500 GeV, while for the heavy scalar mass larger than 500 GeV, the $4b$ channel is better than $bb\gamma\gamma$ and 4τ channel but is not competitive with $bbWW$ channel.

In the EFT di-Higgs project 7, we derive the Wilson coefficients of the 6 dimension six operators related to our di-Higgs study for the scalar extensions that can generate these operators at tree level and investigate the reach of the future 100 TeV collider on the UV parameters in each model by searching a di-Higgs signal with the $bb\gamma\gamma$ final state. We point out that for the triplet and quadruplet models, due to the correlation between the strongly constrained Wilson coefficients of the custodial violation operator $|H^\dagger D_\mu H|^2$ and that of the operator $(H^\dagger H)^3$, the modification of the di-Higgs signal rate is not large enough to be distinguishable from the SM. We also find that with a 30 ab^{-1} integrated luminosity the theoretical uncertainties on the production cross-section will be important to distinguish the new physics signal from the SM one.

In the LRSM project discussed in Chapter 8, we study the prospects of measuring neutrino Dirac masses by searching a resonant production of the W_R boson decaying to a positron e^+ and a lightest heavy neutrino N_1, with N_1 decaying purely leptonically to $e^+\mu^-\nu$. The similar purely leptonic final state has been studied in the fermion singlet extension to the SM with Type-I seesaw in Ref. [164]. we first investigate this channel in measuring neutrino Dirac masses in the framework of the LRSM and point out their advantage comparing with the traditional semi-leptonic channels [118, 150].

This thesis is organized as follows. In Chapter 1, I review the electroweak sector in the SM. In Chapter 2, I introduce the effective field theory framework which will

be used in Chapter 7. In Chapter 3, I discuss the general collider phenomenology related to the di-Higgs production. In Chapter 4, I review several seesaw mechanisms that generate small neutrino masses. In Chapter 5, I discuss in details the future collider constraints on CP violation 2HDMs. In Chapter 6, I present the results for the possibility of testing the generation of a SFOEWPT in Singlet xSM the di-Higgs $4b$ channel in the HL LHC. In Chapter 7, The results of the study of the various scalar extensions to the SM using the di-Higgs channel in the future 100TeV collider are demonstrated. In Chapter 8, I give the detailed analysis of the reach of future collider in constraining the Yukawa couplings between the heavy and light neutrinos in the LRSM.

CHAPTER 1

THE ELECTROWEAK SECTOR IN THE STANDARD MODEL

The Standard Model (SM) is a gauge theory based on the gauge group structure: $\mathrm{SU(3)_c} \times \mathrm{SU(2)_L} \times \mathrm{U(1)_Y}$. The $\mathrm{SU(3)_c}$ part describes the strong interaction between quarks and gluon. The $\mathrm{SU(2)_L} \times \mathrm{U(1)_Y}$ part describes the so-called electroweak interaction, which is spontaneously broken to the $U(1)_{em}$ by Brout-Englert-Higgs (BEH) mechanism [112, 155, 156, 157, 178]. In this chapter, I mainly focus on the electroweak sector and discuss the details of the formulation of the theory and BEH mechanism.

1.1 Electroweak Lagrangian

The SM includes three generations of left-handed and right-handed leptons and quarks. They are denoted as:

$$L_L = \left\{ \begin{pmatrix} \nu_L^i \\ e_L^i \end{pmatrix} \right\}, \quad Q_L = \left\{ \begin{pmatrix} u_L^i \\ d_L^i \end{pmatrix} \right\} \tag{1.1}$$

$$e_R = \{e_R^i\}, \quad u_R = \{u_R^i\}, \quad d_R = \{d_R^i\}, \tag{1.2}$$

where L_L and Q_L are doublets of the left-handed lepton and quark fields in the fundamental representation of the $\mathrm{SU(2)_L}$ gauge group. This is the origin of the subscript L of the $\mathrm{SU(2)_L}$. The e_R, u_R, and d_R are right-handed fields of charged leptons, up type quarks and down type quarks respectively. They are singlets under the $\mathrm{SU(2)_L}$ gauge group. The index i represents the generation of quarks and leptons,

which ranges from 1 to 3. The left-handed and right-handed fields are defined by the projections of the four components of the Dirac spinors ψ: $\psi_{R,L} = (1 \pm \gamma^5)\psi$. The charge assignments for these fields are summarized in Table. 1.1.

Field	$SU(3)_c$	$SU(2)_L$	$U(1)_Y$
L_L	1	2	-1/2
Q_L	3	2	1/6
e_R	1	1	-1
u_R	3	1	2/3
d_R	3	1	-1/3

Table 1.1: Charge assignments for the SM fermion fields. For the $SU(3)_c$ and $SU(2)_L$ the 3 and 2 represent the fundamental representations of the corresponding groups respectively, while 1 represents the singlet representation of the corresponding groups.

The principle of gauge invariance introduces gauge fields for each symmetry group. They are denoted as G^a_μ for $SU(3)_c$, W^i_μ for $SU(2)_L$ and B_μ for $U(1)_Y$, where the index a ranges from 1 to 8 and the index i ranges from 1 to 3 corresponding to the number of the generators of SU(3) and SU(2) group respectively. Under a infinitesimal gauge transformation, the gauge fields transform in the following way:

$$\begin{aligned} B_\mu &\rightarrow B_\mu + \frac{1}{g'}\partial_\mu\theta_1, \\ W^i_\mu &\rightarrow W^i_\mu + \frac{1}{g}\partial_\mu\theta^i_2 + \epsilon^{ijk}\theta^j_2 W^k_\mu, \\ G^a_\mu &\rightarrow G^a_\mu + \frac{1}{g_s}\partial_\mu\theta^a_3 + f^{abc}\theta^b_3 G^c_\mu, \end{aligned} \tag{1.3}$$

where θ_1, θ^i_2 and θ^a_3 are small parameters that parametrize the $U(1)_Y$, $SU(2)_L$ and $SU(3)_c$ transformations. g', g and g_s are the corresponding coupling constants for each group. The ϵ^{ijk} and f^{abc} are structure constants of SU(2) and SU(3) group that satisfy:

$$[T^i, T^j] = i\epsilon^{ijk}T^k, \quad [T^a_C, T^b_C] = if^{abc}T^c, \tag{1.4}$$

where $T^i = 1/2\ \sigma^i$ with σ^i Pauli matrices, the generators of the SU(2) group, and T^a_C are Gell-Mann matrices, the generator of the SU(3) group.

Fermions transform in the following ways:

$$\begin{aligned}
L_L &\rightarrow \left(1 + ig'Y_L\theta_1 + igT^j\theta_2^j\right) L_L \\
Q_l &\rightarrow \left(1 + ig'Y_Q\theta_1 + igT^j\theta_2^j + ig_sT_C^a\theta_3^a\right) Q_L \qquad (1.5) \\
e_R &\rightarrow \left(1 + ig'Y_e\theta_1\right) e_R \qquad (1.6) \\
u_R &\rightarrow \left(1 + ig'Y_u\theta_1 + +ig_sT_C^a\theta_3^a\right) u_R \qquad (1.7) \\
d_R &\rightarrow \left(1 + ig'Y_d\theta_1 + +ig_sT_C^a\theta_3^a\right) d_R, \qquad (1.8)
\end{aligned}$$

where $Y_{L,Q,e,u,d}$ are hypercharges of the $\mathrm{U(1)_Y}$ group listed in the fourth column in Table.1.1. By introducing the covariant derivative D_μ:

$$D_\mu = \partial_\mu - ig'YB_\mu - igT^iW_\mu^i - ig_sT_C^aG_\mu^a. \qquad (1.9)$$

One can find that $\not{D}\psi = \gamma^\mu D_\mu\psi$ transforms the same way as the corresponding fermion field.

Now we arrive at the stage to write down the Lagrangian of the kinetic terms of the gauge fields and fermion fields.

$$\begin{aligned}
\mathcal{L}_{\text{fermion}} &= \sum_{\psi=L_L,Q_L,e_R,u_R,d_R} \bar{\psi}i\not{D}\psi \qquad (1.10) \\
\mathcal{L}_{\text{gauge}} &= -\frac{1}{4}B_{\mu\nu}B^{\mu\nu} - \frac{1}{4}W^i_{\mu\nu}W^{i,\mu\nu} - \frac{1}{4}G^a_{\mu\nu}G^{a,\mu\nu}, \qquad (1.11)
\end{aligned}$$

where the field strength tensors $B_{\mu\nu}$, $W^i_{\mu\nu}$ and $G^a_{\mu\nu}$ are:

$$\begin{aligned}
B_{\mu\nu} &= \partial_\mu B_\nu - \partial_\nu B_\mu, \qquad (1.12) \\
W^i_{\mu\nu} &= \partial_\mu W^i_\nu - \partial_\nu W^i_\mu - g\epsilon^{ijk}W^j_\mu W^k_\nu,\ i,j,k = 1,2,3, \qquad (1.13) \\
G^a_{\mu\nu} &= \partial_\mu G^a_\nu - \partial_\nu G^a_\mu - g_sf^{abc}G^b_\mu G^c_\nu,\ a,b,c = 1,...,8. \qquad (1.14)
\end{aligned}$$

It is easy to verify that the above Lagrangian is manifestly gauge invariant. However, the above Lagrangian cannot give rise to the masses of fermions and gauge bosons. The inclusion of the mass term of either fermion fields and gauge fields will break the gauge symmetry. In this sense, one needs a "mechanism" to explain the observed non-zero masses of fermions and gauge bosons.

1.2 Brout-Englert-Higgs (BEH) mechanism

To Explain the observed masses of fermions and gauge bosons, a $\mathrm{SU(2)_L}$ scalar doublet H, called "Higgs field", is introduced. It has hypercharge $Y_H = 1/2$ and is a singlet under $\mathrm{SU(3)_c}$. Now one can write down the gauge invariant Lagrangian involving the Higgs field:

$$\begin{aligned}
\mathcal{L}_{\text{Yukawa}} &= -Y^e \bar{L}_L H e_R - Y^u \bar{Q}_L \tilde{H} u_R - Y^d \bar{Q}_L H d_R + h.c., && (1.15)\\
\mathcal{L}_{\text{Higgs}} &= (D_\mu H)^\dagger (D^\mu H) - V(H), && (1.16)\\
V(H) &= \mu^2 (H^\dagger H) + \frac{\lambda}{4}(H^\dagger H)^2, && (1.17)
\end{aligned}$$

where $\tilde{H} \equiv i\sigma^2 H^*$, and the $*$ represents the complex conjugate transformation and $Y^{e,u,d}$ represents general 3×3 complex Yukawa matrix.

Let us first focus on the Lagrangian terms purely involving the Higgs field $\mathcal{L}_{Higgs}$. The stability restrict $\lambda > 0$. If $\mu^2 > 0$, then the ground state of the Higgs fields is trivially at $\langle H \rangle = 0$. This just gives several new scalar particles and does not give us anything interesting. However, if $\mu^2 < 0$, then one can find that the ground state which minimizes the Higgs potential $V(H)$ gives rise to:

$$\langle H^\dagger H \rangle = v^2/2, \quad v = 2\sqrt{\frac{-\mu^2}{\lambda}}, \tag{1.18}$$

where the angle bracket in the above equations represents the vacuum expectation value (vev). The Eq. 1.18 shows that only the magnitude of the of the vacuum

expectation value of the Higgs fields is determined, the direction of the vev in the $\mathrm{SU(2)_L}$ isospin space is not determined. The different vacua of the Higgs fields are related by a $\mathrm{SU(2)_L}$ transformation. As long as one specific a vacuum direction is chosen by nature, a $\mathrm{SU(2)_L}$ transformation will no longer preserve the vacuum. We call the symmetry is "spontaneously broken" where the Lagrangian satisfies the given symmetry while the vacuum state does not. We can choose the vacuum of the Higgs field to be real and in the lower component as we will see later this choice is consistent with the definition of the $\mathrm{U(1)_{em}}$ charge. In this case, we can parametrize the Higgs doublet as

$$H = \exp\left(2i\frac{\pi^a\tau^a}{v}\right)\begin{pmatrix} 0 \\ \frac{v+h}{\sqrt{2}} \end{pmatrix}, \tag{1.19}$$

where the vev of h to be zero. We can use the $\mathrm{SU(2)_L}$ gauge transformation to absorb three π^a fields such that $H = (0, (v+h)/\sqrt{2})^T$. This gauge is called the unitary gauge. We now plug H into the $\mathcal{L}_{\mathrm{Higgs}}$, and find that the kinetic term $|D_\mu H|^2$ will generate the masses of the gauge bosons:

$$|D_\mu H|^2 \supset g^2\frac{v^2}{8}\left[(W_\mu^1)^2 + (W_\mu^2)^2 + \left(\frac{g'}{g}B_\mu - W_\mu^2\right)^2\right]. \tag{1.20}$$

One found that B_μ and W_μ^3 are mixed with each other. Hence, we can diagonalize the mass matrix with a rotation angle θ_w, and define a massless photon field A_μ and a massive gauge boson field Z_μ:

$$A_\mu \equiv \sin\theta_w W_\mu^3 + \cos\theta_w B_\mu \tag{1.21}$$

$$Z_\mu \equiv \cos\theta_w W_\mu^3 - \sin\theta_w B_\mu, \tag{1.22}$$

with

$$\tan\theta_w = \frac{g'}{g}. \tag{1.23}$$

The $\mathrm{SU(2)_L}$ gauge bosons W^i_μ transform in the adjoint representation, so the interaction between the photon A_μ and W^i_μ are determined by the commutator:

$$g[A_\mu, W^i_\nu T^i] \;=\; g\sin\theta_w W^3_\mu W^i_\mu [T^3, T^i]. \tag{1.24}$$

We define coupling constant for $\mathrm{U(1)_{em}}$ to be $e = g\sin\theta_w$, and $T^\pm = 1/\sqrt{2}(T^1 \pm iT^2)$ with $W^\pm_\mu = 1/\sqrt{2}(W^1_\mu \pm iW^2_\mu)$ to be charge and mass eigenstate of W boson since $[T^3, T^\pm] = \pm T^\pm$. Now the kinetic terms for the physical gauge bosons become:

$$\begin{aligned}\mathcal{L}_{k-g} \;=\; & -\frac{1}{4}F^2_{\mu\nu} - \frac{1}{4}Z^2_{\mu\nu} + \frac{1}{2}m^2_Z Z^\mu Z_\mu \\ & -\frac{1}{2}W^{*\mu\nu}W_{\mu\nu} + m^2_W W^+_\mu W^{-,\mu},\end{aligned} \tag{1.25}$$

where

$$m_Z = \frac{gv}{2\cos\theta_w},\; m_W = \frac{vg}{2} \tag{1.26}$$

$$Z_{\mu\nu} = \partial_\mu Z_\nu - \partial_\nu Z_\mu \tag{1.27}$$

$$W_{\mu\nu} = \partial_\mu W^-_\nu - \partial_\nu W^-_\mu \tag{1.28}$$

$$F_{\mu\nu} = \partial_\mu A_\nu - \partial_\nu A_\mu, \tag{1.29}$$

and we have the tree level relation between m_Z and m_W:

$$m_Z = \frac{m_W}{\cos\theta_w}. \tag{1.30}$$

We can now write the covariant derivative in Eq. 1.9 in terms of gauge bosons mass eigenstates:

$$
\begin{aligned}
D_\mu &= \partial_\mu - ieA_\mu(T^3 + Y\mathbb{1}) - ieZ_\mu(\cot\theta_w T^3 - \tan\theta_w Y\mathbb{1}) \\
&\quad -i\frac{e}{\sqrt{2}\sin\theta_w}(W_\mu^+ T^+ + W_\mu^- T^-) - ig_s T_C^a G_\mu^a. \qquad (1.31)
\end{aligned}
$$

From the above equation, one can immediately read out the definition of the electric charge:

$$
Q = T^3 + Y, \qquad (1.32)
$$

under which the second component of the Higgs doublet is neutral and is invariant under the $\mathrm{U}(1)_{\mathrm{em}}$ transformation.

Now let us discuss the masses of fermion fields. Plugging H as its vacuum expectation value into the Lagrangian in Eq. 1.15 one can obtain the fermion mass matrices. Here we only focus on the quark sector:

$$
\mathcal{L}_{q-m} = -\frac{v}{\sqrt{2}}[\bar{d}_L Y^d d_R + \bar{u}_L Y^u u_R] + h.c.\ , \qquad (1.33)
$$

where we have suppressed the flavor index. One can use a bi-unitary diagonalization to obtain the mass eigenstates of quark fields. The idea is following, though the Yukawa matrices Y are arbitrary 3×3 complex matrices, $YY^\dagger$ are Hermitian and have real eigenvalues. So we have:

$$
Y^d Y^{d\dagger} = U_d M_d^2 U^{d\dagger}, \quad Y^u Y^{u\dagger} = U_u M_u^2 U^{u\dagger}. \qquad (1.34)
$$

Then we can use the singular value decomposition (SVD) to decompose Y^d and Y^u:

$$
Y^d = U_d M_d K_d^\dagger, \quad Y^u = U_u M_u K_u^\dagger, \qquad (1.35)
$$

where $U_{d,u}$ and $K_{d,u}$ are all unitary matrices. we can now define mass eigenstates of quarks as $u^m_{L,R}$ and $d^m_{L,R}$:

$$u^m_L = U^\dagger_u u_L,\ u^m_R = K^\dagger_u u_R,\ d^m_L = U^\dagger_d d_L,\ d^m_R = K^\dagger_d d_R. \tag{1.36}$$

Now the $\mathcal{L}_{q-m}$ becomes diagonal:

$$\mathcal{L}_{q-m} = -m^u_i \bar{u}^i_L u^i_R - m^d_i \bar{d}^i_L d^i_R + h.c.\ , \tag{1.37}$$

where $m^{u,d}_i$ are the diagonal elements of $v/\sqrt{2}M_{u,d}$. We have already omitted the superscript m for each fermion spinor in the above equation and from now on all the fermion spinors represent their mass eigenstates. Up to now, the Lagrangian has a $\mathrm{U}(1)^6$ symmetry parametrized by six phases δ^1_i and δ^2_i under which

$$d^i_L \to e^{i\delta^1_i} d^i_L, \quad d^i_R \to e^{i\delta^1_i} d^i_R, \quad u^i_L \to e^{i\delta^2_i} u^i_L, \quad u^i_R \to e^{i\delta^2_i} u^i_R. \tag{1.38}$$

These phases can be used to absorb the phases in the CKM matrix as we will see below. Expanding the covariant derivative in Eq. 1.10, we find the interactions for the neutral current and the charged current are:

$$\mathcal{L}_{neutral} = \frac{2e}{\sin 2\theta_w}\left[\bar{q}_L(T^3 - \sin^2\theta_w Q)\not{Z} q_L - \sin^2\theta_w Q \bar{q}_R \not{Z} q_R\right] + eQ\bar{q}\not{A}q \tag{1.39}$$

$$\mathcal{L}_{charged} = \frac{e}{\sqrt{2}\sin\theta_w}\bar{u}^i_L(\not{W}^+)V^{ij}d^j_L + h.c. \tag{1.40}$$

where Q and T_3 are the corresponding electric charge and the weak isospin for quark fields, V^{ij} is the CKM matrix defined by $V \equiv U^\dagger_u U_d$. The indices i and j are quark flavor indices which can be set to $\{1,2,3\}$ corresponding to $\{u,c,t\}$ for up-type quarks and $\{d,s,b\}$ for down-type quarks. One can observe from the above equations that neutral currents mediated by Z bosons and photons do not change the flavor of quarks

while charged currents have the feature of changing the quark flavors. In principle, the CKM matrix is a complex 3×3 unitary matrix with nine real degrees of freedom: 3 rotation angles and 6 phases. However, when taking into account the rephasing degrees of freedoms of six quarks, 5 complex phases can be absorbed, leaving only 3 rotation angles and 1 complex phase. It is this complex phase that triggers the CP violation in the SM through the weak interaction.

1.3 Custodial Symmetry and Electroweak Precision Test

As one can observe from Eq. 1.30 that, at tree level, the mass ratio of W boson to Z bosons is simply $\cos\theta_w$. We define the ρ-parameter:

$$\rho \equiv \frac{m_W^2}{m_Z^2 \cos^2\theta_w}. \tag{1.41}$$

At tree level $\rho_0 = 1$ is guaranteed by a symmetry called the "Custodial Symmetry". To see on earth what this symmetry is, let us first focus on the terms from the Higgs potential. If one parametrize the Higgs field linearly as:

$$H = \frac{1}{\sqrt{2}} \begin{pmatrix} h_3 + ih_4 \\ h_1 + ih_2 \end{pmatrix}, \tag{1.42}$$

then the Higgs potential $V(H)$ becomes:

$$V(H) = \lambda(H^\dagger H - \frac{v^2}{2})^2 = \frac{\lambda}{2}(h_1^2 + h_2^2 + h_3^2 + h_4^2 - v^2)^2. \tag{1.43}$$

The Higgs potential above actually possesses a larger global SO(4) symmetry, which is homomorphic to $\mathrm{SU}(2)\times\mathrm{SU}(2)$. In just a moment, we will demonstrate this two SU(2) can be associated to the $\mathrm{SU}(2)_\mathrm{L} \times \mathrm{SU}(2)_\mathrm{R}$ symmetry in the zero quark mass limit in QCD. When H gets a vev, for example, $\langle h_1 \rangle = v$ and $\langle h_2 \rangle = \langle h_3 \rangle = \langle h_4 \rangle = 0$, then the

ground state actually still has a residual SO(3) symmetry: a 3D rotational symmetry in the 4D Higgs field components spaces that preserve $\langle h_1 \rangle = v$. Since SO(3) is homomorphic to SU(2), it is this residual SU(2) symmetry called the Custodial SU(2).

Let us now consider the fact that the SM is a gauge theory with Yukawa interactions between fermions and Higgs fields and find out what effects break the custodial symmetry. To proceed, we write the Higgs field in terms of 2 doublets such that the SU(2) $\times$ SU(2) symmetry in the potential is more transparent:

$$\Sigma = \left(H, \tilde{H}\right). \tag{1.44}$$

In the meantime, we define the left and right quark fields in two doublets:

$$Q_L = \begin{pmatrix} u_L^i \\ d_L^i \end{pmatrix}, \quad Q_R = \begin{pmatrix} u_R^i \\ d_R^i \end{pmatrix}. \tag{1.45}$$

The kinetic terms for the Higgs field and the Yukawa interactions for quark fields can be written as:

$$\begin{aligned} \mathcal{L}_{LR} &= \frac{1}{2}\mathrm{Tr}\left[D_\mu \Sigma (D^\mu \Sigma)^\dagger\right] - \frac{\mu^2}{2}\mathrm{Tr}\left[\Sigma\Sigma^\dagger\right] - \frac{\lambda}{8}\mathrm{Tr}\left[\Sigma\Sigma^\dagger\right]^2 \\ &\quad -\frac{1}{\sqrt{2}}(\bar{Q}_L \Sigma \mathcal{Y} Q_R + h.c.), \end{aligned} \tag{1.46}$$

where $\mathcal{Y} = \mathrm{diag}(Y^u, Y^d)$, and the covariant derivative of the Σ field is:

$$D_\mu \Sigma = \partial_\mu \Sigma + igW_\mu^a T^a \Sigma + ig' B_\mu \Sigma T^3. \tag{1.47}$$

The above equations illustrate that when $g' = 0$ and $Y^u = Y^d$, the Lagrangian obtains a $\mathrm{SU(2)_L} \times \mathrm{SU(2)_R}$ symmetry, under which:

$$\Sigma \to L\Sigma R^\dagger,\ Q_L \to LQ_L,\ Q_R \to RQ_R. \tag{1.48}$$

After the electroweak symmetry breaking, the Σ gets a vev: $\mathrm{diag}(v, v)$, which is invariant under a $\mathrm{SU(2)_V}$ symmetry where $R = L$. This is exactly the custodial symmetry we are discussing. Meanwhile, we can easily find out the two sources of the custodial symmetry breaking in the SM: the non-vanishing $\mathrm{U(1)_Y}$ coupling and the fact that $Y^u \neq Y^d$. Since Yukawa couplings are generally small in the standard model except for the top quark, the correction to the ρ parameter is dominant by the loop involving the third generation quarks. At one loop level the correction to ρ in the SM is defined by $\Delta\rho^{SM} = \rho - 1$, which is equal to:

$$\Delta\rho^{SM} = \frac{\Pi_{WW}(0)}{m_W^2} - \frac{\Pi_{ZZ}(0)}{m_Z^2}, \tag{1.49}$$

where $\Pi_{WW}(0)$ and $\Pi_{ZZ}(0)$ are the vacuum polarization functions for W and Z bosons at zero momentum. Often, one can absorb $\Delta\rho^{SM}$ from the SM into the definition of the ρ ($\rho \to \rho - \Delta\rho^{SM}$) such that by definition $\rho = 1$ in the SM.

The observable ρ discussed above is one of a set of parameters that measures the level of the deviation from the SM using electroweak precision data (EWPD). Similar to the ρ parameter, Peskin and Takeuchi proposed a set of oblique parameters S, T and U [214] to characterize deviations from the SM using the EWPD such as the electron magnetic dipole moment, the lifetime of the muon, the Z and W pole masses and the polarization asymmetry in the Z boson production etc.. They are defined as:

$$T \equiv \frac{1}{\alpha_e}\left(\frac{\Pi_{WW}^{new}(0)}{m_W^2} - \frac{\Pi_{ZZ}^{new}(0)}{m_Z^2}\right) = \frac{\rho - 1}{\alpha_e}, \tag{1.50}$$

$$S \equiv \frac{4c^2s^2}{\alpha_e}\left[\frac{\Pi_{ZZ}^{new}(m_Z^2)}{m_Z^2} - \frac{c^2 - s^2}{cs}\frac{\Pi_{Z\gamma}^{new}(m_Z^2)}{m_Z^2} - \frac{\Pi^{new}(m_Z^2)}{m_Z^2}\right], \tag{1.51}$$

$$U \equiv \frac{4s^2}{\alpha_e}\left[\frac{\Pi_{WW}^{new}(m_W^2) - \Pi_{WW}^{new}(0)}{m_W^2} - \frac{c}{s}\frac{\Pi_{Z\gamma}^{new}(m_Z^2)}{m_Z^2} - \frac{\Pi_{\gamma\gamma}^{new}(m_Z^2)}{m_Z^2}\right] - S, \tag{1.52}$$

where $c = \cos\theta_w$, $s = \sin\theta_w$, $\alpha_e = \alpha_e(m_Z)$, the *new* in the superscripts of the Π functions represents that only new physics contributions are taken into account. In

the SM, $S = T = U = 0$ by definition. The current global fit results by Gfitter group and related details are in Ref [30]. With $m_t = 173$GeV and $m_h = 125$GeV we obtain: $S = 0.05 \pm 0.11$, $T = 0.09 \pm 0.13$ and $U = 0.01 \pm 0.11$, and the 2D global fit in the $S - T$ plane with U a free parameter is given in Fig. 1.1. Practically, S and

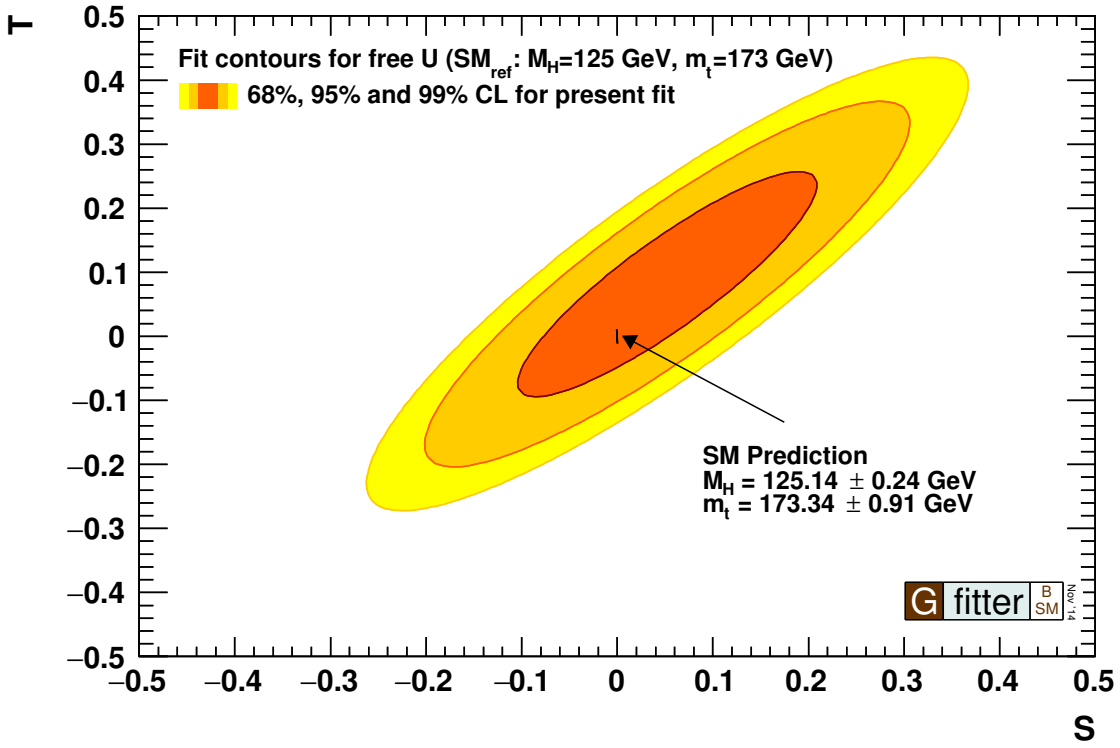

Figure 1.1: The 68%, 95%, and 99% confidence level contours in the TS-plane. with $M_h = 125$ GeV and $m_t = 173$ GeV. The result is given by Giffter group [1]

T will generally give stronger constraints than U. Since T is equivalent with the ρ parameter, it measures the level of the custodial symmetry breaking. On the other hand, the S parameter will get corrections if a new $SU(2)_L$ doublet presents in the new physics model even if there is no new source of the custodial symmetry breaking in it i.e. $T = 0$.

Oblique parameters serve as stringent constraints on the new physics model. We will use the current experimental results mentioned above to constrain the parameter space of new physics models in Chapter 5, 7, and 6.

CHAPTER 2

STANDARD MODEL EFFECTIVE FIELD THEORY

Engineers building the bridge and skyscrapers do not need to know how nuclear interact with each other, chemist do not need to know how quantum electrodynamic works to study how organic molecules synthesize. It is interesting to notice that there are different languages to describe the nature of the world at different scales. For the particle physicist, this fact even becomes one of the most important philosophy in doing research. The fact that the physics law in the large distance is usually independent of fine details in the short distance enables us to use the "Effective Field Theory" (EFT) approach to study the physics phenomena at a certain scale. The words "Effective" has already illustrated the fact that the theory or the model is not a "complete" one but instead an appropriate one. This kind of theories isolate a set of the most important effects in the problems and are able to give accurate enough solutions and predictions.

There are generally two categoriesof approaches for a particle physicist to use EFT. The first one is the "top-down" EFT, it assumes that the high energy theory is already known and the low energy EFT is derived by integrating out the heavy degrees of freedoms. At first glance it seems that you gain nothing from this approach because you have already known everything, why not just use the original theory to study the problem without loss of any information but instead use an approximate one. The reason is that in the regimes of the perturbation theory it is usually harder to compute the physical observables from the full theory, while the EFT approach gives you a convenient way to organize your calculation. One example of this usage is the QCD

correction to the weak interaction at the low energy scale. [136, 130, 23] Another situation that one needs a "top-down" EFT is that you have a strong dynamics is present in the full theory at the low energy scale, and you are not able to use the degrees of freedom in the full theory to compute low energy observables perturbatively. In this case it is easier to use the EFT with new degrees of freedom, usually the composite states, in the low energy regime to give predictive results. The example for this is the chiral perturbation theory. [194]

The second one is "bottom-up" EFT, this is a more intuitive way to use EFT, it assumes that the UV completion is unknown, the only information accessible is the low energy degrees of freedom and symmetries. In this sense, whatever UV completions exist, they must obey the same symmetries and have the same effective degrees of freedom in the low energy. Hence, I can systematically parametrize the UV effects by writing down non-renormalizable terms in the Lagrangian with the low energy degrees of freedom that satisfy the observed low energy symmetries. These non-renormalizable Lagrangian terms are classified by the order of suppression of the scales of the high energy theory and the number of loops in the diagrams that generate certain terms. The example for this is the SM EFT. [52, 147, 137, 145, 151]

In this chapter, I will first discuss the general idea of the effective field theory including the concepts of running and matching, then introduce a specific form of effective field theory, the standard model effective field theory (SMEFT) that will be used in Chapter 5, 7, and 6.

2.1 EFT: General Idea

First of all, I explain the meaning of the "Integrated out" and the processes of matching and running. I start with a UV theory containing heavy degrees of freedom χ with mass scale M and the light degrees of freedom ϕ. In a mass independent renormalization scheme, formally, the matching at the renormalization scale $\mu = M$

means equating the effective action of the effective field theory without the heavy degrees of freedom χ to the effective action of the full theory with the path integral of the heavy degrees of freedom completed:

$$e^{iS_{eff}[\phi]} = \int \mathcal{D}\chi e^{iS[\phi,\chi]}, \tag{2.1}$$

I can proceed with this formal path integral by expanding the heavy field χ around its classical solution:

$$\chi = \chi_c + \eta \quad \text{with} \quad \frac{\delta S}{\delta \chi_c} = 0, \tag{2.2}$$

where η is the quantum fluctuation around the classical solution and $\delta S/\delta\chi_c = 0$ is just the classical equation of motion (EOM) of the field χ. Now I can perform the path integral:

$$\begin{aligned} e^{iS_{eff}[\phi](\mu)} &= \int \mathcal{D}\chi e^{iS[\phi,\chi](\mu)} \\ &= \int \mathcal{D}\eta e^{i(S[\phi,\chi_c]+\frac{1}{2}\eta\frac{\delta^2 S}{\delta\chi_c^2}\eta+...)} \\ &= const \times e^{iS[\phi,\chi_c]}\left[\det\left(-\frac{\delta^2 S}{\delta\chi_c^2}\right)\right]^{1/2}. \end{aligned} \tag{2.3}$$

The ... represents higher order expansions, and one can identify that:

$$S_{eff}[\phi](\mu = M) = S[\phi, \chi_c(\phi)](\mu = M) + \frac{i}{2}\mathrm{Tr}\log\left(-\frac{\delta^2 S}{\delta\chi_c^2}\right) + ... \tag{2.4}$$

The first term on the right-hand side is the tree level matching. It represents to replace the field χ in the original Lagrangian with the solution of the classical EOM of χ in terms of the field ϕ. The second term on the right-hand side corresponds to the one-loop correction. The details of the treatment of these matching procedure in practice can be found in Ref. [151].

After this formal "Integrate out" procedure one can obtain nonlocal expressions for the effective Lagrangian. The idea follows is expanding these nonlocal terms in the momentum space of the order p/M and truncating them to any finite order to obtain the local Lagrangian. In this sense, one can express the local effective Lagrangian at the renormalization scale $\mu = M$ as:

$$\mathcal{L}_{eff}(M) = \mathcal{L}_{full}[\phi](M) + \sum \frac{1}{M^{d_i-4}} c_i(M)\mathcal{O}_i \tag{2.5}$$

where the $\mathcal{L}_{full}[\phi](M)$ represents the terms in the original UV Lagrangian that only contain the field ϕ i.e. the kinetic terms of ϕ and the interaction terms only involving ϕ, d_i is the dimension of the operator $\mathcal{O}_i$, $c_i(M)$ is the Wilson coefficient related to the corresponding operator at the renormalization scale $\mu = M$. In my thesis, I only utilize the tree level matching piece.

As one can see from Eq.2.3 and 2.4, the matching is performed at the scale of the heavy particle mass. If one would like to compute observables at some lower scale, one may need to take into account the renormalization group equation (RGE) correction and run the Wilson coefficients to the lower scale to resum the large logarithm effect. At one loop level, The RGE equations are generally written as:

$$\frac{\mathrm{d}c_i(\mu)}{\mathrm{d}\log\mu} = \sum_i \frac{1}{16\pi^2}\gamma_{ij}c_j \tag{2.6}$$

where γ_{ij} is the matrix of anomalous dimension. Whether to perform the RGE correction strongly depends on the scale of the new physics and the level of precision that the calculation needed. For example, one matches the SM EFT at GUT scale and try to calculate the electroweak precision observable near the Z boson mass scale, then one would need to investigate the RGE corrections carefully. If one assumes the new physics scale is around several TeV, then in general one only needs to consider the RGE corrections for c_i originated from c_j if c_i is not generated at tree level and

c_j is generated at tree level. [151] Theoretically, the RGE running is a consecutive matching procedure from the scale μ to $\mu - d\mu$.

2.2 The SM EFT

In this section, I introduce a specific type of EFT which I will use in the Chapter. 5 and 7, the SM EFT. I will introduce a complete set of dimension six operators that satisfy the SM gauge symmetries and assuming no lepton and baryon number violation (the only dimension five operator turns out to be lepton number violation and generates Majorana masses for neutrinos). Historically, a complete set of dimension six operators that obey the SM symmetry was first lists in Ref. [52] where there are 80 operators. However, Ref. [145] pointed out that only 59 of them are independent, the rest of them can be translated into these 59 by integrating by parts, equation of motions and group identities. This is the first time that people find out a complete basis of dimension six operators without redundancy in the SM EFT, and we call this basis the "Warsaw basis". Several other complete bases are introduced for certain phenomenological concerns, one of the popular basis is "SILH" [109, 110] which concerns the UV completion involving a strong dynamics while the low energy theory still respects linearly realized EW symmetry. Another popular basis is "HISZ" [148], which maximizes the use of the bosonic operators.

In the "Warsaw basis", there are 10 categories of the operators:

1. X^3, the operators contain three gauge field strength tensors

$$Q_G \quad f^{abc} G_\mu^{a\nu} G_\nu^{b\rho} G_\rho^{c\mu} \tag{2.7}$$

$$Q_{\widetilde{G}} \quad f^{abc} \widetilde{G}_\mu^{a\nu} G_\nu^{b\rho} G_\rho^{c\mu} \tag{2.8}$$

$$Q_W \quad \varepsilon^{ijk} W_\mu^{i\nu} W_\nu^{j\rho} W_\rho^{k\mu} \tag{2.9}$$

$$Q_{\widetilde{W}} \quad \varepsilon^{ijk} \widetilde{W}_\mu^{i\nu} W_\nu^{j\rho} W_\rho^{k\mu} \quad . \tag{2.10}$$

2. φ^6 and $\varphi^4 D^2$, the operators only contain Higgs doublet.

$$Q_{\varphi} \qquad (\varphi^\dagger\varphi)^3 \tag{2.11}$$

$$Q_{\varphi\Box} \qquad (\varphi^\dagger\varphi)\Box(\varphi^\dagger\varphi) \tag{2.12}$$

$$Q_{\varphi D} \quad \left(\varphi^\dagger D^\mu\varphi\right)^\star \left(\varphi^\dagger D_\mu\varphi\right) \quad . \tag{2.13}$$

3. $\psi^2\varphi^3$, the operators contain 2 fermions and 3 Higgs doublets

$$Q_{e\varphi} \quad (\varphi^\dagger\varphi)(\bar{l}_p e_r \varphi) \tag{2.14}$$

$$Q_{u\varphi} \quad (\varphi^\dagger\varphi)(\bar{q}_p u_r \widetilde{\varphi}) \tag{2.15}$$

$$Q_{d\varphi} \quad (\varphi^\dagger\varphi)(\bar{q}_p d_r \varphi) \quad . \tag{2.16}$$

4. $X^2\varphi^2$, the operators contain 2 gauge field strength tensors and 2 Higgs doublets

$$Q_{\varphi G} \quad \varphi^\dagger\varphi\, G^A_{\mu\nu} G^{A\mu\nu} \tag{2.17}$$

$$Q_{\varphi\widetilde{G}} \quad \varphi^\dagger\varphi\, \widetilde{G}^A_{\mu\nu} G^{A\mu\nu} \tag{2.18}$$

$$Q_{\varphi W} \quad \varphi^\dagger\varphi\, W^I_{\mu\nu} W^{I\mu\nu} \tag{2.19}$$

$$Q_{\varphi\widetilde{W}} \quad \varphi^\dagger\varphi\, \widetilde{W}^I_{\mu\nu} W^{I\mu\nu} \tag{2.20}$$

$$Q_{\varphi B} \quad \varphi^\dagger\varphi\, B_{\mu\nu} B^{\mu\nu} \tag{2.21}$$

$$Q_{\varphi\widetilde{B}} \quad \varphi^\dagger\varphi\, \widetilde{B}_{\mu\nu} B^{\mu\nu} \tag{2.22}$$

$$Q_{\varphi WB} \quad \varphi^\dagger\sigma^I\varphi\, W^I_{\mu\nu} B^{\mu\nu} \tag{2.23}$$

$$Q_{\varphi\widetilde{W}B} \quad \varphi^\dagger\sigma^I\varphi\, \widetilde{W}^I_{\mu\nu} B^{\mu\nu} \quad . \tag{2.24}$$

5. $\psi^2 X\varphi$, the operators contain 2 fermion fields, 1 Gauge field and 1 Higgs doublet.

$$Q_{eW} \quad (\bar{l}_p \sigma^{\mu\nu} e_r)\sigma^I \varphi W^I_{\mu\nu} \tag{2.25}$$

$$Q_{eB} \quad (\bar{l}_p \sigma^{\mu\nu} e_r)\varphi B_{\mu\nu} \tag{2.26}$$

$$Q_{uG} \quad (\bar{q}_p \sigma^{\mu\nu} T^a u_r)\widetilde{\varphi}\, G^a_{\mu\nu} \tag{2.27}$$

$$Q_{uW} \quad (\bar{q}_p \sigma^{\mu\nu} u_r)\sigma^I \widetilde{\varphi}\, W^I_{\mu\nu} \tag{2.28}$$

$$Q_{uB} \quad (\bar{q}_p \sigma^{\mu\nu} u_r)\widetilde{\varphi}\, B_{\mu\nu} \tag{2.29}$$

$$Q_{dG} \quad (\bar{q}_p \sigma^{\mu\nu} T^a d_r)\varphi\, G^a_{\mu\nu} \tag{2.30}$$

$$Q_{dW} \quad (\bar{q}_p \sigma^{\mu\nu} d_r)\sigma^I \varphi\, W^I_{\mu\nu} \tag{2.31}$$

$$Q_{dB} \quad (\bar{q}_p \sigma^{\mu\nu} d_r)\varphi\, B_{\mu\nu} \quad . \tag{2.32}$$

6. $\psi^2\phi^2 D$, the operators contain 2 fermion fields, 2 Higgs doublets and 1 covariant derivative.

$$Q^{(1)}_{\varphi l} \quad (\varphi^\dagger i \overleftrightarrow{D}_\mu \varphi)(\bar{l}_p \gamma^\mu l_r) \tag{2.33}$$

$$Q^{(3)}_{\varphi l} \quad (\varphi^\dagger i \overleftrightarrow{D}^I_\mu \varphi)(\bar{l}_p \sigma^I \gamma^\mu l_r) \tag{2.34}$$

$$Q_{\varphi e} \quad (\varphi^\dagger i \overleftrightarrow{D}_\mu \varphi)(\bar{e}_p \gamma^\mu e_r) \tag{2.35}$$

$$Q^{(1)}_{\varphi q} \quad (\varphi^\dagger i \overleftrightarrow{D}_\mu \varphi)(\bar{q}_p \gamma^\mu q_r) \tag{2.36}$$

$$Q^{(1)}_{\varphi q} \quad (\varphi^\dagger i \overleftrightarrow{D}_\mu \varphi)(\bar{q}_p \gamma^\mu q_r) \tag{2.37}$$

$$Q^{(3)}_{\varphi q} \quad (\varphi^\dagger i \overleftrightarrow{D}^I_\mu \varphi)(\bar{q}_p \sigma^I \gamma^\mu q_r) \tag{2.38}$$

$$Q_{\varphi u} \quad (\varphi^\dagger i \overleftrightarrow{D}_\mu \varphi)(\bar{u}_p \gamma^\mu u_r) \tag{2.39}$$

$$Q_{\varphi d} \quad (\varphi^\dagger i \overleftrightarrow{D}_\mu \varphi)(\bar{d}_p \gamma^\mu d_r) \tag{2.40}$$

$$Q_{\varphi ud} \quad i(\widetilde{\varphi}^\dagger D_\mu \varphi)(\bar{u}_p \gamma^\mu d_r) \tag{2.41}$$

$$. \tag{2.42}$$

7. $(\bar{L}L)(\bar{L}L)$, the four fermion operators that only involving the left handed fields.

$$Q_{ll} \qquad (\bar{l}_p\gamma_\mu l_r)(\bar{l}_s\gamma^\mu l_t) \tag{2.43}$$

$$Q_{qq}^{(1)} \qquad (\bar{q}_p\gamma_\mu q_r)(\bar{q}_s\gamma^\mu q_t) \tag{2.44}$$

$$Q_{qq}^{(3)} \quad (\bar{q}_p\gamma_\mu \sigma^I q_r)(\bar{q}_s\gamma^\mu \sigma^I q_t) \tag{2.45}$$

$$Q_{lq}^{(1)} \qquad (\bar{l}_p\gamma_\mu l_r)(\bar{q}_s\gamma^\mu q_t) \tag{2.46}$$

$$Q_{lq}^{(3)} \quad (\bar{l}_p\gamma_\mu \sigma^I l_r)(\bar{q}_s\gamma^\mu \sigma^I q_t) \quad . \tag{2.47}$$

8. $(\bar{R}R)(\bar{R}R)$, the four fermion operators that only involving the right handed fields.

$$Q_{ee} \qquad (\bar{e}_p\gamma_\mu e_r)(\bar{e}_s\gamma^\mu e_t) \tag{2.48}$$

$$Q_{uu} \qquad (\bar{u}_p\gamma_\mu u_r)(\bar{u}_s\gamma^\mu u_t) \tag{2.49}$$

$$Q_{dd} \qquad (\bar{d}_p\gamma_\mu d_r)(\bar{d}_s\gamma^\mu d_t) \tag{2.50}$$

$$Q_{eu} \qquad (\bar{e}_p\gamma_\mu e_r)(\bar{u}_s\gamma^\mu u_t) \tag{2.51}$$

$$Q_{ed} \qquad (\bar{e}_p\gamma_\mu e_r)(\bar{d}_s\gamma^\mu d_t) \tag{2.52}$$

$$Q_{ud}^{(1)} \qquad (\bar{u}_p\gamma_\mu u_r)(\bar{d}_s\gamma^\mu d_t) \tag{2.53}$$

$$Q_{ud}^{(8)} \quad (\bar{u}_p\gamma_\mu T^a u_r)(\bar{d}_s\gamma^\mu T^a d_t) \quad . \tag{2.54}$$

9. $(\bar{L}L)(\bar{R}R)$, the four fermion operators with right handed and the left handed vector currents.

$$Q_{le} \qquad (\bar{l}_p\gamma_\mu l_r)(\bar{e}_s\gamma^\mu e_t) \tag{2.55}$$

$$Q_{lu} \qquad (\bar{l}_p\gamma_\mu l_r)(\bar{u}_s\gamma^\mu u_t) \tag{2.56}$$

$$Q_{ld} \qquad (\bar{l}_p\gamma_\mu l_r)(\bar{d}_s\gamma^\mu d_t) \tag{2.57}$$

$$Q_{qe} \qquad (\bar{q}_p\gamma_\mu q_r)(\bar{e}_s\gamma^\mu e_t) \tag{2.58}$$

$$Q_{qu}^{(1)} \qquad (\bar{q}_p\gamma_\mu q_r)(\bar{u}_s\gamma^\mu u_t) \tag{2.59}$$

$$Q_{qu}^{(8)} \quad (\bar{q}_p\gamma_\mu T^a q_r)(\bar{u}_s\gamma^\mu T^a u_t) \tag{2.60}$$

$$Q_{qd}^{(1)} \qquad (\bar{q}_p\gamma_\mu q_r)(\bar{d}_s\gamma^\mu d_t) \tag{2.61}$$

$$Q_{qd}^{(8)} \quad (\bar{q}_p\gamma_\mu T^a q_r)(\bar{d}_s\gamma^\mu T^a d_t). \tag{2.62}$$

10. $(\bar{L}R)(\bar{L}R)$ and $(\bar{L}R)(\bar{R}L)$ the four fermion operators with the scalar and tensor interactions.

$$Q_{ledq} \qquad (\bar{l}_p^j e_r)(\bar{d}_s q_t^j) \tag{2.63}$$

$$Q_{quqd}^{(1)} \qquad (\bar{q}_p^j u_r)\varepsilon_{jk}(\bar{q}_s^k d_t) \tag{2.64}$$

$$Q_{quqd}^{(8)} \quad (\bar{q}_p^j T^a u_r)\varepsilon_{jk}(\bar{q}_s^k T^a d_t) \tag{2.65}$$

$$Q_{lequ}^{(1)} \qquad (\bar{l}_p^j e_r)\varepsilon_{jk}(\bar{q}_s^k u_t) \tag{2.66}$$

$$Q_{lequ}^{(3)} \quad (\bar{l}_p^j \sigma_{\mu\nu} e_r)\varepsilon_{jk}(\bar{q}_s^k \sigma^{\mu\nu} u_t) \quad . \tag{2.67}$$

For the covariant derivatives with double arrow, we define:

$$\varphi^\dagger i\overleftrightarrow{D}_\mu \varphi \equiv i\varphi^\dagger\left(D_\mu - \overleftarrow{D}_\mu\right)\varphi \qquad \text{and} \qquad \varphi^\dagger i\overleftrightarrow{D}^I_\mu \varphi \equiv i\varphi^\dagger\left(\sigma^I D_\mu - \overleftarrow{D}_\mu \sigma^I\right)\varphi, \tag{2.68}$$

where the index I associated with σ is the index of the SU(2) generators, the index a associated with T is the index of the SU(3) generators, the indices $prst$ are the flavor indices of the corresponding fermion fields, the q and l are the left-handed quark and lepton doublets, e, d, u are the right-handed singlets of leptons, up type and down type quarks.

In the Chapter 5, we will use the operator in Eq. 2.8 which gives the Weinberg three Gluon operator, and the operators in Eq. 2.25-Eq. 2.32 that generate quark chromo electric dipole moments and ordinary fermion electric dipole moments to study the constraint on the CPV2HDM parameter space from low energy EDM experiments. In the Chapter 7, I will estimate the sensitivity of the di-Higgs channel in the future 100 TeV collider to the Wilson coefficients of the operators in Eq. 2.11-Eq. 2.16 generated from different scalar extensions to the SM.

CHAPTER 3

DIHIGGS PRODUCTION IN PP COLLIDER

The Higgs pair production channel is one of the most important channels to test the Higgs mechanism and the electroweak symmetry breaking in the SM at proton-proton colliders. One of the reasons this channel is so interesting is that it is sensitive to the trilinear Higgs coupling at tree level. In the meantime, this channel also provides a portal to study various beyond standard model physics. A recent review of the di-Higgs search at the LHC and beyond can be found in Ref. [245]. In this chapter, we will first discuss the influence of BSM physics to this channel.

3.1 Di-Higgs production in the SM

In the SM, one can expand the Higgs potential in Eq. 1.17 in the unitary gauge in terms of the Higgs mass and the vev of the Higgs field:

$$V(h) = V_0 + \frac{1}{2}m_h^2 h^2 + \frac{m_h^2}{2v^2}vh^3 + \frac{m_h^2}{8v^2}h^4. \tag{3.1}$$

One can find that the trilinear Higgs coupling λ_{HHH} is determined by the Higgs mass and vev, which is a unique feature of the spontaneous electroweak symmetry breaking in the SM.

The di-Higgs production in the SM at pp collider is dominant by the gluon fusion mode [32]. Two Feynman diagrams related to this production are shown in Fig. 3.1. The loop is dominant by the top quark contribution, and the sub-dominant contribution from the bottom quark gives about 1% correction. Loops with other light

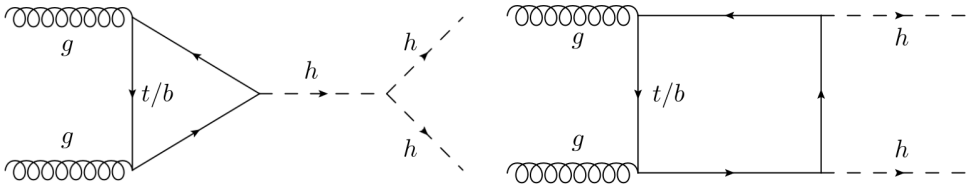

(a) Triangle diagram (b) Box diagram

Figure 3.1: Feynman diagrams for di-Higgs production in SM

fermions are suppressed by their small Yukawa couplings. The amplitude of these two diagrams can be written as:

$$\mathcal{M}_{hh} = -\frac{G_F \alpha_s \hat{s} \delta^{ab}}{2\sqrt{2}\pi} \epsilon^a_\mu(p_1) \epsilon^b_\mu(p_2) \left[\left(\frac{3m_H^2}{\hat{s} - m_H^2} F_\triangle + F_\square \right) A^{\mu\nu} + G_\square B^{\mu\nu} \right], \quad (3.2)$$

where α_s is the strong coupling constant, G_F is the Fermi constant, $\epsilon_\mu(p_1)$ and $\epsilon_\mu(p_2)$ are the wave functions of the gluon field, $\hat{s}$ is the center of mass energy of the gluon system, a and b are the $\mathrm{SU(3)_C}$ indices in the adjoint representation, the $F_\triangle$, $F_\square$ and $G_\square$ are loop functions that can be found in Ref. [215]. The Lorentz structures $A^{\mu\nu}$ and $B^{\mu\nu}$ are defined as:

$$A^{\mu\nu} = g^{\mu\nu} - \frac{p_1^\nu p_2^\mu}{p_1 \cdot p_2}, \quad (3.3)$$

$$B^{\mu\nu} = g^{\mu\nu} + \frac{p_3^2 p_1^\nu p_2^\mu}{p_T^2 p_1 \cdot p_2} - \frac{2p_2 \cdot p_3 p_1^\nu p_3^\mu}{p_T^2 p_1 \cdot p_2} - \frac{2p_1 \cdot p_3 p_2^\mu p_3^\nu}{p_T^2 p_1 \cdot p_2} + \frac{2p_3^\mu p_3^\nu}{p_T^2}. \quad (3.4)$$

Taking into account the relations:

$$A_{\mu\nu} A^{\mu\nu} = B_{\mu\nu} B^{\mu\nu} = 2 \quad A_{\mu\nu} B^{\mu\nu} = 0, \quad (3.5)$$

the amplitude square after summing over the final states and averaging over the initial states is given by:

$$\overline{|M|}^2_{hh} = \frac{1}{4} \cdot \frac{1}{64} \cdot 8 \cdot 2 \cdot \frac{G_F^2 \alpha_s^2 \hat{s}^2}{8\pi^2} \left(\left| \frac{3m_h^2}{\hat{s} - m_h^2} F_\triangle + F_\square \right|^2 + |G_\square|^2 \right). \quad (3.6)$$

In the above equation, the first factor 1/4 is coming from the spin average of the two incoming gluons, the second factor 1/64 is coming from the color average of the two incoming gluons, the third factor 8 is coming from the contraction of two δ^{ab}, the fourth factor 2 is coming from the contraction of the Lorentz structures A and B.

Now let us take a closer look at each term inside the bracket in Eq. 3.6. In the heavy quark limit, the form factors have the following scaling properties:

$$F_{\triangle} = \frac{2}{3} + \mathcal{O}(\hat{s}/m_t^2) \tag{3.7}$$

$$F_{\square} = -\frac{2}{3} + \mathcal{O}(\hat{s}/m_t^2) \tag{3.8}$$

$$G_{\square} = \mathcal{O}(\hat{s}/m_t^2). \tag{3.9}$$

Therefore, the value in the parenthesis in Eq. 3.6 is mainly determined by the values of $F_{\triangle}$ and $F_{\square}$ when the center of mass energy is small. Another important feature is that the signs of $F_{\triangle}$ and $F_{\square}$ are different, which leads to the cancellation effect. This is exactly the origin of the difficulties of the observation of the di-Higgs signal if the SM is true. However, this cancellation effect also provides a good chance to discover the new physics that can significantly change the interference structure of the di-Higgs production amplitude.

Fig. 3.2a shows the contributions from each pieces inside the bracket in the Eq. 3.6 when the center of mass scattering angle $\theta = \pi/2$. The blue and green curves represent the real and imaginary parts of $\frac{3m_h^2}{\hat{s}-m_h^2}F_{\triangle}$, the red and magenta curves show the real and imaginary parts of $F_{\square}$, the purple and yellow curves show the real and imaginary parts of $G_{\square}$, the cyan and brown curves represent the real and imaginary parts of the addition of $F_{\square}$ and $F_{\triangle}$ terms, the black curve represents the module square of the total amplitude. The horizontal axis represents the value of the invariant mass of the di-Higgs system i.e., $\hat{s}$. The vertical axis represents the numerical value of the corresponding quantities. Numerically, one can find that the amplitude of the di-

Higgs process is dominant by Re$[F_\Box]$ in the relatively lower di-Higgs invariant mass region ($M_{hh} \lesssim 500$GeV) and by Im$[F_\Box]$ in the higher di-Higgs invariant mass region ($M_{hh} \gtrsim 500$GeV). The cancellation effect mainly comes from the addition of Re$[F_\Box]$ and Re$[F_\triangle]$ in the low di-Higgs invariant mass region. The strongest cancellation happens when the trilinear Higgs coupling is 2.45 times its SM value, $\lambda_{hhh} = 2.45\lambda_{SM}$, the corresponding contributions of each term in this case can be seen in Fig. 3.2b.

After obtaining the amplitude, one can calculate the parton level differential cross-section in the center of mass frame of the incoming gluon system:

$$\begin{aligned} \frac{d\hat{\sigma}}{d\cos\theta} &= \frac{2\pi}{2E_a 2E_b |v_a - v_b|} \frac{|p_c|}{(2\pi)^4 4E_{cm}} \frac{1}{2} \overline{|M|}^2_{hh} \\ &= \frac{G_F^2 \alpha_s^2 \sqrt{(2m_h^2 - \hat{s})^2 - 4m_h^4}}{1024(2\pi)^3} \left(\left| \frac{3m_h^2}{\hat{s} - m_h^2} F_\triangle + F_\Box \right|^2 + |G_\Box|^2 \right). \end{aligned} \quad (3.10)$$

where $E_{a,b}$ are the energy of the incoming gluons, $|p_c|$ is the magnitude of the three momentum of the out-going Higgs. The factor 1/2 in front of the $\overline{|M|}_{hh}$ in the first line comes from the nature of two identical particles in the final state. Usually in the literature one would convert the dependence on θ to the dependence on $\hat{t}$ which is defined by $\hat{t} = (p_a + p_c)^2$. The relation between θ and $\hat{t}$ is:

$$\hat{t} = (p_a + p_c)^2 = m_h^2 - \frac{1}{2}(s - \cos\theta \sqrt{s(s - 4m_h^2)}), \quad (3.11)$$

with the definition of θ in Fig. 3.3. Then the partonic differential cross-section with respect to $\hat{t}$ can be written as:

$$\frac{d\hat{\sigma}(\hat{s})}{d\hat{t}} = \frac{G_F^2 \alpha_s^2}{512(2\pi)^3} \left(\left| \frac{3m_H^2}{\hat{s} - m_H^2} F_\triangle + F_\Box \right|^2 + |G_\Box|^2 \right). \quad (3.12)$$

The partonic cross-section for a given partonic center of mass energy $\hat{s}$ is given by integrating with $d\hat{t}$:

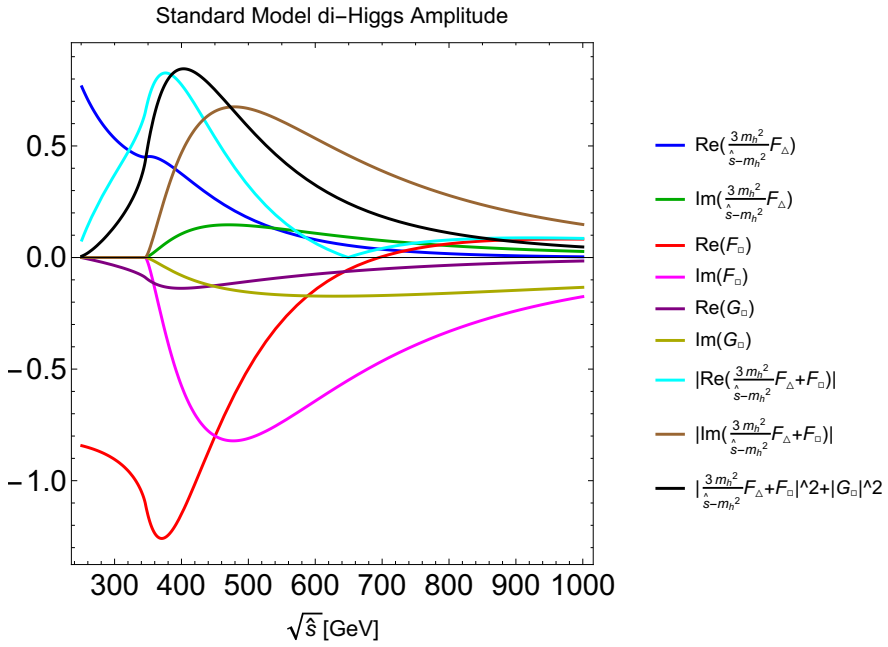

(a) SM

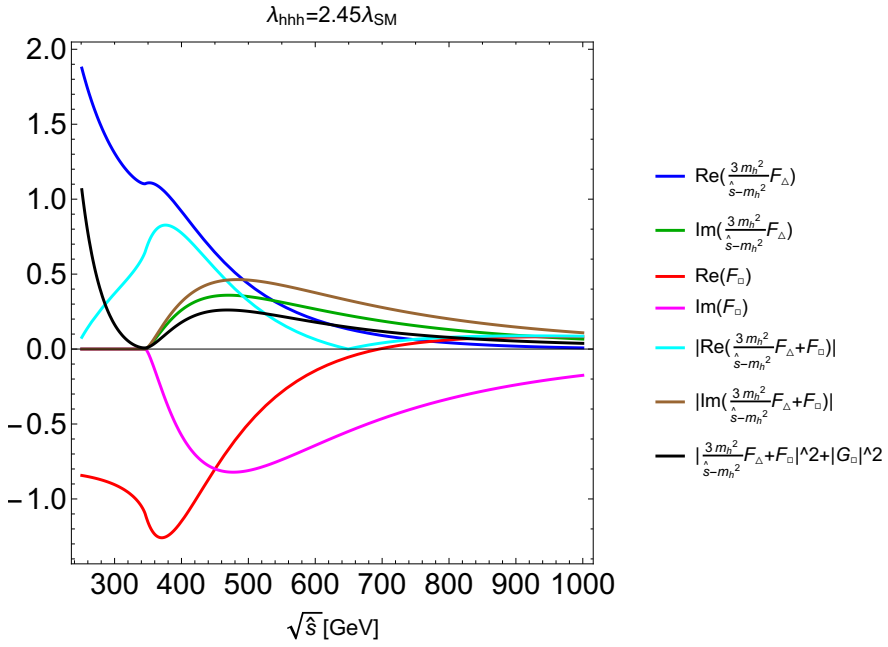

(b) $\lambda_{hhh} = 2.45\lambda_{SM}$

Figure 3.2: The contribution of the each terms in the parentheis in the Eq. 3.6. The color scheme is denoted in legend on the right of the plots. The upper plot shows the SM case. The lower plot represents the case where $\lambda_{hhh} = 2.45\lambda_{SM}$, which gives the strongest cancellation in the production cross-section.

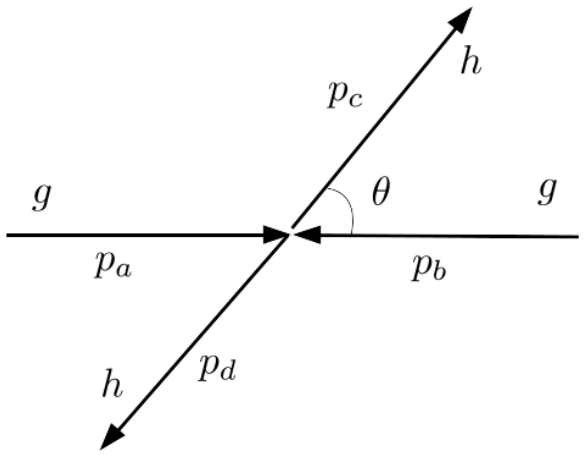

Figure 3.3: The definition of the kinematic variables in the gluon fusion di-Higgs production process.

$$\hat{\sigma}(\hat{s}) = \int_{\hat{t}_{min}}^{\hat{t}_{max}} d\hat{t} \frac{d\hat{\sigma}(\hat{s})}{d\hat{t}}. \tag{3.13}$$

To obtain the cross-section in the pp collider, one need to convolute the partonic cross-section with the parton luminosity [222]:

$$\sigma(pp \to hh) = \int_{\tau_0}^{1} d\tau \ \frac{\mathcal{L}_{gg}}{d\tau} \hat{\sigma}(\tau) \quad \text{with} \quad \tau = \hat{s}/s \tag{3.14}$$

where τ is the ratio of the partonic center of mass energy and the proton center of mass energy, and the parton luminosity for gluons in proton $\frac{d\mathcal{L}_{gg}}{d\tau}$ is defined by:

$$\frac{d\mathcal{L}_{gg}}{d\tau} = \int_{\tau}^{1} dx \ \frac{1}{x} f_g^{(p)}(x,\mu) f_g^{(p)}(\tau/x), \tag{3.15}$$

where $f_g^p(x,\mu)$ is the parton distribution function of gluon with factorization scale μ, which characterize the probability of finding a gluon with an energy fraction of $\sqrt{x}$ with respect to the proton energy. Fig. 3.4 shows the parton luminosity of two gluons for different center of mass energy of the proton proton beam [222] using CTEQ6L1 leading order parton distribution function [220]. The production cross-section for

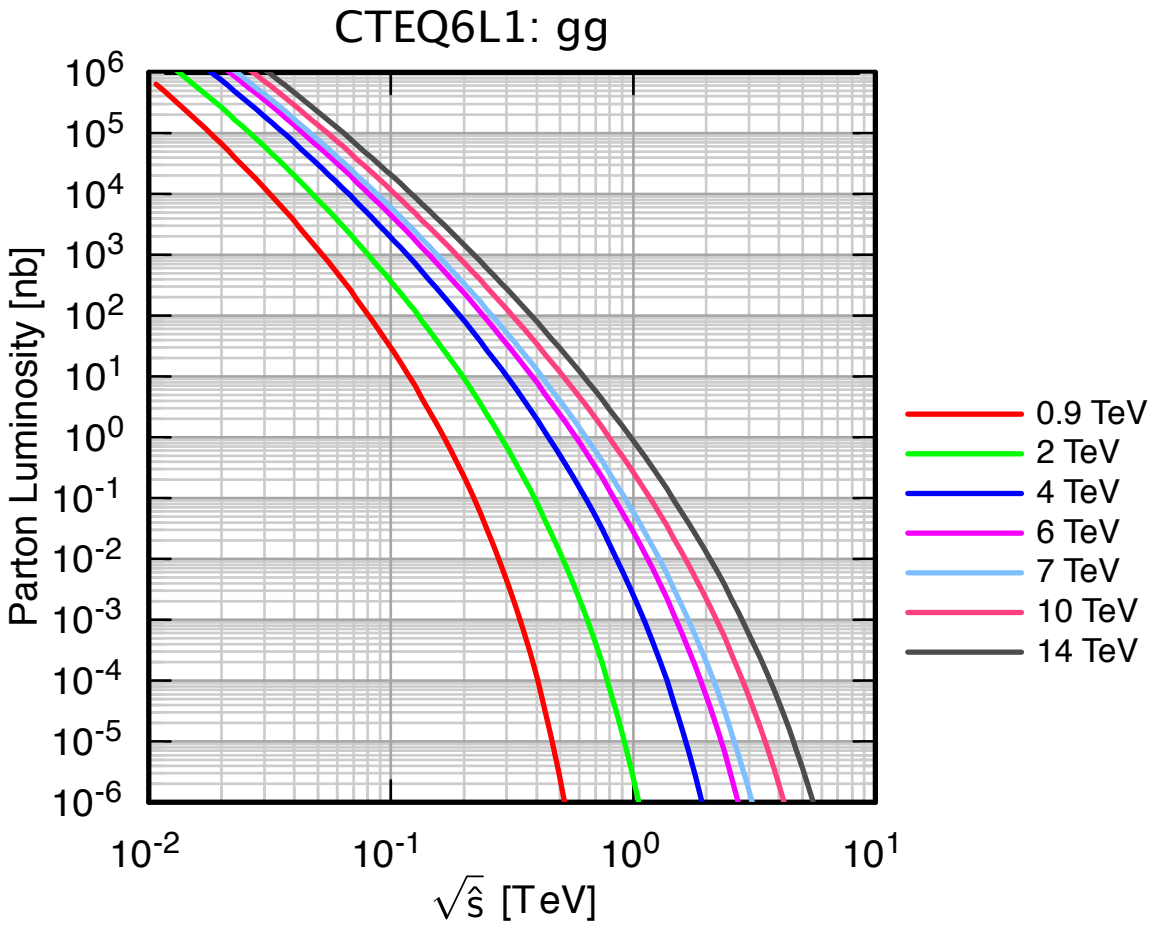

Figure 3.4: The typical gluon-gluon parton luminosity in the pp system with different center of mass energies.

the di-Higgs channel in the pp collider as a function of the rescaled trilinear Higgs couplings is shown in the Fig. 3.5 in Ref [35]. The NNLO K-factor is defined by the ratio between the NNLO cross-section and LO cross-section [101, 94, 140].

In the meantime, various combinations of the final states of di-Higgs decay products also have been investigated both theoretically ($bb\tau\tau$ [104, 208], $bbWW$ [211], $bb\gamma\gamma$ [32, 40], $bbbb$ [119, 183]) and experimentally [11, 203]. The decay branching ratios of the Higgs pair with different combinations of final states are shown in Fig. 3.6.[203]. As one can see from Fig. 3.6, the $bbbb$ final state has the largest branching ratio. However, this channel also suffers from extensive multi-jet backgrounds,

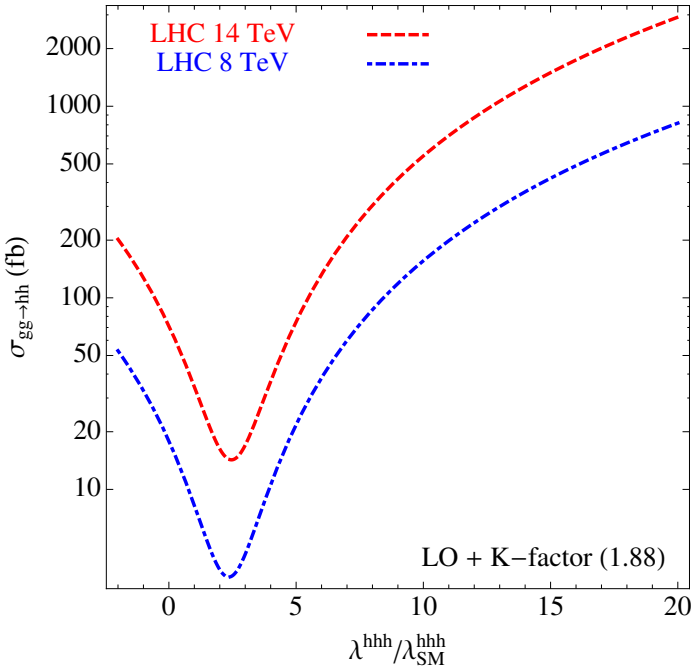

Figure 3.5: The production cross-section as a function of the rescaled tri-Higgs couplings.

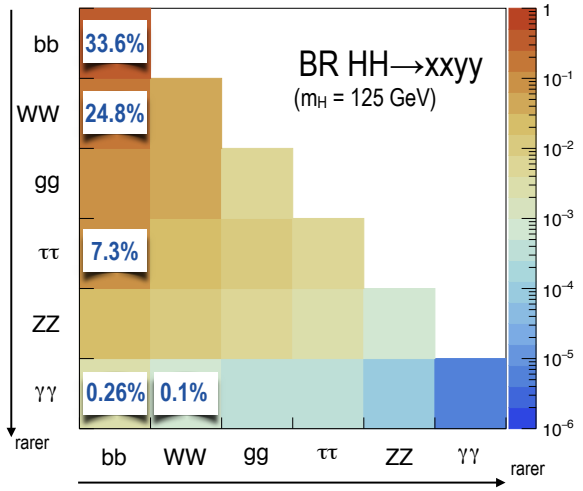

Figure 3.6: Decay Branching ratios for different final states. Image obtained from Ref. [203].

which will significantly reduce the signal sensitivity. The most sensitive channel turns out to be $bb\gamma\gamma$, which uses one Higgs decaying to two b quarks to enhance the total signal rate, and simultaneously takes advantage of the very well reconstructed Higgs mass from the Higgs to di-photon decay to eliminate majority of backgrounds.

3.2 Di-Higgs production Beyond SM

Beyond the SM, there are various ways to modify the di-Higgs production cross-section in the pp collider. We will discuss two scenarios. Firstly, the correction is dominated by the resonant production of new scalar particles; secondly, the new resonance is too heavy to produce in the collider, and the corrections are induced by the modification of various couplings and the diagrams with new topologies.

In Chapter 6, we will use the result for the resonant production to study the process $pp \to S \to hh$ in the singlet model, where S is the heavy Higgs. In Chapter 7, we will use the result for the non-resonant production to estimate the reach of the future 100 TeV collider in testing different scalar extensions in the SMEFT framework.

3.2.1 resonant production

New scalars in the physics models can enhance the di-Higgs signal when the invariant mass of the di-Higgs system is near one of new scalar masses provided that this new scalar interacts with the SM Higgs and is heavier than two times of the SM Higgs mass. Lots of scalar extensions to the SM can provide this kind of signature, for example, the xSM [104] and 2HDMs [208]. Regarding to the di-Higgs decay final states, the $bbWW$ [160] and $bbbb$ channels are believed to be most sensitive to the LHC search for a relatively larger resonance mass (roughly larger than 500 GeV) due to the advantage of the resonant peak, while for the smaller resonance mass $bb\gamma\gamma$ [160] is still the most sensitive channel. With the narrow width approximation ($\Gamma_S/m_S \lesssim 0.1$), the signal rate of the resonant di-Higgs production process can be

written as the multiplication of the production cross-section of the heavy scalar and the decay branching ratio of the heavy scalar to di-Higgs:

$$\sigma(pp \to S \to hh) = \sigma(pp \to S) \cdot \mathrm{Br}(S \to hh). \tag{3.16}$$

The leading order production cross-section of the heavy Higgs through the gluon fusion can be expressed as:

$$\sigma(pp \to S)_{LO} = \int d\tau \hat{\sigma}(gg \to S)_{LO} \frac{d\mathcal{L}_{gg}}{d\tau} = \frac{\pi^2}{8m_S} \Gamma_{LO}(H \to gg) \frac{d\mathcal{L}_{gg}}{dm_S^2}. \tag{3.17}$$

This is based on the Breit-Wigner form of the scalar propagator in the limit of zero-width [102]:

$$\lim_{\Gamma_S \to 0} \frac{1}{\pi} \frac{\hat{s}\Gamma_S/m_S}{(\hat{s} - m_S^2)^2 + (\hat{s}\Gamma_S/m_S)^2} = \delta(\hat{s} - m_S) \tag{3.18}$$

3.2.2 non-resonant production

Now let us discuss the non-resonant production. This is usually studied in the EFT framework where the mass of the heavy scalar is so high such that it cannot be efficiently produced on the pp collider due to the suppressed parton luminosity at the high center of mass energy regime. In this case, people usually parametrize the dependence of the di-Higgs production in the gluon fusion mode with the modification of the relevant Higgs couplings. Meanwhile, new types of Feynman diagrams can also be induced. In Fig. 3.7, I list all the topologies of Feynman diagrams that can produce the di-Higgs signal via the gluon fusion and symbol in the red dots the rescaled new couplings related to each vertex. These couplings are defined with the following Lagrangian:

$$\mathcal{L}_{gghh} = -m_t \bar{t}t \left(\kappa_t \frac{h}{v} + \kappa_{2t} \frac{h^2}{v^2} \right) + \frac{\alpha_s}{12\pi} G^a_{\mu\nu} G^{a\mu\nu} \left(\kappa_g \frac{h}{v} - \frac{1}{2} \kappa_{2g} \frac{h^2}{v^2} \right) - \kappa_\lambda \frac{m_h^2}{2v^2} v h^3 \tag{3.19}$$

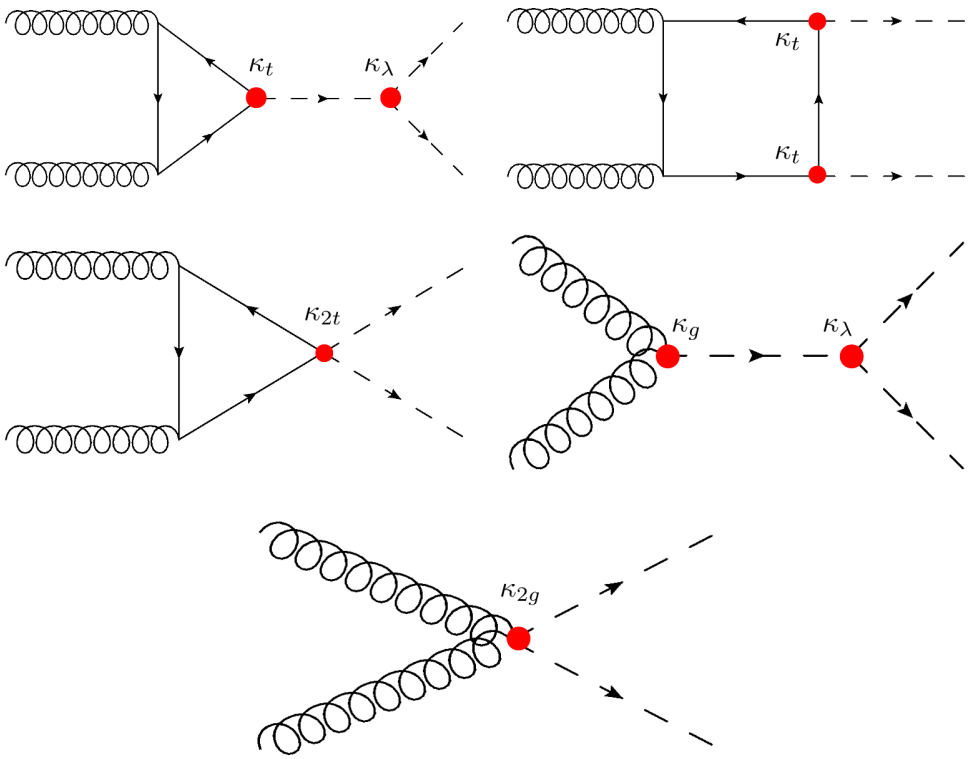

Figure 3.7: The topologies of the Feynman diagrams that related to the di-Higgs production in the gluon fusion mode. The red dots represent the rescaled couplings of those vertices.

In this case, the averaged amplitude for the di-Higgs production can be expressed as:

$$\overline{|M|}^2_{hh} = \frac{G_F^2 \alpha_s^2 \hat{s}^2}{128\pi^2} \left[\left| \left(\frac{3m_h^2 \kappa_t \kappa_\lambda}{\hat{s} - m_h^2} + 2\kappa_{2t} \right) F_\triangle + \kappa_t^2 F_\square + \frac{2\kappa_g}{3} \frac{3m_h^2 \kappa_\lambda}{\hat{s} - m_h^2} - \frac{2\kappa_{2g}}{3} \right|^2 + |G_\square|^2 \right]. \tag{3.20}$$

CHAPTER 4

NEUTRINO MASS AND SEASAW MECHANISM

The neutrino oscillation experiments Super-Kamiokande [128], SNO [18, 17] and KamLAND [108] have confirmed that neutrinos are massive. However, in the SM, the nonexistence of the right-handed neutrino renders no neutrino mass can be generated at renormalizable level. Therefore, the extension must be needed to generate the neutrino masses. Since the neutrinos are not charged under $U(1)_{em}$, two types of mass terms can be written down. One possibility is that the neutrinos are Dirac fermions and have Dirac mass terms in the form:

$$\mathcal{L}_{\nu-mass} = m_{\nu,i}\bar{\nu}_{L,i}\nu_{R,i} + h.c.. \tag{4.1}$$

In this case, a set of right-handed neutrinos must be introduced. It is likely that the set of right-handed neutrinos that are completely neutral under the SM gauge group actually exist in nature, but they have not been observed due to their negligible interactions with ordinary matters. Once right-handed neutrinos are introduced, one can write down the gauge invariant Yukawa interactions involving them like their counterparts in the quark sector involving the right-handed up type quarks:

$$\mathcal{L}_{\nu_R-yukawa} = -Y^{\nu}\bar{L}_L\tilde{H}\nu_R + h.c., \tag{4.2}$$

where we have suppressed the indices for the lepton flavor. After diagonalizing the mass matrix for neutrinos one obtains the relation between the Yukawa couplings and

neutrinos mass: $Y^{\nu} \sim m_{\nu}/v$. However, taking into account the fact that the current upper bound on the sum of the three neutrino masses is around 0.1 to 0.2 eV [210, 99, 98, 85, 138] from the standard cosmology and the observation from the Planck CMB experiment [16], one finds that the Yukawa coupling Y^{ν} is exceptionally small compare to other charged fermions in the SM as one can see from Fig. 4.1. Therefore, various

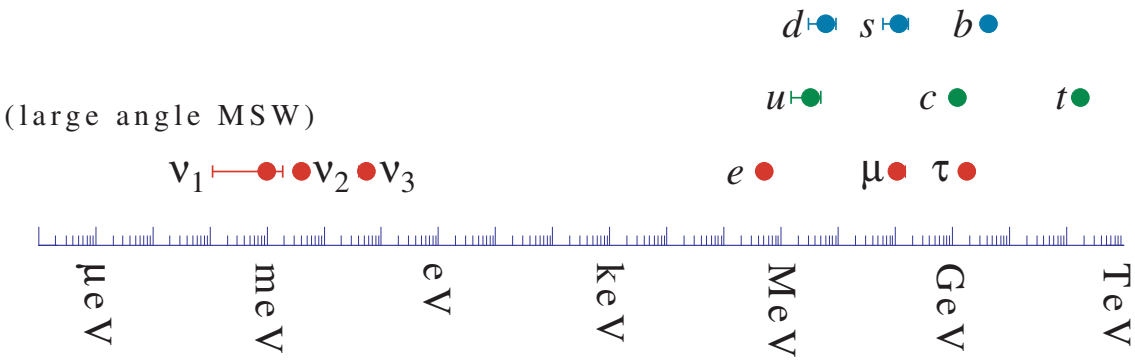

Figure 4.1: The masses of the SM fermions in log scale [153], one can see that neutrinos are relatively isolated in the mass spectrum compared with other charged fermions.

theories are proposed to explain the smallness of neutrino masses. This naturally leads us to consider the possibilities that neutrinos are Majorana particles. Ettore Majorana in 1937 proposed a mathematical way to describe the particles that are their own antiparticles [190]. In terms of the four components spinor this relation can be written as:

$$\psi = \psi^{C} \, where, \;\; \psi^{C} = C\bar{\psi}^{T}. \tag{4.3}$$

C is the charge conjugation operator for the four components spinor, in the Weyl representation it can be express as $C = i\gamma^2\gamma^0$, where γ is Dirac matrices. With this definition one can write down the mass terms in the following forms:

$$\mathcal{L}_{\nu-Majorana} = -\frac{m_{L,i}}{2}\overline{\nu^{c}_{L,i}}\nu_{L,i} - \frac{m_{R,i}}{2}\overline{\nu^{c}_{R,i}}\nu_{R,i} + h.c., \tag{4.4}$$

where the factor 1/2 is added to ensure that the parameter $m_{L/R,i}$ can be interpreted as the mass of the particle in the equation of motion. Within the SM, the Majorana mass related to the left-handed neutrino cannot be generated at the renormalizable level since the ν_L is charged under the SM gauge group. The lowest dimensional operator that obeys the SM symmetry and gives rise to the Majorana mass for the ν_L is the Weinberg operator [240]:

$$\frac{c^{ij}}{\Lambda}\bar{L}_{L,i}\tilde{H}\tilde{H}^T L^c_{L,j}, \tag{4.5}$$

where the i, j are the flavor indices, $\tilde{H}$ is defined below Eq. 1.17, the Λ characterize the heavy new physics scale that accounts for the generation of the Majorana mass, c^{ij} are the corresponding Wilson coefficients.

One of the greatest difference between the Majorana neutrino and the Dirac neutrino is that the Majorana mass terms violate the lepton number L in low energy experiments while the Dirac mass terms do not[1]. Hence, the experiment searching for the lepton number violation is helpful to determine the nature of the neutrinos. Neutrinoless double beta decay ($\beta\beta0\nu$), the idea introduced by Wendell Furry [129], is one of the most sensitive ways to test lepton violation, see Ref. [97, 221] for reviews. Another important difference between the Majorana neutrino and the Dirac neutrino is that the number of CP phases in the PMNS matrix [191, 217] in the leptonic charged current interaction is different. The interaction of the charged current involving the W boson is given by:

$$\mathcal{L}_{l-\nu} = -\bar{l}_L \not{W} U_{PMNS} \nu_L + h.c. \tag{4.6}$$

[1]In the SM, L is violated by global electroweak anomalies with $B - L$ exactly conserved. While at the temperature much lower than the electroweak scale v, the violation of L is negligible, see Ref. [111] an estimation of SM lepton number violation process in pp collider

The reason for the difference of the number of CP phases is that the Majorana mass term, $m\bar{\psi^C}\psi$ is not invariant under the rephasing $\psi \to e^{i\alpha}\psi$. So the rephasing degrees of freedom only come from the charged leptons, which leaves 3 CP phases in the U_{PMNS}.

Three types of "Seesaw" mechanism can generate the Weinberg operator in Eq. 4.5 at tree level.

- Type-I seesaw: SM + heavy singlet fermions

  The type-I seesaw [198, 134, 243, 200] generates the Weinberg operator by introducing singlet fermions. One example is the right-handed neutrino ν_R. In this case, aside from the Yukawa interactions with the SM leptons and Higgs doublet, a Majorana mass terms for the right-handed neutrinos $1/2 m_R \overline{\nu^c_{R,i}} \nu_{R,i}$ can be written down without violating the SM symmetry. The Feynman diagram in Fig. 4.2a will generate the Weinberg operators. One can read off from the diagram that $c/\Lambda \sim Y_\nu^2/m_R$, where c is the Wilson coefficient in the Eq. 4.5 and we have suppressed the flavor indices. If we impose the relation:

  $$\frac{cv^2}{\Lambda} \sim m_{\nu_L}, \tag{4.7}$$

  then we will get the scale of the right-handed neutrino mass as $m_R \sim Y_\nu^2 \times 10^{14}$ GeV, where we have taken the typical light neutrino mass as 10^{-1} eV. The phenomenology related to the Type-I model is limited because the right-handed neutrino can only be probed through the Yukawa interaction. An enhancement in the Yukawa coupling Y_ν will generally increase the mass of the right-handed neutrino, i.e. make it harder to be produced in experiments.

- Type-II see saw: SM + triplet scalars.

The type-II seesaw [189, 229, 185] generates neutrino masses with the help of a $SU(2)_L$ triplet with hypercharge $Y = 2$. The Yukawa interaction

$$Y_{\Delta_L} \overline{L_L} \Delta_L L_L^C, \tag{4.8}$$

combined with the scalar coupling

$$\mu H H \Delta_L, \tag{4.9}$$

will generate the Weinberg operator through the diagram in Fig. 4.2b. One can read off the Wilson coefficient:

$$c/\Lambda \sim Y\mu/M_\Delta^2. \tag{4.10}$$

Similarly the above relation translates into the scale of the mass of the triplet: $M_\Delta \sim 10^7 \times \sqrt{\mu Y_{\Delta_L}} GeV$, where μ is in the unit of GeV. If one chooses μ small enough ($\mathcal{O}(10^{-4}$ GeV)) as it is a free parameter, then one can obtain a relatively small triplet mass M_Δ ($\mathcal{O}$(TeV)) with a relatively large Yukawa coupling Y_{Δ_L} (for example $\mathcal{O}(10^{-3})$), which in principle can be tested at the near future collider. Moreover, the triplet scalar also contains a doubly charged particle Δ^{++}, which will decay to a pair of same sign leptons serving as a unique signature in the collider searches.

- Type-III seesaw: SM + triplet fermions.

  The type-III seesaw [123, 187, 244] introduces a $SU(2)_L$ triplet fermion Σ with zero hypercharge. In this case, the mass of the triplet fermion scale as: $m_\Sigma \sim Y_\Sigma^2 \times 10^{14} GeV$ which is similar to the case of the Type-I. Regarding to the phenomenology, the triplet fermion decays to the $W(Z)$ bosons with leptons

will provide a unique signature in the collider experiments. See Ref. [131, 121] for detailed discussions.

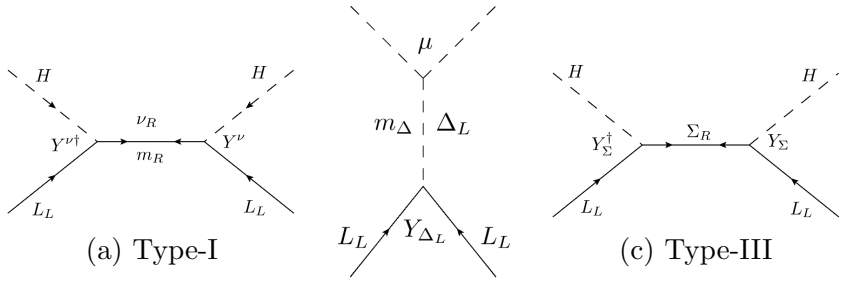

Figure 4.2: Feynman diagrams that generate the Weinberg operator in three types of seesaw model.

Apart from the three types of seasaw mechanism discussed above, there are other types of seasaw mechanism that can also explain the smallness of the neutrino masses naturally e.g. the inverse seasaw mechanism [199]. Another approach to explain the smallness of the neutrino mass is to generate them through loops e.g. Zee model [244] which is naturally suppressed by the quantum effect. One can refer to Ref. [188, 238] for more detailed discussions.

CHAPTER 5

CP VIOLATION 2HDMS

With the discovery of the Higgs-like boson at the LHC [8, 58], the remaining particle predicted by the Standard Model (SM) has been found. Up to now, the measured properties of this new resonance show no significant deviation from the SM predictions. Nevertheless, the new boson could reside in a larger structure with an extended scalar sector that incorporates the SM. The possibilities for such extended scalar sectors abound. Among the most widely considered and theoretically well-motivated are Two Higgs Doublet Models (2HDMs). Even with the rather minimal introduction of a second $\mathrm{SU}(2)_L$ scalar doublet, the possible phenomenological consequences of 2HDMs are rich and diverse. The possibility of new sources of CP-violation is one of the most interesting but, perhaps, less extensively studied.

Explaining the cosmic matter and anti-matter asymmetry requires the existence of additional CP-violation (CPV) beyond that of the SM. Electroweak Baryogenesis (EWBG) is one of the most compelling solutions to this problem [239, 68, 202]. EWBG fulfills the Sakharov conditions for successful baryogenesis [228] (B violation, out-of-equilibrium dynamics, and both C and CP-violation) through $B + L$ violating sphaleron transitions, a strong first order electroweak phase transition that proceeds through bubble nucleation, and CPV interactions at the bubble wall. While the SM would in principle provide these ingredients, it is known that the CPV effects generated by the Cabibbo-Kobayashi-Maskawa matrix and QCD θ term are too feeble and that the SM-like Higgs scalar is too heavy for a strongly first order electroweak phase transition [169, 84, 227].

The 2HDMs provide possible solutions to these shortcomings. The viability of a strong first order electroweak phase transition and the favored parameter space of the 2HDMs have been studied in Refs. [107, 127, 69]. In the CPV sector, the LHC has already excluded the new boson as a pure CP odd scalar at 99.98% CL and 97.8% CL in Ref. [172] and Ref. [4] respectively.

If the boson is a part of the 2HDM, it could nevertheless receive a small CP-odd admixture from CP-violating terms in the scalar potential. This possibility for 2HDM CP-violation is strongly bounded by the non-observation of permanent electric dipole moments (EDMs) of the neutron, electron, and diamagnetic atoms, including mercury and radium [38, 33, 144, 184], as analyzed recently in Refs. [163, 234, 44, 242, 168]. The authors of Refs. [61, 43, 19, 63, 70] also pointed out that LHC searches for additional, heavy scalars can be complementary to EDM searches, especially in regions of 2HDM parameter space where strong cancellations between Barr-Zee EDM diagrams occur. Nonetheless, there exists a window for sufficient CPV to generate the matter-antimatter asymmetry, as shown in Ref. [105].

In what follows, we analyze the prospects for future LHC probes of the CPV 2HDM, building on the previous studies in Ref. [163] and Ref. [61], where EDMs constraints and 8 TeV LHC results in CPV 2HDMs are analyzed in detail. We adopt the framework of CPV 2HDMs with a softly-broken Z_2 symmetry to avoid a problematic tree level flavor changing neutral currents (FCNCs). We consider future LHC searches for a heavy Higgs of mixed CP (denoted $h_{i=2,3}$) which decays to a Z boson and a SM-like Higgs (h_1), and obtain the prospective reach for Run II and the high luminosity phase (HL-LHC). We concentrate on the $llb\bar{b}$ final state, where the Z boson decays to a pair of leptons (e *or* μ), and the SM-like Higgs decays to a pair of b quarks, because it is one of the most sensitive channels and because the final state particles allow for a relatively high reconstruction efficiency. We first follow the cut-based analysis procedure described in Ref. [10] to reproduce the ATLAS 8 TeV

results and validate our Monte Carlo signal and background generation, then use the Boosted Decision Tree (BDT) [126] method to obtain the 95% CLs exclusion limit for future 14 TeV experiments with integrated luminosities equal to 300 fb^{-1}, and 3000 fb^{-1}, respectively. We subsequently translate the prospective exclusion limits into constraints on the parameter space, and find that a large portion of parameter space can be tested with both future LHC and EDMs experiments.

From the global fit of Higgs coupling measurements [72, 71], one find that the current data favor the 2HDMs to be close to the alignment limit: $\beta - \alpha = \pi/2$ where α and β are defined in Sec. 5.1.2 and Sec. 5.1.1 respectively.

In this chapter, I will first introduce the theoretical framework we used for CP violation 2HDMS in Sec. 6.1. In Sec. 5.2, we show the analytical formulas used to derive constraints on the parameter space. In Sec. 5.3 we describe details of our simulation and analyses. In Sec. 5.4, we exhibit future LHC constraints and discuss possible issues arising from the interference between the resonant and non-resonant diagrams. The distributions of kinematic variables used in BDT analysis and the formulas for two-body decay rates of heavy Higgses are given in Appendix.

5.1 CPV 2HDM Model Description

In this section, we describe details of the CPV 2HDM framework that will be used in the following discussions.

5.1.1 General 2HDM Scalar Potential

The most general 2HDM scalar potential containing two Higgs doublets ϕ_1 and ϕ_2 can be expressed in the following form:

$$
\begin{aligned}
V(\phi_1,\phi_2) &= -\frac{1}{2}\left[m_{11}^2(\phi_1^\dagger\phi_1)+\left(m_{12}^2(\phi_1^\dagger\phi_2)+\text{h.c.}\right)+m_{22}^2(\phi_2^\dagger\phi_2)\right] \\
&\quad +\frac{\lambda_1}{2}(\phi_1^\dagger\phi_1)^2+\frac{\lambda_2}{2}(\phi_2^\dagger\phi_2)^2+\lambda_3(\phi_1^\dagger\phi_1)(\phi_2^\dagger\phi_2)+\lambda_4(\phi_1^\dagger\phi_2)(\phi_2^\dagger\phi_1) \\
&\quad +\frac{1}{2}\left[\lambda_5(\phi_1^\dagger\phi_2)^2+\lambda_6(\phi_1^\dagger\phi_2)(\phi_1^\dagger\phi_1)+\lambda_7(\phi_1^\dagger\phi_2)(\phi_2^\dagger\phi_2)+\text{h.c.}\right] \ . \quad (5.1)
\end{aligned}
$$

Two fields ϕ_1 and ϕ_2 can be expressed as

$$
\phi_1=\begin{pmatrix} H_1^+ \\ \frac{1}{\sqrt{2}}(v_1+H_1^0+iA_1^0)\end{pmatrix}, \quad \phi_2=\begin{pmatrix} H_2^+ \\ \frac{1}{\sqrt{2}}(v_2+H_2^0+iA_2^0)\end{pmatrix} \tag{5.2}
$$

with in general v_1 and v_2 complex and $v=\sqrt{|v_1|^2+|v_2|^2}=246$ GeV. We also denote that $\tan\beta=|v_2|/|v_1|$. One can always perform a $SU(2)_L\times U(1)_Y$ gauge transformation to go into a basis where v_1 is real while $v_2=|v_2|e^{i\xi}$ is still complex.

To guarantee that there are no FCNCs at tree level, one can assign Z_2 charges to the two Higgs doublets as well as the fermion fields such that each fermion can only couple to one of the Higgs doublets. Depending on the transformation of the fermion fields under the Z_2 symmetry, there can be various types of 2HDMs that we will introduce in Sec. 5.1.3. The Z_2 symmetry implies the potential parameters m_{12}^2 and $\lambda_{6,7}$ vanish, which in turn forbids the presence of CP phases in the potential. Therefore, we retain the m_{12}^2 term which only softly breaks the Z_2 symmetry. In general, this soft Z_2 symmetry breaking term together with quartic Z_2 conserving term would induce new quartic Z_2 breaking terms by renormalization, but they are at one-loop level and thus do not induce new FCNC at tree level.

Hermicity implies that there are only two complex parameters, m_{12}^2 and λ_5, in the potential. With the global phase redefinition of the fields $\phi_j\to e^{i\theta_j}\phi_j$, one may define two rephasing invariant phases as in Ref [163],

$$
\begin{aligned}
\delta_1 &= \text{Arg}\left[\lambda_5^*(m_{12}^2)^2\right] \ , \\
\delta_2 &= \text{Arg}\left[\lambda_5^*(m_{12}^2)v_1v_2^*\right] \ . \quad (5.3)
\end{aligned}
$$

The minimization of the potential yields that:

$$m_{11}^2 = \lambda_1 v^2 \cos^2\beta + (\lambda_3+\lambda_4) v^2 \sin^2\beta - \mathrm{Re}(m_{12}^2 e^{i\xi}) \tan\beta + \mathrm{Re}(\lambda_5 e^{2i\xi}) v^2 \sin^2\beta \ , \tag{5.4}$$

$$m_{22}^2 = \lambda_2 v^2 \sin^2\beta + (\lambda_3+\lambda_4) v^2 \cos^2\beta - \mathrm{Re}(m_{12}^2 e^{i\xi}) \cot\beta + \mathrm{Re}(\lambda_5 e^{2i\xi}) v^2 \cos^2\beta \ , \tag{5.5}$$

$$\mathrm{Im}(m_{12}^2 e^{i\xi}) = v^2 \sin\beta\cos\beta \mathrm{Im}(\lambda_5 e^{2i\xi}) \ . \tag{5.6}$$

Eq. 5.6 above indicates that the value of ξ is determined by given m_{12}^2 and λ_5. Expressing this equation with rephasing invariant phases implies:

$$|m_{12}^2| \sin(\delta_2 - \delta_1) = |\lambda_5 v_1 v_2| \sin(2\delta_2 - \delta_1) \quad . \tag{5.7}$$

In short, there is only one CP independent phase in the potential after electroweak symmetry breaking(EWSB). Using this rephasing freedom of the fields, we will work in a basis where $\xi = 0$ and encode this invariant CPV phase into a CPV angle in the diagonalization matrix for the neutral Higgs sector.

5.1.2 Higgs Mass Eigenstates

After EWSB, we can use the following relations to diagonalize the mass matrix for the charged Higgs sector, which separates the physical charged Higgs and would-be Goldstone bosons:

$$\begin{pmatrix} H^+ \\ G^+ \end{pmatrix} = \begin{pmatrix} -s_\beta & c_\beta \\ c_\beta & s_\beta \end{pmatrix} \begin{pmatrix} {H_1}^+ \\ {H_2}^+ \end{pmatrix} \tag{5.8}$$

This leads to a relationship between the mass of the charged Higgs and parameters in the scalar potential:

$$m_{H^+}^2 = \frac{1}{2}\left(2\nu - \lambda_4 - \mathrm{Re}\lambda_5\right) v^2, \quad \nu \equiv \frac{\mathrm{Re}m_{12}^2 \csc\beta \sec\beta}{2v^2} \ . \tag{5.9}$$

where the parameter ν sets the hierarchy between the SM-like Higgs and charged Higgs. The mass term in the Lagrangian is given by $\mathcal{L}_{\text{neutral}}^{\text{mass}} = -(H_1^0, H_2^0, A^0)\mathcal{M}^2(H_1^0, H_2^0, A^0)^T$ gives,

$$\mathcal{M}^2 = v^2 \begin{pmatrix} \lambda_1 c_\beta^2 + \nu s_\beta^2 & (\lambda_{345} - \nu) c_\beta s_\beta & -\frac{1}{2}\mathrm{Im}\lambda_5 \, s_\beta \\ (\lambda_{345} - \nu) c_\beta s_\beta & \lambda_2 s_\beta^2 + \nu c_\beta^2 & -\frac{1}{2}\mathrm{Im}\lambda_5 \, c_\beta \\ -\frac{1}{2}\mathrm{Im}\lambda_5 \, s_\beta & -\frac{1}{2}\mathrm{Im}\lambda_5 \, c_\beta & -\mathrm{Re}\lambda_5 + \nu \end{pmatrix} , \tag{5.10}$$

where λ_{345} represents $\lambda_3 + \lambda_4 + \mathrm{Re}(\lambda_5)$. A rotation matrix R defined below can be used to diagonalize the mass matrix:

$$R = \begin{pmatrix} -s_\alpha c_{\alpha_b} & c_\alpha c_{\alpha_b} & s_{\alpha_b} \\ s_\alpha s_{\alpha_b} s_{\alpha_c} - c_\alpha c_{\alpha_c} & -s_\alpha c_{\alpha_c} - c_\alpha s_{\alpha_b} s_{\alpha_c} & c_{\alpha_b} s_{\alpha_c} \\ s_\alpha s_{\alpha_b} c_{\alpha_c} + c_\alpha s_{\alpha_c} & s_\alpha s_{\alpha_c} - c_\alpha s_{\alpha_b} c_{\alpha_c} & c_{\alpha_b} c_{\alpha_c} \end{pmatrix} , \tag{5.11}$$

where s_α and c_α are short hands for $\sin\alpha$ and $\cos\alpha$. Under this rotation matrix, we have $\mathcal{M}^2 = R^T \mathrm{diag}(m_{h_1}^2, m_{h_2}^2, m_{h_3}^2) R$, and $R(H_1^0, H_2^0, A^0)^T = (h_1, h_2, h_3)^T$. We demand that three rotation angles are in the following range:

$$-\frac{\pi}{2} < \alpha, \alpha_b, \alpha_c < \frac{\pi}{2} \tag{5.12}$$

With this diagonalization procedure, one can obtain six linearly independent equations which can be solved for the parameters in the scalar potential in terms of the physical parameters, as shown below [163],

$$\lambda_1 = \frac{m_{h_1}^2 \sin^2\alpha \cos^2\alpha_b + m_{h_2}^2 R_{21}^2 + m_{h_3}^2 R_{31}^2}{v^2 \cos\beta^2} - \nu \tan^2\beta \ , \tag{5.13}$$

$$\lambda_2 = \frac{m_{h_1}^2 \cos^2\alpha \cos^2\alpha_b + m_{h_2}^2 R_{22}^2 + m_{h_3}^2 R_{32}^2}{v^2 \sin\beta^2} - \nu \cot^2\beta \ , \tag{5.14}$$

$$\mathrm{Re}\lambda_5 = \nu - \frac{m_{h_1}^2 \sin^2\alpha_b + \cos^2\alpha_b (m_{h_2}^2 \sin^2\alpha_c + m_{h_3}^2 \cos^2\alpha_c)}{v^2} \ , \tag{5.15}$$

$$\lambda_3 = \nu - \frac{m_{h_1}^2 \sin\alpha\cos\alpha\cos^2\alpha_b - m_{h_2}^2 R_{21}R_{22} - m_{h_3}^2 R_{31}R_{32}}{v^2 \sin\beta\cos\beta} - \lambda_4 - \mathrm{Re}\lambda_5 \ , \tag{5.16}$$

$$\begin{aligned}\mathrm{Im}\lambda_5 = {} & 2\cos\alpha_b \{(m_{h_2}^2 - m_{h_3}^2)\cos\alpha \sin\alpha_c \cos\alpha_c \\ & + (m_{h_1}^2 - m_{h_2}^2 \sin^2\alpha_c - m_{h_3}^2 \cos^2\alpha_c)^2 \sin\alpha \sin\alpha_b\}/(v^2 \sin\beta),\end{aligned} \tag{5.17}$$

$$\tan\beta = \frac{(m_{h_2}^2 - m_{h_3}^2)\cos\alpha_c \sin\alpha_c + (m_{h_1}^2 - m_{h_2}^2 \sin^2\alpha_c - m_{h_3}^2 \cos^2\alpha_c)\tan\alpha \sin\alpha_b}{(m_{h_2}^2 - m_{h_3}^2)\tan\alpha\cos\alpha_c \sin\alpha_c - (m_{h_1}^2 - m_{h_2}^2 \sin^2\alpha_c - m_{h_3}^2 \cos^2\alpha_c)\sin\alpha_b} \ . \tag{5.18}$$

The last equation relates the two CPV angles, α_c and α_b, and indicates that there exists only one independent CPV phase in our model. Using Eq. (5.9) and the minimization condition Eq. (5.4) we obtain the full relationships between model parameters (λ_1, λ_2, λ_3, λ_4, $\mathrm{Re}\lambda_5$, $\mathrm{Im}\lambda_5$, m_{11}^2, m_{22}^2, $\mathrm{Re}m_{12}^2$, $\mathrm{Im}m_{12}^2$) and phenomenological parameters (v, $\tan\beta$, ν, α, α_b, α_c, m_{h_1}, m_{h_2}, m_{h_3}, m_{H^+}). Through Eq. (5.18), one can solve for the angle α_b in terms of α_c,

$$\alpha_b = -\arcsin\left[\frac{(m_{h_2}^2 - m_{h_3}^2)\sin 2\alpha_c \cot(\beta+\alpha)}{2(m_{h_1}^2 - m_{h_2}^2 \sin^2\alpha_c - m_{h_3}^2 \cos^2\alpha_c)}\right] \ . \tag{5.19}$$

Conversely, one could obtain the formula for α_c in terms of α_b. However, two solutions will be generated when solving the second order equation for $\tan\alpha_c$. Here we adopt the convention in Ref. [61],

$$\alpha_c = \begin{cases} \alpha_c^-, & \alpha+\beta \le 0 \\ \alpha_c^+, & \alpha+\beta > 0 \end{cases} \ , \qquad \tan\alpha_c^{\pm} = \frac{\mp|\sin\alpha_b^{\max}| \pm \sqrt{\sin^2\alpha_b^{\max} - \sin^2\alpha_b}}{\sin\alpha_b} \sqrt{\frac{m_{h_3}^2 - m_{h_1}^2}{m_{h_2}^2 - m_{h_1}^2}} \ . \tag{5.20}$$

where $\sin\alpha_b^{\max}$ sets a theoretical bound on the CPV angle α_b which comes from the requirement of the existence of a real solution for $\tan\alpha_c$:

$$\sin^2\alpha_b \leq \frac{(m_{h_3}^2 - m_{h_2}^2)^2\cot^2(\alpha+\beta)}{4(m_{h_2}^2 - m_{h_1}^2)(m_{h_3}^2 - m_{h_1}^2)} \equiv \sin^2\alpha_b^{\max} \ . \tag{5.21}$$

5.1.3 Interaction Terms

To eliminate the tree level FCNCs, one can assign Z_2 charges to different fermion fields. In general, this would lead to four possible arrangements in the Yukawa sector, which are often dubbed Type-I, Type-II, Lepton-specific and Flipped 2HDMs [139, 34, 48]. In this work, we only concentrate on the first two, since Type-I (Type-II) differs from Lepton-specific (Flipped) only in the lepton sector and they should behave similarly to the first two in our collider and EDMs experiments. Under the Z_2 symmetry fermion fields transform as

$$Q_L \to Q_L \quad u_R \to u_R \quad d_R \to d_R, \qquad \text{Type I} \quad , \tag{5.22}$$

$$Q_L \to Q_L \quad u_R \to u_R \quad d_R \to -d_R, \qquad \text{Type II} \quad . \tag{5.23}$$

The corresponding Yukawa interactions invariant under the Z_2 symmetry are:

$$\mathcal{L}_{\rm I} = -Y_U\overline{Q}_L(i\tau_2)\phi_2^* u_R - Y_D\overline{Q}_L\phi_2 d_R + \text{h.c.} \ , \tag{5.24}$$

$$\mathcal{L}_{\rm II} = -Y_U\overline{Q}_L(i\tau_2)\phi_2^* u_R - Y_D\overline{Q}_L\phi_1 d_R + \text{h.c.} \ . \tag{5.25}$$

The interaction of the physical Higgs with fermions and with vector bosons can be parametrized as

$$\mathcal{L}_{int} = -\frac{m_f}{v}h_i\left(c_{f,i}\bar{f}f + \tilde{c}_{f,i}\bar{f}i\gamma_5 f\right) + a_i h_i\left(\frac{2m_W^2}{v}W_\mu W^\mu + \frac{m_Z^2}{v}Z_\mu Z^\mu\right) \ , \tag{5.26}$$

where $c_{f,i}(\tilde{c}_{f,i})$ represents the scalar (pseudo-scalar) component of the physical Higgs h_i coupling to fermions while a_i stands for the coefficient of h_i coupling to the vector

bosons. Analytic expressions for these coefficients are given in terms of the phenomenological parameters in Table 5.1. Higgs global fits to the CP conserving 2HDM

	$c_{t,i}$	$c_{b,i} = c_{\tau,i}$	$\tilde{c}_{t,i}$	$\tilde{c}_{b,i} = \tilde{c}_{\tau,i}$	a_i
Type I	$R_{i2}/\sin\beta$	$R_{i2}/\sin\beta$	$-R_{i3}\cot\beta$	$R_{i3}\cot\beta$	$R_{i2}\sin\beta + R_{i1}\cos\beta$
Type II	$R_{i2}/\sin\beta$	$R_{i1}/\cos\beta$	$-R_{i3}\cot\beta$	$-R_{i3}\tan\beta$	$R_{i2}\sin\beta + R_{i1}\cos\beta$

Table 5.1: Couplings to Higgs mass eigenstates.

from current LHC measurements indicate that the couplings are close to the alignment limit: $\beta - \alpha = \pi/2$ [72, 71].

Hence, we concentrate on the region having only small deviations from this limit in our study. The interaction between the heavy Higgses, SM Higgs and Z bosons can be parametrized in the following form:

$$\mathcal{L}_{h_i \to Z h_1} = g_{iz1} Z^\mu (\partial_\mu h_i h_1 - h_i \partial_\mu h_1) \ , \tag{5.27}$$

with the coefficient g_{iz1} expressed as:

$$g_{iz1} = \frac{e}{\sin 2\theta_W} \left[(-\sin\beta R_{11} + \cos\beta R_{12}) R_{i3} - (-\sin\beta R_{i1} + \cos\beta R_{i2}) R_{13} \right] . \tag{5.28}$$

We parametrize the deviation from the alignment limit by a small variable θ where $\beta - \alpha = \pi/2 + \theta$. Then we expand coupling g_{iz1} in the limits of small α_b (CPV angle) and θ , which gives,

$$g_{2z1} \ \propto \ -\alpha_b + O(\alpha_b \theta) \tag{5.29}$$

$$g_{3z1} \ \propto \ -\theta + O(\alpha_b^2) \tag{5.30}$$

Thus, near the alignment limit, the decay $h_2 \to Z h_1$ could occur only if $\alpha_b \neq 0$, assuming it is kinematically allowed. In contrast, the decay $h_3 \to Z h_1$ could arise

even in the $\alpha_b = 0$ limit so long as there exists a departure from exact alignment. Consequently, one may interpret null results of any search for a heavy scalar decaying to a Z-boson and a SM-like Higgs boson in terms of constraints on either α_b or θ. In what follows we will, thus, consider the present and prospective constraints on α_b in two cases: $\theta = 0$ and $\theta \neq 0$.

5.2 Production and Decay of Heavy Higgs

5.2.1 Production of Heavy Higgs

At the LHC, the dominant production mode for a heavy Higgs is via gluon fusion. Therefore, we restrict our study on this specific production mode. The one loop gluon fusion production cross-section of a heavy Higgs is obtained by rescaling the value of the production cross-section for the SM-like Higgs:

$$\sigma(gg \to h_i) = \sigma(gg \to H_{\rm SM}) \frac{\left| c_{t,i} F^H_{1/2}(\tau^i_t) + c_{b,i} F^H_{1/2}(\tau^i_b) \right|^2 + \left| \tilde{c}_{t,i} F^A_{1/2}(\tau^i_t) + \tilde{c}_{b,i} F^A_{1/2}(\tau^i_b) \right|^2}{\left| F^H_{1/2}(\tau^i_t) + F^H_{1/2}(\tau^i_b) \right|^2}, \tag{5.31}$$

with $\tau^i_f = m^2_{h_i}/(4m^2_f)$, the ratio of the mass squared of the heavy Higgs (h_i) to 4 times the mass squared of the fermion running in the loop. Here, $\sigma(gg \to H_{\rm SM})$ represents the gluon fusion production cross-section of a heavy Higgs with SM couplings. The functions $F^H_{1/2}$ and $F^A_{1/2}$ are defined in the following:

$$F^H_{1/2}(\tau) = 2\left(\tau + (\tau - 1) f(\tau)\right) \tau^{-2}\,, \tag{5.32}$$

$$F^A_{1/2}(\tau) = 2 f(\tau) \tau^{-1}\,, \tag{5.33}$$

$$f(\tau) = \begin{cases} \arcsin^2\left(\sqrt{\tau}\right), & \tau \leq 1 \\ \frac{1}{4}\left[\log\left(\frac{1+\sqrt{1-\tau^{-1}}}{1-\sqrt{1-\tau^{-1}}}\right) - i\pi\right]^2, & \tau > 1 \end{cases}. \tag{5.34}$$

As one can see from Eq. (5.31), the numerator involves the sum of two contributions arising from the CP-odd and CP-even components of the physical Higgs boson, respectively. Denoting $\mathcal{M}^{gg\to h_i}_{\rm CP-odd}$ and $\mathcal{M}^{*gg\to h_i}_{\rm CP-even}$ as the CP-odd and CP-even parts of the gluon fusion matrix elements, we see that the interference term $\mathcal{M}^{gg\to h_i}_{\rm CP-odd}\mathcal{M}^{*gg\to h_i}_{\rm CP-even}$ vanishes after integrating over final state phase space due to parity. The heavy Higgs production cross-section in this form automatically takes into account the K-factor, if one uses the production $\sigma(gg \to H_{\rm SM})$ with higher order corrections. Here we obtain the values of $\sigma(gg \to H_{\rm SM})$ from the website [2].

5.2.2 Decay of Heavy Higgs

The dominant two body decay modes of the heavy Higgses are taken into account with $\Gamma_{\rm tot}$ expressed in the following form:

$$\begin{aligned}\Gamma_{\rm tot}(h_i) &= \Gamma(h_i \to gg) + \Gamma(h_i \to Zh_1) + \Gamma(h_i \to W^+W^-) + \Gamma(h_i \to ZZ) + \Gamma(h_i \to t\bar{t}) \\ &+ \Gamma(h_i \to b\bar{b}) + \Gamma(h_i \to \tau^+\tau^-) + \Gamma(h_i \to h_1h_1) + \cdots \ , \end{aligned} \tag{5.35}$$

where the "$+\cdots$ denote the tiny decay rates to a pair of light fermions and photons, and Z boson and photon, which we have neglected. In addition, we ignore decay rate of a heavy Higgs to one SM-like Higgs and another heavy Higgs, as well as a pair of heavy Higgses because they are forbidden by kinematics due to the mass hierarchy we choose in our benchmark model. The analytical expression for each two-body decay rate can be found in the Appendix A.2.

5.3 Simulation detail

In this section, we will discuss details of our collider simulation. We first reproduce the result of 8 TeV ATLAS exclusion limit on $\sigma(gg \to h_i) \times {\rm Br}(h_i \to Zh_1) \times {\rm Br}(h_1 \to b\bar{b})$ obtained by searching for a heavy Higgs $h_{i=2,3}$ decaying to $Z(\ell^+\ell^-)h_1(b\bar{b})$ [10] (As

in Ref. [10] we do not include a Br($Z \to \ell^+\ell^-$) factor because it is assumed to have the SM value) . We then use a BDT method to perform events classification and derive the projected exclusion limit for a future 14 TeV search. Events are generated by `MadGraph 5 aMC@NLO` [24] and then passed through PYTHIA6 [237] for parton showering. Finally Delphes3 [92] is used for fast detector simulation.

5.3.1 8 TeV Result Reproduction

We use the cuts described in Ref. [10] as follow:

- The events must have 2 electrons or 2 opposite charged muons with $p_T^{e,\mu} > 7$ GeV and $|\eta_e|(|\eta_\mu|) < 2.5(2.7)$
- The leptons must have $p_{T,lead}^{e,\mu} > 25$ GeV, and if the leptons are $\mu^+\mu^-$ pairs, then one of the μ must satisfy $|\eta_\mu| < 2.5$
- The events must have exactly 2 tagged b-jets with $p_{b,T}^{\rm lead} > 45$ GeV and $p_{b,T}^{\rm sub} > 20$ GeV
- The reconstructed invariant mass for dilepton and dijet systems should satisfy: $83 < m_{\ell\ell} < 99$ GeV and $95 < m_{bb} < 135$ GeV
- $E_T^{\rm miss}/\sqrt{H_T} < 3.5$ GeV$^{1/2}$ where H_T is defined as the scalar sum of all jets and leptons in the events
- $p_T^{\rm Z} > 0.44 \times M_{h2,3}^{\rm rec} - 106$ GeV where $M_{h2,3}^{\rm rec}$ is the reconstructed mass of heavy Higgs.

For the detector simulation, we use the default Delphes ATLAS cards with b tagging efficiency equal to 70% as used in the ATLAS analysis [10]. In the mean time we also modify the following value to match the ATLAS analysis:

- The isolation conditions for leptons:

Change DeltaRMax from 0.5(default) to 0.2; Change PTMin from 0.5(default) to 0.4(1) for electron(muon); Change PTRatio from 0.1(default) to 0.15. These changes will increase the lepton identification in the boosted regime.

- Change the ParameterR for jet-clustering(anit-kt) algorithm from 0.6 to 0.4.

For the signal process, we only take into account the gluon fusion production mode of the heavy Higgs. As for the background processes, we consider the two major backgrounds Zbb and $t\bar{t}$ as well as to sub-leading backgrounds SM Zh and diboson ZZ backgrounds. For all the backgrounds, we generate events with one additional jet with jet matching. The numbers of events generated and the corresponding acceptance times efficiency are given in Table 5.2. The cross-sections are normalized to the values with higher order corrections. The K-factors for Zbb , $t\bar{t}$, Zh, ZZ are calculated based on the result in Ref. [117, 88, 3]. One can observe that the $Z(\ell\ell)bb$ background is a bit larger than the ATLAS result in Table 5.2. This maybe due to the fact that ATLAS used a data- driven method to estimate the number of $Z(\ell\ell)bb$ background events, which may include some effects that our fast detector simulation cannot fully replicate. However, one can also see that these kinds of effects are at a controllable level; our simulation result agrees with ATLAS results within at most 20% uncertainty. Since we may also expect the same kind of effect in 14 TeV simulations, our projected exclusion limit result will be conservative.

We present the reconstructed invariant mass of the heavy Higgs in Fig. 5.1a which can be compared with the ATLAS result in Fig.3(b) in Ref. [10]. With this binned distribution we use a profile likelihood method as used in the ATLAS paper to reproduce the 95% CLs exclusion limit. A comparison with ATLAS result is given in Fig. 5.1b, the red curve is our reproduced exclusion limit, and the blue curve is the ratio of the ATLAS results to our reproduced values. One can see that, the ratio is generally less than one which corresponds to the excess of $Z(\ell\ell)bb$ background in our simulation. The peak at 800 GeV is due to the lack of background statis-

Backgrounds/ Signal	σ(pb)	$\sigma \times \int \mathcal{L}$	simulated # of events after cuts	# of expected event in Ref. [10]	A $\times$ ϵ
$Z(\ell\ell)bb$	12.91	2.620×10^5	1,788	1443±60	6.825×10^{-3}
$t(bl\nu)\bar{t}(bl\nu)$	18.12	3.678×10^5	359	317±28	9.761×10^{-4}
SM $Z(\ell\ell)h(bb)$	0.02742	5.566×10^2	47	31±1.8	8.443×10^{-2}
Diboson($Z(\ell\ell)Z(bb)$)	0.2122	4.308×10^3	28	30±5	6.679×10^{-3}
Signal(500 GeV)	0.03	4.06×10^2	54	-	1.332×10^{-1}

Table 5.2: Summary of the 8 TeV simulation. The second column gives the cross-section of each background process at 8 TeV LHC with generator level cuts. The signal distributions are normalized to 0.03 pb as suggested in Ref. [10]. The third column is the total number of events produced at 8TeV LHC with the integrated luminosity equal to 20.3 fb^{-1}. The fourth column is the number of events left for each background after all the cuts with the integrated luminosity equal to 20.3 fb^{-1}. The fifth column gives the number of events left with the same cuts estimated by ALTAS in Ref. [10]. The last column gives the acceptance times the efficiency after all the cuts obtained by our simulation.

tics and downward fluctuation near $m_{hi} = 800$ GeV, but for our benchmark models where $m_{h2} = 550, m_{h3} = 600$ GeV and $m_{h2} = 400, m_{h3} = 450$ GeV , the ratio seems reasonably close to one.

5.3.2 14 TeV Prediction

We use the same Delphes card when generating events for the 14 TeV case. The preselection cuts we use are almost the same as those for the 8 TeV case. In order to get a sufficiently large sample for BDT analysis, we expand the mass window for m_{bb} from $95 \sim 135$ GeV to $60 \sim 140$ GeV. Also, rather than implementing the $E_T^{miss}/\sqrt{H_T}$ and p_T^Z cuts, we allow the BDT to optimize them. The numbers of events generated and the acceptance times efficiency after preselection for signal and backgrounds are given in Table 5.3. After preselection, we use a built-in package in ROOT, Toolkit for Multivariate Data Analysis (TMVA) [159] and the BDT method for the classification of signal and background events. The variables used for the classification are listed below:

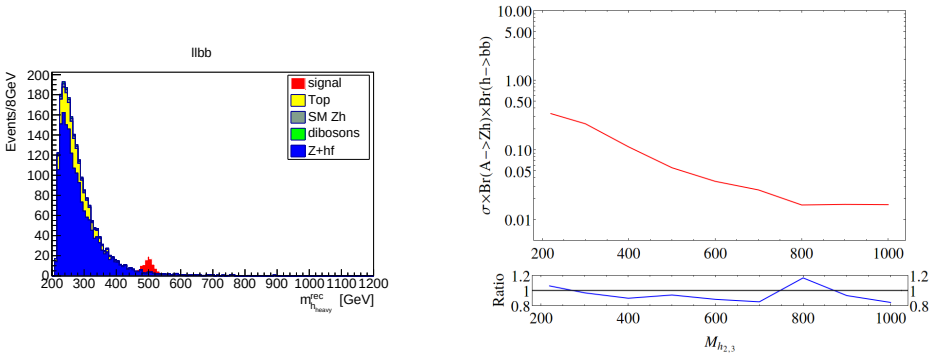

(a) $M_{h_2}^{\text{rec}}$ Distribution (b) exclusion limit

Figure 5.1: Fig.(a) shows the reconstructed invariant mass distributions with $\ell^+\ell^- b\bar{b}$ final state. The signal comes from a heavy Higgs of mass 500 GeV and production cross-section 0.03 pb with an integrated luminosity 20.3 fb^{-1}. Fig.(b) demonstrates the 95% exclusion limit on the signal $\sigma(gg \to A)Br(A \to Zh)Br(h \to bb)$. The red curve is our result using the distribution in Fig.(a) with profile likelihood method while the blue curve is the ratio of the ATLAS result (in Fig.3(b) of Ref. [10]) to our reproduced expected exclusion limit.

$$p_{T,\ell}^{\text{lead}}, p_{T,\ell}^{\text{sub}}, p_{T,b}^{\text{lead}}, p_{T,b}^{\text{sub}}, m_{\ell\ell}, m_{bb}, p_T^Z, p_T^h, E_T^{\text{miss}}/\sqrt{H_T}, \Delta R_{\ell\ell}, \Delta R_{jj}, \Delta R_{Zh}, \Delta\phi_{Zh}, \quad (5.36)$$

where $p_{T,(j,\ell)}^{\text{lead,sub}}$ represent the leading and subleading p_T of leptons and jets; $m_{\ell\ell}$ and m_{bb} are the invariant masses of dijet and dilepton systems, respectively; $p_T^{h,Z}$ stands for the reconstructed p_T of the Z boson and the SM Higgs; $E_T^{\text{miss}}/\sqrt{H_T}$ is the ratio of the missing transverse energy to $\sqrt{H_T}$ defined in the previous subsection; $\Delta R_{\ell\ell,bb,Zh}$ are the angular separations of two leptons, two bjets and reconstructed Zh, respectively, with $\Delta R_{ab} = \sqrt{(\eta_a - \eta_b)^2 + (\phi_a - \phi_b)^2}$. $\Delta\phi_{Zh}$ is the separation of the azimuthal angles between Z and h. The distributions of these variables are shown in Appendix A.1.

We select representative points with $M_{h2} = 400$, $M_{h3} = 450$, $M_{h2} = 550$ and $M_{h3} = 600$ GeV as the signal to train the BDT. The BDT algorithm settings in TMVA are:

Backgrounds/ Signal	σ(pb)	# of events generate	# of events remaining after cuts	ϵ_{pre}
$Z(\ell\ell)bb$	36.57	7.084×10^6	94,323	1.331×10^{-2}
$t(bl\nu)\bar{t}(bl\nu)$	68.11	3.276×10^7	120,627	3.680×10^{-3}
SM $Z(\ell\ell)h(bb)$	0.0502	1.429×10^5	14,380	1.006×10^{-1}
Diboson($Z(bb)Z(\ell\ell)$)	0.3833	1.780×10^6	80,887	4.554×10^{-3}
Signal(550 GeV)	0.06	1.0×10^5	20,645	0.2065
Signal(600 GeV)	0.06	1.0×10^5	21,392	0.2139

Table 5.3: Summary of the 14 TeV simulation after preselection cuts. The second column gives the cross-sections for each background process after generator level cuts at the 14 TeV LHC. The signal distributions are normalized to 0.06 pb. The third column gives the number of events generated in our simulation. The fourth column shows the number of events left after the preselection cuts described in Sec. 5.3.2 before training the BDT. The last column gives the efficiency of the preselection cuts for each process.

$$NTrees = 850 : MiniNodeSize = 2.5\% : MaxDepth = 3 : BoostType = AdaBoost$$
$$: AdaBoostBoostBeta = 0.5 : UseBaggedBoost : BaggedSampleFraction = 0.5$$
$$: SeparationType = GiniIndex : nCuts = 20 .$$

The distributions of the BDT ouput for two heavy Higgs masses are shown in figs. 5.2c and 5.2d. One could find that the discriminating power is a bit better for the heavier Higgs as we expected.

The next step is to select a cut on the BDT output to obtain the most stringent 95% exclusion limits. After applying the BDT cuts shown in Table. 5.6 and 5.7, we use the reconstructed heavy Higgs mass distribution of the remaining events to derive the 95% exclusion limit on $\sigma(gg \to h_{2,3})Br(h_{2,3} \to Zh_1)Br(h_1 \to b\bar{b})$. We show the resulting prospective exclusion limits in Tables 5.6 and 5.7. We also perform a cut-based analysis with the same ATLAS cuts described in 5.3.1, and the results are shown in the "cut-based result" column in Tables 5.6 and 5.7. One can see that the exclusion limits of our BDT analysis are 30% to 50% better (lower) than the cut-based analysis results.

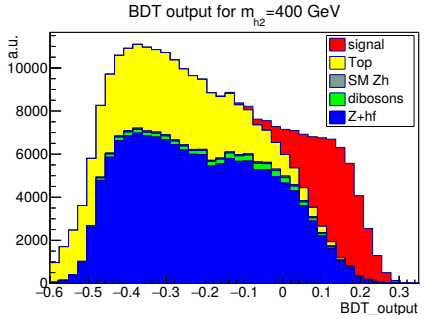

(a) BDT output for $M_{h2} = 400$ GeV

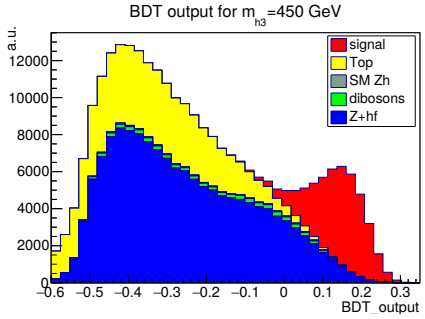

(b) BDT output for $M_{h3} = 450$ GeV

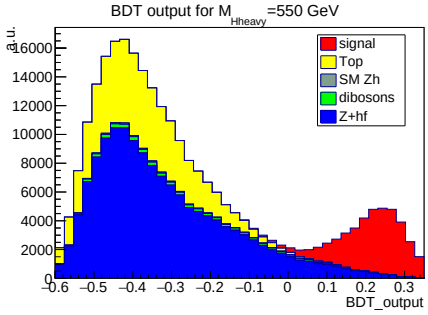

(c) BDT output for $M_{h2} = 550$ GeV

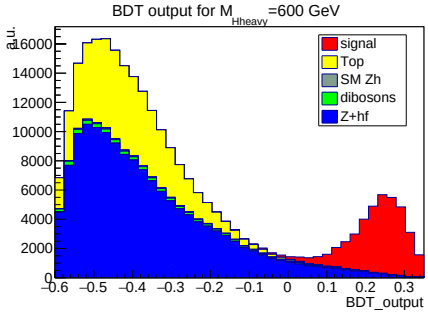

(d) BDT output for $M_{h3} = 600$ GeV

Figure 5.2: The BDT output distributions for both signal and backgrounds. The signals in Figs. (a) and (b) are for heavy Higgses with masses 400, 450, 550 and 600 GeV, respectively. The background distributions are normalized to the actual 14 TeV cross-sections in Ref. [2], while the signal distributions are normalized to 0.06 pb.

$M_{h_2} = 400$ GeV (14 TeV)			
Luminosity(fb^{-1})	Best Cut	exclusion limit σ_L (pb)	cut-based result (pb)
100	0.14	0.0582	0.1003
300	0.14	0.0336	0.0571
3000	0.14	0.0103	0.0185

Table 5.4: Exclusion limits σ_L for $\sigma(gg \to h_2) \times Br(h_2 \to Zh_1) \times Br(h_1 \to b\bar{b})$ and best cuts on BDT output of different luminosities for $M_{h_2} = 400$ GeV. The column "cut-based result" gives the exclusion limit derived from the ATLAS cut-based analysis described in Section 5.3.1.

$M_{h_3} = 450$ GeV (14 TeV)			
Luminosity(fb^{-1})	Best Cut	exclusion limit Fig (pb)	cut-based result (pb)
100	0.15	0.0506	0.0700
300	0.16	0.0292	0.0571
3000	0.16	0.00901	0.0185

Table 5.5: Exclusion limits σ_L for $\sigma(gg \to h_2) \times Br(h_2 \to Zh_1) \times Br(h_1 \to b\bar{b})$ and best cuts on BDT output of different luminosities for $M_{h_2} = 450$ GeV. The column "cut-based result" gives the exclusion limit derived from the ATLAS cut-based analysis described in Section 5.3.1.

$M_{h_2} = 550$ GeV (14 TeV)			
Luminosity(fb^{-1})	Best Cut	exclusion limit σ_L (pb)	cut-based result (pb)
100	0.22	0.0299	0.0443
300	0.22	0.0167	0.0261
3000	0.22	0.00510	0.00782

Table 5.6: Exclusion limits σ_L for $\sigma(gg \to h_2) \times Br(h_2 \to Zh_1) \times Br(h_1 \to b\bar{b})$ and best cuts on BDT output of different luminosities for $M_{h_2} = 550$ GeV. The column "cut-based result" gives the exclusion limit derived from the ATLAS cut-based analysis described in Section 5.3.1.

$M_{h_3} = 600$ GeV (14 TeV)			
Luminosity(fb^{-1})	Best Cut	exclusion limit σ_L (pb)	cut-based result (pb)
100	0.21	0.0248	0.0340
300	0.22	0.0138	0.0192
3000	0.22	0.00423	0.00598

Table 5.7: Exclusion limits σ_L for $\sigma(gg \to h_3) \times Br(h_3 \to Zh_1) \times Br(h_1 \to b\bar{b})$ and best cuts on BDT output of different luminosities for $M_{h_3} = 600$ GeV. The column "cut-based result" gives the exclusion limit derived from the ATLAS cut-based analysis described in 5.3.1.

5.4 Results and Discussion

We now translate our simulated exclusion limit into constraints on the parameter space of CPV 2HDMs. We mainly focus on the benchmark point below which is consistent with the electroweak precision measurements and muon $g-2$ data as discussed in Ref. [61]:

$$m_{h_2} = 550 \text{ GeV},\ m_{h_3} = 600 \text{ GeV},\ m_{H^\pm} = 620 \text{ GeV}, \nu = 1 \tag{5.37}$$

and show the constraints on $\sin\alpha_b$ vs $\tan\beta$. As a comparison we also include the constraints in the alignment limit for a lighter mass benchmark point: $m_{h_2} = 400$ GeV, $m_{h_3} = 450$ GeV, $m_{H^\pm} = 420$ GeV, $\nu = 1$. The reason we choose a relatively small mass splitting between the two heavy Higgses is that this splitting is tightly constrained by bounds on the T parameter from electroweak precision data. The study in Ref. [61] shows that a splitting round 50 GeV is already marginally consistent with electroweak precision data.

The 95% CLs exclusion limit is given by:

$$\sigma(gg \to h_{2,3}) \times Br(h_{2,3} \to Zh_1) \times Br(h_1 \to b\bar{b}) < \sigma_L \tag{5.38}$$

where σ_L are the exclusion limit for different luminosity for $m_{h2} = 400$ GeV, $m_{h2} = 450$ GeV, $m_{h2} = 550$ GeV and $m_{h3} = 600$ GeV that listed in 5.4, 5.5, 5.6 and 5.7 respectively. We assume that the resonance process is dominant when the invariant mass of two gluons is approaching the mass of the heavy Higgs. This is not always true in the parameter space we consider, especially in the limit of small θ. The gluon fusion to Zh_1 box diagram may become important and interfere with the resonant triangle diagram. This may change the distribution of the invariant mass of Zh_1. Here, we will simply identify the region of parameter space that may suffer from this effect, leaving a detailed analysis for future study. To proceed, we will compare the relative

scale of the amplitude squared of the resonant and non-resonant $gg \to Zh_1$ processes at the center of mass energy $\sqrt{s} = m_{h_2}$, and m_{h_3}. For the resonance contribution we use the following formula

$$\begin{aligned}\overline{|M_i|^2} &= \frac{G_F \alpha_s^2 |g_{iz1}|^2 s^2}{512\pi^2\sqrt{2}} [|\sum_{f=t,b} c_{f,i} F_{1/2}^H(\tau_f^i)|^2 + |\sum_{f=t,b} \tilde{c}_{f,i} F_{1/2}^A(\tau_f^i)|^2] \\ &\times \frac{M_Z^2 - 2m_{h_1}^2 - 2s + (m_{h_i}^2 - s)^2/M_Z^2}{(s - m_{h_i}^2)^2 + m_{h_i}^2 \Gamma_{h_i}^2} \end{aligned} \tag{5.39}$$

where G_F and α_s are the Fermi constant and strong coupling constant, respectively, while g_{iz1}, $F_{1/2}^{A/H}$, c_f, $\tilde{c_f}$, and Γ_{h_i} are defined in Sections 6.1 and 5.2. For the non-resonant piece we obtain the scale of $\overline{M_{\rm box}^2} \simeq 10^{-5}$ from Ref. [154]. In presenting our results in Figs. 5.3-5.5, we include contours of constant $\overline{|M_i|^2}$ in order to identify regions where the resonant and non-resonant contributions are commensurate in scale.

We now consider the prospective future reach at the LHC. In the alignment limit, the sensitivity comes primarily from the resonant production of h_2, as expected from Eqs. 5.29 and 5.30. We show the prospective exclusion regions associated with $h_{2,3}$ production separately in Fig. 5.3. The pink region is forbidden by the requirement of the electroweak symmetry breaking. The green, blue, and magenta regions represent the prospective exclusion limits for the LHC integrated luminosities equal to 100 fb^{-1}, 300 fb^{-1} and 3000 fb^{-1}, respectively. The black contours correspond to $\log_{10} \overline{|M|_i^2}$ in Eq. (5.39) with $s = m_{h_{2,3}}$ for $i = 2, 3$. If we require $\overline{|M|_i^2} > 10^{-4}$ to guarantee the dominance of the resonant production, then there will be some parts of the prospective exclusion region for 3000 fb^{-1} at low $\tan\beta$ that may not be valid for our analysis. One could observe that from Fig. 5.6b and Fig. 5.6d there is a loss of sensitivity for h_3 near $\tan\beta \approx 1$ in the alignment limit for both Type-I and Type-II models. This is due to the cancellation effect in the coupling g_{3z1} when $-\alpha = \beta = \pi/4$.

The situation is similar for non-vanishing but small θ. An illustration for $\cos(\beta - \alpha) = 0.02$ is shown in Fig. 5.4. However, for a large deviation, for example $\cos(\beta - \alpha) =$

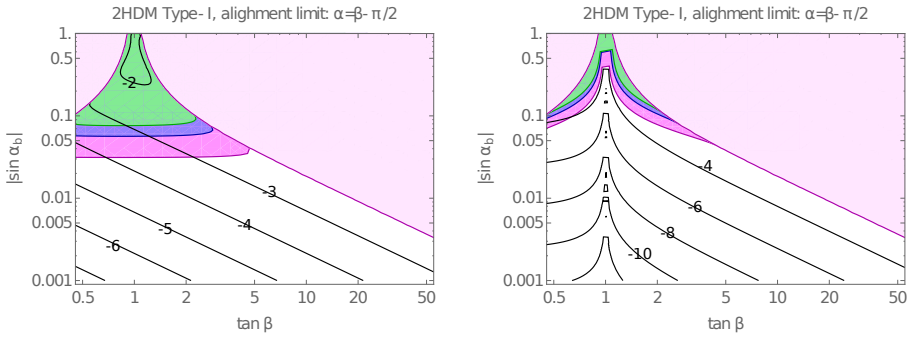

(a) Type-I Alignment limit constraint on h_2

(b) Type-I Alignment limit constraint on h_3

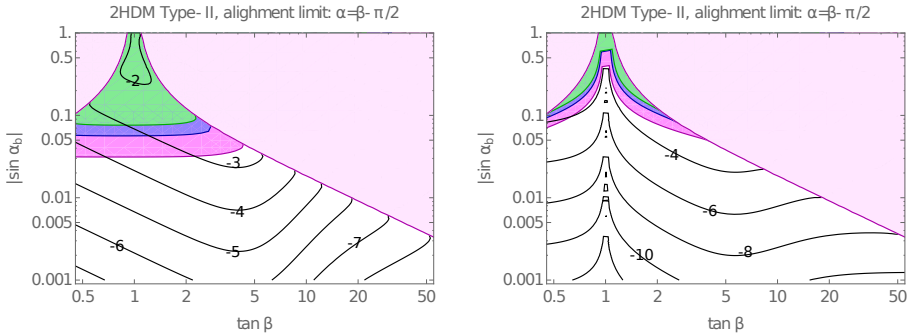

(c) Type-II Alignment limit constraint on h_2

(d) Type-II Alignment limit constraint on h_3

Figure 5.3: Exclusion limits for the heavy Higgs resonant productions in the alignment limit with $m_{h_2} = 550$ GeV, $m_{h_3} = 600$ GeV, $m_{H^\pm} = 620$ GeV, $\nu = 1$. The plots in the first and second row represent the constraints for the Type-I and Type-II models, respectively. The left (right) column shows the constraints from the resonant production of $h_2(h_3)$. The pink region is theoretically inaccessible as described in the text. The green, blue, and magenta regions represent the exclusion limits for the LHC integrated luminosities equal to 100 fb^{-1}, 300 fb^{-1} and 3000 fb^{-1}, respectively. The black contour represents the logarithm of $\log \overline{|M|}_i^2$ in Eq. 5.39 with $s = m_{h_{2,3}}$ for $i = 2, 3$.

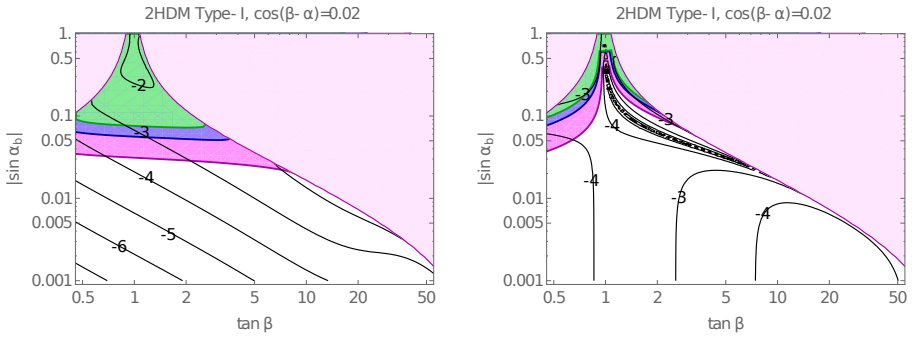

(a) Type-I constraint on h_2 (b) Type-I constraint on h_3

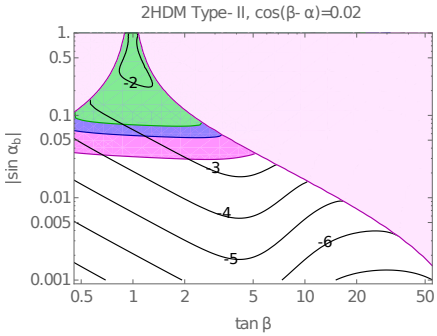

(c) Type-II Constraint on h_2

Figure 5.4: Exclusion limits for the heavy Higgs resonant productions in the Type-I and Type-II 2HDMs with $\cos(\beta-\alpha) = 0.02$, $m_{h_2} = 550$ GeV, $m_{h_3} = 600$ GeV, $m_{H^\pm} = 620$ GeV, $\nu = 1$. The plots in the first and second row represent the constraints for the Type-I and Type-II models, respectively. The left (right) column shows the constraints from the resonance production of $h_2(h_3)$. The pink region is theory-inaccessible. The green, blue, and magenta regions represent the exclusion limits for the LHC integrated luminosities equal to 100 fb^{-1}, 300 fb^{-1} and 3000 fb^{-1}, respectively. The black contour represents the logarithm of $\log \overline{|M|^2_i}$ in Eq. 5.39 with $s = m_{h_{2,3}}$ for $i = 2, 3$.

0.05 in the Type-II model and $\cos(\beta-\alpha)=0.1$ in the Type-I model, the constraints from the resonance production of h_3 become important, and can cover large part of the parameter space. In this situation, the effect of the non-resonant production is negligible due to a relatively large $\overline{|M|^2_3}$. This can be seen in Fig. 5.5.

In Fig. 5.6, we show the corresponding separate exclusion limit for $m_{h_2}=400$ GeV and $m_{h_3}=450$ GeV and contours for $\log\overline{|M|^2_i}$. Compare with Fig. 5.3 we find that the values of $\overline{|M_i|^2}$ at $s=m^2_{h_i}$ are larger than those of heavier Higgs mass. In other word, the peak in the distribution of the invariant mass of final state particles is more prominent for smaller heavy Higgs mass and the interference effects are rather small. Hence, all the exclusion regions we derive satisfy the requirement $\overline{|M|^2_i}>10^{-4}$.

In addition, we take into account the constraint from the Higgs coupling measurements at 7 and 8 TeV LHC as what was done in Ref. [61]. The channels included in the χ^2 analysis are: $h_1\to WW$, ZZ, $\gamma\gamma$, bb, $\tau\tau$. We also include the present and prospective constraints from EDM searches given in Ref. [163], which are summarized in Table 5.8. We find that the constraints from LHC and low energy experiments are complementary. Figures 5.7 and 5.8 demonstrate the exclusion limits from both LHC and EDM searches. In each figure, the orange region gives the current LHC exclusion limit. The blue, and magenta regions represent prospective future LHC limits for integrated luminosities equal to 300 fb^{-1} and 3000 fb^{-1}, respectively. The light green and light blue regions are excluded by the neutron EDM and electron EDM searches, respectively. The light red and light yellow represents current constraints from the mercury and prospective radium atomic EDM searches. The gray regions are excluded by the Higgs coupling measurements. The pink region is again as described above theory-inaccessible. There are also constraints that we do not show in Fig. 5.7 and Fig. 5.8 from heavy flavor physics [113], which exclude the regions of parameter space with $\tan\beta$ less than 0.9 in both Type-I and Type-II models for the benchmark point we choose. These constraints can be relaxed if other new particles are intro-

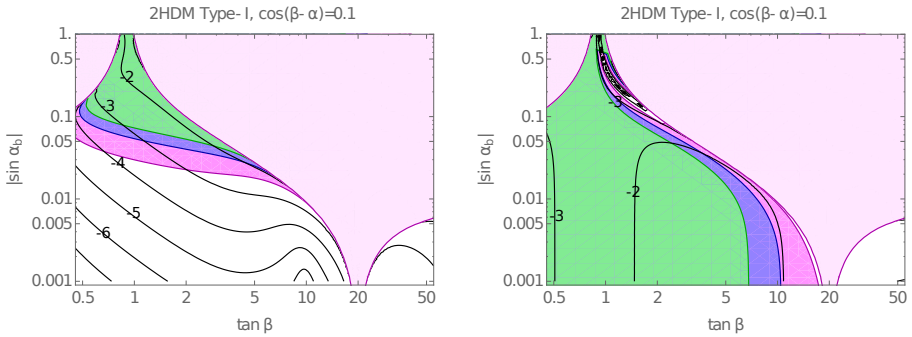

(a) Type-I constraint on h_2

(b) Type-I constraint on h_3

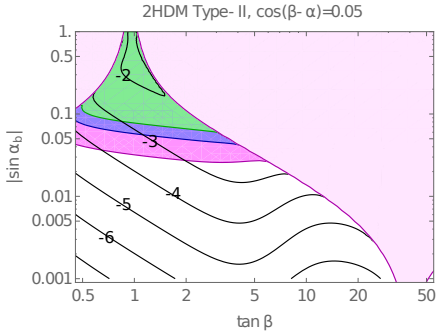

(c) Type-II constraint on h_2

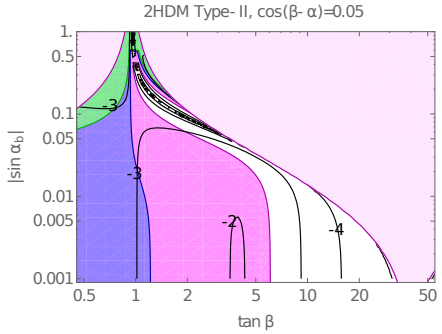

(d) Type-II constraint on h_3

Figure 5.5: Exclusion limits for the heavy Higgs resonant productions with $m_{h_2} = 550$ GeV, $m_{h_3} = 600$ GeV, $m_{H^\pm} = 620$ GeV, $\nu = 1$, and $\cos(\beta - \alpha) = 0.1$ (Type-I), $\cos(\beta - \alpha) = 0.05$ (Type-II). The plots in the first and second row represent the constraints for the Type-I and Type-II models, respectively. The left (right) column shows the constraints from the resonance production of $h_2(h_3)$. The pink region is theoretically inaccessible. The green, blue, and magenta regions represent the exclusion limits for the LHC integrated luminosities equal to 100 fb^{-1}, 300 fb^{-1} and 3000 fb^{-1}, respectively. The black contour represents the logarithm of $\log \overline{|M|_i^2}$ in Eq. 5.39 with $s = m_{h_{2,3}}^2$ for $i = 2, 3$.

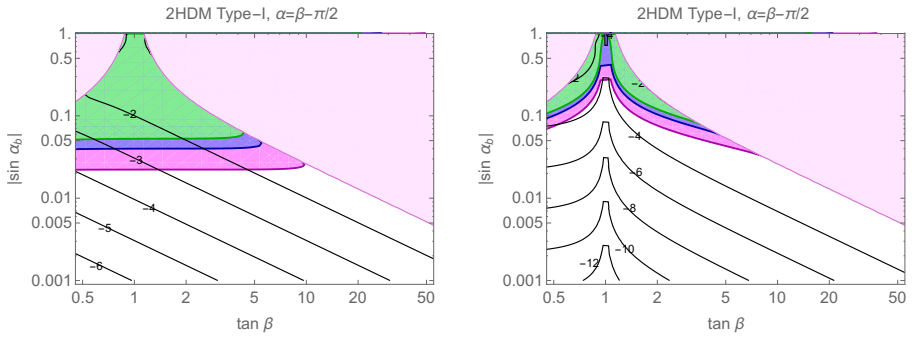

(a) Type-I Alignment limit constraint on h_2

(b) Type-I Alignment limit constraint on h_3

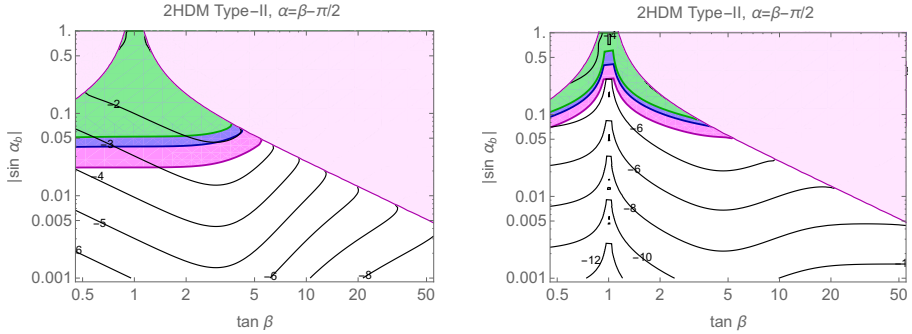

(c) Type-II Alignment limit constraint on h_2

(d) Type-II Alignment limit constraint on h_3

Figure 5.6: Exclusion limits for the heavy Higgs resonant productions in the alignment limit $m_{h_2} = 400$ GeV, $m_{h_3} = 450$ GeV, $m_{H^\pm} = 420$ GeV, $\nu = 1$. The plots in the first and second row represent the constraints for the Type-I and Type-II models, respectively. The left (right) column shows the constraints from the resonant production of $h_2(h_3)$. The pink region is theoretically inaccessible as described in the text. The green, blue, and magenta regions represent the exclusion limits for the LHC integrated luminosities equal to 100 fb^{-1}, 300 fb^{-1} and 3000 fb^{-1}, respectively. The black contour represents the logarithm of $\log \overline{|M|_i^2}$ in Eq. 5.39 with $s = m_{h_{2,3}}^2$ for $i = 2, 3$.

dueced in addition to the 2HDMs or some non-trivial flavor structure [55, 57]. Figure 3 of Ref. [113] demonstrates the constraints on the $\tan\beta$ vs m_{H^+} plane for the Type-I and Type-II 2HDMs. The most stringent bounds on $\tan\beta$ come from $B_s - \bar{B}_s$ mixing and $B_s^0 \to \mu^+\mu^-$ for the Type-I model, and from $B_s - \bar{B}_s$ and $B_d - \bar{B}_d$ mixing for the Type-II model.

Source	Current EDM (e cm)	Projected EDM (e cm)
Electron (e)	$d_{\rm e} < 8.7 \times 10^{-29}$ at 90% CL[38]	$d_{\rm e} < 8.7 \times 10^{-30}$ [184]
Neutron (n)	$d_{\rm n} < 2.9 \times 10^{-26}$ at 90% CL[33]	$d_{\rm n} < 2.9 \times 10^{-28}$ [184]
Mercury (Hg)	$d_{\rm Hg} < 7.4 \times 10^{-30}$ at 95% CL[143]	-
Radium (Ra)	-	$d_{\rm Ra} < 10^{-27}$ [184]

Table 5.8: Current and projected EDM constraints in units of e-cm. For the projected limits we assume that the sensitivity of nEDM is improved by two orders of magnitude, and eEDM is improved by one order of magnitude. The mercury EDM remains the same while future projected sensitivity of the radium EDM is assumed to be $d_{\rm Ra} < 10^{-27}$ e-cm.

In Figs. 5.7a and 5.7b, we show the current and prospective exclusion regions for the Type-I model in the alignment limit. One can see that the reach of the collider search is not competitive with that of the electron EDM search even at the end of the HL-LHC phase, especially in the low $\tan\beta$ region. This is due to the fact that the collider search is sensitive to $\mathrm{Br}(h_{2,3} \to Zh_1)$ in addition to the $h_{2,3}$ production cross sections. In the alignment limit, the Zh_1 channel is fed mainly from the decay of h_2, and the coupling g_{2z1} is suppressed by the CPV angle α_b as shown in Eq. (5.29). Moreover, for low $\tan\beta$, the couplings of h_2 to quarks are enhanced, which leads to a suppression on $\mathrm{Br}(h_2 \to Zh_1)$ and an increasing gluon fusion h_2 production cross section. However, the increase of the latter cannot compensate for the decreasing $\mathrm{Br}(h_2 \to Zh_1)$. The net effect is a reduced Zh_1 signal strength. In contrast, the electron EDM is sensitive to the pseudo-scalar couplings that are enhanced at low $\tan\beta$ in the Type-I model, so electron EDM searches exclude a large part of parameter space in the low $\tan\beta$ region in Fig. 5.7b.

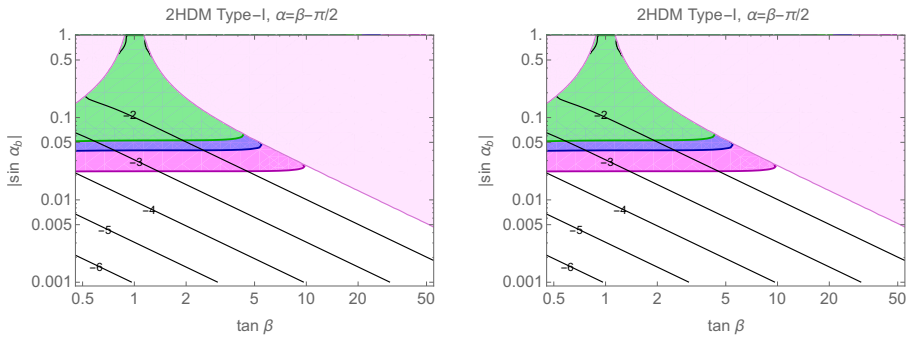

(a) Type-I Alignment limit current (b) Type-I Alignment limit future

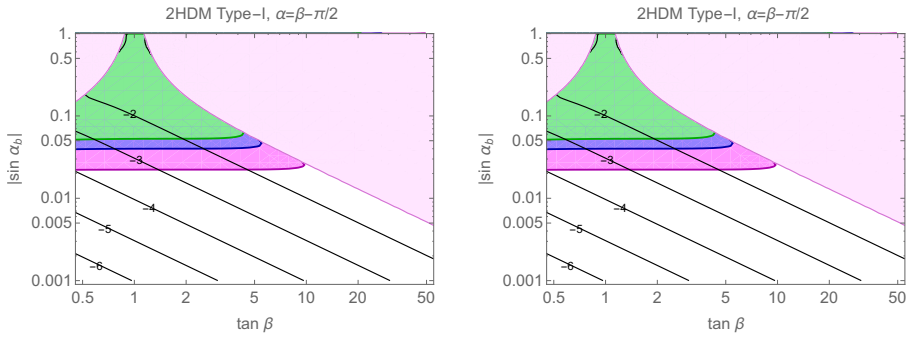

(c) Type-I $\cos(\beta-\alpha)=0.02$ current (d) Type-I $\cos(\beta-\alpha)=0.02$ future

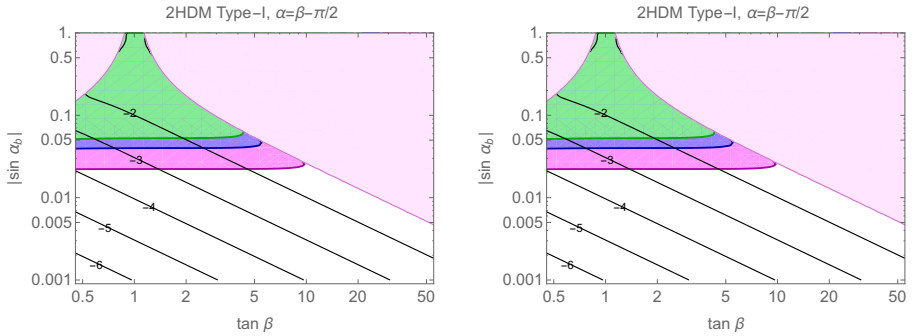

(e) Type-I $\cos(\beta-\alpha)=0.1$ current (f) Type-I $\cos(\beta-\alpha)=0.1$ future

Figure 5.7: Exclusion regions for the collider and EDM experiments in the type-I 2HDM. The left (right) column is for the current (future) exclusion limit. The orange region is excluded by the current LHC data. The blue and magenta regions represent the future LHC limit with integrated luminosities equal to 300 fb^{-1} and 3000 fb^{-1}, respectively. Light transparent red represents the constraint from mercury EDM, light blue denotes electron EDM, light transparent green stands for neutron EDM, and light yellow signifies future prospective radium EDM. The gray region is excluded by the coupling measurement of the SM-like Higgs and the pink region is theoretically inaccessible due to the absence of a real solution for α_c. The benchmark point used here is $m_{h_2}=550$ GeV, $m_{h_3}=600$ GeV, $m_{H^\pm}=620$ GeV, $\nu=1$.

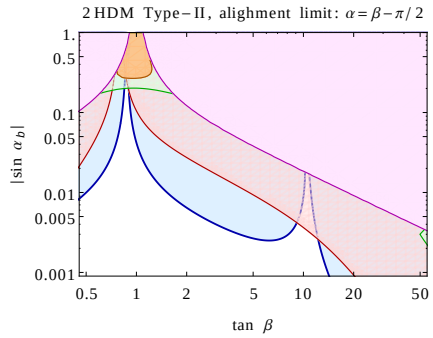

(a) Type-II Alignment limit current

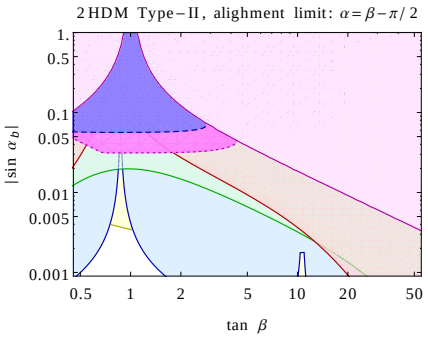

(b) Type-II Alignment limit future

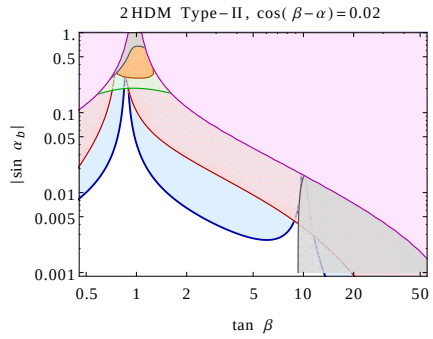

(c) Type-II $\cos(\beta-\alpha) = 0.02$ current

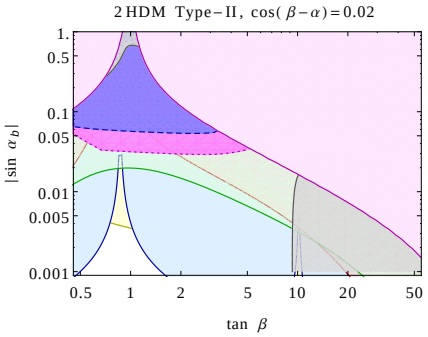

(d) Type-II $\cos(\beta-\alpha) = 0.02$ future

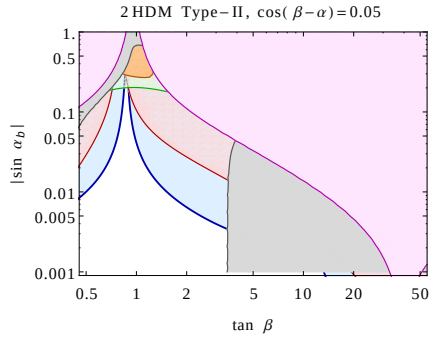

(e) Type-II $\cos(\beta-\alpha) = 0.05$ current

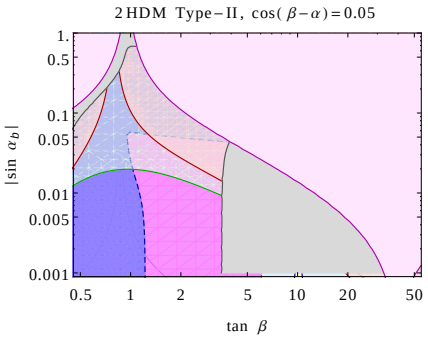

(f) Type-II $\cos(\beta-\alpha) = 0.05$ future

Figure 5.8: Exclusion regions for the collider and EDM experiments in the type-II 2HDM. The left (right) column is for the current (future) exclusion limit. The orange region is excluded by the current LHC data. The blue and magenta regions represent the future LHC limit with integrated luminosities equal to 300 fb^{-1} and 3000 fb^{-1}, respectively. Light transparent red represents the constraint from mercury EDM, light blue denotes electron EDM, light transparent green stands for neutron EDM, and light yellow signifies future prospective radium EDM. The gray region is excluded by the coupling measurement of the SM-like Higgs and the pink region is theoretically inaccessible due to the absence of a real solution for α_c. The benchmark point used here is $m_{h_2} = 550$ GeV, $m_{h_3} = 600$ GeV, $m_{H^\pm} = 620$ GeV, $\nu = 1$.

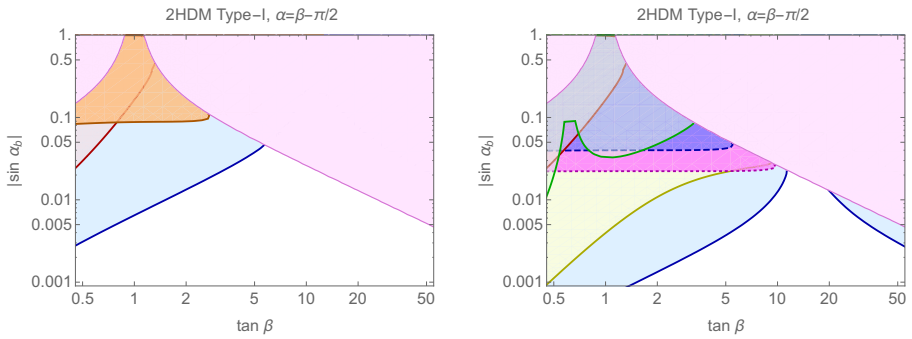

(a) Type-I Alignment limit current (b) Type-I Alignment limit future

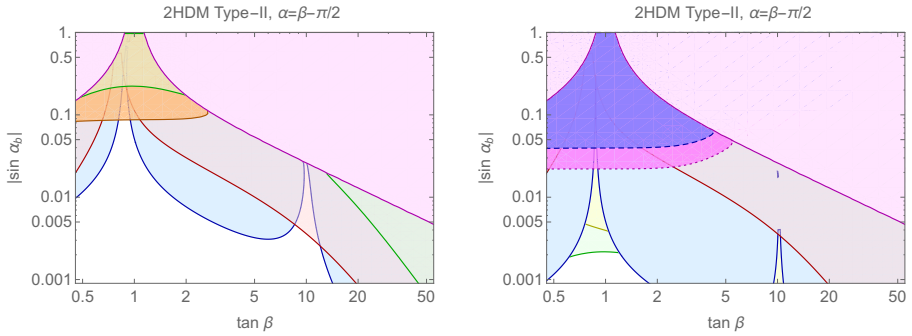

(c) Type-II Alignment limit current (d) Type-II Alignment limit future

Figure 5.9: Exclusion regions for the collider and EDM experiments in the type-I and type-II 2HDM with lighter Higgs mass hierarchy. The left (right) column is for the current (future) exclusion limit. The orange region is excluded by the current LHC data. The blue and magenta regions represent the future LHC limit with integrated luminosities equal to 300 fb^{-1} and 3000 fb^{-1}, respectively. Light transparent red represents the constraint from mercury EDM, light blue denotes electron EDM, light transparent green stands for neutron EDM, and light yellow signifies future prospective radium EDM. The gray region is excluded by the coupling measurement of the SM-like Higgs and the pink region is theoretically inaccessible due to the absence of a real solution for α_c. The benchmark point used here is $m_{h_2} = 400$ GeV, $m_{h_3} = 450$ GeV, $m_{H^\pm} = 420$ GeV, $\nu = 1$.

In Figs. 5.7c to 5.7f, we present the current and prospective exclusion regions away from the alignment limit. We can observe that the current collider constraints are not as strong as those from EDMs . However, the future LHC reach can be comparable to that of the EDMs searches, and even better at moderate $\tan\beta$. One can observe this feature from Eq. (5.30), where g_{3z1} is proportional to θ which describes the level of deviation from the alignment limit, in contrast to Eq. (5.29) where g_{2z1} is suppressed by the small CPV angle α_b. One can also observe that in the large $\tan\beta$ region the LHC loses sensitivity. The reason is that at large $\tan\beta$, pseudo-scalar couplings of both t and b quarks to h_3 are suppressed, so the total partonic production cross-section $\hat{\sigma}(gg \to h_3)$ decreases as $\tan\beta$ increases. Despite the possible increase in $\mathrm{Br}(h_3 \to Zh_1)$, the over all effect is a decreasing trend of signal rate towards large $\tan\beta$ resulting in an untestable region for the LHC search.

In the Type-II model, the results are shown in Fig. 5.8. In contrast to the Type-I model, the electron and mercury EDMs are not able to probe the parameter space when $\tan\beta$ is close to one due to the cancellation in Barr-Zee diagrams indicated in [163] and [44], whereas the neutron and radium EDMs retain sensitivity in this region. In the situation that is close to the alignment limit, as one can observe from Fig. 5.8a to 5.8d, the future LHC reach can help to test the region where $\tan\beta$ is close to one. However, the reach of future neutron and radium EDM constraints still exceeds that of the LHC. When the deviation from the alignment limit is as large as $\cos(\beta-\alpha) = 0.05$, the future LHC may probe a large portion of the parameter space for reasons similar to those for the Type-I model: g_{3z1} is sensitive to this deviation and is not suppressed by the CPV angle. Moreover, some portions of the large $\tan\beta$ region cannot be accessed, but for reasons different from the Type-I case. In the Type-II model, the pseudo-scalar coupling of the t-quark to h_3 is suppressed at large $\tan\beta$, while the pseudo-scalar coupling of the b-quark to h_3 is enhanced. However, for the range of $\tan\beta$ we are interested in, the enhancement of the b-quark loop contribution

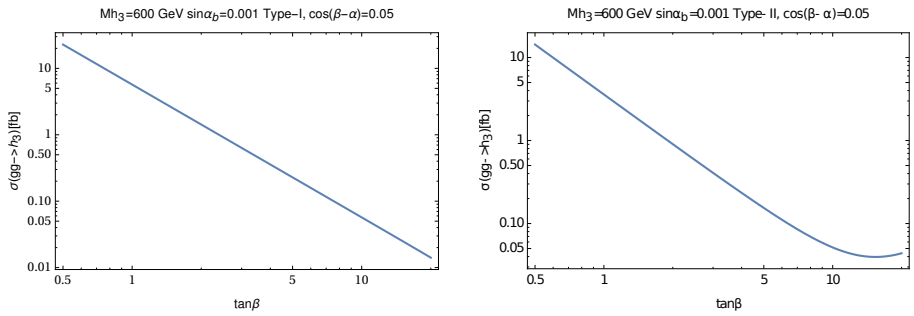

(a) Type-I production cross-section for h_3

(b) Type-II production cross-section for h_3

Figure 5.10: Production cross-section for h_3 for Type-I(left), Type-II(right) model.

to $\hat{\sigma}(gg \to h_3)$ cannot compensate for the suppression of the t-quark loop effect as one can see from Fig. 5.10b. Thus, $\hat{\sigma}(gg \to h_3)$ decreases with increasing $\tan\beta$. As for $Br(h_3 \to Zh_1)$, due to the increasing $Br(h_3 \to \bar{b}b)$ and decreasing $Br(h_3 \to \bar{t}t)$, the overall effect leads to a decreasing $Br(h_3 \to Zh_1)$. A decreasing production cross-section combined with a decreasing decay branching ratio makes the large $\tan\beta$ region relatively inaccessible for the LHC in the Type-II model.

To show the influence of the overall mass scale on the exclusion regions, we present the current and future prospective exclusion limits for both Type-I and Type-II models in the alignment limit in Fig 5.9. Comparing Fig. 5.9a and 5.9b with Fig. 5.7a and Fig. 5.7b, one finds that for the lighter mass benchmark point the exclusion region is generally larger than that of heavier mass point. The reason is that for lighter mass point the resonant production cross-sections for the heavy Higgses increase, so the signal rates are larger compared with those in the heavier mass case. Another feature for the lighter mass scale is that in the region with small $\tan\beta$, the future exclusions are not restricted by the interference effects as the peak value of the amplitude of the resonant process grows. A similar situation occurs for $\cos(\beta-\alpha)$ away from the alignment limit, though we do not show this explicitly. Larger exclusion regions are obtained for the lighter mass point with the same $|\sin\alpha_b|$, $\tan\beta$, and $\cos(\beta-\alpha)$.

Now we argue that the future result of EDM and LHC experiments are expected to be complementary to each other and combining information from two kinds of experiments would help us better determine if the 2HDMs are realized in the nature. Since the global fit of the Higgs coupling measurements constrains 2HDMs in the parameter space that are close to the alignment limit, we summarize our results in two categories: 2HDMs are in the exact alignment limit ($\cos(\beta-\alpha)=0$), 2HDMs deviate from the alignment limit (i.e. $\cos(\beta-\alpha)\neq 0$).

- 2HDMs in the alignment limit:

  - **Future LHC makes a discovery**

    As discussed above, in the alignment limit, the productions of the heavy Higgses h_2 and h_3 are purely determined by the size of CPV angle α_b, so the reach of future LHC is merely sensitive to the CPV effect in the model. From Fig. 5.7b, one can observe that, in the Type-I model, the reach of future LHC is entirely inside the reach of future radium and electron EDM experiments. Thus, one can conclude that if Type-I model is true, with a discovery at the future LHC one should also observe non-zero radium and electron EDMs, otherwise the null results of radium and electron EDMs will veto the Type-I CPV 2HDM. A similar conclusion can be drawn for the Type-II model by observing Fig. 5.8b, where one can find that the LHC sensitive region is well within the reaches of radium and neutron EDMs. Hence, if the Type-II model is true, the discovery of the future LHC should lead to the observations of non-zero radium and neutron EDMs.

  - **Future LHC gives a null result**

    For both Type-I and Type-II models, a null result from future LHC does not exclude the possibility of CPV in 2HDM as long as CPV angle α_b is sufficiently small. Meanwhile, any non-zero EDMs that correspond to the

regions of parameter space within the reach of LHC would disfavor the CPV 2HDMs.

- 2HDMs away from the alignment limit:

  - **Future LHC makes a discovery**

    In this case, the result from future LHC is not purely sensitive to the CPV effect since the coupling of h_3 to Zh_1 is proportional to the level of deviation from the alignment limit and is not suppressed by the CPV angle α_b. A discovery at the future LHC may or may not imply a non-zero EDM result, a situation that depends largely on the magnitude of deviation from the alignment limit. Moreover, if the deviation is relatively small, such as $\cos(\beta - \alpha) = 0.02$, the exclusion limit would mainly come from h_2, for which production is purely sensitive to the CPV angle α_b, as shown in Fig. 5.7d and Fig. 5.8d for the Type-I and Type-II models, respectively. In addition, one would expect the non-zero radium and electron EDMs for the Type-I model and non-zero radium and neutron EDMs for the Type-II model. Thus, a null EDM result would disfavor both Type-I and Type-II CPV 2HDMs. On the other hand, if the deviation is relatively large, such as $\cos(\beta-\alpha) = 0.1$ in the Type-I model (Fig. 5.7f) and $\cos(\beta-\alpha) = 0.05$ in the Type-II model (Fig. 5.8f), the exclusion power would be dominated by the h_3 decay. As mentioned above, the discovery of h_3 does not necessarily lead to sizable EDMs, and therefore a more detailed study of the CP properties of the newly discovered particle would be needed.

  - **Future LHC gives a null result**

    In this case, for sufficiently large deviations as shown in Fig. 5.7f and Fig. 5.8f, the discovery of any EDM results would indicate that the CPV source is not consistent with the CPV 2HDMs. On the other hand, for

relatively a small deviation as shown in Fig. 5.7d and Fig. 5.8d, the CPV 2HDMs is still available if CPV angle α_b is sufficiently small. Moreover, any non-zero EDMs that correspond to the regions of parameter space within the reach of LHC would disfavor the CPV 2HDMs.

Finally, we comment on the potential constraints from the viability of successful EWBG in 2HDMs. One can potentially include the allowed regions where EWBG is viable in Figs. 5.7 and 5.8. For example, the authors of Ref. [105] studied the CPV for EWBG and identified some regions of parameter space that seem favorable. They pointed out that the CP violating phase necessary for successful baryogenesis is sensitive to $\tan\beta$ and the masses of the heavy Higgses. That work also concentrated on parameter space region where the dominant decay channel of h_3 is to the Zh_2 final state ($A \to ZH$ in the CP-conserving limit), based on earlier studies of the electroweak phase transition[107, 106]. A strong first order electroweak phase transition favors – but does not absolutely require – regions of parameter space leading to dominance of this decay mode. In this paper our main focus is on constraints of the CP violating phases from the LHC and EDMs in 2HDMs. It is possible that for the spectra considered here, the CPV 2HDMs can accommodate a strong first order electroweak phase transition and give rise to the CPV asymmetries needed for successful baryogenesis. A detailed and general analysis of this possibility is beyond the scope of the present paper and will be left for future study.

CHAPTER 6

ELECTROWEAK PHASE TRANSITION IN XSM

In this chapter, we focus on the singlet extension to the SM, the xSM, which is proven to be able to give a strong first order electroweak phase transition in Ref. [218]. In the xSM, after EWSB, the gauge eigenstates of the singlet scalar and the SM Higgs mix with each other to form the mass eigenstates h_1 (SM-like) and h_2 (singlet-like). Further, we restrict our study to searching for a signal of the on-shell production of the heavy singlet-like Higgs h_2 decaying to two SM-like Higgs h_1 (i.e. $m_2 > 2m_1$), because the regions of parameter space that can generate SFOEWPT simultaneously tend to enhance the $h_2h_1h_1$ tri-linear couplings [218, 114, 208]. Currently, the ATLAS and CMS experiments have already begun to search for a resonant di–Higgs signal through different Higgs decay final states: $4b$ [6, 175], $bb\gamma\gamma$ [176, 11], $\gamma\gamma WW^*$ [11] and $bb\tau\tau$ [11] and so far have not found any significant deviation from SM backgrounds. On the theoretical side, for the parameter regions that are viable for SFOEWPT, the $bb\tau\tau$ final state has been studied in Ref. [208] and found that at the 14 TeV LHC with a 100 fb^{-1} luminosity, the singlet-like h_2 with a relatively light mass e.g. 270 GeV can be discovered; the $bb\gamma\gamma$ and 4τ final states can discover m_2 up to 500 GeV at the 14 TeV LHC with a 3 ab^{-1} luminosity [181]; the $bbWW$ final state studied in Ref. [160] found that the resonant signal is discoverable for m_2 range from 350 GeV to 600 GeV at the 13 TeV LHC with a 3 ab^{-1} luminosity.

In this context, we study the prospective discovery/exclusion of $4b$ final state at the 14 TeV LHC with a 3 ab^{-1} luminosity. We first find out the 11 benchmark points with $m_2 \in [300, 850]$ GeV that produce the maximum and minimal di–Higgs

signal rate $\sigma_{h_2} \times \mathrm{BR}_{h_2 \to h_1 h_1}$ in consecutive 50 GeV intervals and satisfies all the current phenomenological constraints from the Higgs signal rate, electroweak precision data and also the theoretical constraints from stability, perturbativity and viable for SFOEWPT. Then we do a full simulation of signal and background events with the parton level events generator Madgraph5 [24], showering with PYTHIA6 [237] and using DELPHES3 [92] to do the fast detector simulation. Further, we use the TMVA package in ROOT to implement the Boosted Decision Tree (BDT) algorithm to optimize the cuts, finally obtain the significance from the BDT score distributions of background and signal events.

6.1 The xSM

6.1.1 The Model

The most general scalar potential in the xSM model is given by:

$$\begin{aligned} V(H,S) = & -\mu^2 \left(H^\dagger H\right) + \lambda \left(H^\dagger H\right)^2 + \frac{a_1}{2} \left(H^\dagger H\right) S \\ & + \frac{a_2}{2} \left(H^\dagger H\right) S^2 + \frac{b_2}{2} S^2 + \frac{b_3}{3} S^3 + \frac{b_4}{4} S^4, \end{aligned} \tag{6.1}$$

where S is the real singlet and H is the SM Higgs doublet. The a_1 and a_2 parameters induce the mixing between the singlet scalar and the SM Higgs doublet which provide a portal for the singlet scalar interacts with SM particles. A $\mathbb{Z}_2$ symmetry is presented in the absence of a_1 and b_3, we however retain both parameters in our study as they play an important role in the strength of EWPT and also di-Higgs signal rate at collider experiments.

After EWSB, $H \to (v_0 + h)/\sqrt{2}$ with $v_0 = 246$ GeV, and $S \to x_0 + s$ where x_0 is the vev for S without loss of generality. The stability of the scalar potential requires the quartic coefficients along all the directions in the field space to be positive. This

translates into a requirement of a positive the Hessian determinant of the potential with respect to fields s and h:

$$\det \begin{pmatrix} \partial^2 V/(\partial s^2) & \partial^2 V/(\partial s \partial h) \\ \partial^2 V/(\partial h \partial s) & \partial^2 V/(\partial h^2) \end{pmatrix} > 0. \tag{6.2}$$

This leads the bounds $\lambda > 0$, $b_4 > 0$ and $a_2 > -\sqrt{\lambda b_4}$. Another way to obtain these bounds is by parameterizing (h,s) as ($r\cos\alpha$, $r\sin\alpha$) in the field space, and we are able to extract the quartic coefficients of r along the α direction in the field space:

$$\frac{1}{4}\left((b_4 + \lambda - a_2)\cos^4\alpha + (a_2 - 2b_2)\cos^2\alpha + b_4\right). \tag{6.3}$$

Requiring the above equation larger than zero for any value of $\cos\alpha$ also leads to the same conditions.

Utilizing the minimization conditions,

$$\left.\frac{dV}{dh}\right|_{h=0,s=0} = 0, \quad \left.\frac{dV}{ds}\right|_{h=0,s=0} = 0, \tag{6.4}$$

one can express two potential parameters in the Eq. 6.1 in terms of the vevs and other parameters.

$$\begin{aligned} \mu^2 &= \lambda v_0^2 + (a_1 + a_2 x_0)\frac{x_0}{2} \\ b_2 &= -b_3 x_0 - b_4 x_0^2 - \frac{a_1 v_0^2}{4x_0} - \frac{a_2 v_0^2}{2}. \end{aligned} \tag{6.5}$$

Two additional conditions need to be satisfied for (v_0, x_0) to be a stable minimum. One of them is (v_0, x_0) minimizing the potential locally, which requires:

$$b_3 x_0 + 2b_4 x_0^2 - \frac{a_1 v_0^2}{4x_0} - \frac{(a_1 + 2a_2 x_0)^2}{8\lambda} > 0. \tag{6.6}$$

Also, this minimum point should be a global minimum, which we impose numerically.

As for the perturbativity, we have requirements on the quartic couplings:

$$\left|\frac{a_1}{2}\right|, \left|\frac{a_2}{2}\right|, \left|\frac{b_4}{4}\right| < 4\pi. \tag{6.7}$$

However, when scanning the parameter space for benchmark points we implement more stringent bounds on those parameters as discussed in Sec.6.2 compared with the above requirements. One can refer to Ref. [224] and Ref. [225] for more details about the perturbativity bound in the xSM.

Now we obtain the elements of mass-squared matrix by:

$$\begin{aligned} m_h^2 &\equiv \frac{d^2V}{dh^2} = 2\lambda v_0^2 \\ m_s^2 &\equiv \frac{d^2V}{ds^2} = b_3 x_0 + 2b_4 x_0^2 - \frac{a_1 v_0^2}{4x_0} \\ m_{hs}^2 &\equiv \frac{d^2V}{dhds} = (a_1 + 2a_2 x_0)\,\frac{v_0}{2}. \end{aligned} \tag{6.8}$$

After the diagonalization of the above mass matrix, the physical masses of two neutral scalars can be expressed as:

$$m_{2,1}^2 = \frac{m_h^2 + m_s^2 \pm |m_h^2 - m_s^2| \sqrt{1 + \left(\frac{4m_{hs}^2}{m_h^2 - m_s^2}\right)^2}}{2}, \tag{6.9}$$

with $m_2 > m_1$ by construction. The mass eigenstates and gauge eigenstates are related by a rotation matrix:

$$\begin{pmatrix} h_1 \\ h_2 \end{pmatrix} = \begin{pmatrix} \cos\theta & \sin\theta \\ -\sin\theta & \cos\theta \end{pmatrix} \begin{pmatrix} h \\ s \end{pmatrix} \tag{6.10}$$

where h_1 is the SM-like Higgs boson with $m_1 = 125$, and h_2 is identified as the most singlet-like mass eigenstate. The mixing angle θ can be expressed with the vevs, physical masses and potential parameters:

$$\sin 2\theta = \frac{2m_{hs}^2}{(m_1^2 - m_2^2)} = \frac{(a_1 + 2a_2 x_0)\, v_0}{(m_1^2 - m_2^2)}. \tag{6.11}$$

From Eq. 6.10, one can observe that the couplings of h_1 and h_2 to the SM vector bosons and fermions are changed by rescales of their SM Higgs couplings,

$$g_{h_1 XX} = \cos\theta\; g_{hXX}^{\rm SM}, \quad g_{h_2 XX} = \sin\theta\; g_{hXX}^{\rm SM}, \tag{6.12}$$

where XX represents final states of SM vector bosons and fermions pairs In this case, all the signal rates associated with the single Higgs measurments are rescaled by the mixing angle only:

$$\mu_{h_1 \to XX} = \frac{\sigma_{h_1} \cdot {\rm BR}}{\sigma_{h_1}^{SM} \cdot {\rm BR}^{\rm SM}} = \cos^2\theta, \tag{6.13}$$

where σ_{h_1} and BR are the production cross section and branching ration in our model, and the quantities with the superscript SM are the corresponding values in the SM. In our model, we have ${\rm BR} = {\rm BR}^{SM}$ because the partial width of each decay mode is rescaled by $\cos^2\theta$ and there is no new decay channel appearing.

In order to investigate the di-Higgs production in following sections, one also need to derive the tri-Higgs couplings. The one relevant for the resonant di-Higgs production is λ_{211},

$$\begin{aligned}\lambda_{211} = \frac{1}{4}\big[&(a_1 + 2a_2x_0)\cos^3\theta + 4v_0(a_2 - 3\lambda)\cos^2\theta\sin\theta \\ &+(a_1 + 2a_2x_0 - 2b_3 - 6b_4x_0)\cos\theta\sin^2\theta - 2a_2v_0\sin^3\theta\big]\,. \end{aligned} \tag{6.14}$$

In this work, we focus on the situation where $m_2 > 2m_1$ such that a resonant production of h_2 and a subsequent decay to h_1h_1 is allowed. Therefore, we are able to calculate the partial width $\Gamma_{h_2\to h_1h_1}$:

$$\Gamma_{h_2\to h_1h_1} = \frac{\lambda_{211}^2\sqrt{1 - 4m_1^2/m_2^2}}{8\pi m_2}, \tag{6.15}$$

and the total width of h_2:

$$\Gamma_{h_2} = \sin^2\theta\;\Gamma^{\rm SM}(m_2) + \Gamma_{h_2\to h_1h_1}, \tag{6.16}$$

where $\Gamma^{\rm SM}(m_2)$ represents the total width of SM Higgs with a mass of m_2, which is taken from [25]. The singnal rate for $pp \to h_2 \to XX$ (X is SM vector bosons and fermions) normalized to the SM value is given by:

$$\mu_{h_2\to XX} = \sin^2\theta\left(\frac{\sin^2\theta\;\Gamma^{\rm SM}(m_2)}{\Gamma_{h_2}}\right), \tag{6.17}$$

which will be used to constrain the parameter space in the next section. The production cross section for the process $pp \to h_2 \to h_1h_1$ can also be calculated:

$$\sigma_{h_1h_1} = \sigma^{SM}(m_2) \times s_\theta^2\frac{\Gamma_{h_2\to h_1h_1}}{s_\theta^2\Gamma^{SM}(m_2) + \Gamma_{h_2\to h_1h_1}}. \tag{6.18}$$

6.1.2 Phenomenological Constraints on the Model Parameters

Now we discuss current phenomenological constraints on the xSM. The mixing angle θ between the singlet and the SM Higgs doublet is constrained by measurements of the single SM-like Higgs signal strengths. A global analysis by the ATLAS group gives the 95% CL upper limit on $\sin^2\theta$ as 0.12 [9].

The LHC searches for the heavy neutral Higgs also provide constraints on the parameter space, typically, we take into account the existing limits on both the $h_2 \to VV$ [15, 12, 60, 174] and the $h_2 \to h_1 h_1$ final states, where $h_1 h_1$ decay to $b\bar{b}b\bar{b}$ [6, 175], $b\bar{b}\gamma\gamma$ [176], $b\bar{b}\tau\tau$ [11]. The constraints on the (m_2, c_θ) plane can be found in our previous work [160]. We will also guarantee each benchmark point in the parameter scan in the next section satisfies all the limits mentioned above.

Finally, we discuss the constraints from electroweak precision observables (EWPO). The mixing between the singlet scalar and the SM Higgs doublets induces the modification of the oblique parameters S, T and U with respect to their SM values. From Eq. 6.10, the deviation in an oblique parameters $\mathcal{O}$, denoted by $\Delta\mathcal{O}$, can be expressed in terms of the SM Higgs contribution to that parameter, $\mathcal{O}^{SM}(m)$ [214, 149] and the mixing angle θ, where m is either m_1 or m_2. So we have:

$$\Delta\mathcal{O} = (c_\theta^2 - 1)\mathcal{O}^{\rm SM}(m_1) + s_\theta^2\, \mathcal{O}^{\rm SM}(m_2) = s_\theta^2 \left[\mathcal{O}^{\rm SM}(m_2) - \mathcal{O}^{\rm SM}(m_1)\right] . \qquad (6.19)$$

In the xSM the parameter $U = 0$ is a good approximation, we therefore focus on only the deviations in the S and T parameters, which is given by the Gfitter group [30]:

$$\begin{aligned} \Delta S &\equiv S - S_{\rm SM} = 0.06 \pm 0.09 \\ \Delta T &\equiv T - T_{\rm SM} = 0.10 \pm 0.07 \end{aligned} \qquad \rho_{ij} = \begin{pmatrix} 1 & 0.91 \\ 0.91 & 1 \end{pmatrix}, \qquad (6.20)$$

where $\rho_{i,j}$ is the covariance matrix in the (S,T) plane. Again, we will impose the criteria in the parameter scan in the next section such that for each benchmark point,

$\Delta\chi^2(m_2, c_\theta)$ defined below is less than 5.99, which corresponds to the deviations of S and T parameters are within 95% C.L.

$$\Delta\chi^2(m_2, c_\theta) = \sum_{i,j} \left[\Delta\mathcal{O}_i(m_2, c_\theta) - \Delta\mathcal{O}_i^0\right] (\sigma^2)_{ij}^{-1} \left(\Delta\mathcal{O}_j(m_2, c_\theta) - \Delta\mathcal{O}_j^0\right) , \qquad (6.21)$$

where $\Delta\mathcal{O}_i^0$ denote the central values in (6.20) and $(\sigma^2)_{ij} \equiv \sigma_i \rho_{ij} \sigma_j$, with σ_i the S or T standard deviation from (6.20).

6.2 Electroweak Phase Transition and Benchmarks for Di-Higgs Production

The character of EWPT is understood in terms of the finite-temperature effective potential, $V_{eff}^{T\neq 0}$ However, the fact that the standard derivation of $V_{eff}^{T\neq 0}$ suffers from gauge dependence is well known which is discussed in depth in Ref. [223]. Here we employ a high-temperature expansion to restore the gauge independence in6 our analysis (see Ref. [219] for details). In such a case, we include in our finite temperature effective potential the $T = 0$ tree level potential and the gauge-independent thermal mass corrections to $V_{eff}^{T\neq 0}$, which are crucial to restore electroweak symmetry at high temperature. In this limit, a_1 and b_3 parameters in the xSM will generates the barrier between the broken and unbroken electroweak phases for a first-order EWPT at tree-level. In the high-temperature limit, we follow Ref. [223] and write the T-dependent, gauge-independent (indicated by the presence of a bar) vevs in a cylindrical coordinate representation as

$$\bar{v}(T)/\sqrt{2} = \bar{\phi}(T)\cos\alpha(T), \quad \bar{x}(T) = \bar{\phi}(T)\sin\alpha(T), \qquad (6.22)$$

with $\bar{v}(T = 0) = v_0$ and $\bar{x}(T = 0) = x_0$. The critical temperature T_c is defined as the temperature at which the broken and unbroken phases are degenerate, i.e.

$V_{eff}^{T\neq 0}(\phi, \alpha \neq \pi/2, T_c) = V_{eff}^{T\neq 0}(\phi, \alpha = \pi/2, T_c)$. Once the critical temperature is found one is able to evaluate the quenching effect of the sphaleron transitions in the broken electroweak phase (see, e.g., Ref. [202]), which is related to the energy of the electroweak sphaleron that is proportional to the vev of $\mathrm{SU}(2)_L$ doublet $\bar{v}(T)$. A first-order EWPT is strong when the quenching effect is sufficiently large, and the criterion is approximately given by:

$$\cos\alpha(T_c)\,\frac{\bar{\phi}(T_c)}{T_c} \gtrsim 1. \tag{6.23}$$

To select the benchmarks to do the collider simulation, we perform a scan of parameters a_1, b_3, x_0, b_4 and λ within the following range:

$$a_1/\mathrm{TeV}, b_3/\mathrm{TeV} \in [-1, 1], \quad x_0/\mathrm{TeV} \in [0, 1], \quad b_4, \lambda \in [0, 1] \tag{6.24}$$

the remaining parameters are fixed by input values of $v_0 = 246$ GeV and $m_h = 125$ GeV. Our lower bound on quartic couplings b_4 and λ guarantee the vacuum stability. We also require a naive perturbativity bound on the Higgs portal coupling $a_2/2 \lesssim 5$. For each set of scanning parameters, we calculate the c_θ, m_2 and λ_{211}, and only keep the points that satisfies all the phenomenological constraints mentioned in the previous section (Higgs signal rate, LHC search for heavy Higgs h_2, EWPO). Then we pass these sets of parameters into the CosmoTransitions and evaluate all the quantities that related to the EWPT numerically, such as critical temperature, sphaleron energy, tunneling rate into the electroweak symmetry broken phase with an input of the finite temperature effective potential of the xSM in the high-temperature limit. Finally we only keep the sets of parameters that satisfies the strong first-order EWPT defined above and also has a sufficient tunneling rate to prevent the universe stucking in a metastable vacuum.

We choose benchmark points with the maximum and minimum signal rate $\sigma(pp \to h_2)\mathrm{BR}_{h_2 \to h_1 h_1}$ from 11 consective h_2 mass windows range from 300 to 850 GeV with 50 GeV width. The upper bound of $m_2 = 850$ GeV is obtained by the logic that we did not find the mass of m_2 larger than 850 GeV that gives a strong first-order EWPT even though in our scan m_2 can potentially reach 1 TeV. We list all the benchmark points in Table. 6.1 and 6.2.

	$\cos\theta$	m_2 (GeV)	Γ_{h_2} (GeV)	x_0 (GeV)	λ	a_1 (GeV)	a_2	b_3 (GeV)	b_4	λ_{111} (GeV)	λ_{211} (GeV)	σ (pb)	BR
B1	0.974	327	0.929	60.9	0.17	-490	2.65	-361	0.52	45	62.2	0.56	0.33
B2	0.980	362	1.15	59.6	0.17	-568	3.26	-397	0.78	44.4	76.4	0.48	0.40
B3	0.983	415	1.59	54.6	0.17	-642	3.80	-214	0.16	44.9	82.5	0.36	0.33
B4	0.984	455	2.08	47.4	0.18	-707	4.63	-607	0.85	46.7	93.5	0.26	0.31
B5	0.986	511	2.44	40.7	0.18	-744	5.17	-618	0.82	46.6	91.9	0.15	0.24
B6	0.988	563	2.92	40.5	0.19	-844	5.85	-151	0.08	47.1	104	0.087	0.23
B7	0.992	604	2.82	36.4	0.18	-898	7.36	-424	0.28	45.6	119	0.045	0.30
B8	0.994	662	2.97	32.9	0.17	-976	8.98	-542	0.53	44.9	132	0.023	0.33
B9	0.993	714	3.27	29.2	0.18	-941	8.28	497	0.38	44.7	112	0.017	0.20
B10	0.996	767	2.83	24.5	0.17	-920	9.87	575	0.41	42.2	114	0.0082	0.22
B11	0.994	840	4.03	21.7	0.19	-988	9.22	356	0.83	43.9	83.8	0.0068	0.079

Table 6.1: Values of the various xSM independent and dependent parameters for each of the benchmark values chosen to **maximize** the $\sigma_{h_2} \times \mathrm{BR}_{h_2 \to h_1 h_1}$ value at the LHC.

Benchmark	$\cos\theta$	m_2	Γ_{h_2}	x_0	λ	a_1	a_2	b_3	b_4	λ_{111}	λ_{211}	σ	BR
			(GeV)	(GeV)		(GeV)		(GeV)		(GeV)	(GeV)	(fb)	
BM1	0.9999	329.2	0.005925	111.1	0.129	-811.7	3.612	-99.83	0.353	31.79	7.297	1.116	0.7066
BM2	0.9995	362.9	0.05491	80.57	0.1298	-699.4	4.158	-91.47	0.570	32.18	21.61	8.19	0.6756
BM3	0.9803	418.8	1.324	234.2	0.1802	-980.6	1.558	0.4173	0.963	38.95	17.5	6.857	0.01763
BM4	0.9997	463.4	0.08635	56.85	0.1299	-763.2	6.348	112.8	0.731	32.21	27.4	2.989	0.6288
BM5	0.9994	545.	0.2779	50.25	0.1317	-948.9	8.644	151.5	0.570	32.99	51.56	2.871	0.6203
BM6	0.9991	562.5	0.4594	33.03	0.1335	-716.	9.248	-448.1	0.964	33.74	66.8	3.715	0.6154
BM7	0.9836	608.6	4.027	34.24	0.2241	-821.9	4.533	-183.2	0.566	47.82	45.17	2.216	0.0302
BM8	0.987	676.3	4.475	30.29	0.2231	-930.9	5.964	-679.6	0.428	48.36	55.18	1.289	0.03719
BM9	0.9904	729.3	4.222	27.32	0.2098	-908.9	6.152	603.	0.935	45.69	61.04	0.7799	0.04522
BM10	0.9945	792.4	3.363	22.18	0.1838	-935.7	9.469	-848.2	0.655	43.51	92.38	0.7651	0.1209
BM11	0.9944	840.5	3.952	21.17	0.192	-955.4	8.688	683.9	0.530	43.27	73.39	0.287	0.06159

Table 6.2: Values of the various xSM independent and dependent parameters for each of the benchmark values chosen to **minimize** the $\sigma \cdot BR(h_2 \to h_1 h_1)$ at a 14 TeV pp collider.

6.3 4b Final State Analysis

In this section, we discuss the simulation and analysis details for 4b final state. The di-Higgs to 4b final state gives the largest branching ratio among all the di-Higgs decay channel, which potentially gives the largest signal rate. However, 4b channel also suffer from large SM multi-jet backgrounds, which may reduce the signal significance. This is why we implement Boosted Decision Tree (BDT) to better separate the signal and background events and to enhance signal significance. In what follows, we first reproduce the result of the 13 TeV ATLAS analysis and then evaluate the significance for the future HL-LHC.

6.3.1 13 TeV result revisit

We follow the ATLAS resolved analysis in Ref. [6], and reproduce the signal efficiency and background distributions in Fig.2 and Fig.4. We generate the parton level signal and background with MG5_ AMC@NLOv2.4.3 [24] and then use PYHIA6 [237] for QCD showering, fragmentation and hadronization, finally we use the DELPHES3 [92] to simulate the detector effect. For the detector simulation, we used the default CMS DELPHES card, though we are following the ATLAS analysis. The reason we use the CMS card rather than the ATLAS card in DELPHES is that the CMS card is better in reproducing the real experimental effects than the ATLAS card and we believe that the detector responses are similar in the real world for the ATLAS and CMS experiments. The b-tagging rate is set to 70% and parameter R in anti-kt jet clustering algorithm is set to 0.4 to follow the ATLAS analysis.

For the signal process, we scan the mass of h_2 from 300 GeV to 1500 GeV with a interval of 100 GeV. For the backgrounds, we generate $pp \to 4b$ and $pp \to t\bar{t}$. To increase the sample efficiency, for $pp \to 4b$ process, we set the parton level cuts $\Delta R_{bb} > 0.3$, which is consistent with the parameter R=0.4 in anti-kt algorithm that

set an effective lower bound on $\Delta R = 0.4$ of two jets. For $pp \to t\bar{t}$, we enforce top quarks decaying hadronically.

Here we summarize the cut flow used in the ATLAS analysis:

- Select the events with at least 4 b-tagged jets with $p_t^b > 40$ GeV and $|\eta| < 2.5$. If the number of b-tagged jets is larger than 4, then the jets with 4 highest p_t are selected to reconstruct dijet system.

- Use the selected 4 b-tagged jets to form two dijet systems. The dijet system is defined by the two jets with $\Delta R < 1.5$. We also require that the transverse momentum (p_t) of the leading (subleading) dijet system to be greater than 200 (150) GeV.

- Depending on the reconstructed invariant mass of 4 b-tagged jets we put following mass dependent cuts

$$p_T^{lead} > \begin{cases} 400\,\text{GeV} & \text{if } m_{4j} > 910\,\text{GeV}, \\ 200\,\text{GeV} & \text{if } m_{4j} < 600\,\text{GeV}, \\ 0.65\,m_{4j} - 190\,\text{GeV} & \text{otherwise}, \end{cases}$$

$$p_T^{subl} > \begin{cases} 260\,\text{GeV} & \text{if } m_{4j} > 990\,\text{GeV}, \\ 150\,\text{GeV} & \text{if } m_{4j} < 520\,\text{GeV}, \\ 0.23\,m_{4j} + 30\,\text{GeV} & \text{otherwise}, \end{cases}$$

$$|\Delta\eta_{\text{dijets}}| < \begin{cases} 1.0 & \text{if } m_{4j} < 820\,\text{GeV}, \\ 1.6 \times 10^{-3} m_{4j} - 0.28 & \text{otherwise}. \end{cases}$$

- To reduce $t\bar{t}$ background, we impose the "$t\bar{t}$ veto" in the following method: if there are extra jets in the events with $p_T > 30$ GeV and $\eta < 2.5$, then we

will test if this extra jet has $\Delta R < 1.5$ relative to the dijet. Given the above condition is true, we will calculate the invariant mass of the extra jet and one of the b-tagged jet in the dijet system as the mass of W boson candidate m_W and the invariant mass of the extra jet and dijet system as the mass of top quark candidate m_t. We will veto the events if the following requirement is satisfied:

$$X_{tt} = \sqrt{\left(\frac{m_W - 80.4\,\mathrm{GeV}}{0.1\,m_W}\right)^2 + \left(\frac{m_t - 172.5\,\mathrm{GeV}}{0.1\,m_t}\right)^2} < 3.2, \qquad (6.25)$$

- Finally, we will retain the events as a signal candidate if the invariant masses of the two Higgs boson candidates are in the signal region defined by:

$$X_{hh} = \sqrt{\left(\frac{m_{2\mathrm{j}}^{\mathrm{lead}} - 120\,\mathrm{GeV}}{0.1\,m_{2\mathrm{j}}^{\mathrm{lead}}}\right)^2 + \left(\frac{m_{2\mathrm{j}}^{\mathrm{subl}} - 113\,\mathrm{GeV}}{0.12\,m_{2\mathrm{j}}^{\mathrm{subl}}}\right)^2} < 1.6. \qquad (6.26)$$

  Comparing with the same requirement in the ATLAS analysis in Ref. [6] we change the central value of $(m_{2\mathrm{j}}^{\mathrm{lead}}, m_{2\mathrm{j}}^{\mathrm{subl}})$ in the above equation from (124 GeV, 115 GeV) to (120 GeV, 112 GeV) to compensate for the discrepancy of the jet energy smearing between the Delphes simulation and the ATLAS simulation.

The efficiencies of signal events with m_H ranging from 500 GeV to 1500 GeV a interval of 100 GeV comparing with the ATLAS results in Ref. [6] are shown in the Fig. 6.1. The solid lines represent the results from our simulation, the dashed lines represent the results in Fig.2(b) in Ref. [6]. The five different lines correspond to five cuts described in the five bullet points above. We found that for the final signal efficiency our results agree with the ALTAS results very well.

We estimate the backgrounds yields after the same cuts and summarize them in Table 6.3. Apart from $4b$ and $t\bar{t}$ background we also estimate the number of *bbcc* background with two c quarks faking to two b quarks by the following formula under

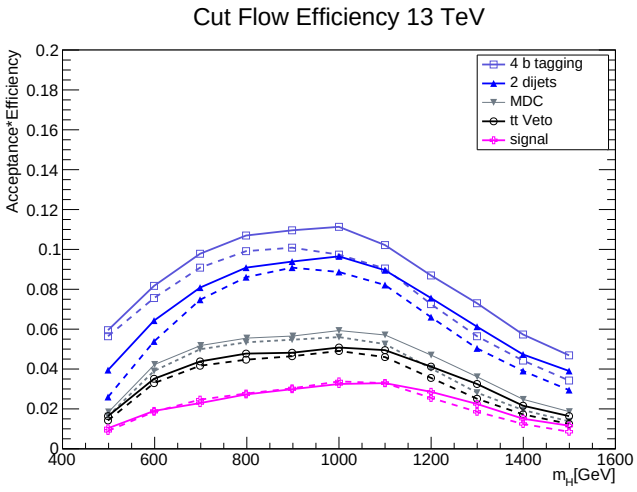

Figure 6.1: The comparison of the cut flow efficiencies with the ATLAS result. The solid lines are our simulation results, the dashed lines represent the ATLAS results in Ref. [6]. The five cuts are correspond to five bullet points described in the section 6.3.1.

the assumption that the kinetic distribution of $bbcc$ events are similar to those of $4b$ events:

$$N_{bbcc} = N_{4b} \times \frac{\sigma_{bbcc}}{\sigma_{4b}} \times (\frac{f_{c\to b}}{f_{b\to b}})^2, \tag{6.27}$$

where N_{4b} is the estimated number of QCD 4b events after all the cuts, σ_{bbcc} and σ_{4b} are parton level cross-sections for $bbcc$ and $4b$ processes, $f_{c\to b}$ is the c originated mis-tag efficiency which is taken to be 0.2 [14], $f_{b\to b}$ is the b jet tag efficiency which is taken to be 0.7. The expected number of the $bbcc$ background is 2, which contribute less than 2.5% of the total background. We also plot the distribution of the $4b$ invariant mass for the background events in Fig. 6.2, where before calculating the $4b$ invariant mass we rescale the four momentums of dijet systems such that their invariant masses are equal to the physical mass of the SM-like Higgs 125 GeV. One can compare the same distribution from the ATLAS experiments in the Fig.4 in Ref. [6], again we find they are identical within the uncertainties.

All of the above 13 TeV analysis gives us the confidence to study the prospective results in the 14 TeV HL LHC.

Backgrounds	$\sigma^{\rm NLO}_{\rm parton}$(pb)	K factor	efficiency	# of remaining events (L= 3.2fb^{-1})	ATLAS results[6]
$bbbb$	287.24	1.72 [24]	4.02×10^{-5}	37	43
$t\bar{t}$	72	1.60 [204]	1.87×10^{-5}	4.0	4.3

Table 6.3: Estimated number of background events and comparison with ATLAS results at the 13 TeV LHC.

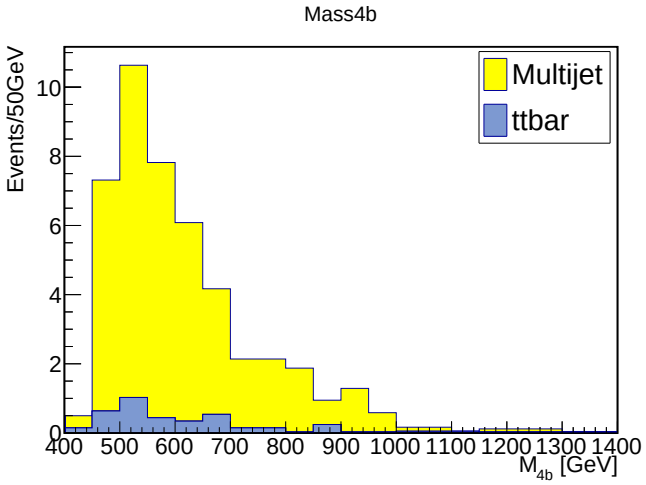

Figure 6.2: The distribution of the 4b invariant mass for backgrounds events after all the cuts in this section.

6.3.2 14 TeV HL-LHC Reuslt Predictions

In the analysis of the 14 TeV HL LHC prospective results, we first select events with two dijet systems following the cuts in Ref. [73] described below:

- Select events with at least 4 b-tagged jets with $p_T > 30$ GeV.
- Pairing two of them such that ΔR_{jj} satisfies the following cuts:

$$\left.\begin{aligned} \frac{360}{m_{4\rm j}} - 0.5 < \Delta R_{jj,\rm lead} < \frac{655}{m_{4\rm j}} + 0.475 \\ \frac{235}{m_{4\rm j}} < \Delta R_{jj,\rm subl} < \frac{875}{m_{4\rm j}} + 0.35 \end{aligned}\right\} \text{if } m_{4\rm j} < 1250\text{GeV}$$

$$\left.\begin{aligned} 0 < \Delta R_{jj,\rm lead} < 1 \\ 0 < \Delta R_{jj,\rm subl} < 1 \end{aligned}\right\} \text{if } m_{4\rm j} > 1250\text{GeV}$$

- If more than one pairing system satisfied this constraint, we use the one with the smallest variable D_{hh} defined by :

$$D_{hh} = \sqrt{(m_{2\mathrm{j}}^{\mathrm{lead}})^2 + (m_{2\mathrm{j}}^{\mathrm{subl}})^2} \left| \sin\left(\tan^{-1}\left(\frac{m_{2\mathrm{j}}^{\mathrm{subl}}}{m_{2\mathrm{j}}^{\mathrm{lead}}} \right) - \tan^{-1}\left(\frac{115}{120} \right) \right) \right| \quad (6.28)$$

After selecting the events with two dijets we calculate following kinematic variables and feed them into a Boosted Decision Tree (BDT) to optimize the separation between signal and background events:

$$p_T^{\mathrm{lead}},\ p_T^{\mathrm{subl}}, \Delta R^{\mathrm{lead}}, \Delta R^{\mathrm{subl}}, \Delta R_{hh}, \Delta\phi_{hh}, \Delta\eta_{hh}, m_{2\mathrm{j}}^{\mathrm{lead}}, m_{2\mathrm{j}}^{\mathrm{subl}}, X_{hh}, m_{4b}. \quad (6.29)$$

The variables with superscripts "lead" and "sub" correspond to the value of the leading and sub-leading dijet systems ordered by their p_T, and X_{hh} are defined below:

$$X_{hh} = \sqrt{\left(\frac{m_{2\mathrm{j}}^{\mathrm{lead}} - 120\,\mathrm{GeV}}{0.1\, m_{2\mathrm{j}}^{\mathrm{lead}}} \right)^2 + \left(\frac{m_{2\mathrm{j}}^{\mathrm{subl}} - 115\,\mathrm{GeV}}{0.1\, m_{2\mathrm{j}}^{\mathrm{subl}}} \right)^2}, \quad (6.30)$$

m_{4b} represents the invariant mass of four b jets. After training the BDT, we obtain the BDT score distributions of signal and backgrounds events. To derive the optimal sensitivity, we re-bin the signal and background distributions such that each bin contributes the maximum $S/\sqrt{B}$ (S and B are the numbers of signal and background events in that bin), starting from the right edge of the histogram where the signal peaks.

We summarize the production cross-sections and the preliminary cut efficiencies before the BDT analysis in Table 6.4.

Then we calculate the CL_b with the profiled likelihood method using the asymptotic formula described in Ref. [82, 83], and then convert the quantity $1 - \mathrm{CL}_b$, which represents the probability that the background-only model produce the observed events by fluctuation that can imitate the expectation of the signal plus background model, into the correspoinding N_σ Gaussian significance. As an illustration,

Backgrounds	$\sigma^{\rm NLO}_{\rm parton}$(pb)	K factor	efficiency
$bbbb$	$131.075^{+28\%}_{-24\%}$	1.4 [87]	0.02987
$t\bar{t}$	$110.065^{+3.8\%}_{-5.8\%}$	2.03 [88]	0.005579

.

Table 6.4: Estimated number of background events for 14 TeV HL-LHC and the theretical uncertainties.

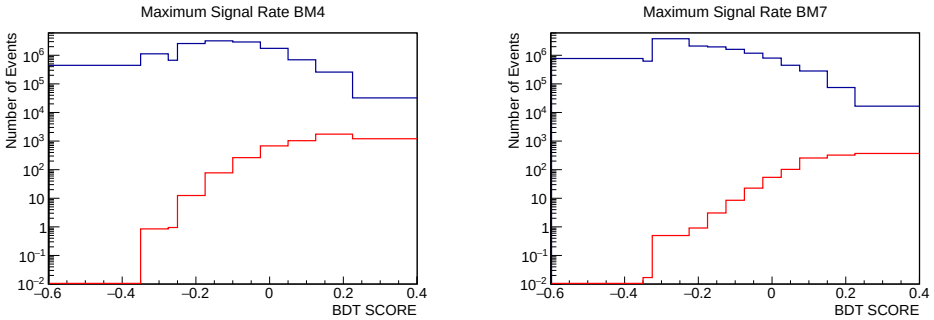

(a) re-binned BDT score BM4 (b) re-binned BDT score BM7

Figure 6.3: Re-binned histograms for BM4 and BM7 with the maximum signal rates, the red line represents the signal distribution, the blue line represents the backgrounds distribution, they are all normalized to their real expected number of events in the 14 TeV HL LHC with 3 ab^{-1}.

we show the re-binned histograms of the BDT output for two benchmark points in Fig. 6.3.

We also plot the significance N_σ with uncertainty bands in Fig. 6.4. The upper and lower bands correspond to the variation of production cross section of $4b$ and $t\bar{t}$ backgrounds within $\pm 1\sigma$ uncertainties as one can find in the Table 6.4. One can observe that with a 3 ab^{-1} luminosity at the 14TeV LHC the benchmark points with maximum signal rate up to m_H =500 GeV can be discovered with N_σ >5. If the future HL LHC experiments does not observe the signal, then one can exclude the maximum signal rate benchmark points up to m_H =680 GeV.

We compare the significance that obtained with the same method for the $bb\gamma\gamma$ and 4τ channels at the 14 TeV HL LHC [181] and for the $bbWW$ channel at the 13 TeV LHC [160] in Fig. 6.5. We only compare the benchmark points from BM3 to BM11

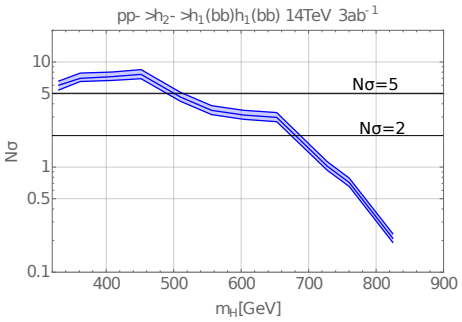

(a) N_σ for $\mathrm{BM}_{\mathrm{max}}$

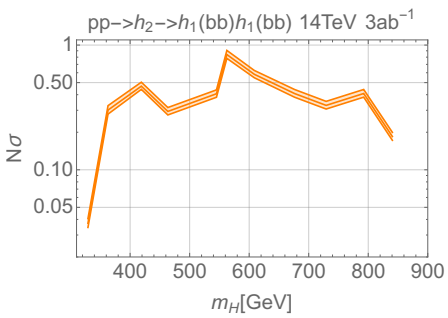

(b) N_σ for $\mathrm{BM}_{\mathrm{min}}$

Figure 6.4: The significance N_σ calculated from 1-CL_b. The upper and lower bands represent the $\pm 1\sigma$ variation of uncertainties on the theoretical backgrounds cross-sections.

because the first two BM points are different from that in Ref. [181]. We find that for the mass with heavy Higgs mass m_H less than 500 GeV, the $bb\gamma\gamma$ channel seems to be the most sensitive channel for searching a resonant di-Higgs signal, and the $4b$ channel is competitive with the $bb\gamma\gamma$ channel, which could serve as a complementary check if the $bb\gamma\gamma$ channel observe the signal. However, the m_H larger than 500 GeV the $4b$ channel demonstrates their better sensitivities compare with the $bb\gamma\gamma$ channel and 4τ but not as good as the $bbWW$ channel in our analysis.

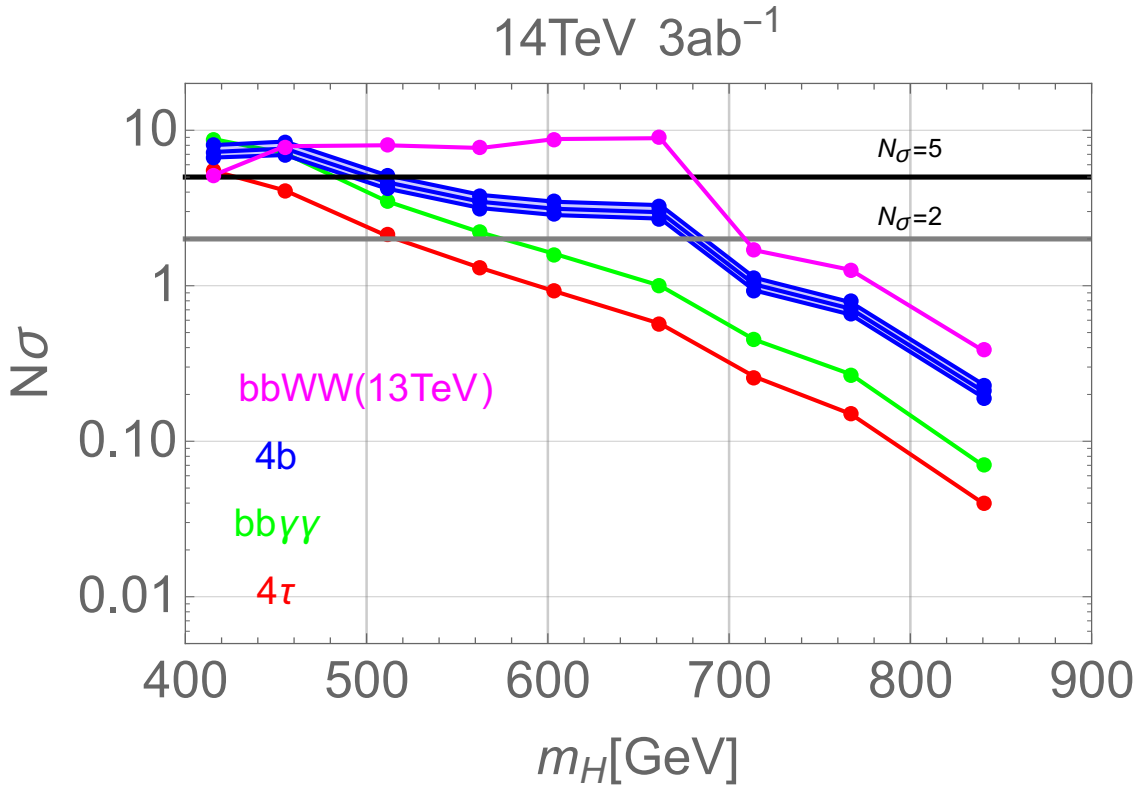

Figure 6.5: The significance N_σ calculated from 1-CL$_b$ for the 14 TeV LHC with a 3 ab^{-1} luminosity for different channels. The values for $bb\gamma\gamma$ and 4τ channels are obtained from Ref. [181]

CHAPTER 7

EXPLORING EXTENDED SCALAR SECTORS WITH DI-HIGGS SIGNALS: A HIGGS EFT PERSPECTIVE

Precision measurements of the Higgs couplings are a major goal for current and future high energy experiments. Current experimental results provide strong evidence that the nature of the Higgs boson is consistent with the predictions of the SM. The measurement of this behavior is entirely dependent on single Higgs phenomena through precision measurements of the Higgs couplings to the vector bosons and the SM fermions. On the other hand, the Higgs self-interactions, responsible for Electroweak Symmetry Breaking (EWSB), still remain undetermined experimentally. The Higgs self-coupling directly determines the shape of the Higgs potential and therefore measuring possible deviations of the Higgs self-coupling from its SM value is a crucial step in understanding the nature of EWSB, electroweak vacuum stability, and the nature of the electroweak phase transition (EWPT).

In order to investigate the generic features of the trihiggs coupling at the LHC and a future collider we adopt an Effective Field Theory (EFT) approach [52, 145, 137, 196]. In doing so we assume some possible new physics beyond the SM which modifies the Higgs couplings and is heavy with, for example, new physics scales such as $\Lambda_{\rm NP} \sim$ TeV. The effects of the new physics are parametrized by higher dimension effective operators, and the dimension-six $Q_H = (H^\dagger H)^3$ operator is the leading operator which modifies the momentum independent Higgs self-couplings at low energy. The Q_H operator remains the only operator related to the Higgs sector unconstrained by current experiment. In order to motivate this study of the effective operator Q_H we consider ultraviolet (UV) complete models which may generate this

operator at tree level and therefore with a larger Wilson coefficient. This requirement combined with Lorentz invariance then limits our consideration to extended scalar sectors[1]. Additionally the new scalar must not be charged under $SU(3)_c$ as closure of color indices requires Q_H be generated at one loop. Such scalar extensions of the SM constitute relatively simple scenarios beyond the SM which are also well-motivated by studies of the electroweak phase transition and baryogenesis [36, 37], having dark matter candidates [197, 53, 122], or mechanisms for neutrino mass generation [180, 189, 229, 64]. The complete list of the scalar extensions which generate a tree-level Q_H are real [197, 53, 209, 36] and complex singlets [37], the two Higgs doublet model (2HDM) [48, 186, 146], real [46, 122] and complex [180, 189, 229, 64] triplets, and complex quadruplets. Assuming the new scalars in these models are heavy, we utilize an EFT approach to study their effects on electroweak precision tests, modifications of the single Higgs couplings, and the di-Higgs production process in a model-independent and predictive way.

Many new physics models with SM-compatible single Higgs phenomena could exhibit di-Higgs phenomenology distinct from that of the SM [93, 29]. The modifications of the Higgs trilinear couplings can only be directly observed in Higgs boson pair production, therefore the di-Higgs process at the LHC and future colliders is the only direct way to measure the Wilson coefficient of the effective Q_H operator. Alternatively the trilinear Higgs coupling can be studied indirectly [96, 100, 192, 96, 141, 45, 100]. However our paper will focus on the direct constraints, we discuss the indirect constraints briefly at the end of Section 6.1. The di-Higgs production mechanism at hadronic colliders is dominated by the gluon fusion process which includes the triangle and the box contributions from the top quark. Due to destructive interference

[1]Requiring closure of spinor and Lorentz indices implies fermions may only generate the Q_H operator at one-loop and vectors may only generate dimension-six-operators with two derivatives at tree-level.

between these two contributions, the di-Higgs production cross section in the SM is typically small and thus challenging to observe in the near future. However, in the scalar extended models, the di-Higgs cross section may be increased considerably making measurement a possibility at the proposed 100 TeV collider [27, 74]. In this paper we investigate the di-Higgs production cross sections in the EFT framework, and study the discovery potential of the Wilson coefficients in the EFT at the proposed 100 TeV collider.

In this chapter

7.1 The Effective Lagrangian

We enumerate all the ultraviolet (UV) complete models which include one additional heavy scalar which generate, after integrating out the new scalar, dimension-six operators affecting the trihiggs vertex at tree level. The fermion and vector boson cannot generate Q_H at tree level because they need loops to close the Lorentz indices as one can see from Fig. 7.1. HS^3 cannot generate Q_H at tree level, and there is no representation for scalar S such that HS^2 become $SU(2)$ invariant. So the only possibility is to have a interaction term H^2S or H^3S, The relevant Feynman diagrams is shown in Fig. 7.2 Now let us find out the all the representations that can contain H^2S and H^3S representations. The group theory tell us how to decompose the direct product of $\mathrm{SU(2)_L}$ doublet representations:

$$2 \otimes 2 = 3_S \oplus 1_A \tag{7.1}$$

$$2 \otimes 2 \otimes 2 = 4_S \oplus 2 \tag{7.2}$$

where the subscript A and S denoted the representation as antisymmetric and symmetric. Therefore, we concluded that the scalar S can be singlet and triplet to produce the H^2S and can be doublet and quadruplet to produce H^3S. Next, let use find out

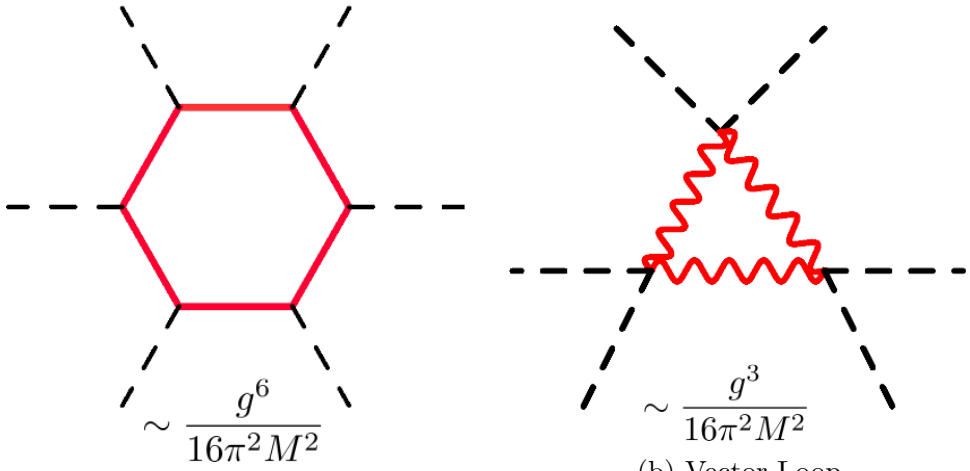

(a) Fermion Loop (b) Vector Loop

Figure 7.1: A illustration that new fermion and vector mediators can not generate H_Q operators at tree level.

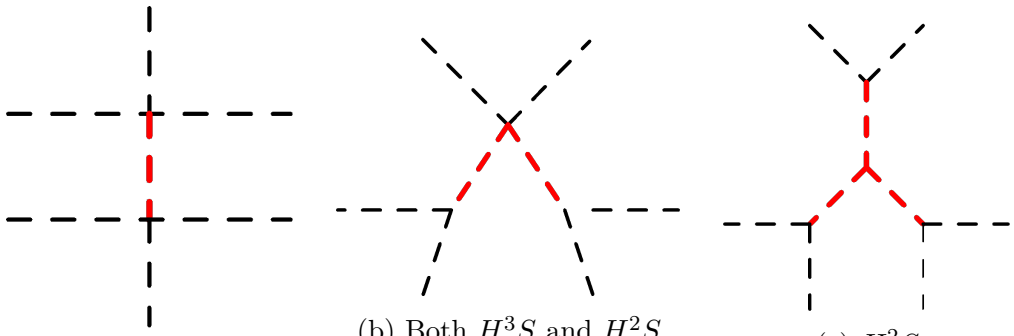

(a) Only H^3S (b) Both H^3S and H^2S (c) H^2S

Figure 7.2: The topologies that can generate Q_H at Tree level through new scalar mediators

possible hypercharge assignments for these possible representations. For singlet, HH must be $H^\dagger H$, so the hypercharge of the singlet S must be zero. For triplet, HH can either be $H_i H_j$ with hypercharge of the triplet $Y_S = -2Y_H$ (complex triplet) or be $H_i^* H_j$ with hypercharge of the triplet $Y_S = 0$ (Real triplet). For doublet, the H^3 must be $H^dagger H H^dagger$, so the hypercharge of the new doublet must be $Y_S = Y_H$. For quadruplet, similar to the triplet case, the hypercharge could be $Y_S = Y_H or 3Y_H$.

For each model we write down the Lagrangians for each UV-model along with the corresponding effective field theory (EFT) to dimension-six at tree level, we will only write the new terms in addition to the standard model terms for convenience. In writing the EFTs we will follow the procedure of Henning et al. [151, 152], the detailed matching procedure can be found in Appendix. To clarify our notation and conventions, we write here the general Lagrangian for all UV complete models, neglecting SM fermionic and gauge boson terms, considered:

$$\mathcal{L} = (D^\mu H)^\dagger (D_\mu H) - \mu^2 (H^\dagger H) - \lambda (H^\dagger H)^2 + \Delta\mathcal{L} \tag{7.3}$$

Where $\Delta\mathcal{L}$ contains all terms containing new fields (in the case of the models we consider this is one new scalar multiplet of $SU(2)$ which may or may not have hypercharge). μ^2 becoming negative signals spontaneous symmetry breaking leading to the massive gauge bosons of the SM. After deriving the EFTs we employ the Warsaw basis [145] for the dimension-six operators, translations between the various bases are included throughout much of the recent literature including a package for relating the bases [115]. The operators which are relevant to our analyses are:

$$\begin{aligned}
Q_H &= (H^\dagger H)^3\,, & Q_{eH} &= (H^\dagger H)(\bar{L} e_R H)\,,\\
Q_{H\Box} &= (H^\dagger H)\Box(H^\dagger H)\,, & Q_{uH} &= (H^\dagger H)(\bar{Q} u_R \tilde{H})\,,\\
Q_{HD} &= (D^\mu H)^\dagger H H^\dagger (D_\mu H)\,, & Q_{dH} &= (H^\dagger H)(\bar{Q} d_R H)\,.
\end{aligned} \tag{7.4}$$

The fermionic operators should be summed over each generation with an appropriate Wilson coefficient. In general the fermionic operators can have off diagonal components, however for the models considered this is only possible for the two-Higgs doublet model and we will employ particular choices of the fermionic matrices in the model to suppress off diagonal components, as is motivated by studies of flavor changing neutral currents, and therefore assume these operators to be diagonal.

7.1.1 Real Scalar Singlet

The real scalar singlet has $Y = 0$, it has been studied extensively in the literature both from the UV complete [197, 53, 209, 36] and EFT perspectives [79, 151, 142]. The Lagrangian, neglecting SM terms, is given by:

$$\Delta\mathcal{L} = \frac{1}{2}(\partial^\mu S)(\partial_\mu S) - \frac{M^2}{2}S^2 - \frac{g}{3}S^3 - g_{HS}(H^\dagger H)S - \frac{\lambda_S}{4}S^4 - \frac{\lambda_{HS}}{2}(H^\dagger H)S^2\,. \quad (7.5)$$

After integrating out the S field we find the EFT:

$$\Delta\mathcal{L} \to \frac{g_{HS}^2}{2M^2}(H^\dagger H)^2 - \left(\frac{\lambda_{HS}}{2} - \frac{g g_{HS}}{3M^2}\right)\frac{g_{HS}^2}{M^4}Q_H - \frac{g_{HS}^2}{2M^4}Q_{H\Box}\,. \quad (7.6)$$

We note that there are corrections to the renormalizable $|H|^4$ vertex, which we will find is a common feature of integrating out scalars in our models, as well as the dimension-six operators Q_H and $Q_{H\Box}$ which affect the trihiggs couplings. Additionally the term $g g_{HS}^3/3/M^6$ appears to be of the next order in the EFT expansion, we will retain these terms in the text, however in our summary Tables 7.2 and 7.3 we neglect such corrections.

7.1.2 Complex Scalar Singlet

For the complex scalar singlet we consider the case of $Y = 0$. While the complex scalar singlet is technically the same as introducing two real singlets, and therefore

doesn't fit our criteria for considered models, we consider it here as it has been studied extensively in the literature. Some examples from the literature which study the complex singlet case and its implications for inflation, the electroweak phase transition, enhancement of the di-Higgs signal, and vacuum stability include [37, 120, 66, 89, 65]. The Lagrangian is then:

$$\begin{aligned}\Delta\mathcal{L} &= (\partial^\mu\Phi)^\dagger(\partial_\mu\Phi) - M^2|\Phi|^2 - \frac{(M')^2}{2}\left(\Phi^2 + h.c.\right) \\ &\quad - \left(g_{HS}(H^\dagger H)\Phi + h.c.\right) - \left(\frac{g}{3}\Phi^3 + h.c.\right) - \left(\frac{g'}{3}\Phi(\Phi^\dagger)^2 + h.c.\right) \\ &\quad - \left(\frac{\lambda_{H\Phi}}{2}(H^\dagger H)\Phi^2 + h.c.\right) - \frac{\lambda'_{H\Phi}}{2}(H^\dagger H)|\Phi|^2 - \left(\frac{\lambda}{4}\Phi^4 + h.c.\right) \\ &\quad - \frac{\lambda'}{4}|\Phi|^4 - \left(\frac{\lambda_1}{4}\Phi(\Phi^\dagger)^3 + h.c.\right) \end{aligned} \tag{7.7}$$

The M' term corrects the dimension-six operator coefficients with terms proportional to M'/M which must be small for the validity of the EFT so we neglect them[2]. Integrating out Φ and $\Phi^\dagger$ gives the effective Lagrangian:

$$\Delta\mathcal{L} \to \frac{|g_{HS}|^2}{M^2}(H^\dagger H)^2 - \left(\frac{|g_{HS}|^2\lambda'_{H\Phi}}{2M^4} + \frac{\mathrm{Re}[g_{HS}^2\lambda_{H\Phi}]}{M^4} - \frac{2\mathrm{Re}[g_{HS}^3 g^* + g_{HS}^2 g' g_{HS}]}{M^6}\right) Q_H - \frac{|g_{HS}|^2}{M^4}Q_{H\Box} \tag{7.8}$$

Again we induce corrections to the $|H|^4$ vertex as well as the effective operators Q_H and $Q_{H\Box}$.

7.1.3 Two Higgs Doublet Model

Of the many extended scalar sectors studied in the literature the two Higgs doublet model is the most well studied, reviews on the status of the model from the UV

[2] M' is the parameter which dictates the size of the mass splitting between the components of the complex scalar field. If M' were to become large it is possible that the lighter resonances would enter the low energy spectrum and invalidate our EFT approach. Therefore it is a requirement of our EFT approach that this parameter be small. For the same reason we will neglect the effects of Y_3 in the 2HDM below.

	L	U	D
Type I:	Φ_2	Φ_2	Φ_2
Type II:	Φ_1	Φ_2	Φ_1
Lepton-Specific:	Φ_1	Φ_2	Φ_2
Flipped:	Φ_2	Φ_2	Φ_1

Table 7.1: List of Fermion couplings used for various Types of 2HDM.

perspective have a long history (some extensive reviews include [48, 186, 146]), the two Higgs doublet model has also recently been studied in the EFT framework in great detail [41, 91, 142] including comparisons between the phenomenological aspects of both the UV complete and EFT frameworks at tree and one-loop levels [49, 125].

We begin in the "Higgs basis", where the doublets have already been rotated to a basis where the physical CP even state is the observed 125 GeV Higgs. This rotation is performed by rotation of H_1 and H_2 by the angle β. We follow the notation of [41]. Note the Yukawa couplings are entered generically and later will be recast in terms of each of the four "types" usually considered to evade flavor changing neutral currents when we write the EFT. These various types considered are outlined in Table 7.1.

$$\begin{aligned}\Delta\mathcal{L} &= (D^\mu H_2)^\dagger (D_\mu H_2) - M^2|H_2|^2 - Y_3(H_1^\dagger H_2 + h.c.) - \frac{Z_2}{2}|H_2|^4 - Z_3|H_1|^2|H_2|^2 \\ &\quad - Z_4(H_1^\dagger H_2)(H_2^\dagger H_1) - \frac{Z_5}{2}(H_1^\dagger H_2)(H_1^\dagger H_2) - \frac{Z_5^*}{2}(H_2^\dagger H_1)(H_2^\dagger H_1) \\ &\quad - Z_6|H_1|^2(H_1^\dagger H_2) - Z_6^*|H_1|^2(H_2^\dagger H_1) - Z_7|H_2|^2(H_1^\dagger H_2) - Z_7^*|H_2|^2(H_2^\dagger H_1) \\ &\quad - \left(H_{2,i}\bar{Q}_j Y_u u_R \epsilon_{ij} + H_{2,i}\bar{Q}_i Y_d d_R + H_{2,i}\bar{L}_i Y_l e_R + h.c.\right) \end{aligned} \tag{7.9}$$

The effective Lagrangian for each "type" of 2HDM is then given below. Note we have neglected terms suppressed by Y_3/M^2 as explained above in the complex scalar discussion. We adopt the notation $\cos\beta = c_\beta$ and $\sin\beta = s_\beta$, where the mixing angle β is the angle which diagonalizes the mass matrices of the charged scalars and pseudoscalars, to allow us to rewrite the Higgs-fermion couplings in terms of the mixing angle and the parameter Z_6.

- *Type I:*

$$\begin{aligned}\Delta\mathcal{L} &= \frac{Z_6}{M^2}\frac{2vh+h^2}{2}\left(\frac{\sqrt{2}m_l c_\beta}{vs_\beta}\bar{L}H_1 e_R + \frac{\sqrt{2}m_u c_\beta}{vs_\beta}\bar{Q}\tilde{H}_1 u_R + \frac{\sqrt{2}m_d c_\beta}{vs_\beta}\bar{Q}H_1 d_R + h.c.\right) \\ &\quad + \frac{|Z_6|^2}{M^2}Q_H + \frac{1}{M^2}\left(4-\text{Fermi}\right) \qquad (7.10)\end{aligned}$$

- *Type II:*

$$\begin{aligned}\Delta\mathcal{L} &= \frac{Z_6}{M^2}\frac{2vh+h^2}{2}\left(-\frac{\sqrt{2}m_l s_\beta}{vc_\beta}\bar{L}H_1 e_r + \frac{\sqrt{2}m_u c_\beta}{vs_\beta}\bar{Q}\tilde{H}_1 u_R - \frac{\sqrt{2}m_d s_\beta}{vc_\beta}\bar{Q}H_1 d_R + h.c.\right) \\ &\quad + \frac{|Z_6|^2}{M^2}Q_H + \frac{1}{M^2}\left(4-\text{Fermi}\right) \qquad (7.11)\end{aligned}$$

- *Lepton Specific:*

$$\begin{aligned}\Delta\mathcal{L} &= \frac{Z_6}{M^2}\frac{2vh+h^2}{2}\left(-\frac{\sqrt{2}m_l s_\beta}{vc_\beta}\bar{L}H_1 e_r + \frac{\sqrt{2}m_u c_\beta}{vs_\beta}\bar{Q}\tilde{H}_1 u_R + \frac{\sqrt{2}m_d c_\beta}{vs_\beta}\bar{Q}H_1 d_R + h.c.\right) \\ &\quad + \frac{|Z_6|^2}{M^2}Q_H + \frac{1}{M^2}\left(4-\text{Fermi}\right) \qquad (7.12)\end{aligned}$$

- *Flipped:*

$$\begin{aligned}\Delta\mathcal{L} &= \frac{Z_6}{M^2}\frac{2vh+h^2}{2}\left(\frac{\sqrt{2}m_l c_\beta}{vs_\beta}\bar{L}H_1 e_r + \frac{\sqrt{2}m_u c_\beta}{vs_\beta}\bar{Q}\tilde{H}_1 u_R - \frac{\sqrt{2}m_d s_\beta}{vc_\beta}\bar{Q}H_1 d_R + h.c.\right) \\ &\quad + \frac{|Z_6|^2}{M^2}Q_H + \frac{1}{M^2}\left(4-\text{Fermi}\right) \qquad (7.13)\end{aligned}$$

We see that the 2HDM only induces one purely bosonic operator, Q_H, at leading order in Y_3/M^2, and induces various combinations of rescalings of the Yukawa couplings, i.e. the operators Q_{eH}, Q_{uH}, and Q_{dH}. The only difference between the various realizations of the 2HDM considered are differences in the weight of the fermionic operators, i.e. by $\tan\beta$ or $\cot\beta$. To make manifest the mass dependence of the Higgs

couplings to fermions above we have expanded the fermionic dimension-six operators (in the unitary gauge for convenience) to recast the couplings of H_1 to fermions in terms of their masses, Z_6, and the mixing angle β. In particular the first line of each expression indicates the shift of the Higgs-fermion couplings relative to the SM prediction,

$$\mathcal{L}_{H\psi\psi} = \frac{\sqrt{2}m_\psi}{v} h\bar{\psi}_R\psi_L \,. \tag{7.14}$$

Another unique feature of the 2HDM effective Lagrangians is that they also contain 4-Fermi operators. These are not relevant to our analysis and, as they are weighted by the square of the Yukawa, are unlikely to have large Wilson coefficients except possibly in the case of the top quark which has $Y_t \sim 1$.

7.1.4 Real Scalar Triplet

The real scalar triplet model [46, 62, 67] has been studied in the literature with ambitions of making the electroweak phase transition first order, e.g. in [162], with the possibility of the neutral component being a dark matter candidate [122], as well as from an EFT point of view in [177, 151].

The relevant Lagrangian is given by,

$$\Delta\mathcal{L} = \frac{1}{2}(D_\mu\Phi^a)^2 - \frac{1}{2}M^2\Phi^a\Phi^a + gH^\dagger\tau^a H\Phi^a - \frac{\lambda_{H\Phi}}{2}(H^\dagger H)\Phi^a\Phi^a - \frac{1}{4}\lambda_\Phi(\Phi^a\Phi^a)^2 \,. \tag{7.15}$$

Integrating out the heavy triplet then gives the effective Lagrangian:

$$\Delta\mathcal{L} = \frac{g^2}{8M^2}(H^\dagger H)^2 - \frac{g^2}{2M^4}Q_{HD} - \frac{g^2}{8M^4}Q_{H\Box} + \frac{g^2}{2M^4}(H^\dagger H)(D_\mu H)^\dagger(D^\mu H) - \frac{g^2\lambda_{H\Phi}}{8M^4}Q_H \,. \tag{7.16}$$

It is convenient to make a change of basis here, we may exchange the operator $|H|^2(D_\mu H)^\dagger(D^\mu H)$ for the other dimension-six operators at the cost of an error of the next order in the EFT (i.e. $\mathcal{O}(1/\Lambda^4)$). While it is frequently simpler to maintain the basis obtained after integrating out the heavy states [241], for the sake of this

work which will consider many UV completions and their effective field theories we choose to project onto a common basis. Discussions of the validity of this method including proofs of the invariance of the S-matrix can be found in [216, 135, 28, 235]. We perform the change of basis by using the Higgs equation of motion, scaled up to dimension-six through multiplication by additional Higgs fields,

$$\begin{aligned}(H^\dagger H)(D^\mu H)^\dagger(D_\mu H) &= -\lambda_R v^2 (H^\dagger H)^2 + \frac{1}{2}Q_{H\Box} + 2\lambda_R Q_H \\ &\quad + \frac{1}{2}(Y_l Q_{lH} + Y_d Q_{dH} + Y_u Q_{uH} + h.c.) + \mathcal{O}(1/\Lambda^4)\end{aligned} \tag{7.17}$$

labeleq:EOMH where we have called the renormalized $(H^\dagger H)^2$ coupling, $\lambda_R = \lambda + g^2/8/M^2$ with λ the $(H^\dagger H)^2$ coupling of Eq. 7.3, yielding the new form of Eq. 7.16:

$$\begin{aligned}\Delta\mathcal{L} &= \frac{g^2}{M^2}\left(\frac{1}{8} - \frac{\lambda v^2}{2M^2} - \frac{g^2 v^2}{16M^4}\right)(H^\dagger H)^2 - \frac{g^2}{2M^4}Q_{HD} + \frac{g^2}{8M^4}Q_{H\Box} - \frac{g^2}{M^4}\left(\frac{\lambda_{H\Phi}}{8} - \lambda - \frac{g^2}{8M^2}\right)Q_H \\ &\quad + \frac{g^2}{4M^4}\left(Y_l Q_{lH} + Y_d Q_{dH} + Y_u Q_{uH} + h.c.\right) .\end{aligned} \tag{7.18}$$

Consistent with our other examples we have again generated the Q_H and $Q_{H\Box}$ operators, however interestingly we have also generated the Q_{HD} operator which will have important phenomenological implications which we discuss in Section 7.2.

7.1.5 Complex Scalar Triplet

Charging the Scalar Triplet under hypercharge, $Y = -1$, has important uses in the Type II seesaw [180, 189, 229, 64]. The relevant UV complete Lagrangian is then,

$$\begin{aligned}\Delta\mathcal{L} &= |D_\mu \Phi^a|^2 - M^2|\Phi^a|^2 + (gH^T i\sigma_2 \tau^a H\Phi^a + h.c.) - \frac{\lambda_{H\Phi}}{2}|H|^2|\Phi^a|^2 \\ &\quad - \frac{\lambda'}{4}(H^\dagger\tau^a\tau^b H)\Phi^a(\Phi^b)^\dagger - \frac{1}{4}\lambda_\Phi|\Phi^a|^4 - \frac{1}{4}\lambda'_\Phi \mathrm{Tr}[\tau^a\tau^b\tau^c\tau^d](\Phi^a)^\dagger\Phi^b(\Phi^c)^\dagger\Phi^d .\end{aligned} \tag{7.19}$$

Integrating out the heavy complex triplet yields the effective Lagrangian,

$$\Delta\mathcal{L} = \frac{|g|^2}{2M^2}(H^\dagger H)^2 + \frac{|g|^2}{M^4}(H^\dagger H)(D^\mu H)^\dagger(D_\mu H) + \frac{|g|^2}{M^4}Q_{HD} - \frac{|g|^2}{2M^4}\left(\frac{\lambda_{H\Phi}}{2} + \frac{\lambda'}{4}\right)Q_H\,, \tag{7.20}$$

which after applying the equation of motion from Eq. 7.17 (notice here $\lambda_R = \lambda + |g^2|/2/M^2$) gives the final form for the effective Lagrangian:

$$\begin{aligned}\Delta\mathcal{L} \;=\; & \frac{|g|^2}{M^2}\left(\frac{1}{2} - \frac{\lambda v^2}{M^2} - \frac{|g|^2 v^2}{2M^4}\right)(H^\dagger H)^2 + \frac{|g|^2}{2M^4}Q_{H\Box} + \frac{|g|^2}{M^4}Q_{HD} \\ & - \frac{|g|^2}{M^4}\left(\frac{\lambda_{H\Phi}}{4} + \frac{\lambda'}{8} - 2\lambda - \frac{|g|^2}{M^2}\right)Q_H + \frac{|g|^2}{2M^4}\left(Y_l Q_{lH} + Y_d Q_{dH} + Y_u Q_{uH} + h.c.\right) \\ & .\end{aligned} \tag{7.21}$$

This effective Lagrangian and the effective operators it contains are consistent with our expectations from the other models, particularly the real scalar triplet.

7.1.6 Quadruplet with $Y = 3Y_H$

For the two quadruplet models we follow the notation of [158], the UV Lagrangian is then given by:

$$\begin{aligned}\Delta\mathcal{L} \;=\; & (D^\mu \Phi^{*ijk})(D_\mu \Phi_{ijk}) - M^2 \Phi^{*ijk}\Phi_{ijk} - (\lambda_{H3\Phi} H^{*i} H^{*j} H^{*k} \Phi_{ijk} + h.c.) \\ & - \lambda_{H2\Phi 2} H^{*i} H_i \Phi^{*lmn}\Phi_{lmn} - \lambda'_{H2\Phi 2} H^{*i}\Phi_{ijk}\Phi^{*jkl} H_l - \lambda_\Phi (\Phi^{*ijk}\Phi_{ijk})^2 \\ & - \lambda'_\Phi (\Phi^{*ijk}\Phi_{ilm}\Phi^{*lmn}\Phi_{jkn})\,.\end{aligned} \tag{7.22}$$

Integrating out the quadruplet leads to the simple EFT,

$$\Delta\mathcal{L} \;=\; \frac{|\lambda_{H3\Phi}|^2}{M^2}(H^\dagger H)^3\,. \tag{7.23}$$

Note that for a quadruplet we expect a contribution to the T-parameter. This operator does not occur at dimension-six, but does at dimension-eight. Deriving only the dimension-eight operator contributing to the T-parameter yields:

$$\mathcal{L}_8^T = \frac{6|\lambda_{H3\Phi}|^2}{M^4}|H^\dagger D^\mu H|^2|H|^2 \tag{7.24}$$

Here we have confirmed the sign of [90]. We will see in the case of $Y = Y_H$ we obtain a different sign from this work.

7.1.7 Quadruplet with $Y = Y_H$

The UV complete Lagrangian is given by,

$$\begin{aligned}\Delta\mathcal{L} &= (D^\mu \Phi^{*ijk})(D_\mu \Phi_{ijk}) - M^2 \Phi^{*ijk}\Phi_{ijk} - (\lambda_{H3\Phi} H^{*i}\Phi_{ijk}H^{*j}\epsilon^{kl}H_l + h.c.) \\ &\quad -\lambda_{H2\Phi2} H^{*i}H_i \Phi^{*lmn}\Phi_{lmn} - \lambda'_{H2\Phi2} H^{*i}\Phi_{ijk}\Phi^{*jkl}H_l - \lambda_\Phi(\Phi^{*ijk}\Phi_{ijk})^2 \\ &\quad -\lambda'_\Phi(\Phi^{*ijk}\Phi_{ilm}\Phi^{*lmn}\Phi_{jkn})\,. \end{aligned} \tag{7.25}$$

Again we find a very simple EFT to dimension-six:

$$\Delta\mathcal{L} = \frac{|\lambda_{H3\Phi}|^2}{M^2}(H^\dagger H)^3\,. \tag{7.26}$$

which we supplement with the dimension-eight T-parameter operator.

$$\mathcal{L}_8^T = \frac{2|\lambda_{H3\Phi}|^2}{M^4}|H^\dagger D^\mu H|^2|H|^2 \tag{7.27}$$

This expression agrees with [90] up to a sign. As the sign of the dimension-eight T parameter operators in each quadruplet model come purely from the covariant derivative term of the Lagrangians (other contributions cancel) they should be the same in both Eqs. 7.24 and 7.26.

7.1.8 Summary of EFTs

Finally after deriving the corresponding EFTs for each model we may construct a table with the Wilson coefficients for each operator for each model considered. We summarize the renormalization of the $(H^\dagger H)^2$ term in Table 7.2 and the Wilson coefficients of the dimension-six operators in Table 7.3. While it appears that of all the theories the 2HDM is the only which does not generate a correction to the renormalizable $(H^\dagger H)^2$, this is a reflection of neglecting terms suppressed by Y_3/M^2, these corrections are generated first at $\mathcal{O}(Y_3/M^2)$. Unsurprisingly neither the 2HDM nor the two singlet models generate Q_{HD}, also referred to as the T-parameter operator as they are known not to shift the relation between the W- and Z-masses. It is, however, expected from studies of the dynamics of the triplet models below EWSB that the triplet models considered in this work correct the T-parameter. This is consistent with our findings in Equations 7.18 and 7.21. In the case of the quadruplet we found they were unique in that at dimension-six they generate only one operator, Q_H, and that the T-parameter operator was generated at dimension-eight. Additionally, as there are no allowed tree level couplings to Fermions in any of the theories except the 2HDM none of the other theories generate the fermionic operators, however after trading the operator $(H^\dagger H)(D^\mu H)^\dagger(D_\mu H)$ in the triplet models via the EOM we do generate the fermionic operators for the two triplet models.

The case of the quadruplets is particularly interesting as studies which indirectly probe the Higgs self coupling, such as [96], only allow the SM coupling λ to vary. Our work indicates that, within the assumptions of our EFT[3], such a study corresponds to a very specific UV complete scenario, in the case where one expects the NP to come from dimension-six operators this corresponds to the quadruplets. In the case of the

[3]For example relaxing the assumptions of a single new multiplet one could envision a scenario with multiple quadruplets in which the T-parameter bounds may be evaded allowing for a sizable H^6 operator coefficient and no other operators at dimension-six. In the case where only the H^6 operator is generated the indirect constraints may be more stringent than those of di-Higgs production [141].

Theory:	$\lambda_{RF} = \lambda + \cdots$
$\mathbb{R}$ Singlet	$\frac{g_{HS}^2}{2M^2}$
$\mathbb{C}$ Singlet	$\frac{\lvert g_{HS}\rvert^2}{M^2}$
2HDM	0
$\mathbb{R}$ Triplet ($Y = 0$)	$\frac{g^2}{M^2}\left(\frac{1}{8} - \frac{\lambda v^2}{2M^2}\right)$
$\mathbb{C}$ Triplet ($Y = -1$)	$\frac{\lvert g\rvert^2}{M^2}\left(\frac{1}{2} - \frac{\lambda v^2}{M^2}\right)$
$\mathbb{C}$ Quadruplet ($Y = 1/2$)	0
$\mathbb{C}$ Quadruplet ($Y = 3/2$)	0

Table 7.2: Summary of the tree-level renormalization of the $(H^\dagger H)^2$ operator in the effective field theory. λ_{RF} indicates the final renormalized $(H^\dagger H)^2$ coupling (i.e. after shifting the operators by the EOM) including λ from Eq. 7.3. In this Table, as mentioned in the text in the Real Scalar singlet discussion, we neglect terms which are of $\mathcal{O}(g^4/M^6)$.

quadruplets the shift in λ due to the effective operators is restricted to be extremely small since the same UV parameter that generates the operator Q_H contributes to the strongly constrained T-parameter. This demonstrates that indirect probes of the Higgs self coupling which don't vary other Higgs couplings are incomplete or correspond to specific UV completions which do not satisfy the criterion of the UV complete models considered. Other studies which vary these additional couplings of the Higgs such as [100, 192] indicate the bounds on the Higgs self coupling are weakened or even lost without the inclusion of the direct di-Higgs probe.

It is useful to project these effective Lagrangians into Lorentz forms relevant to the di-Higgs analysis performed. We do so here, from the perspective of arbitrary Wilson coefficients, when the final analyses are performed we use the expressions for the Wilson coefficients expressed in Table 7.3. We assume that only the heaviest generation for each fermion has a non-negligible contribution to the EFT. Starting

Theory:	$\mathbf{c_H}$	$\mathbf{c_{H\Box}}$	$\mathbf{c_{HD}}$	$\mathbf{c_{eH}}$	$\mathbf{c_{uH}}$	$\mathbf{c_{dH}}$
$\mathbb{R}$ Singlet	$-\frac{\lambda_{HS}}{2}\frac{g_{HS}^2}{M^4}$	$-\frac{g_{HS}^2}{2M^4}$	-	-	-	-
$\mathbb{C}$ Singlet	$-\left(\frac{\lvert g_{HS}\rvert^2\lambda'_{H\Phi}}{2M^4}+\frac{\mathrm{Re}[g_{HS}^2\lambda_{H\Phi}]}{M^4}\right)$	$-\frac{\lvert g_{HS}\rvert^2}{M^4}$	-	-	-	-
2HDM, Type I	$\frac{\lvert Z_6\rvert^2}{M^2}$	-	-	$\frac{Z_6}{M^2}Y_l c_\beta$	$\frac{Z_6}{M^2}Y_u c_\beta$	$\frac{Z_6}{M^2}Y_d c_\beta$
Type II:	$\frac{\lvert Z_6\rvert^2}{M^2}$	-	-	$-\frac{Z_6}{M^2}Y_l s_\beta$	$\frac{Z_6}{M^2}Y_u c_\beta$	$-\frac{Z_6}{M^2}Y_d s_\beta$
Lepton-Specific:	$\frac{\lvert Z_6\rvert^2}{M^2}$	-	-	$-\frac{Z_6}{M^2}Y_l s_\beta$	$\frac{Z_6}{M^2}Y_u c_\beta$	$\frac{Z_6}{M^2}Y_d c_\beta$
Flipped:	$\frac{\lvert Z_6\rvert^2}{M^2}$	-	-	$\frac{Z_6}{M^2}Y_l c_\beta$	$\frac{Z_6}{M^2}Y_u c_\beta$	$-\frac{Z_6}{M^2}Y_d s_\beta$
$\mathbb{R}$ Triplet ($Y=0$)	$-\frac{g^2}{M^4}\left(\frac{\lambda_{H\Phi}}{8}-\lambda\right)$	$\frac{g^2}{8M^4}$	$-\frac{g^2}{2M^4}$	$\frac{g^2}{4M^4}Y_l$	$\frac{g^2}{4M^4}Y_u$	$\frac{g^2}{4M^4}Y_d$
$\mathbb{C}$ Triplet ($Y=-1$)	$-\frac{\lvert g\rvert^2}{M^4}\left(\frac{\lambda_{H\Phi}}{4}+\frac{\lambda'}{8}-2\lambda\right)$	$\frac{\lvert g\rvert^2}{2M^4}$	$\frac{\lvert g\rvert^2}{M^4}$	$\frac{\lvert g\rvert^2}{2M^4}Y_l$	$\frac{\lvert g\rvert^2}{2M^4}Y_u$	$\frac{\lvert g\rvert^2}{2M^4}Y_d$
$\mathbb{C}$ Quadruplet ($Y=1/2$)	$\frac{\lvert\lambda_{H3\Phi}\rvert^2}{M^2}$	-	$\frac{2\lvert\lambda_{H3\Phi}\rvert^2v^2}{2M^4}$	-	-	-
$\mathbb{C}$ Quadruplet ($Y=3/2$)	$\frac{\lvert\lambda_{H3\Phi}\rvert^2}{M^2}$	-	$\frac{6\lvert\lambda_{H3\Phi}\rvert^2v^2}{2M^4}$	-	-	-

Table 7.3: Summary of the tree-level effective field theory to dimension-six for the scalar theories considered. "-" indicates the operator is not generated in this theory. The UV operators with normalizations corresponding to each coupling constant should be read directly from the relevant Lagrangians in text. In this Table, as mentioned in the text in the Real Scalar singlet discussion, we neglect terms which are of $\mathcal{O}(g^4/M^6)$. While the operator Q_{HD} is not generated in the quadruplet models we have entered the contributions to the T parameter in terms of an effective coefficient for this operator into the table.

from the effective Lagrangian,

$$\begin{aligned}\mathcal{L} &= (D^\mu H)^\dagger (D_\mu H) + |\mu|^2 (H^\dagger H) \\ &\quad -\lambda_{RF}(H^\dagger H)^2 + c_H Q_H + c_{H\Box} Q_{H\Box} + c_{HD} Q_{HD} + c_{eH} Q_{eH} + c_{uH} Q_{uH} + c_{dH} Q_{dH}\end{aligned} \tag{7.28}$$

we can proceed to expand the operators to find the relevant Lorentz forms. Here we have used λ_{RF} to represent the final renormalized coefficient of the $(H^\dagger H)^2$ operator, the expression for λ_{RF} may be found in Table 7.2 in terms of λ of Eq. 7.3 and the parameters of each UV-model. This involves finite field renormalizations as the operators $Q_{H\Box}$ and Q_{HD} both alter the Higgs kinetic term below EWSB. Details of this procedure may be found in, for example, [77, 78, 22]. Below EWSB expanding out the Lorentz forms we find (employing the unitary gauge):

$$\begin{aligned}\mathcal{L} &= g^{(3)}_{HZZ} h Z_\mu Z^\mu + g_{HWW} h W^+_\mu W^{-\mu} + g^{(1)}_{HHH} h^3 + g^{(2)}_{HHH} h(\partial_\mu h)(\partial^\mu h) \\ &\quad + \left(g_{He} h \bar{e}_L e_R + g_{Hu} h \bar{u}_L u_R + g_{Hd} h \bar{d}_L d_R + h.c.\right) + \left(g_{HHu} h^2 \bar{u}_L u_R + h.c.\right) + \cdots .\end{aligned} \tag{7.29}$$

Here "$\cdots$" indicates the various operators and Lorentz forms which have no impact on our analysis. The coefficients of the terms in the Lagrangian of Eq. 7.29 are given by:

$$
\begin{aligned}
g_{HWW} &= 2m_W^2(\sqrt{2}G_F)^{1/2}\left[1-\frac{v^2}{4}(c_{HD}-4c_{H\Box})\right] \\
g_{HZZ} &= m_Z^2(\sqrt{2}G_F)^{1/2}\left[1+\frac{v^2}{4}(c_{HD}+4c_{H\Box})\right] \\
g^{(1)}_{HHH} &= -\frac{m_H^2}{2}(\sqrt{2}G_F)^{1/2}\left[1-\frac{v^2}{4}(c_{HD}-4c_{H\Box}+\frac{4}{\lambda_{RF}}c_H)\right] \\
g^{(2)}_{HHH} &= \frac{1}{2(\sqrt{2}G_F)^{1/2}}(c_{HD}-4c_{H\Box}) \\
g_{H\psi} &= -m_\psi(\sqrt{2}G_F)^{1/2}\left[1-\frac{v^2}{4}(c_{HD}-4c_{H\Box})\right]+\frac{c_{\psi H}v^2}{\sqrt{2}}\,, \\
g_{HHu} &= \frac{3c_{uH}}{2}\frac{v}{\sqrt{2}}\,.
\end{aligned}
\tag{7.30}
$$

Note in Eq. 7.30 we have introduced m_ψ and $c_{\psi H}$ as placeholders for the relevant fermion type (i.e. e, u, or d), and in this analysis we only consider couplings to the third generation of each. We have only included g_{HHu} and its corresponding operator as only the top quark $h^2\bar{\psi}\psi$ operator will have an effect on our analyses as it is proportional to the top-quark Yukawa coupling which is the only large Yukawa in the SM. It is possible to remove the $g^{(2)}_{HHH}$ operator by a field redefinition of h, however as pointed out in [212] removing this operator by a field redefinition of h (not the full doublet H) requires a nonlinear field redefinition which may prove to make one loop calculations difficult and if done incorrectly gauge dependent. Therefore we retain the $g^{(2)}_{HHH}$ coupling in favor of easier comparison with other works, such as those which study globally the constraints on the h^3 coupling via one loop dependent processes [182, 95, 96, 141, 45, 100].

7.2 Higgs Coupling Measurements at the LHC

In this section we consider important constraints on our EFTs in Section 6.1. We begin by considering the constraints from electroweak precision data along with a discussion of the loop order at which the S- and T-operators are generated either explicitly via integrating out at the mass scale of the extended scalar sectors or via

operator mixing in the EFT while running down to the Higgs mass scale. Next we introduce the effective $h\gamma\gamma$ coupling in order to add an additional constraint to our global fit to single Higgs processes. Finally with our precision constraints on the EFTs we project these constraints into the UV complete models parameter spaces, this is especially useful in helping to limit the size of the c_H coupling which is partially dependent on the same couplings as the $h\gamma\gamma$ effective coupling.

7.2.1 Electroweak Precision Measurements

Electroweak precision data (EWPD) provide very strong constraints on the Wilson coefficients of effective operators. We note that the operator Q_{HD} contributes at tree level to the T-parameter, while the operator,

$$Q_{HWB} = H^\dagger B^{\mu\nu} W_{\mu\nu} H \,, \tag{7.31}$$

contributes to the S-parameter at tree level. However, the only operators contributing to EWPD that are generated at tree- or one-loop level in our theories are $Q_{H\Box}$ and Q_{HD} the operator Q_{HWB} is only generated at two-loop or higher order. From Jenkins et al. [166, 165, 22] we have the elements of the anomalous dimension matrix for each of these operators:

$$\begin{aligned}
\dot{c}_H &= \left(-\frac{27}{2}g_2^2 - \frac{9}{2}g_1^2\right) c_H + \lambda\left[\frac{40}{3}g_2^2 c_{H\Box} + (-6g_2^2 + 24 g_1^2 y_h^2) c_{HD}\right] + \cdots \\
\dot{c}_{H\Box} &= -\left(4g_2^2 + \frac{16}{3}g_1^2 y_h^2\right) c_{H\Box} + \frac{20}{3} g_1^2 y_h^2 c_{HD} + \cdots \qquad (7.32) \\
\dot{c}_{HD} &= \frac{80}{3} g_1^2 y_h^2 c_{H\Box} + \left(\frac{9}{2}g_2^2 - \frac{10}{3} g_1^2 y_h^2\right) c_{HD} + \cdots \\
\dot{c}_{HWB} &= 6 g_1 g_2^2 c_W + \left[-2y_h^2 g_1^2 + \frac{9}{2}g_2^2 - \left(-\frac{1}{6} - \frac{20}{9}n_g\right) g_1^2 - \left(\frac{43}{6} - \frac{4}{3}n_g\right) g_2^2\right] c_{HWB} \\
&\quad + 4 g_1 g_2 y_h c_{HB} + 4 g_1 g_2 y_h c_{HW} \qquad (7.33)
\end{aligned}$$

Where we have introduced the $U(1)_Y$, $SU(2)_L$, and $SU(3)_C$ couplings g_1, g_2, and g_3 respectively, n_g is the number of active generations at the relevant energy scale, the operators corresponding to the wilson coefficients c_W, c_{HB} and c_{HW} are given by,

$$\begin{aligned} Q_W &= \epsilon^{ijk} W^{i,\nu}_{\mu} W^{j,\rho}_{\nu} W^{k,\mu}_{\rho} \,, \\ Q_{HB} &= (H^\dagger H) B_{\mu\nu} B^{\mu\nu} \,, \\ Q_{HW} &= (H^\dagger H) W^{i}_{\mu\nu} W^{i,\mu\nu} \,, \end{aligned} \tag{7.34}$$

and "$\cdots$" represents other operators not generated at tree-level in our EFTs. The final line of Eq. 7.32 is included to indicate that c_{HWB} is not generated at 1-loop by operator mixing and therefore must be generated at two- or higher loop order. However, the T-parameter is generated at tree-level by the triplet models, and one-loop by any theory which induces $c_{H\Box}$ (namely all but the 2HDM). In the quartet models, since the only dimension-six operator is the H^6 operator, there is no contribution to S and T from the H^6 operator. However, the T-parameter can be generated at tree-level by dimension-eight operators.

Including both the one-loop and running effects we have for the S and T parameters (see e.g. [20] and [77]):

$$\alpha \Delta S = 2 s_{\theta_W} c_{\theta_W} v^2 c_{HWB} - \frac{1}{6} \frac{e^2}{16\pi^2} \left[4 v^2 c_{H\Box} \log\left(\frac{M^2}{m_H^2} \right) + \cdots \right], \tag{7.35}$$

$$\alpha \Delta T = -\frac{1}{2} v^2 c_{HD} + \frac{3}{4c^2} \frac{e^2}{16\pi^2} \left[2 v^2 c_{H\Box} \log\left(\frac{M^2}{m_H^2} \right) + \cdots \right]. \tag{7.36}$$

Again we have used $\cdots$ to represent operators generated at higher loop order in our theories. For the quadruplet models, the dimension-eight operators generate the following T-parameter

$$\alpha \Delta T \simeq -\frac{v^4}{4} c_{T8}, \tag{7.37}$$

where we have defined the Wilson coefficient c_{T8} to be the coefficient of the T-parameter operator at dimension-eight. This coefficient c_{T8} is then given by,

$$c_{T8} = \frac{2|\lambda_{H3\Phi}|^2}{M^4} \quad \& \quad c_{T8} = \frac{6|\lambda_{H3\Phi}|^2}{M^4}\,, \tag{7.38}$$

for the $Y = Y_H$ and $Y = 3Y_H$ quadruplet models respectively. Note that the coefficients c_{T8} depend on the same quadruplet parameters as the operator H^6, and therefore the Wilson coefficient of H^6 is also strongly constrained through this correlation.

From GFitter [31] we have the central values of the S and T parameters with correlation matrix ρ as follows,

$$\begin{pmatrix} S \\ T \end{pmatrix} = \begin{pmatrix} 0.06 \pm 0.09 \\ 0.10 \pm 0.07 \end{pmatrix}, \quad \rho = \begin{pmatrix} 1.00 & 0.91 \\ 0.91 & 1.00 \end{pmatrix}. \tag{7.39}$$

When considering all of the operators discussed above one may perform a sophisticated fit to the EWPD of the many operator coefficients (see e.g. [116]), however for our study we need only consider $c_{H\Box}$ and c_{HD} as discussed above. Therefore performing a simplified chi-square fit relevant to our EFTs, we obtain constraints on the Wilson coefficients $(c_{HD}, c_{H\Box})$:

$$\begin{pmatrix} v^2 c_{HD} \\ v^2 c_{H\Box} \end{pmatrix} = \begin{pmatrix} -0.003654 \pm 0.002677 \\ 8.935 \pm 9.086 \end{pmatrix}, \quad \rho = \begin{pmatrix} 1.00 & -0.97 \\ -0.97 & 1.00 \end{pmatrix}. \tag{7.40}$$

We note that c_{HD} is tightly constrained while $c_{H\Box}$ is not as its contribution to S and T is generated at one-loop.

7.2.2 Higgs Diphoton Rate

In Section II, only the leading tree-level effective operators are written when integrating out the heavy scalars. The leading effective operators which contribute to

the Higgs diphoton signature are not included in our framework as they originate from the one-loop contributions. However because of the precision of the $H \to \gamma\gamma$ measurements we will include them in this section. Note that after integrating out the heavy scalars at one loop one may expect contributions to the $H \to \gamma\gamma$ coupling from the following gauge-invariant dimension-six operators,

$$\mathcal{L}_{H\gamma\gamma} = c_{HB}(H^\dagger H)B^{\mu\nu}B_{\mu\nu} + c_{HW}(H^\dagger H)W^{i,\mu\nu}W^i_{\mu\nu} + c_{HWB}(H^\dagger \tau^i H)W^i_{\mu\nu}B^{\mu\nu} \quad (7.41)$$

However, since we are only interested in the diphoton rate, and not in corrections to the $h \to ZZ$ and $h \to WW$ rates we may simplify the calculation of the Wilson coefficients by only considering one effective operator in the broken phase:

$$\mathcal{L}_{H\gamma\gamma} \to \frac{\alpha}{4\pi} c_{\gamma\gamma} \frac{h}{2v} F_{\mu\nu}F^{\mu\nu} \quad (7.42)$$

The general Higgs diphoton Wilson coefficient $c_{\gamma\gamma}$ for new scalars and fermions at one loop may be found in, e.g. [103]. For the UV complete models considered in Section 6.1 we find the wilson coefficients in Table 7.4. As mentioned in the previous section the Wilson coefficients of the Quadruplet model are all proportional to the parameters contributing to the T-parameter. As such we will not consider the Quadruplet models for the rest of this section.

Finally the diphoton rate relevant to our models is,

$$\Gamma(h \to \gamma\gamma) \quad = \quad \frac{\alpha^2 G_F m_h^3}{128\sqrt{2}\pi^3} |c_{\gamma\gamma}^{\delta\mathrm{SM}} + c_{\gamma\gamma}|^2 \,, \quad (7.43)$$

Where we have defined

$$c_{\gamma\gamma}^{\delta\mathrm{SM}} = \sum_{f=t,b,\tau} N_{c,f} Q_f^2 A_{1/2}(\tau_f) + A_1(\tau_W), \quad (7.44)$$

Model	$c_{\gamma\gamma}$
($\mathbb{R}$ & $\mathbb{C}$) Singlet	0
2HDM	$\frac{v^2}{2M^2} Z_3 \left(\frac{1}{3} + \frac{2m_H^2}{45M^2}\right)$
$\mathbb{R}$ Triplet (Y=0)	$\frac{v^2}{4M^2} \lambda_{H\Phi} \left(\frac{1}{3} + \frac{2m_H^2}{45M^2}\right)$
$\mathbb{C}$ Triplet (Y=-1)	$\frac{v^2}{4M^2} \left(5\lambda_{H\Phi} + \frac{\lambda'}{2}\right) \left(\frac{1}{3} + \frac{2m_H^2}{45M^2}\right)$

Table 7.4: Wilson coefficient $c_{\gamma\gamma}$ for each UV Complete model in Section 6.1.

as the SM part of the $h \to \gamma\gamma$ width taking into account shifts in the couplings of the Higgs to the t-quark and W-bosons due to the effective Lagrangian of Eq. 7.29. Here the loop functions $A_{1/2}(\tau)$ and $A_1(\tau)$ are defined in Ref. [103].

7.2.3 Higgs Global Fits

The Run-I Higgs measurements [8, 58, **?**, 173] provide constraints on some Wilson coefficients in the effective Lagrangian. For convenience we reproduce our effective Lagrangian below EWSB here:

$$\begin{aligned}\mathcal{L} &= g^{(3)}_{HZZ} h Z_\mu Z^\mu + g_{HWW} h W^+_\mu W^{-\mu} + g^{(1)}_{HHH} h^3 + g^{(2)}_{HHH} h(\partial_\mu h)(\partial^\mu h) \\ &\quad + \left(g_{He} h \bar{e}_L e_R + g_{Hu} h \bar{u}_L u_R + g_{Hd} h \bar{d}_L d_R + h.c.\right) + c_{\gamma\gamma} \frac{h}{2v} F_{\mu\nu} F^{\mu\nu} \,. \quad (7.45)\end{aligned}$$

The corresponding Wilson coefficient dependence can be found in Eq. 7.30 while the Wilson coefficients for each model can be found in Tables 7.2, 7.3, and 7.4. We note that the modified Yukawa coupling of the top-quark also causes a shift the Higgs-digluon effective coupling which we have taken into account in our analyses.

These Wilson coefficients contribute to the Higgs signal strengths $\mu = \frac{\sigma \times A \times \epsilon}{[\sigma \times A \times \epsilon]^{\rm SM}}$ extracted from the Higgs coupling data, where $A \times \epsilon$ is the product of the acceptance and the efficiency. Since the Higgs discovery global fits to the effective operators relevant to Higgs physics have become an important area of research [77, 75, 76]

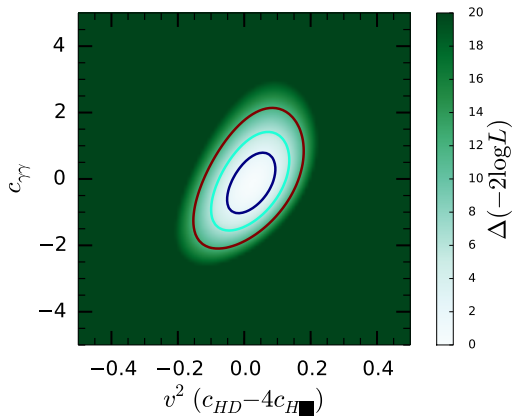

Figure 7.3: The 1, 2, and 3 σ level profiled contours between $v^2(c_{HD} - 4c_{H\Box})$ and $c_{\gamma\gamma}$, given that other operators are fixed to be the local best values.

and recently they have gone beyond simple inclusion of signal strengths to inclusion of kinematic variables and off-shell measurements [80, 54]. They have also been considered in scenarios where EWSB is not linearly realized [50, 81, 51]. However for the sake of our analyses we require a much smaller set of effective operators, therefore we perform a simplified global fit to the Higgs signal strengths μ_i using the program Lilith [42].

In Lilith, all the Run I LHC Higgs measurements [8, 58, **?**, 173] are taken into account, and a likelihood statistical procedure is performed to obtain the constraints on the signal strengths. It is based on the assumption that the Higgs measurements are approximately Guassian and thus the likelihood function $L(\mu)$ could be simply reconstructed. Under this assumption adapted by Lilith, the $-2\log L(\mu)$ follows a χ^2 law for each observable,

$$-2\log L(\mu_i) = \left(\frac{\mu_i - \hat{\mu}_i}{\Delta\mu_i}\right)^2, \tag{7.46}$$

where $\hat{\mu}_i$ is the theoretical prediction of the measured Higgs signal strengths μ_i with Gaussian uncertainty $\Delta\mu_i$. The full likelihood $L(\mu) = \prod_i L(\mu_i)$ is defined as

$$-2\log L(\mu) = \chi^2(\mu) = (\mu - \hat{\mu})^T C^{-1} (\mu - \hat{\mu}), \tag{7.47}$$

where C^{-1} is the inverse of the $n \times n$ covariance matrix, with $C_{ij} = \mathrm{cov}[\hat{\mu}_i, \hat{\mu}_j]$.

Then the constraints on the signal strengths are recast as bounds on the Wilson coefficients. We perform a global fit on these Wilson coefficients $(c_{HD}, c_{H\Box}, c_{\gamma\gamma}, c_{iH})$ with $i = t, b, \tau$, and then project our results into the sub-space in each scalar model. First we perform the six-parameter fit, and obtain

$$\begin{pmatrix} v^2 * c_{tH} \\ v^2 * c_{bH} \\ v^2 * c_{\tau H} \\ v^2 * c_{HD} \\ v^2 * c_{H\Box} \\ c_{\gamma\gamma} \end{pmatrix} = \begin{pmatrix} -0.02224 \pm 0.4609 \\ -0.111 \pm 0.5933 \\ 0.02993 \pm 0.4859 \\ 0.1399 \pm 0.6514 \\ 0.02283 \pm 0.2255 \\ -0.3373 \pm 2.028 \end{pmatrix},$$

$$\rho = \begin{pmatrix} 1.00 & 0.60 & 0.40 & 0.21 & -0.26 & -0.48 \\ 0.60 & 1.00 & 0.38 & 0.19 & 0.43 & -0.47 \\ 0.40 & 0.38 & 1.00 & 0.29 & -0.11 & -0.46 \\ 0.21 & 0.19 & 0.29 & 1.00 & 0.19 & -0.39 \\ -0.26 & 0.43 & -0.11 & 0.19 & 1.00 & 0.16 \\ -0.48 & -0.47 & -0.46 & -0.39 & 0.16 & 1.00 \end{pmatrix}, \tag{7.48}$$

where ρ is the correlation matrix for this global fit. These Wilson coefficients are typically small due to suppression by $\frac{v^2}{M^2}$. However from Subsection 7.2.1 we know we must also consider the EWSB constraints. Assuming equal weight and combining with the constraints coming from the S and T parameters, we find that C_{HD} is very tightly constrained:

$$\begin{pmatrix} v^2 * c_{tH} \\ v^2 * c_{bH} \\ v^2 * c_{\tau H} \\ v^2 * c_{HD} \\ v^2 * c_{H\Box} \\ c_{\gamma\gamma} \end{pmatrix} = \begin{pmatrix} -0.04967 \pm 0.4551 \\ -0.121 \pm 0.5917 \\ -0.003816 \pm 0.4722 \\ -0.0004666 \pm 0.0003861 \\ 0.02302 \pm 0.2184 \\ -0.1513 \pm 1.891 \end{pmatrix},$$

$$\rho = \begin{pmatrix} 1.00 & 0.58 & 0.35 & 0.07 & -0.32 & -0.43 \\ 0.58 & 1.00 & 0.35 & -0.08 & 0.39 & -0.44 \\ 0.35 & 0.35 & 1.00 & 0.04 & -0.18 & -0.40 \\ 0.07 & -0.08 & 0.04 & 1.00 & -0.20 & -0.05 \\ -0.32 & 0.39 & -0.18 & -0.20 & 1.00 & 0.27 \\ -0.43 & -0.44 & -0.40 & -0.05 & 0.27 & 1.00 \end{pmatrix}. \tag{7.49}$$

We also obtain that $v^2 * (c_{HD} - 4c_{H\Box}) = -0.09256 \pm 0.8731$, which by Eq. 7.30 we see is a very important constraint on both the momentum dependent and momentum independent tri-higgs couplings. In Figure 7.3 we show the $v^2(c_{HD} - 4c_{H\Box}) \times c_{\gamma\gamma}^{\text{scalar}}$ plane where we have marginalized over the parameters not shown.

We see from Figure 7.3 that the independent constraint on $c_{\gamma\gamma}$ provides an important constraint in the space of Wilson coefficients which will translate to a constraint on the various four scalar couplings of the UV models and therefore through their correlation with the Wilson coefficient c_H on the affects of the Q_H operator. We project these constraints in the EFT framework onto the UV complete model parameters in the next subsection.

7.2.4 Implications for the UV Physics

In the global fitting procedure, all the Wilson coefficients are assumed to be independent. We know from Section 6.1 that in the specific scalar extended models some Wilson coefficients are correlated and some Wilson coefficients may be absent

Model	Z_6/M^2 or g/M^2 or $\lambda_{H3\Phi}/M^2$	Z_3 or $\lambda_{H\Phi}$
($\mathbb{R}$ & $\mathbb{C}$) Singlet	$g/\sqrt{2}M^2$ or $g/M^2 = 0.00 \pm 0.131$ TeV^{-1}	N/A
2HDM	0.016 ± 0.144 TeV^{-2}	$-4\pi \pm 25.29$
$\mathbb{R}$ Triplet (Y=0)	-0.03 ± 0.007 TeV^{-1}	$-4\pi \pm 19.97$
$\mathbb{C}$ Triplet (Y=-1)	0 ± 0.0071 TeV^{-1}	$5\lambda_{H\Phi} + \lambda'/2 = -22\pi \pm 141.3$
$\mathbb{C}$ Quadruplet ($Y = 1/2$ & $Y = 3/2$)	$\lambda_{H3\Phi}/M^2$ or $3\lambda_{H3\Phi}/M^2 = 0.00 \pm 0.053$ TeV^{-2}	N/A

Table 7.5: The central values and 1σ errors of the model parameters for each UV complete model. We also limit the range of the dimensionless Higgs couplings to be less than $\pm 4\pi$.

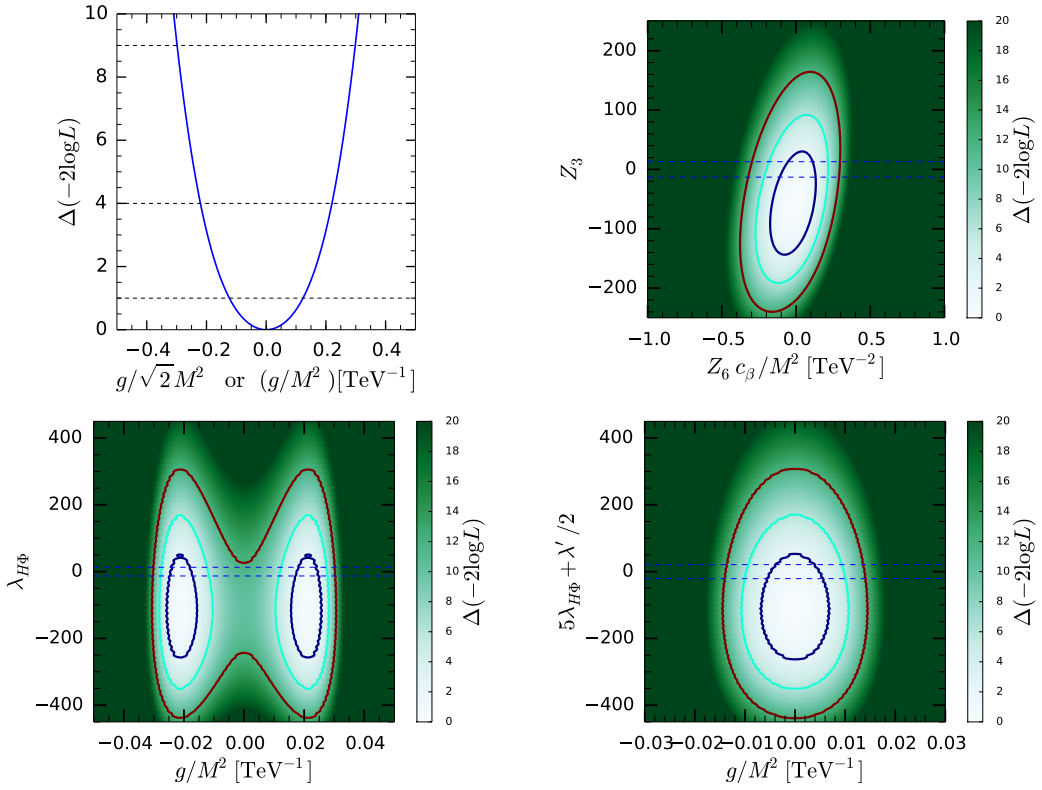

Figure 7.4: In the upper left panel, the log likelihood vs the coupling $g/\sqrt{2}M^2$ (g/M^2) in the real (complex) singlet model. In the others, we show the 1, 2, and 3 σ contours on the model parameters in the Type-I 2HDM (top right), the real triplet (bottom left) and complex triplet model (bottom right). The colored contours show the log likelihood values in the global fit. The blue dashed lines denotes the perturbativity bounds of the dimensionless scalar couplings: $\pm 4\pi$.

altogether. These correlations and absences may be seen in Table 7.3. Therefore, it proves useful to recast the global fit results to obtain constraints on the UV model parameters in each model.

We perform the global fit using the Lilith program in each scalar extended model. In Fig. 7.4, we show the 1, 2, and 3σ contours on the model parameters in the real and complex singlet, Type-I doublet, and complex/real triplet models. At the same time, we also show the central values and errors for the model parameters in Tab. 7.5. These plots exhibit similar features. First, the Higgs-Higgs-scalar coupling g/M^2 or Z_6/M^2 is constrained to be $\mathcal{O}(0.1-1)$ by the Higgs gauge boson couplings in the

singlet and doublet models, while in the triplet models the T-parameter puts tighter constraints on the parameter g/M^2. Secondly, for the doublet and triplets, the Higgs to diphoton rate puts additional constraints on the couplings which contribute to the $c_{\gamma\gamma}$. Converting to the couplings in the UV model, we are not further able to constrain the Higgs-Higgs-scalar-scalar couplings of the triplet models $\lambda_{H\Phi}$ and λ', because the constraints shown in Fig. 7.4 and Tab. 7.5 are very loose. Even the perturbativity constraint, shown as the blue dashed lines in Fig. 7.4, is tighter than the constraint from the global fit. So to place constraints on the Wilson coefficients of Q_H for the 2HDM and triplet models, we have to rely on di-Higgs collider constraints. Finally, we note that although the global fit cannot constrain the renormalizable Higgs self coupling λ, it is able to constrain the dependence of the $h(\partial h)^2$ effective coupling indirectly. We have neglected to project our global fit into the parameter space of the quadruplet as it is so strongly constrained by the T-parameter and the triplet serves as an example of the affects.

While these indirect constraints on the UV models from the global fit are interesting and useful for our di-Higgs analysis in the following section, stronger constraints may of course be found in UV complete considerations of these models. The ability to loosely constrain numerous models at once from simple Higgs global fits is nonetheless intriguing and (especially in the advent of a significant deviation from the SM expectation) a useful way to direct UV complete searches of greater depth in the future.

7.3 Di-Higgs Production at the 100 TeV Collider

Three different topologies of Feynman diagrams of the $pp \to hh$ process via the gluon fusion production are shown in Fig. 7.5. Due to the destructive interference between the triangle and box diagram for the di-Higgs production in the gluon fusion channel, it is believed that at 14 TeV LHC with 3 ab^{-1} luminosity, the triple Higgs

coupling $-g^{(1)}_{HHH}/\lambda_{SM}v$ would be constrained to only $[-0.8, 7.7]$ at 95% CL [5]. In all models considered in this article, the Wilson coefficients of the $|H|^6$ operator cannot be chosen arbitrarily large. Based on the considerations of the validity of EFT and perturbative constraints, we estimate the value of the modified trilinear Higgs coupling to be within the range $(-0.1\lambda_{\rm SM}, 2\lambda_{\rm SM})$, and take the cutoff scale to be 2 TeV. The higher the cutoff scale, we expect the narrower range of the trilinear Higgs coupling. On the other hand, at a 100 TeV collider with 30 ab^{-1} luminosity, the SM value of the triple Higgs coupling can be measured with around 10% uncertainty [74], and even around 4% based on the latest study [231]. Therefore, we expect that 100 TeV collider provides a good opportunity to explore the Wilson coefficients c_H in various models we have considered[4].

7.3.1 General Formalism on Di–Higgs Production

In our EFT framework, the effective Lagrangian relevant to the di-Higgs production is

$$\begin{aligned}\mathcal{L} &= g^{(1)}_{HHH}h^3 + g^{(2)}_{HHH}h(\partial_\mu h)(\partial^\mu h) \\ &\quad + \left(g_{tH}h\bar{t}_L t_R + g_{bH}h\bar{b}_L b_R + g_{HHt}hh\bar{t}_L t_R + g_{HHb}hh\bar{b}_L b_R + h.c.\right) , \quad (7.50)\end{aligned}$$

where

[4]Though in 2HDM the modification of the Wilson coefficient c_{tH} (not yet constrained tightly) can be large enough to modify the di-Higgs production cross section to give some evidence in 14 TeV LHC, yet other models we considered definitely need the help of 100 TeV collider to probe, due to small or zero c_{tH}.

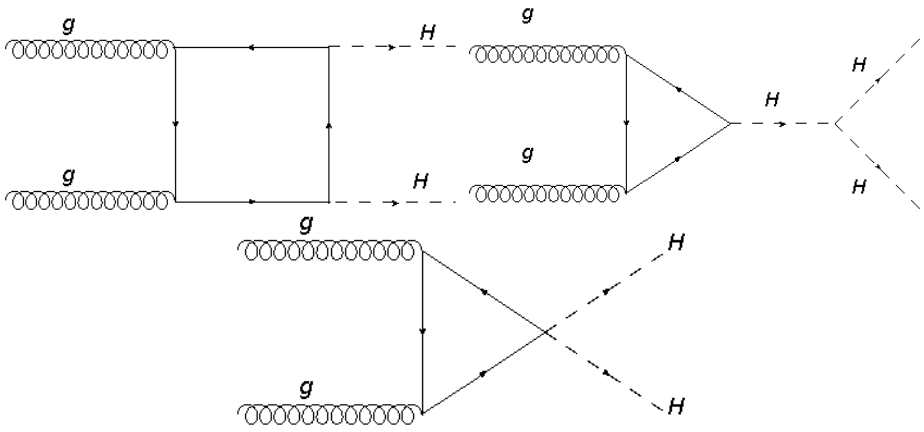

Figure 7.5: Different topologies of the $gg \to hh$ process via the gluon fusion production.

$$g^{(1)}_{HHH} = -\lambda_{SM} v \left[1 - \frac{v^2}{4}(c_{HD} - 4c_{H\Box} + \frac{4}{\lambda_{RF}} c_H)\right], \tag{7.51}$$

$$g^{(2)}_{HHH} = v(c_{HD} - 4c_{H\Box}), \tag{7.52}$$

$$g_{\psi H} = -\frac{m_\psi}{v}\left[1 - \frac{v^2}{4}(c_{HD} - 4c_{H\Box})\right] + \frac{c_{\psi H} v^2}{\sqrt{2}}, \tag{7.53}$$

$$g_{HH\psi} = \frac{3 c_\psi v}{2\sqrt{2}} \tag{7.54}$$

with the SM vacuum expectation value $v \equiv \frac{1}{2(\sqrt{2}G_F)^{1/2}}$ and the SM dimensionless coupling $\lambda_{SM} \equiv \sqrt{2} G_F m_H^2$. From the above Lagrangian, we note that in the Warsaw basis, in addition to the SM trihiggs couplings, we also have derivative triple-Higgs couplings, which may contribute differently to the distribution compared with solely non-derivative couplings.

According to Fig. 7.5, the parton amplitude of the di-Higgs production $g(p_1)g(p_2) \to h(p_3)h(p_4)$ via the gluon fusion process is

$$\begin{aligned}\mathcal{M}_{hh} = & -\frac{\alpha_s \hat{s} \delta^{ab}}{4\pi v^2} \epsilon^a_\mu(p_1)\epsilon^b_\mu(p_2)\left\{\left(\frac{g_{Ht} v}{m_t}\frac{g^{(1)}_{HHH}}{v}\frac{3m_H^2}{\hat{s} - m_H^2} - g^{(2)}_{HHH} v \frac{\hat{s} + 2m_H^2}{\hat{s} - m_H^2} + \frac{2v^2}{m_t} g_{HHt}\right) F_\triangle A^{\mu\nu}\right. \\ & \left. + \frac{g^2_{Ht} v^2}{m_t^2} F_\Box A^{\mu\nu} + \frac{g^2_{Ht} v^2}{m_t^2} G_\Box B^{\mu\nu}\right\},\end{aligned} \tag{7.55}$$

where the Lorentz structures are defined in Eq. 3.3 and Eq. 3.4 and $F_{\triangle}$, $F_{\square}$, and $G_{\square}$ are the form factors for triangle and box diagrams which can be found in Ref. [215]. Correspondingly, the differential cross-section for di-Higgs production is given by:

$$\frac{d\sigma(pp \to hh)}{d\hat{s}d\hat{t}} = \frac{1}{S}\mathcal{L}_{gg}\left(\frac{\hat{s}}{S}, \sqrt{\hat{s}}\right)\frac{|\mathcal{M}_{hh}|^2}{32\pi\hat{s}}, \tag{7.56}$$

where S is the center-of-mass energy squared of the proton-proton system, $\hat{s} = (p_1 + p_2)^2$, $\hat{t} = (p_1 - p_3)^2$ and the parton luminosity function is defined as

$$\mathcal{L}_{gg}(y, \mu_F) = \int_y^1 \frac{dx}{x} f_{g/p}(x, \mu_F) f_{g/p}(\frac{y}{x}, \mu_F), \tag{7.57}$$

with $f_{g/p}$ the gluon distribution function, and μ_F the factorization scale. As we have previously noted, the triangle diagram and box diagram interfere destructively and the smallest cross section is obtained when $g^{(1)}_{HHH}/v \approx -2.5\lambda_{SM}$ assuming no derivative interaction and no corrections to the quark-Higgs couplings. Due to this fact, the variation in the gluon fusion to di-Higgs cross section about the SM value of $g^{(1)}_{HHH} = -\lambda_{SM}v$ is not symmetric. When $g^{(1)}_{HHH}$ decreases, the total cross section decreases, till $g^{(1)}_{HHH}$ reaches $-2.5\lambda_{SM}$. Any further decrease in $g^{(1)}_{HHH}$ results in increasing of the cross section with respect to its minimum value at $g^{(1)}_{HHH}/v \approx -2.5\lambda_{SM}$ eventually surpassing the SM value for $g^{(1)}_{HHH}$ values lower than $-5\lambda_{SM}$. On the other hand as $g^{(1)}_{HHH}$ increases from zero, the total cross section increases. In our case, the situation is more complicated, we now have both an additional vertex and corrections to the quark Higgs couplings.

7.3.2 Di–Higgs Cross Section

In Figure 7.6 we show the cross section contours of the $pp \to hh$ process in the $(g^{(1)}_{HHH}/v, g^{(2)}_{HHH}v)$ plane with three different values of c_{tH}. To evaluate the range of trihiggs couplings $g^{(1)}_{HHH}/v$ and $g^{(2)}_{HHH}v$, we first use the Eq. 7.30 and Table 7.3 to

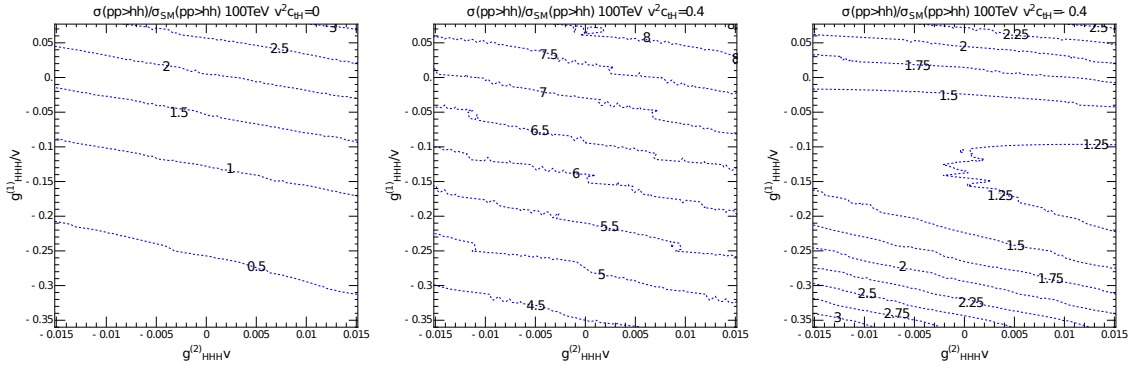

Figure 7.6: The ratio of the cross sections of the $pp \to hh$ process to the SM di-Higgs cross section denoted by the dashed blue contours in the $(g^{(1)}_{HHH}, g^{(2)}_{HHH})$ plane, the plots from left to right correspond to three different value of $c_{tH} = 0,\ 0.4,\ -0.4$. We adopt the NNLL matched NNLO SM di-Higgs cross section: 1.75 pb [74].

express the two couplings in terms of the parameters in the UV model, then varies the dimensionless parameters in the UV models within the range $\pm 4\pi$, couplings with mass dimension to be in the range ± 1 TeV, and the cutoff scale are set to be 2 TeV. These values are chosen such that our EFT matching procedure is valid (dimension-eight operators will not be enhanced by the factor g^2/M^2) and the contribution of the kinematic region larger than cutoff scale to the total rate is negligible due to the suppression of the parton luminosity. After these consideration, we choose relatively loose ranges for the two couplings: $g^{(1)}_{HHH} \subset (-0.36, 0.07)$ and $g^{(2)}_{HHH} \subset (-0.015, 0.015)$.

For $c_{tH} = 0$, the anomalous Higgs fermion coupling g_{HHt} in Eq. 7.54 vanishes and the corrections to the quark Higgs couplings are proportional to $c_{HD} - 4c_{H\Box}$. In such a case, only the first triangle and box diagrams of Figure 7.5 contribute to the cross section with approximate SM quark Higgs couplings. Hence, one can find that, along the positive vertical direction, given a fixed value of $g^{(2)}_{HHH}$, the cross section increases. Along the $g^{(2)}_{HHH}$ direction, one can find that a positively increasing value of $g^{(2)}_{HHH}$ will lead to an increase in the total cross-section. This can be understood from Eq. 7.55, where we observe that, with a positive $g^{(2)}_{HHH}$, the second term inside the bracket in front of the $F_\triangle$ which is induced by the derivative interaction will add destructively

with the first term which is induced by the ordinary triple Higgs interaction, such that the effect of destructive interference between the box and triangle diagrams is alleviated.

In the case of $c_{tH} = 0.4$, the cross section increases significantly when compared with the cross section for $c_{tH} = 0$, this can also be understood from Eq. 7.55 and Eq. 7.53: The positive c_{tH} will decrease the magnitude of g_{tH} and also gives a new positive term generated by $tthh$ vertex, which will alleviate the destructive interference. In the case of $c_{tH} = -0.4$, the cross section will reach some minimum value between $g^{(1)}_{HHH}/v = -0.1$ and -0.15 due to the destructive interference. Below the miminum points, for a fixed $g^{(1)}_{HHH}$, increasing $g^{(2)}_{HHH}$ will decrease the cross section, because at this point the amplitude from the triangle diagram becomes dominant, increasing $g^{(2)}_{HHH}$ will decrease the magnitude of the term inside the bracket in front of the $F_{\triangle}$, thereby decreasing the cross section.

7.3.3 Monte Carlo Simulation and Validation

In order to perform our simulations we begin by using FeynRules [21] to generate an UFO model file adding the effects of the dimension-six operators in Eq. 7.50. We then modify the model file to include the full triangle and box form factors as computed in [124]. Then we implement MadGraph 5.2.4.3 [24] to generate events. We use Pythia 6 [237] for the parton shower and the FCC card in Delphes 3.4 [230] for simulating the detector. The following analysis is only concerned with statistical uncertainties as the systematical uncertainties are unknown at the moment. When taken into account they will lower the significance levels given in this section.

We refer to the cuts applied while generating the events in MadGraph/Delphes as preselection cuts in the Table 7.6. They are as follows[5]:

[5]For $bb\gamma\gamma$ and $bbj\gamma$ events, we also implement the $50 < m_{bb} < 250$GeV and $90 < m_{j\gamma,\gamma\gamma} < 160$GeV to increase the efficiency of the sample, and we found that the events outside these cuts contribute negligibly to the final results.

$$|\eta_{j,b,\gamma}| < 2.5, \qquad \Delta R_{jj,j\gamma} > 0.4,\, pT_{j,b} > 20\,\text{GeV}, \qquad pT_{\gamma} > 10\,\text{GeV} \tag{7.58}$$

Important irreducible backgrounds consist of $Z(b\bar{b})h(\gamma\gamma)$, $t\bar{t}h(\gamma\gamma)$, $b\bar{b}h(\gamma\gamma)$, $b\bar{b}\gamma\gamma$ production. Apart from these, there are $bbj\gamma$, $jj\gamma\gamma$, $c\bar{c}\gamma\gamma$ and $bbjj$ channel that can potentially have a contribution to the background. Jet fake rates to photons are taken to be 0.012%, while jet and charm mistagging rates to bottom quarks are taken to be 1% and 10% respectively [92]. The backgrounds can be greatly reduced by vetoing extra jets, i.e., by demanding exact two b-tagged jets in each event. This is particularly helpful in reducing the $t\bar{t}h$ background. Applying a Higgs mass window cut of $112.5 < m_{bb} < 137.5$ GeV, to the invariant mass of b-jets results in a large reduction in the Zh background due to exclusion of the Z-peak region.

The Higgs mass window cut for the di-photon invariant mass is sharper than that for the invariant mass of b-jets and helps to reduce the background in all the channels. Furthermore, from the normalized distributions for b-jet-pair p_T and di-photon p_T in Fig. 7.7 indicate that the signal is favored for p_T values larger than 150 GeV and 140 GeV respectively. Therefore, we further apply these cuts in order to enhance the statistical significance. The resulting efficiencies and cross sections at each stage due to these cuts in our analysis for leading backgrounds and three benchmark (BM) points for the signal are tabulated in Table 7.6.

We first investigate the sensitivity of the trilinear Higgs coupling $\lambda_{HHH} = -g^{(1)}_{HHH}/v$ in the absence of the derivative Higgs coupling $g^{(2)}_{HHH}$. In this case, we recover the scenario widely discussed in the literature: how to probe the deviation of the λ_{HHH} from its SM value λ_{SM} at the future collider. Compared with the work in [39], we obtain comparable significance of about 8.25σ for the SM di-Higgs production for luminosity of 3 ab^{-1}. This corresponds to the significance of $\sim 26\sigma$ for 30 ab^{-1} as can be seen from the black line in the left panel of Fig. 7.8, where we plot the $S/\sqrt{B}$ for 30 ab^{-1} and zero derivative interaction.

Channel	**Pre-selection** σ **(fb)**	**Basic Cuts** + **#bjet=2;#γ=2**		$110 < m_{bb} < 140$ **GeV** $120 < m_{\gamma\gamma} < 130$ **GeV**		$pT_{bb} > 150$ **GeV**		$pT_{\gamma\gamma} > 140$ **GeV**	
		Efficiency	σ **(fb)**	**Efficiency**	σ **(fb)**	**Efficiency**	σ **(fb)**	**Efficiency**	σ **(fb)**
Bckgs									
$b\bar{b}\gamma\gamma$	50500	5.64×10^{-4}	28.5	1.54×10^{-5}	0.776	4.05×10^{-7}	2.04×10^{-2}	3.89×10^{-7}	1.97×10^{-2}
$b\bar{b}j\gamma$	8424 [a]	4.98×10^{-3}	42.0	3.83×10^{-5}	0.322	1.56×10^{-6}	1.31×10^{-2}	1.39×10^{-6}	1.17×10^{-2}
$c\bar{c}\gamma\gamma$	1454.31 [b]	7.14×10^{-2}	104.0	1.64×10^{-4}	0.238	3.63×10^{-6}	5.28×10^{-3}	2.90×10^{-6}	4.22×10^{-3}
$b\bar{b}h(\gamma\gamma)$	35.26	3.67×10^{-3}	0.129	4.36×10^{-4}	1.54×10^{-2}	8.72×10^{-5}	3.07×10^{-3}	8.33×10^{-5}	2.94×10^{-3}
$jj\gamma\gamma$	145.33 [c]	7.90×10^{-2}	11.5	1.89×10^{-4}	2.75×10^{-2}	1.48×10^{-5}	2.15×10^{-3}	1.44×10^{-5}	2.09×10^{-3}
$t\bar{t}\mathrm{h}(\gamma\gamma)$	38.27	2.24×10^{-3}	8.55×10^{-2}	3.22×10^{-4}	1.23×10^{-2}	5.01×10^{-5}	1.92×10^{-3}	2.71×10^{-5}	1.04×10^{-3}
$Zh(\gamma\gamma)$	1.36	3.21×10^{-2}	4.36×10^{-2}	4.56×10^{-4}	6.21×10^{-4}	1.12×10^{-4}	1.52×10^{-4}	1.09×10^{-4}	1.48×10^{-4}
$b\bar{b}\mathrm{jj}$	84.96 [d]	1.09×10^{-2}	0.927	1.08×10^{-4}	9.14×10^{-3}	3.25×10^{-6}	2.76×10^{-4}	1.39×10^{-6}	1.18×10^{-4}
Total			187.0		1.40		4.64×10^{-2}		4.19×10^{-2}
Sig. BMs									
SM	4.60	3.20×10^{-2}	0.147	1.36×10^{-2}	6.25×10^{-2}	7.60×10^{-3}	3.50×10^{-2}	7.25×10^{-3}	3.33×10^{-2}
BM1	9.920	3.16×10^{-2}	0.313	1.24×10^{-2}	0.123	5.30×10^{-3}	5.26×10^{-2}	5.01×10^{-3}	4.97×10^{-2}
BM2	9.094	3.04×10^{-2}	0.275	1.25×10^{-2}	0.113	5.96×10^{-3}	5.39×10^{-2}	5.73×10^{-3}	5.18×10^{-2}
BM3	5.329	3.16×10^{-2}	0.168	1.39×10^{-2}	0.074	7.70×10^{-3}	4.10×10^{-2}	7.34×10^{-3}	3.91×10^{-2}

Table 7.6: Cut-flow table for the analysis we perform. Basic cuts refer to generator level cuts described in Eq. 7.58. In the cross sections we have multiplied by the following NLO k-factors [74]: $k_{zh} = 0.87$, $k_{t\bar{t}h} = 1.3$, $k_{bbjj} = 1.08$, $k_{jj\gamma\gamma} = 1.43$. Signal benchmarks in the $(g^{(1)}_{HHH}/v, g^{(2)}_{HHH}v)$ plane are as follows: BM1=$(0.0225, 0)$, BM2=$(-0.032, 0.0152)$, and BM3=$(-0.141, 0.0152)$

[a] including fake rate of $j \to \gamma$: 0.012%.

[b] including fake rate of $c \to b$: 10%.

[c] including fake rate of $j \to b$: 1%.

[d] including fake rate of $j \to \gamma$: 0.012%.

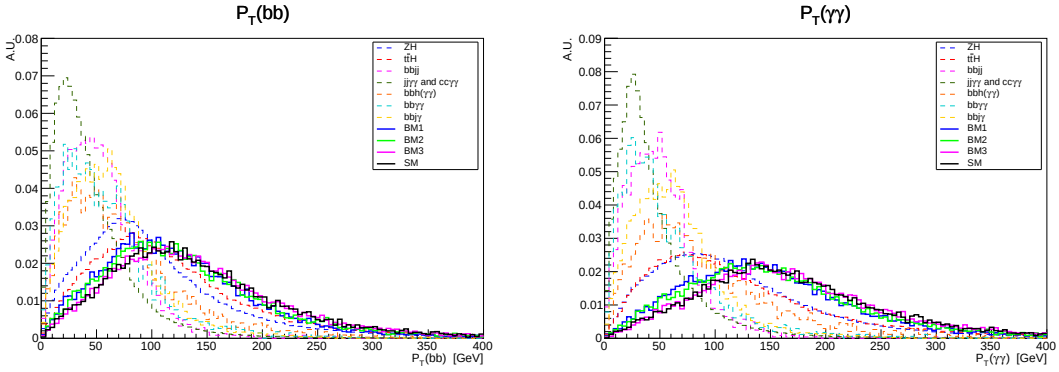

Figure 7.7: Normalized distributions for b-jet-pair and di-photon p_T for signals and various backgrounds as described in the legend. Solid histograms correspond to different signal benchmarks (BMs) considered. Dashed histograms correspond to various SM backgrounds as indicated in the legend.

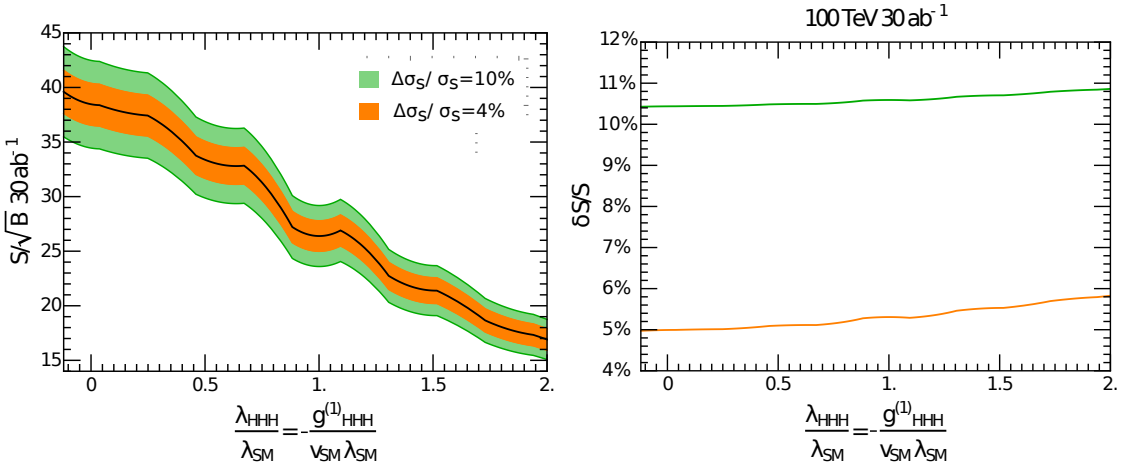

Figure 7.8: Left panel: The significance of the di-Higgs process as a function of the trilinear Higgs coupling $\lambda_{HHH} = -g^{(1)}_{HHH}/v$ assuming that the derivative Higgs coupling $g^{(2)}_{HHH}$ is zero. The orange and green bands correspond to the 1σ uncertainty in the $S/\sqrt{B}$ with assumptions of the theoretical uncertainty for the di-Higgs production cross-section to be 4% and 10% respectively. Right panel: The percentage uncertainties on the measured number of signal events varies with the value of trilinear Higgs coupling. Orange and green lines correspond to theoretical uncertainties of 4% and 10% respectively.

We also estimate the uncertainty in the value of $S/\sqrt{B}$ by taking into account the statistical uncertainty for the signal and background as well as the theoretical uncertainty on the di-Higgs production cross-section. It turns out that for a 30 ab^{-1} luminosity, the statistical uncertainty in the number of signal events due to Poisson fluctuations is around 3%, which is less than the 10% theoretical uncertainty coming from the infinite top mass approximation, the scale, and the PDF uncertainties [74]. The 1σ uncertainty due to this is denoted by the green band in the left panel of Fig. 7.8. However, the latest estimation on the theoretical uncertainties places them as low as 4% [231]. Therefore, we also include this case denoted by orange band in the plot shown in the left panel of Fig. 7.8.

The right panel of Fig. 7.8 represents the percentage uncertainties for the measured number of signal events as a function of the ratio of the triple Higgs coupling to its SM predicted value. Orange and green lines here correspond to the theoretical uncertainty of 4% and 10% respectively. As expected from the above quoted numbers, the theoretical uncertainty dominates except where the ratio of triple Higgs couplings is close to 2.5, where the cross section for di-Higgs production is the lowest leading to enhanced uncertainty due to Poisson fluctuations.

Here we comment on the validity of EFT in our collider analysis. The EFT breaks down when the parton collision center of mass energy approaches the scale of the cutoff scale $M = 2$ TeV. Therefore, we should in principle add a cut on the kinematic variables like invariant mass of di-Higgs to only keep the events produced in low energy regime to make our EFT analysis valid. The di-Higgs spectrum is peaked at an invariant mass m_{hh} near the two higgs threshold indicating our EFT approach should be valid (i.e. the processes considered have energy well below our cutoff of 2 TeV). Additionally we have investigated the number of events below 1 TeV, 1.5 TeV, and 2 TeV for three benchmark points: the SM, $\lambda_{HHH}/\lambda_{SM} = 2$, $\lambda_{HHH}/\lambda_{SM} = -0.9$, and finding the results in Table. 7.7. As there are only a small

$\frac{\lambda_{HHH}}{\lambda_{SM}}$	$m_{hh} > 1$TeV	$m_{hh} > 1.5$ TeV	$m_{hh} > 2$TeV
1	2.5%	0.38%	0.16%
2	5.1%	1.0%	0.35%
-0.9	1.3%	0.26%	0.05%

Table 7.7: The percentage of events with m_{hh} above 1, 1.5 and 2 TeV.

number of outlying events with higher energies these numbers support the assertion that the EFT approach is valid in our Monte Carlo simulation. One should note that even if the heavy particles were to be discovered at higher energies that in order to extract the trilinear couplings of the SM Higgs one would still employ an EFT. Such a procedure is analogous to the use of an effective four fermion theory for flavor physics where the heavy Ws have been integrated out of the theory in favor of unrenormalizable operators.

7.3.4 Determination of Wilson Coefficients

Equation 7.30 and Table 7.3 demonstrate it is necessary to investigate the discovery potential at the 100 TeV collider when both the deviation of the λ_{HHH} coupling from the SM value, and non-zero $g^{(2)}_{HHH}$ exist. Turning on the derivative Higgs coupling $g^{(2)}_{HHH}$ will change the significance of the di-Higgs signatures. In Fig. 7.9 we present the reach of the 100 TeV collider with integrated luminosity of 30 ab^{-1} in the space of $g^{(1)}_{HHH} - g^{(2)}_{HHH}$ in the left panel as well as in the space of Wilson coefficients c_H and $c_{HD} - 4c_{H\Box}$ in the right panel, each with $c_{tH} = 0$. The left and right panels of the Fig. 7.9 are not independent. Their values are connected by Eq. 7.30, where the contours in the right panel are essentially rotated around the SM values as governed by the Eq. 7.30. This represents only a class of models, in which c_{tH} is not important, for example, singlet, triplet and quadruplet models. We plot the statistical significance contours for 2HDMs in $c_{tH} - c_H$ space as shown in separate plots of Fig. 7.10.

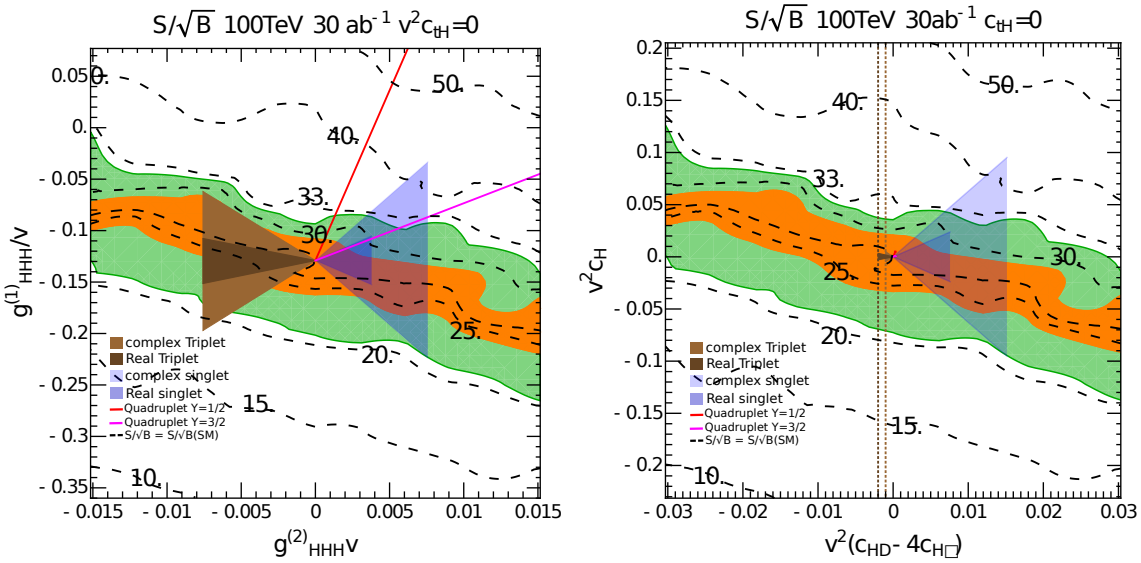

Figure 7.9: Black dashed contours denote statistical significance, $S/\sqrt{B}$, for identifying the signal at 100 TeV with integrated luminosity of 30 ab^{-1}. Left panel: The significance contours are plotted in the $g^{(1)}_{HHH}/v$ vs. $g^{(2)}_{HHH}$ plane, the shaded region is constrained by dimensionless couplings in the Lagrangian within the range $\pm 4\pi$ for couplings with mass dimension within the range ± 1 TeV and cutoff scale $M = 2$ TeV. The light and dark shaded brown and blue regions are allowed by all the global fit constraints. The Red line and magenta line corresponds to quadruplet model with $Y = 1/2$ and $1/3$ respectively. Orange and green regions correspond to the 1σ uncertainty on the significance with assumptions of the theoretical uncertainty for the di-Higgs production cross-section to be 4% and 10% respectively. Right panel: The significance contours are plotted in the $v^2 c_H$ vs. $v^2(c_{HD} - 4c_{H\Box})$ plane. The darker brown and light brown dotted lines on the right panel correspond to the Wilson coefficient constraints from the Higgs coupling measurements and the T-parameter in the real and complex triplet models. Shaded regions on the right have the same meaning as in the left panel. Both plots are with $c_{tH} = 0$ and the SM limit in both is located at $(0, 0)$ with $S/\sqrt{B} \sim 26$.

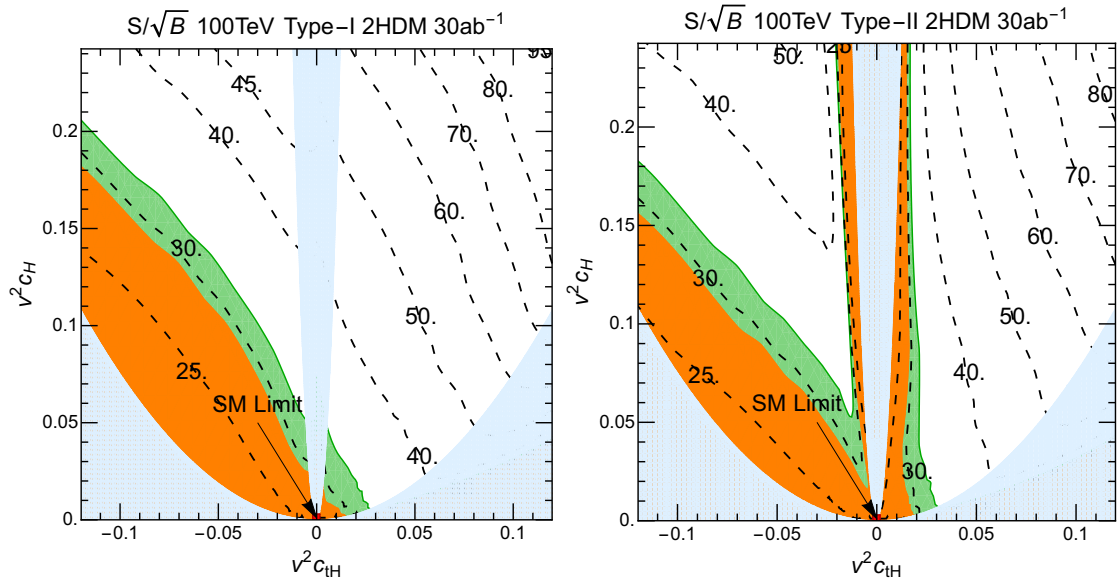

Figure 7.10: Dark cyan dashed contours denote statistical significance, $S/\sqrt{B}$, for identifying the signal at 100 TeV with integrated luminosity of 30 ab^{-1}. The left and right plots represents Type-I and Type-II 2HDM respectively. The light blue regions correspond to the parameter regions in $\tan\beta$ which has been ruled out by experimental data from flavor physics. The orange and green regions are within the SM 2σ uncertainty with assumption of the percentage uncertainty of di-Higgs production cross section equal to 4% and 10% respectively.

$c_{tH} = 0$ corresponds to $\tan\beta \to \infty$, which is outside the experimental bounds on $\tan\beta$ in 2HDMs.

Fig. 7.9 shows the allowed parameter regions in singlet, triplet and quadruplet models, which overlap within the significance contours. In these models, according to Table 7.3, the Wilson coefficients c_H and $c_{HD} - 4\,c_{H\Box}$ are not independent. More specifically, they are related by linear relations such as $c_H \simeq \lambda_{HS(\Phi)}(c_{HD} - 4\,c_{H\Box})$. This linear relation then implies that the boundaries of these regions are governed by the input perturbative limit $|\lambda_{HS(\Phi)}| \leq 4\pi$ and are straight lines as can be seen in Figure 7.9. The values of the dimensionless Higgs scalar couplings, such as λ_{HS}, $\lambda_{H\Phi}$, determine the slopes of the parameter region in each model. For example, in the real singlet case, along the boundary of the parameter region, the Higgs scalar coupling λ_{HS} should be around $\pm 4\pi$. In the region far from the boundary, the dimensionless Higgs scalar couplings appearing in c_H should be small. We choose c_{tH} to be equal to zero in these two plots. This condition is automatically satisfied by singlet and quadruplet models, and also approximately satisfied by triplet models. This is because c_{tH} in triplet models is suppressed by the coupling g^2 which is constrained to be very small by EWPD due to its relation to the T-parameter.

In addition to the allowed region in each model, we also illustrate the region that will generate the expected significance within the 2σ uncertainties around SM value.

Therefore we simply estimate that this 2σ region roughly gives the region that is hard to differentiate from the SM in the future experiments.

One can observe that, the future di-Higgs experiment is not sensitive to the $c_{H\Box}$ and c_{HD} which have already been strongly constraint by the EWPD. On the other hand, it can constrain the value of c_H. Depending on the theoretical uncertainties that can be achieved, it may also be possible to exclude some parameter space of the singlet models, which represents the region outside the 2σ region.

The case of the 2HDM is much more promising for distinguishing between the SM and the NP model as c_{tH} is non-zero. We demonstrate the significance for 100 TeV collider at 30 ab^{-1} integrated luminosity in $v^2 c_{tH}$ vs $v^2 c_H$ plane, shown in Fig. 7.10. Both $v^2 c_{tH}$ vs $v^2 c_H$ depend on $\tan\beta$. Here we choose the range of $\tan\beta$ such that it satisfies the constraints from flavor physics according to Ref. [113]. This rules out some parameter regions as shown in Fig. 7.10 by blue regions. We note that the significance in the 2HDM is generally larger than that of the singlet, triplet and quadruplet models due to typical enhancement from the Yukawa couplings, and it is very likely to observe a significant deviation from the SM signal. We also find that, unlike the singlet and triplet, signal significances in the 2HDM are much more enhanced compared to the ones in the SM. The plots also show that the contours of significance of two types of 2HDMs are different despite the coupling to up-type quarks being the same in both Type I and Type II, the reason being that we are using the $bb\gamma\gamma$ final state and the branching ratio of $h \to bb$ are different between the two versions of the 2HDM.

From Fig. 7.9 and Fig. 7.10, if we limit ourselves in these models with all the heavy particles integrated out, the di-Higgs process puts additional constraints on the scalar model parameters. Our analysis in Fig. 7.9 and Fig 7.10 shows that the Complex singlet and 2HDM (triplet and quadruplet) scalar models are the most (least) sensitive, among those resulting from the models under consideration, to the collider search. As a consequence, the di-Higgs process probes the allowed region of c_H, and thus the Higgs scalar couplings in the UV models.

7.3.5 Exploring Parameter Region in UV Models

We project the sensitivity of the Wilson coefficients into the parameter space corresponding to the models under consideration. In the real singlet model, the parameter space of the effective coefficients allowed is indicated by the light blue

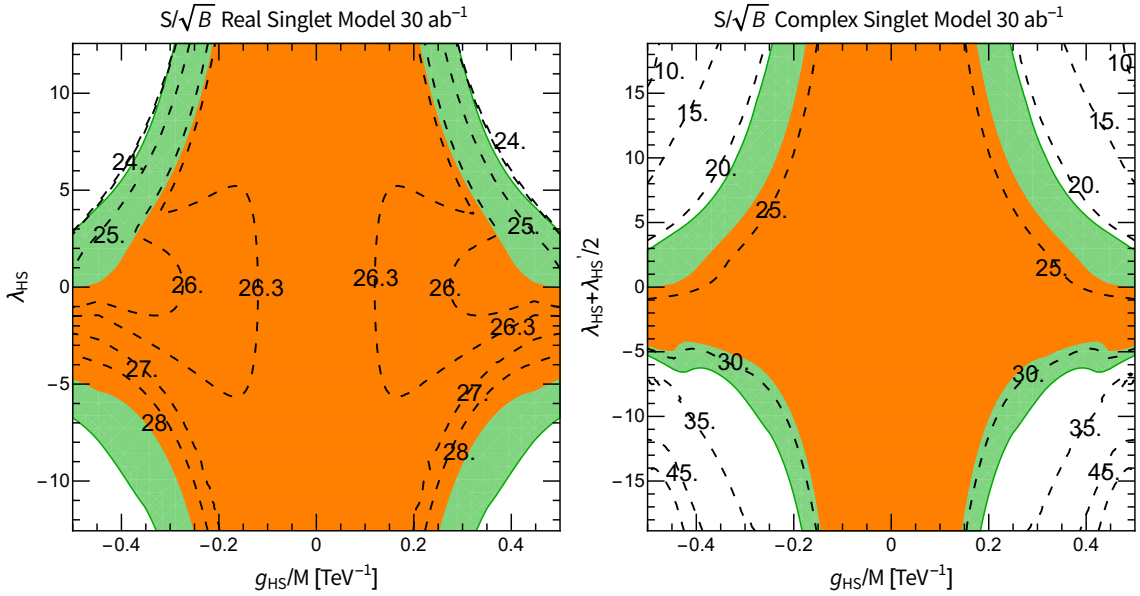

Figure 7.11: The discovery potential of the model parameters (g_{HS}, λ_{HS}) in the real (left panel) and complex (right panel) singlet models. The contours correspond to the significance given integrated luminosity of 30 ab^{-1}. The orange and green regions are with in the SM 2σ uncertainty with assumption of the percentage uncertainty of di-Higgs production cross-section equal to 4% and 10% respectively.

region in Fig. 7.9, can be probed with $S/\sqrt{B}$ more than 25, while in the complex singlet model, the Wilson coefficients resulting from integrating out the complex singlet can be probed to $S/\sqrt{B}$ values higher than even 40. In Fig. 7.11, we show the possible reach of the model parameters (λ_{HS}, g_{HS}) in the real singlet model, and $(\lambda_{HS} + \lambda'_{HS}/2, g_{HS})$ in the complex singlet model, given 30 ab^{-1} luminosity data set. One can see that, most of the region in the singlet and triplet models are within the 1σ uncertainty band for $S/\sqrt{B}$ reach for the SM, so that they are hard to differentiate from the SM.

The 2HDM, owing to its preservation of custodial symmetry, resides on the line $c_{HD} = 4c_{H\Box} = 0$ (up to the assumptions made in this paper, that is a tree-level dimension-six analysis). Therefore, the Higgs coupling measurements and the electroweak precision tests do not place strong constraints on the model parameters. On the other hand, the di-Higgs signature starts to provide a strong constraint on c_H. In Fig. 7.12 we show the significance contour on the model parameter Z_6 vs $\tan\beta$ plane for Type-I model and Type-II model with the 30 ab^{-1} luminosity. Note that when $Z_6 = 0$, the SM limit is recovered (see Table 7.3). We also find that in the Type-II model, for negative Z_6 and large $tan\beta$ (left top corner in the right plot in Fig. 7.12), the significance approaches to the SM value. This is because the decreasing of the Higgs to b quark coupling reduces the Higgs to b decay branching ratio, which ameliorate the increasing of the di-Higgs production rate.

In the real and complex triplet models, both c_{HD} and $c_{H\Box}$ in the EFTs obtained by integrating out real and complex triplet models are very tightly constrained as shown by the vertical dashed lines, shown in Fig. 7.9 (right panel). These vertical darker and lighter green lines represent the 3σ bounds allowed by the Higgs data global fit on the Wilson coefficient linear combination of $c_{HD} - 4c_{H\Box}$ for the real and complex triplet model respectively. The reason that these stringent bounds only exist for the triplets and not the singlets is that the coefficient c_{HD} is connected with custodial

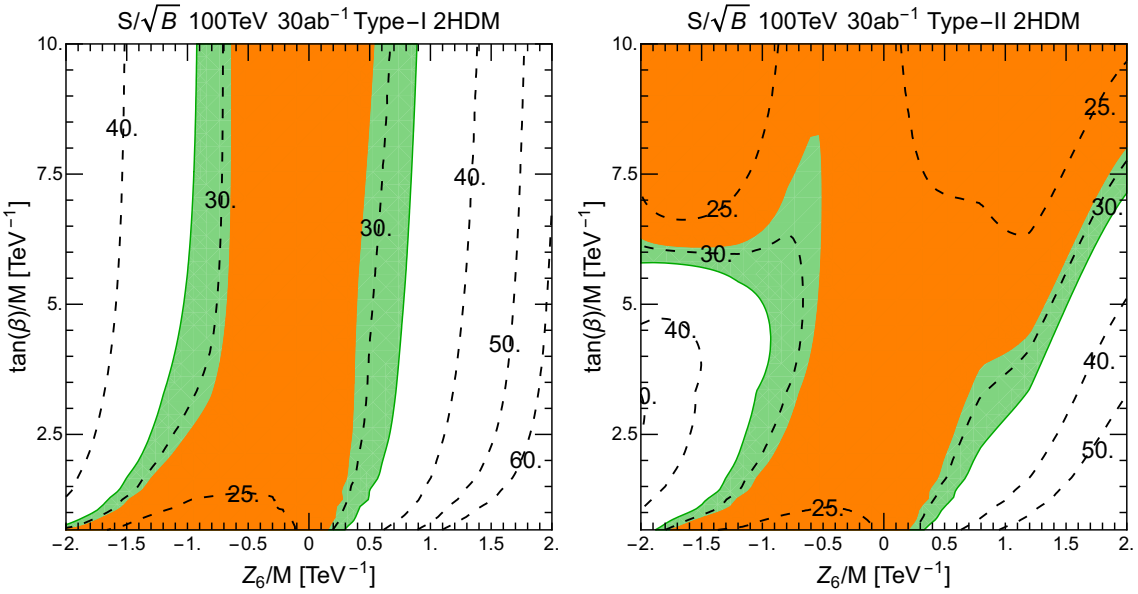

Figure 7.12: The discovery potential of the model parameters $(Z_6, \tan\beta)$ in the Type-I (left panel), Type-II (right panel) 2HDM. The contours correspond to the significance given integrated luminosity of 30 ab^{-1}. The orange and green regions are with in the SM 2σ uncertainty with assumption of the percentage uncertainty of di-Higgs production cross-section equal to 4% and 10% respectively.

symmetry breaking and is tightly constrained by the electroweak precision parameter T.

As Table 7.3 denotes, the c_{HD} and $c_{H\Box}$ are tightly related for the triplet models and therefore the stringent bounds on c_{HD} translate into stringent bounds on the $c_{HD} - 4c_{H\Box}$ as well. In the case of the singlet models, there are no couplings of the singlets to the gauge bosons resulting in c_{HD} being identically zero as indicated in Table 7.3, liberating them from these constraints suffered by the triplet models. As a result of these, c_H is also strongly constrained from the small allowed values of $c_{HD} - 4c_{H\Box}$, as shown in Fig. 7.9 (right panel). However, the dimensionless Higgs potential parameters, such as $\lambda_{H\Phi}$ and λ, are still very loosely constrained due to $c_H \sim \frac{g^2}{M^4}\lambda_{H\Phi}$. Therefore, it is very hard for us to extract the Higgs scalar couplings from the c_H operator, because the deviation of the Higgs coupling from the SM value is very small in the triplet case.

For the quadruplet model, at dimension-six, only the Wilson coefficient of Q_H operator is non zero. However, we include the c_{HD} generated by dimension 8 operator because it is strongly constraint by EWPD. In the left plot in Fig. 7.13, the allowed region for two types of quadruplet models are denoted by two lines with different slopes. The reason can be seen from Table. 7.3, the c_H and c_{HD} are correlated, all proportional to the coupling $|\lambda_{\Phi 3H}|^2$. So given a fixed cut off scale M, both $g^{(1)}_{HHH}$ and $g^{(2)}_{HHH}$ can be parameterized by a single parameter $|\lambda_{\Phi 3H}|^2$. In the right plot in Fig. 7.13, we find that the allowed parameter space from the global fit to EWPD for quadruplet models is tightly constrained, and almost becomes a point near the SM value. In Fig. 7.11, we show the significance of the model parameter $\lambda_{\Phi 3H}$ vs new physics scale M varies with the 30 ab^{-1} in contours, while the blue region is excluded by the constraint on c_{HD} from EWPD. One could observe that, the T-parameter constraint on $\lambda_{\phi 3H}$ is very sensitive to the cutoff scale, the reason is that the c_{HD} is

generated by dimension-eight operator so that it is proportional to the fourth power of (v/M).

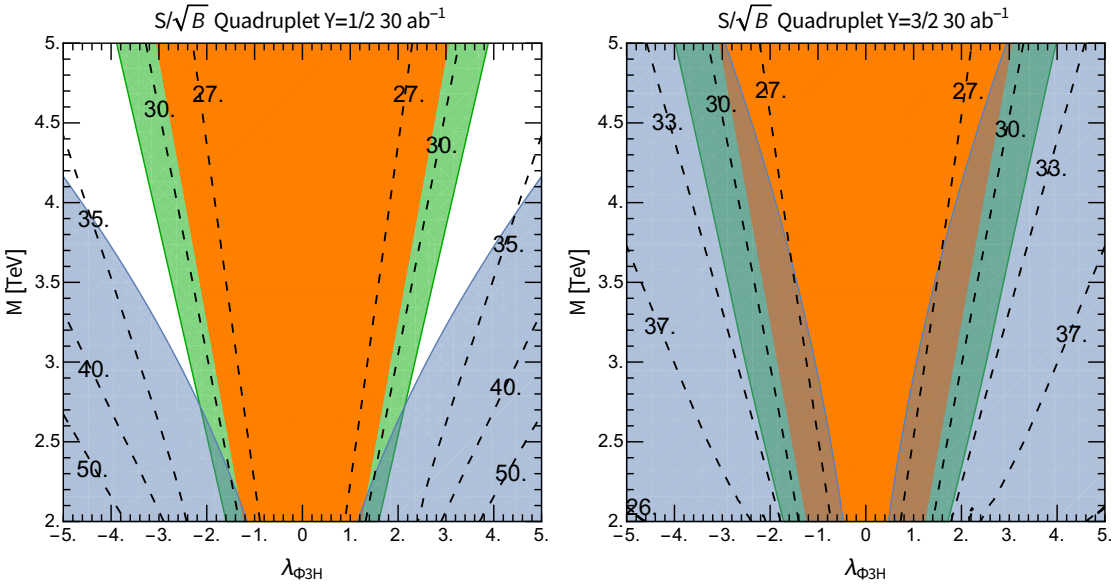

Figure 7.13: The discovery potential of the model parameters ($\lambda_{H3\Phi,M}$) in the quadruplet. The dashed black contours correspond to the $S/\sqrt{B}$ values for an integrated luminosity of 30 ab^{-1}. The blue region is excluded by constraints from the electroweak precision tests. The orange and green regions are within the SM 2σ uncertainty with an assumption of the percentage theoretical uncertainty of diHiggs production cross-section equal to 4% and 10% respectively.

Our collider analysis demonstrates that the potential of the 100 TeV collider in probing the Wilson coefficients resulting from the five scenarios considered here is very promising with the 2HDM. The singlet, triplet and quadruplet models on the other hand are restricted due to electroweak precision measurements and their effective coefficients will have less sensitivity. These restrictions also manifest in the constraints on the deviation of the triple Higgs couplings in such models owing to the direct relation between c_H and the triple and quadruplet Higgs coupling as shown in Eq. 7.30.

An interesting consequence of our analysis is that, due to the difference in the allowed region for each model under the theoretical bound and the global fit constraints,

it is possible to differentiate the 2HDM model from singlet, triplet and quadruplet models with the observation of a large deviation of the signal rate from the SM expectation. If a future experiment detects a significantly larger signal rate compared with the expected SM model value, then it should favor the presence of an extended scalar sector consisting of the 2HDM the assumptions of this work. If the future experiment does not detect a significant deviation from the SM expectation, then one may have hard time to differentiate SM from all the models considered here as well as models where the wilson coefficients are induced at loop level. Both a reduction in the theoretical uncertainty estimation and higher luminosities will be needed to make a more precise measurement of the di-Higgs signal rate.

CHAPTER 8

TESTING SEASAW MECHANISM IN LRSM WITH FUTURE COLLIDER

The minimal left-right symmetric model (mLRSM) has been proposed to connect the smallness of neutrino masses with the spontaneous violation of parity at high energy scale [232, 200, 201]. Within the mLRSM, both Dirac masses and Majorana masses can be generated for the heavy and light neutrinos through the Yukawa couplings with Higgs bi-doublet and triplets. It is already known that, the Majorana mass matrices for the light and heavy neutrino can be probed with the light neutrino oscillation experiments and the Keung-Senjanović (KS) process [171] in collider experiments respectively. Further, it is recently pointed out that [205, 233] if in addition the mixing between the light and heavy neutrinos are measured, then the Dirac mass matrix i.e. the Yukawa couplings between leptons and Higgs bi-doublet will be uniquely determined, which are directly related to the test of the Leptogensis in the LRSM [167]. It is worth to emphasize that without the left-right symmetry, there will be no such a connection between the masses and mixing of the neutrinos and the Dirac mass matrix. This can be seen in the Casas-Ibarra parametrization [56], where the Dirac mass matrix is given in terms of the heavy and light neutrino mass matices up to an arbitrary complex, orthogonal matrix. Therefore, measuring the light and heavy neutrino mixing will be crucial to veriy the LRSM as a complete model explaining the origin and smallness of neutrino masses.

Previously, the Dirac mass matrix of the light and heavy neutrino mixing is studied in Ref. [118, 150] by searching one right-handed charged lepton, one left-handed charged lepton and two jets in the final state in the collider experiments. In this work,

we proposed that the ideal channel for probing the Dirac mass matrix is through the purely leptonic decay of $W_R^{\pm} \to l^{\pm} N_1 \to l^{\pm}(N_1 \to l'^{\pm} W^{\mp} \to l^{\pm} l'^{\mp} \nu)$, where N_1 is the lightest heavy neutrino. This channel has been studied in the singlet fermion extension of the SM with Type-I seesaw mechanism in Ref. [164] and also has been searched for at the CMS experiment [236]. The advantage of this channel compare with the KS channel is that it does not need to analysis the handness of the leptons in the final state, the reconstruction of the W transverse mass from the charged lepton and the missing E_T automatically guarantees the heavy-light mixing in the heavy neutrino decay.

8.1 Theoretical Framework of LRSM

The gauge group structure in the LRSM is $\mathcal{G} = SU(2)_L \times SU(2)_R \times U(1)_{B-L}$, with an additional discrete symmetry that may be generalized as parity ($\mathcal{P}$) or charge conjugation ($\mathcal{C}$). The left-handed and right-handed quarks and leptons fields transform as $SU(2)_L$ and $SU(2)_R$ doublets respectively. The quantum numbers corresponding to the gauge groups $SU(2)_L$, $SU(2)_R$ and $U(1)_{B-L}$ are listed in the parenthesis next to the colons in the equations below:

$$q_L = \begin{pmatrix} u \\ d \end{pmatrix}_L : (2, 1, \frac{1}{3}), \quad q_R = \begin{pmatrix} u \\ d \end{pmatrix}_R : (1, 2, \frac{1}{3}),$$

$$L_L = \begin{pmatrix} \nu \\ l \end{pmatrix}_L : (2, 1, -1), \quad L_R = \begin{pmatrix} N \\ l \end{pmatrix}_R : (1, 2, -1), \tag{8.1}$$

where N represents the new heavy neutrino states

The Higgs sector of the mLRSM [198, 200], consists of one bi-doublet Φ, in the (2,2,0) representation of $\mathcal{G}$ and two scalar triplets Δ_L and Δ_R, belonging to (3,1,2) and (1,3,2) representation respectively

$$\Phi = \begin{pmatrix} \phi_1^0 & \phi_2^+ \\ \phi_1^- & \phi_2^0 \end{pmatrix}, \quad \Delta_{L,R} = \begin{pmatrix} \delta_{L,R}^+/\sqrt{2} & \delta_{L,R}^{++} \\ \delta_{L,R}^0 & -\delta_{L,R}^+/\sqrt{2} \end{pmatrix}. \tag{8.2}$$

The scalar potential is rather complicate which does not directly related to our analysis which can be found in Appendix.

After spontaneous symmetry breaking (SSB), the vevs of the scalar fields can be written as [201]

$$\langle \Phi \rangle = \begin{pmatrix} v_1 & 0 \\ 0 & -v_2 e^{-i\alpha} \end{pmatrix}. \tag{8.3}$$

$$\langle \Delta_R \rangle = \begin{pmatrix} 0 & 0 \\ v_R & 0 \end{pmatrix}, \quad \langle \Delta_L \rangle = \begin{pmatrix} 0 & 0 \\ v_L e^{i\theta_L} & 0 \end{pmatrix}, \tag{8.4}$$

where α and θ_L are called the "spontaneous" CP phases, and the magnitudes of the vevs have the following hierarchy $v_L \ll v_1^2 + v_2^2 \ll v_R^2$. All the physical effects due to θ_L, can be neglected, since this phase is always accompanied by the small v_L.

The Yukawa interactions in the lepton sector are:

$$\mathcal{L}_{L-\Phi} = \overline{L_L}(y_1\Phi + y_2\Phi^c)L_R + h.c. \tag{8.5}$$

$$\mathcal{L}_{L-\Delta} = -\frac{1}{2}y_{\Delta_L}\overline{(L_L)^c}\epsilon\Delta_L L_L - \frac{1}{2}\overline{(L_R)^c}\epsilon\Delta_R L_R + h.c., \tag{8.6}$$

where $\Phi^c = \epsilon\Phi^*\epsilon$ and ϵ is the 2-D total antisymmetric tensor.

Under the generalized Parity $\mathcal{P}$ symmetry and the generalized charge conjugation $\mathcal{C}$ symmetry, the transformation of the fields are:

$$\mathcal{P} : \{W_L, q_l, L_L, \Phi, \Delta_{L,R}\} \quad \leftrightarrow \quad \{-W_R^*, q_R, L_R, \Phi^\dagger, \Delta_{R,L}\} \tag{8.7}$$

$$\mathcal{C} : \{W_L, q_l, L_L, \Phi, \Delta_{L,R}\} \quad \leftrightarrow \quad \{-W_R^*, (q_R)^c, (L_R)^c, \Phi^T, \Delta_{R,L}^*\}. \tag{8.8}$$

The left-right symmetry impose the conditions on the $SU(2)$ gauge couplings g_L, g_R and Yukawa couplings $y_{1,2}$ and $y_{\Delta_{L,R}}$:

$$g_L = g_R = g, \tag{8.9}$$

$$\mathcal{P} : y_{1,2} = y_{1,2}^\dagger, \quad y_{\Delta_L} = y_{\Delta_R}, \tag{8.10}$$

$$\mathcal{C} : y_{1,2} = y_{1,2}^T, \quad y_{\Delta_L} = y_{\Delta_R}^*. \tag{8.11}$$

The neutrino mass matrix after SSB becomes:

$$\mathcal{L}_{\nu-N} = -\begin{pmatrix} \overline{(\nu_L)^c} & \overline{N_R} \end{pmatrix} \begin{pmatrix} M_L & M_D^T \\ M_D & M_R \end{pmatrix} \begin{pmatrix} \nu_L \\ (N_R)^c \end{pmatrix} + h.c. \, . \tag{8.12}$$

We define this mass matrix in gauge eigenstates as M_{ori}:

$$M_{ori} = \begin{pmatrix} M_L & M_D^T \\ M_D & M_R \end{pmatrix}, \tag{8.13}$$

with the entries expressed as:

$$M_L = y_{\Delta_L} v_l \quad M_R = y_{\Delta_R} v_R \quad M_D^\dagger = -(y_1 v_1 + y_2 v_2 e^{ia}). \tag{8.14}$$

Two steps are needed to diagonalize the mass matrix, in the first step we utilize the rotation matrix R to bring the 6×6 mass matrix to a block diagonal form:

$$\begin{pmatrix} 1 & -\Theta^T \\ \Theta^* & 1 \end{pmatrix} \begin{pmatrix} M_L & M_D^T \\ M_D & M_R \end{pmatrix} \begin{pmatrix} 1 & \Theta^\dagger \\ -\Theta & 1 \end{pmatrix} = \begin{pmatrix} M_\nu & 0 \\ 0 & M_N \end{pmatrix}, \tag{8.15}$$

with

$$R = \begin{pmatrix} 1 & -\Theta^T \\ \Theta^* & 1 \end{pmatrix}. \tag{8.16}$$

In the limit $v_L \ll v_R$, we have at leading order:

$$M_N \approx M_R \tag{8.17}$$

$$M_\nu = M_L - M_D^T M_N^{-1} M_D \tag{8.18}$$

$$\Theta^T \approx M_D^T M_N^{-1}. \tag{8.19}$$

With $\mathcal{C}$ as generalized parity, we have:

$$M_D = M_D^T \tag{8.20}$$

$$M_L = \epsilon M_R \approx \epsilon M_N \text{ with } \epsilon = \mathrm{v_L}/\mathrm{v_R} \tag{8.21}$$

$$\Theta = \sqrt{\epsilon - M_N^{-1} M_\nu}. \tag{8.22}$$

The next step is to bring M_ν and M_N to diagonal forms:

$$M_\nu = V_L^* m_\nu V_L^\dagger \tag{8.23}$$

$$M_N = V_R m_N V_R^T, \tag{8.24}$$

where $V_{L,R}$ are 3×3 unitary matrices, m_ν and m_N are diagonal matrices. Now we have:

$$M_{ori} = R^\dagger V \begin{pmatrix} m_\nu & 0 \\ 0 & m_N \end{pmatrix} V^T R^*, \tag{8.25}$$

with V a 6×6 matrix:

$$V = \begin{pmatrix} V_L^* & 0 \\ 0 & V_R \end{pmatrix}. \tag{8.26}$$

The mass eigenstates for the light and heavy neutrinos are denoted as: $\nu_{L,m}$ and $N^c_{R,m}$. Then we have relations between the gauge eigenstates and the mass eigenstates:

$$\begin{aligned}
\nu_L &= V_L \nu_{L,m} + \Theta^\dagger V^* - (N_{R,m})^c & (8.27)\\
N_R^c &= -\Theta V_L \nu_{L,m} + V_R^* (N_{R,m})^c & (8.28)\\
\overline{(\nu_L)^c} &= \overline{(\nu_{L,m})^c} V^T + \overline{N_{R,m}} V_R^\dagger \Theta^* & (8.29)\\
\overline{(N_R)} &= -\overline{(\nu_{L,m})^c} V^T \Theta^T + \overline{N_{R,m}} V_R^\dagger. & (8.30)
\end{aligned}$$

Now we can write down the charged current interaction in lepton sector:

$$\begin{aligned}
\overline{\nu_L} \gamma^\mu e_L W^+_{L,\mu} &= \left[\overline{\nu_{L,m}} \gamma^\mu (V_L^\dagger U_L^e) e_{L,m} + \overline{(N^c_{R,m})} \gamma^\mu (V_R^T \Theta U_L^e) e_{L,m} \right] W^+_{L,\mu} & (8.31)\\
\overline{N_R} \gamma^\mu e_R W^+_{R,\mu} &= \left[\overline{(N_{R,m})} \gamma^\mu (V_R^\dagger U_L^e) e_{R,m} - \overline{(\nu_{L,m})^c} \gamma^\mu (V_L^T \Theta^T U_R^e) e_{R,m} \right] W^+_{R,\mu}, & (8.32)
\end{aligned}$$

where $U^e_{L,R}$ are unitary matrices that diagonalize the charged lepton mass matrix, which can be set to identities by a change of flavor basis at the beginning. This leads

to the definition of the PMNS matrices for the right-handed and left-handed lepton sectors:

$$V^L_{PMNS} = V_L \tag{8.33}$$

$$V^R_{PMNS} = V_R. \tag{8.34}$$

In the following we will focus on the channel where a W_R is on-shell produced and then decays to a positron and the lightest heavy neutrino N_1, with N_1 decaying to a positron, a muon and a light neutrino. Symbolically, this process can be written as: $pp \to W_R \to e^+ N_1 \to e^+ e^+ \mu^- \nu$. We also assume that the mass of the W_R boson is much larger than the mass of the lightest heavy neutrino, i.e. $m_{N_1} \ll m_{W_R}$. This will ensure that the lightest heavy neutrino is on-shell produced.

The topologies of Feynman diagrams that are related to this process are list in Fig. 8.1, where the vertices with red dots contain the information of the heavy and light neutrino mixing, which are sensitive to the neutrino Dirac masses. The decays of N_1 through a off-shell W^*_R are shown in Fig. 8.1c and Fig. 8.1d, they are in general suppressed by $m^2_{N_1}/m^2_{W_R}$ comparing with the processes where N_1 decays through an on-shell W shown in Fig 8.1a and Fig 8.1b. This is the key point of our study, the purely leptonic decay of the heavy neutrino N_1 is dominated by the W boson mediated processes which naturally contain the information of the heavy-light mixing with the presence of $N_1 W l$ vertices, so no handness properties of the charged leptons needed to be further assessed.

In principle, for $m_{N_1} > m_W$, the diagram 8.1a and the diagram 8.1b can be distinguished by the relative P_T order of the muon and sub-leading positron and the reconstructed transverse mass of the sub-leading positron and missing ET system. However, we found in our study that for the mass range of m_{N_1} we are interested in (roughly $m_{N_1} < 500 GeV$), the power of this discriminant is not good enough to isolate either one of the contributions. For $m_{N_1} < m_W$, since the decay of the N_1 goes

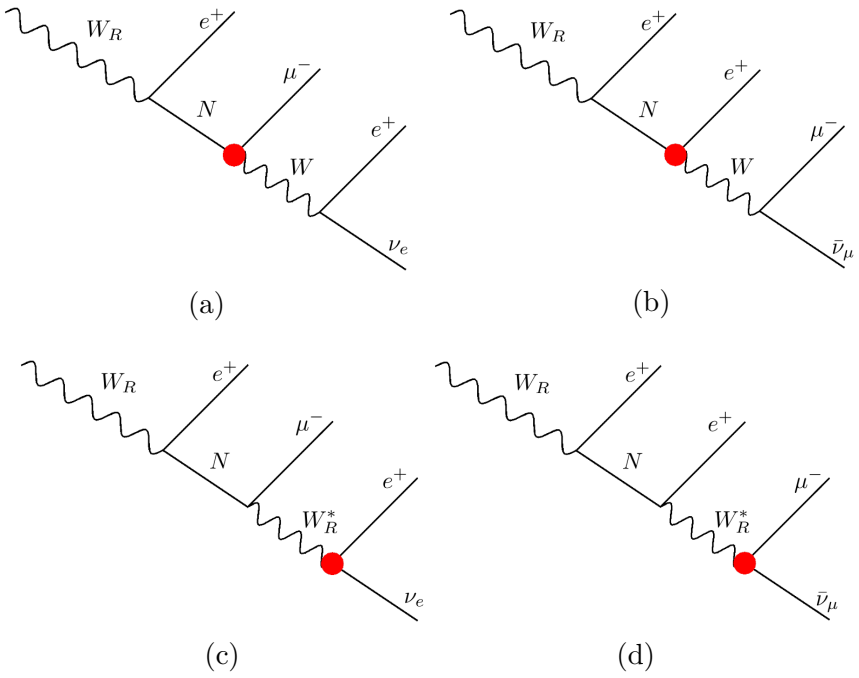

Figure 8.1: The topologies that can contribute to the $e^+e^+\mu^-\nu$ final state through a on-shell W_R decaying to e^+N_1. The red dots denote the vertices where the heavy and light neutrino mixings enter in.

through the off-shell W, essentially there is no such a single physical cut that can effectively distinguish the two diagrams. One way to extract the relative contributions of these two diagrams is proposed in Ref. [26], where the distribution of the angular observable θ, the polar angle formed by the momentum of the muon and the W_R momentum in the N_1 rest frame, is used.As pointed out in Ref. [26], the differential decay rates with respect to θ of the polarized heavy neutrino of the two different channels have the following forms:

$$\frac{d\Gamma}{d\cos\theta}(N_{1,pol} \to \mu^-(W^+ \to e^+\nu_e)) \sim |(V_R)_{N\mu}|^2\Big\{1 + A\left(x_{N_1}\right)\cos\theta\Big\} \tag{8.35}$$

and

$$\frac{d\Gamma}{d\cos\theta}(N_{1,pol} \to e^+(W^- \to \mu^-\bar{\nu}_\mu)) \sim |(V_R)_{Ne}|^2\Big\{1 - \cos\theta\Big\}, \tag{8.36}$$

where $x_{N_1} \equiv m_{N_1}/M_{W_R}$ and $A\left(x_{N_1}\right)$ is calculated in Ref. [26] and $A(x_{N_1}) = 0$ for $x_{N_1} \geq 1$. In practice, one can fit with this distribution to extract the mixing parameters for the two diagrams.

Now one can calculate the decay width of heavy neutrinos into three leptons $\Gamma(N_1 \to l^\pm l'^\mp \nu)$, which is proportional to the heavy-light mixing as one can see from Eq. 8.37. As I mentioned earlier, we assume the ratio of the vev of two triplet ϵ =0.

$$\Gamma(N_1 \to l^\pm l'^\mp \nu) = (|\Theta_{l'N_1}|^2 + |\Theta_{lN_1}|^2)\frac{G_F^2}{96\pi^4 m_N}\int_0^{m_{N_1}^2} dx \frac{\pi}{m_{N_1}^2}\frac{(m_{N_1}^2 - x)(m_{N_1}^4 + x m_{N_1}^2 - 2x^2)}{(1 - \frac{x}{M_W^2})^2 + \frac{\Gamma_W^2}{M_W^2}}, \tag{8.37}$$

One can found the branching ratio in the Fig. 8.2 for different mass of m_{W_R} and the lightest heavy neutrino mass m_{N_1}. From the Fig. 8.2, one can found that for a fixed mass of the lightest heavy neutrino m_N, the branching ratio $\mathrm{Br(N_1 \to \mu^- e^+ \nu)}$ is increasing. This is because the decay channel $N_1 \to ljj$ through the off shell W_R is suppressed. The increase of the branching ratio around the m_W is due to the on-shell production of W_L. The sharp drop around top mass is due to the opening of

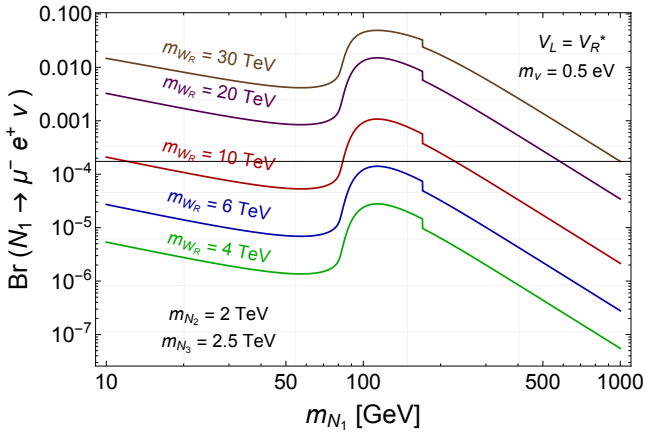

Figure 8.2: Branching ratio of the purely leptonic decays of the heavy neutrino N.

the channel $N_1 \to ltb$. The further decrease as m_{N_1} increase is because the decay channel $N_1 \to \mu^- e^+ \nu$ is suppressed by decreasing mixing couping Θ as one can see from Eq. 8.22.

8.2 Collider Analysis

As mentioned above, it is hard to distinguish the two processes with the same final state in the mass range of the lightest heavy neutrino N_1 we are interested in. Therefore, we will first derive the sensitivity bounds on the decay branching ratio $\mathrm{Br}(\mathrm{N}_1 \to \mu^- \mathrm{e}^+ \nu)$ and then translate them into the bound on the mixing parameters $|\Theta_{l' N_1}|$ and $|\Theta_{l N_1}|$.

For the signal generation, we use the extension of the FeynRules package [21] for the minimal LR model used in Ref. [226] and expanded in Ref. [207]. The signal and background events were generated at the LO using Madgraph 5 [24], Pythia 6 [237] for hadronization and Delphes 3 [92] for detector simulation, using the JetFake module developed in [207]. The dominant sources of background are found to be $\bar{t}W(j)$, $t\bar{t}(j)$ and $WWW(j)$, while $ZW(j)$, $t\bar{t}Z$ and eej with jet fake to muon to be sub-dominant. The j in the parenthesis means we generate the corresponding background with one jet matching. Table. 8.2 show the the cut flow of the main sources of background for this process, together with two benchmark points, for 100 TeV respectively. In what follows we also assume the left and right leptonic mixing matrices are connected with the relation $V_L = V_R^*$. The backgrounds for this process were studied in Ref. [164]. Finally, a description of the selection criteria is shown in table 8.1. We first demand the event contains exactly 2 positron, 1 muon and no b tagged jet. The event with extra jets that are not b tagged are retained. Secondly, we select events with High PT leptons and a large missing ET, this will cut a lot of background even in 100TeV collider. Then we require that the reconstructed invariant mass of the positron pair is not closed to the Z boson mass. This will reduce the background that the positron pair comes from the Z decay with the electron charged flipped. We also enforce that the reconstructed transverse mass of sub-leading positron and $\not{E}_T$ is less than 150 GeV. This cut ensures that the sub-leading positron is coming from the W boson

decay. Finally we require the transverse mass of the $e^+e^+\mu^-\not{E}_T$ system is larger than the half mass of the right-handed W_R.

Cut description	
$e^+e^+\mu^-$, no b jets and no additional leptons	signal selection
$P^{lead}_{T,e^+} > 200$ GeV, $P^{sub}_{T,e^+} > 100$ GeV, $P^{lead}_{T,\mu^-} > 100$ GeV	reduce all backgrounds
$\not{E}_T > 100$ GeV	reduce mostly $t\bar{t}j$ and eej
$\lvert m_{inv}(e^+e^+ - 91.2\rvert) < 10$ GeV	reduce mostly WZj
$m_T(e^+_{sub}\not{E}_T) < 150$ GeV	reduce all backgrounds except $ZW(j)$
$m_T(e^+e^+\mu^-\not{E}_T) > M_{W_R}/2$	reduce all backgrounds

Table 8.1: Selection criteria used to reduced the SM background for 100 TeV. For 13 TeV and 28 TeV we apply the same cuts, excepting that $P^{lead}_{T,e^+} > 100$ GeV.

We first require that the event contains two positron and one muon (we also require the number of the additional jets not exceed two). Secondly, we require the leading positron has $P_T > 200$ GeV, and subleading positron and muon have $P_T > 100$ GeV. Then a missing ET cut is applied to reduce eej background, a mass window cut on the positron pair is applied to ensure that one of the positron is not coming from the charge conversion from the Z boson decay. A cut on the transverse mass of subleading positron and missing ET system is applied to ensure that the subleading positron is coming from the decay of a on-shell W boson, which reduces the $t\bar{t}$ background and reduce the contamination from the decay of heavy neutrino through an off-shell W_R. Finally, a cut on the transverse mass of the system of $e^+e^+\mu^-\not{E}_T$ is applied to ensure decay produce is coming from the high invariant mass region which reduces all kinds of SM backgrounds. In the estimation of the SM background we take the probability of the charge misidentification of electron as a function of pt and eta taking from the current ATLAS results [7], while for muon we assume the charge misidentification rate is zero. For the jet fake to electron and muon rate we take them equal to 10^{-4} as indicated in Ref. [59, 86].

In Fig. 8.3, we show for $m_{W_R} = 6$ TeV that the purely leptonic signal can be discovered(excluded) with $5\sigma(2\sigma)$ sensitivity for heavy neutrino masses below 170

	Backgrounds					
$\sqrt{s}$ =100TeV	$t\bar{t}Z^{(*)}$	$t\bar{t}W^{(*)}(j)$	$t\bar{t}(j)$	$WZ(j)$	$3W(j)$	eej
$N_{e^+} = 2$ $N_{\mu^-} = 1$ $N_b = 0$	199	1114	1178	8645	735	1128
P_T cuts	18.7	387	226	2350	254	244
$\not{E}_T > 100$ GeV	12.6	312	138	1140	165	18.7
$m_{inv}(e^+\ e^+)$cuts	12.1	311	136	122	164	5.19
$m_T(e^+_{sub}\ \not{E}_T) < 150$ GeV	4.42	116	65.1	22	85.9	0.344
$m_{inv}(e^+e^+\mu^-\not{E}_T) > 3$ TeV	0.126	7.60	5.82	0.336	9.72	2.75×10^{-2}
$m_{inv}(e^+e^+\mu^-\not{E}_T) > 5$ TeV	0	0.918	1.11	0	1.94	0
$m_{inv}(e^+e^+\mu^-\not{E}_T) > 10$ TeV	0	2.62×10^{-2}	6.16×10^{-2}	0	8.05×10^{-2}	0

Table 8.2: SM background processes at 100 TeV and 30 ab^{-1} for the trilepton signal $e^+e^+\mu^-\nu$ and $m_{W_R} = 6$ TeV, for two benchmark values of the heavy Neutrino masses. Backgrounds ending with the parenthesis j represent that we did the plus one jet matching in the simulation. The charge misidentification probability has been taken from current ATLAS result from Ref. [7]. The jet to lepton fake rates for $ttbar(j)$ and eej have been taken as 10^{-4} universally. The NLO K-factor for backgrounds are taken from Ref. [193]

M_{N_1}[GeV]	1000	500	100
$e^+e^+\mu^-\nu$	0.364	0.349	0.319
P_T	0.273	0.241	0.234
$\not{E}_T$	0.239	0.196	0.199
$m_{inv}(e^+e^+)$	0.239	0.196	0.199
$m_T(e^+_{sub}\not{E}_T)$	0.223	0.188	0.189
$m_T(e^+e^+\mu^-\not{E}_T)$	0.217	0.185	0.187

Table 8.3: signal efficiency for 100TeV collider with $m_{W_R} = 6$ TeV for different mass of the lightest heavy neutrino. The charge misidentification rate for electron is take from [7].

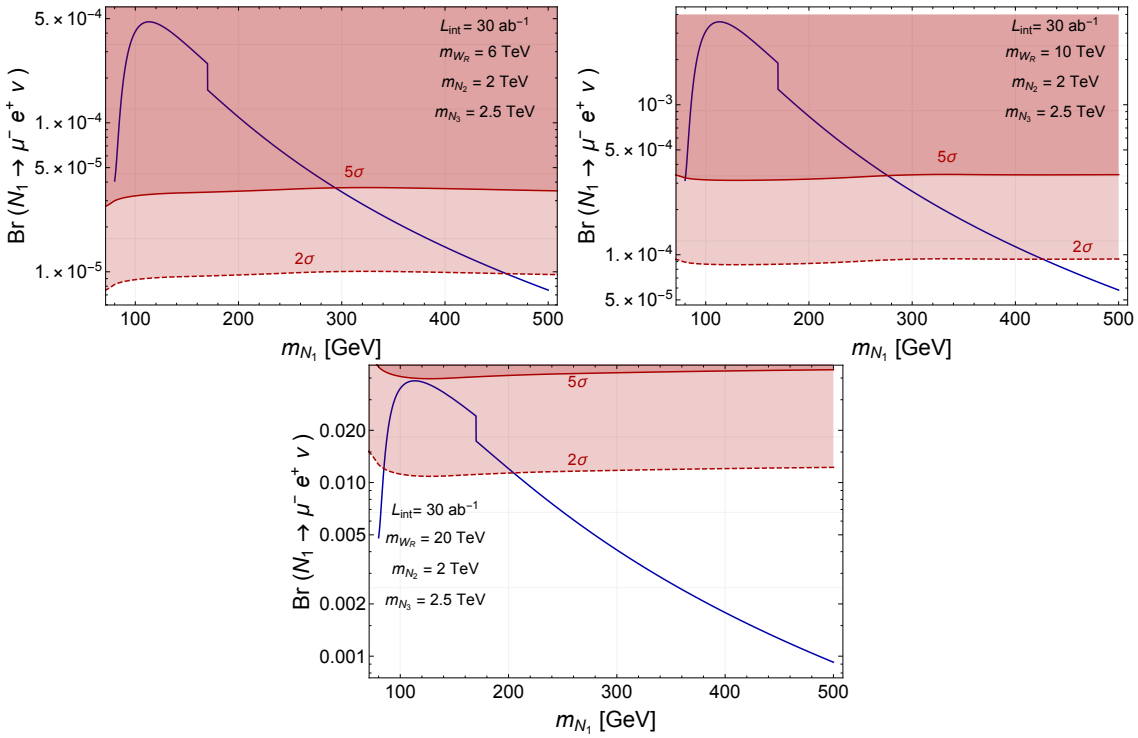

Figure 8.3: FCC reach to the branching ratio of the purely leptonic decays of the heavy neutrino. The blue line denotes the branching ration within the mLRSM and the shadowed thick(dashed) regions show the reach at $5\sigma(2\sigma)$, for an integrated luminosity of $L_{int} = 30\text{ab}^{-1}$ and center of mass energy $\sqrt{s} = 100$ TeV.

GeV(220 GeV). This result shows that there exist the possibility of discovering the W_R boson at the LHC [206] and probing HN mass generation at the next generation of hadronic colliders. For $m_{W_R} = 10$ TeV the purely leptonic signal can be discovered(excluded) with $5\sigma(2\sigma)$ sensitivity for heavy neutrino masses below 300 GeV(460 GeV). Instead the upper limit on the m_{W_R} mass for the 2σ exclusion limit is around $m_{W_R} = 20$ TeV.

In the left plot of Fig. 8.4, we have translated the 2σ bound from the 100 TeV collider to the upper bound on the combined value of $|\Theta_{l'N_1}|^2 + |\Theta_{lN_1}|^2$ for $m_{W_R} = 6$ TeV, $m_{N_2} = 2$ TeV and $m_{N_3} = 2.5$ TeV. One can observe that If both $|\Theta_{l'N_1}|$ and $|\Theta_{lN_1}|$ are in the same scale, a bound around $\sim 10^{-12}$ on those two quantities can be derived can be derived on these two quantities. This can be further translate in to bound on the neutrino Dirac masses $(M_D)_{N_1 e}$ and $(M_D)_{N_1 \mu}$ as shown in the right plot of Fig. 8.4, where we fixed the value $|\Theta_{l'N_1}|^2 = |\Theta_{lN_1}|^2 = 10^{-12}$.

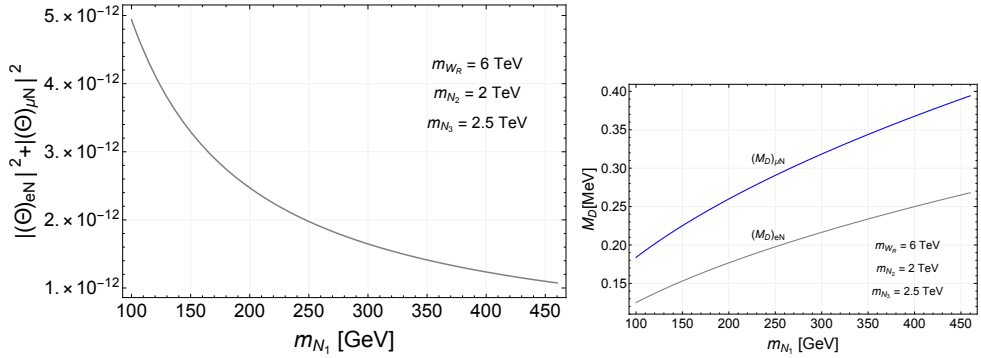

Figure 8.4: Smallest value for the heavy-light mixing angle Θ and the Dirac Mass $(MD)_{\mu e}$ as a function of the heavy neutrino mass, for $m_{W_R} = 6$ TeV at 2σ.

CONCLUSION

The Standard Model, though successful, has shortcomings in explaining various phenomena in nature. The matter anti-matter asymmetry, the non-zero neutrino masses are two puzzles that indicate the existence of new physics beyond the SM. Future colliders are great machines to scrutinize the proposed new physics models trying to solve these two puzzles.

The CPV is a requirement for a successful EWBG to explain the matter-antimatter asymmetry. The 2HDMs are possible to provide a new CP violation source at tree level and can be tested in both of pp collider and EDM experiments. My study demonstrates that the combination of the future LHC and EDM results will be complementary to each other and will provide a better examination of the CPV2HDMs.

Apart from the CPV, a SFOEWPT is also necessary for a successful EWBG. The singlet extended SM (xSM) provides the most simple scenario to modify the scalar potential and to make the EWPT strong and first-order in the early universe. The correlation between the SFOEWPT and the enhancement of the coupling of the heavy Higgs to the SM-like Higgs pair indicates an excellent opportunity to test the xSM triggered SFOEWPT by searching a heavy Higgs decaying to two SM-like Higgs particles. In my study, I point out that, the 4b final state of the di-Higgs channel, despite substantial SM backgrounds, is a great channel to search for the resonant di-Higgs signal.

In the case where the scale of the new physics is high, one may implement the EFT to parametrize the deviation from the SM in a systematic way. In addition to the precision measurements related to the single Higgs production, the precision

measurement of the di-Higgs signature in the future 100 TeV collider will offer a new possibility to look for the new physics in the scalar sector. In this thesis, I study the potential to probe the modification of the trilinear Higgs couplings originated from the scalar extensions that can generate the dimension six operator $(H^\dagger H)^3$ at tree level, and show that the theoretical uncertainties related to the di-Higgs production cross-section will be critical to distinguish the new physics from the SM.

Regarding the origin of the neutrino masses, the LRSM provided a natural way to relate the smallness of the light to the high scale parity violation in the electroweak sector. In this thesis, I study the reach of the future 100 TeV collider in measuring the neutrino Yukawa couplings using the purely leptonic decay of heavy neutrinos and show that this can be compatible with the traditional semi-leptonic searches.

The road to the new physics is dim. I believe the development of the future technology and the wisdom of our physicist will shed light on the darkness of this road.

APPENDIX A

DISTRIBUTIONS OF KINEMATIC VARIABLES USED IN BDT AND FORMULAE OF HIGGS DECAYS IN THE STUDY OF CPV2HDM

A.1 Distributions of BDT Input Variables

We demonstrate the distributions of BDT input variables after our primary cuts described in Sec. 5.3.2

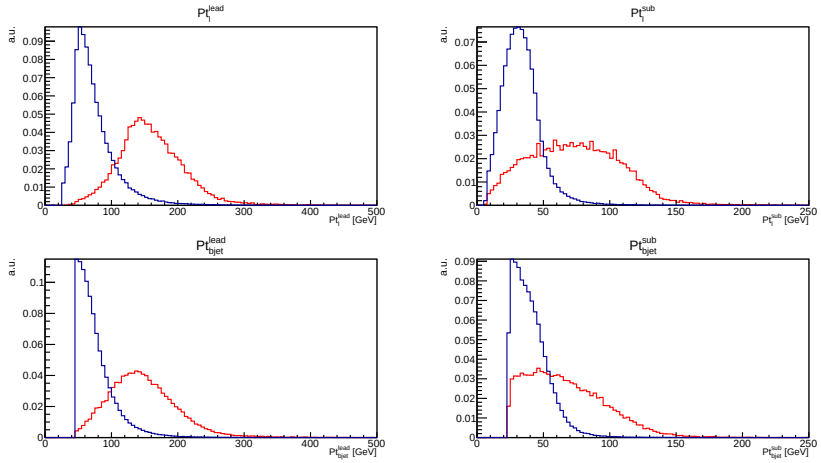

Figure A.1: Plots indicated by their titles showing the distributions of the lepton leading p_T, lepton subleading p_T, b-jet leading p_T, and b-jet subleading p_T, respectively. The units of the horizontal axes are GeV. The red histogram is for signal with heavy Higgs mass 550 GeV, and the blue histogram is for the combined background.

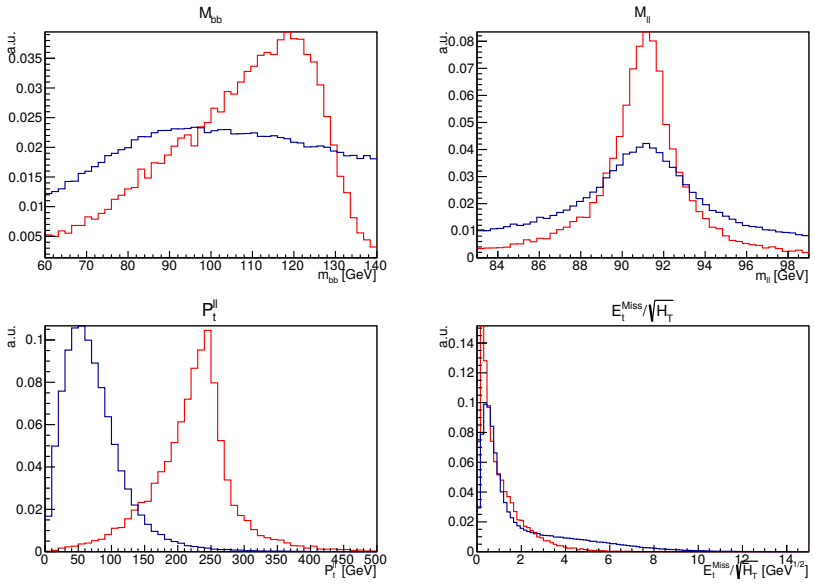

Figure A.2: Plots indicated by their titles showing the distributions of the reconstructed invariant mass for dijet system m_{bb}, reconstructed invariant mass for dilepton system m_{ll}, $E_T^{miss}/\sqrt{H_T}$, and reconstructed transverse momentum for Z boson p_T^Z, respectively. The units of the horizontal axes are GeV for m_{bb}, m_{ll}, p_T^Z, and GeV$^{1/2}$ for $E_T^{miss}/\sqrt{H_T}$. The red histogram is for the signal with heavy Higgs mass 550 GeV, and the blue histogram is for the combined background.

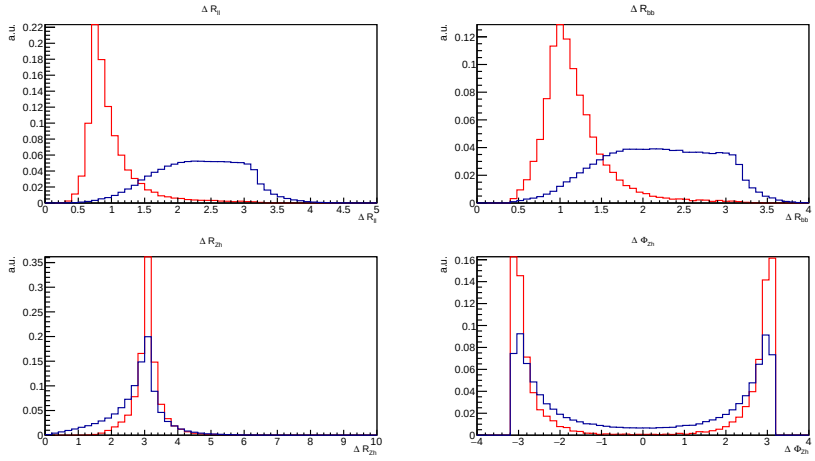

Figure A.3: Plots indicated by their titles showing the distributions of ΔR_{ll}, ΔR_{jj}, ΔR_{Zh} and $\Delta\Phi_{Zh}$, respectively. The red histogram is for signal with heavy Higgs mass 550 GeV, and the blue histogram is for the combined background.

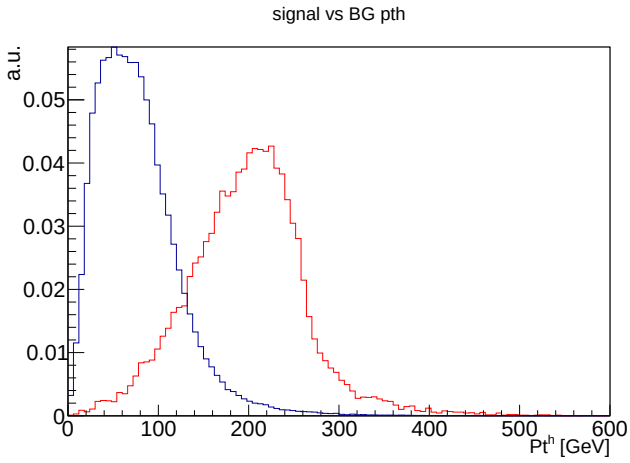

Figure A.4: Reconstructed transverse momentum for Higgs p_t^h, the unit of the horizontal axis is GeV. The red histogram is for signal with heavy Higgs mass 550 GeV; the blue histogram is for the combined background.

A.2 Analytical Formulas for Higgs Tow Body Decays

Higgs two body decay rates are listed in the following,

- $h_i \to gg$, heavy Higgs decays to two gluons

$$\Gamma(h_i \to gg) = \frac{\alpha_s^2 G_F m_{h_i}^3}{64\sqrt{2}\pi^3} \left[\left| c_{t,i} F_{1/2}^H(\tau_t^i) + c_{b,i} F_{1/2}^H(\tau_b^i) \right|^2 + \left| \tilde{c}_{t,i} F_{1/2}^A(\tau_t^i) + \tilde{c}_b^i F_{1/2}^A(\tau_b^i) \right|^2 \right] . \quad \text{(A.1)}$$

where the functions $F_{1/2}^H$ and $F_{1/2}^A$ and the variable τ_f^i are defined in Eqs. 5.33 to 5.34.

- $h_i \to Z h_1$, heavy Higgs decays to Z boson and SM-like Higgs

$$\begin{aligned} \Gamma(h_i \to Z h_1) &= \frac{|g_{iz1}|^2}{16\pi m_{h_i}^3} \sqrt{\left(m_{h_i}^2 - (m_{h_1} + M_Z)^2\right)\left(m_{h_i}^2 - (m_{h_1} - M_Z)^2\right)} \\ &\quad \times \left[-(2m_{h_i}^2 + 2m_{h_1}^2 - M_Z^2) + \frac{1}{M_Z^2}(m_{h_i}^2 - m_{h_1}^2)^2 \right] , \quad \text{(A.2)} \end{aligned}$$

where g_{iz1} is defined in Eq. (5.28).

- $h_i \to VV$, heavy Higgs decays to two vector bosons

$$\Gamma(h_i \to VV) = (a_i)^2 \frac{G_F m_{h_i}^3}{16\sqrt{2}\pi} \delta_V \left(1 - \frac{4M_V^2}{m_{h_i}^2}\right)^{1/2} \left[1 - \frac{4M_V^2}{m_{h_i}^2} + \frac{3}{4}\left(\frac{4M_V^2}{m_{h_i}^2}\right)^2\right] \quad \text{(A.3)}$$

where $V = W, Z$ and $\delta_Z = 1, \delta_W = 2$, $i = 2, 3$.

- $h_i \to f\bar{f}$, heavy Higgs decays to a fermion pair

$$\Gamma(h_i \to \bar{f}f) = \left[(c_{f,i})^2 + (\tilde{c}_{f,i})^2\right] \frac{N_c G_F m_f^2 m_{h_i}}{4\sqrt{2}\pi} \left(1 - \frac{4m_f^2}{m_{h_i}^2}\right)^{3/2} , \quad \text{(A.4)}$$

where $N_c = 3$ for quarks, $N_c = 1$ for leptons.

- $h_i \to h_1 h_1$ heavy Higgs decays to a pair of SM Higgs

$$\Gamma(h_i \to h_1 h_1) = \frac{g_{i11}^2 v^2}{8\pi m_{h_i}} \sqrt{1 - \frac{4m_{h_1}^2}{m_{h_i}^2}} , \quad \text{(A.5)}$$

where g_{i11} is defined by

$$g_{i11} = \frac{\partial^3 V}{\partial h_i \partial h_1 \partial h_1} \, |_{H^\pm, h_i = 0} \quad . \quad \text{(A.6)}$$

APPENDIX B

DISTRIBUTIONS OF KINEMATIC VARIABLES USED IN BDT IN THE STUDY OF SINGLET EXTENDED STANDARD MODEL

B.1 Distribution used in di-Higgs 4b BDT analysis

We plot the signal and background distributions of kinematic variables used in BDT analysis here:

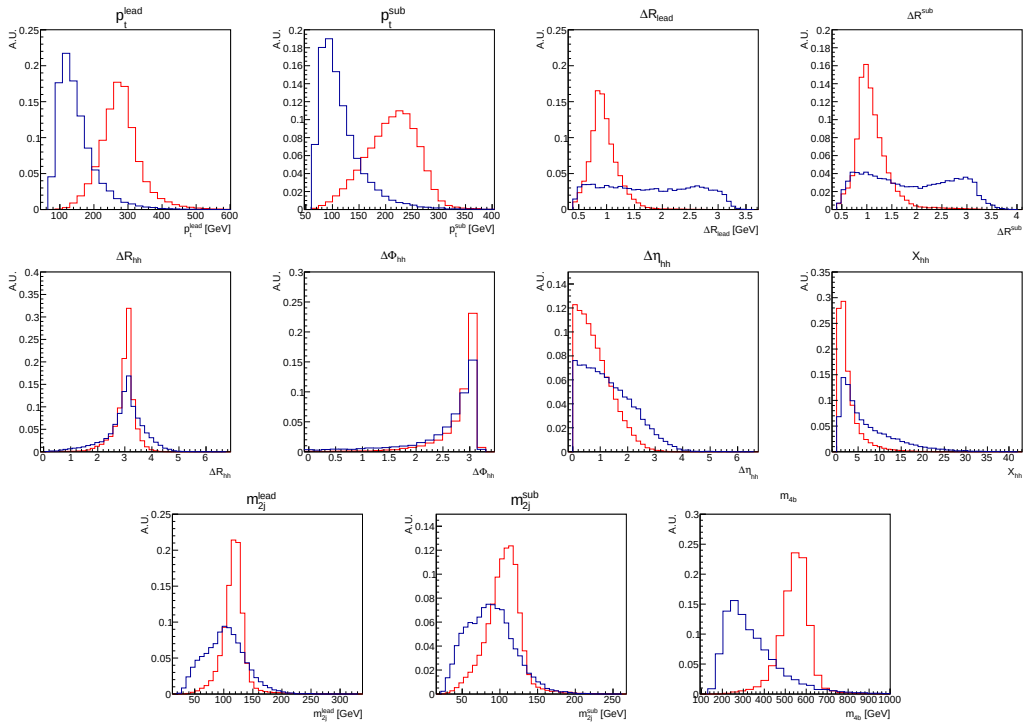

Figure B.1: Distributions of the kinematic variables used in training BDT, the red line represents signal distribution, the blue line represents the background distribution.

APPENDIX C

DERIVATIONS OF EFT FOR EACH EXTENDED SCALAR SECTOR

C.1 Real Singlet

Taking the Lagrangian with normalizations such that the EOM are nicely normalized:

$$\Delta\mathcal{L} = \frac{1}{2}(\partial^\mu S)(\partial_\mu S) - \frac{M_S^2}{2}S^2 - \frac{g}{3}S^3 - g_{HS}|H|^2 S - \frac{\lambda_S}{4}S^4 - \frac{\lambda_{HS}}{2}|H|^2 S^2 \tag{C.1}$$

The classical EOM are:

$$\Box S = -M_S^2 S - gS^2 - g_{HS}|H|^2 - \lambda_S S^3 - \lambda_{HS}|H|^2 S \tag{C.2}$$

Linearizing the EOM in S and solving for "S_c" as defined by Murayama [151] we find,

$$S_c = -\frac{1}{\Box + M_S^2 + \lambda_{HS}|H|^2} g_{HS}|H|^2 \tag{C.3}$$

For M_S sufficiently larger than the momenta ($\Box$) and the excitations of the field H this gives the approximation,

$$\begin{aligned} S_c &= -\frac{g_{HS}}{M_S^2}|H|^2 + \frac{\Box + \lambda_{HS}|H|^2}{M_S^4} g_{HS}|H|^2 + \cdots \\ &= -\frac{g_{HS}}{M_S^2}|H|^2 + \frac{\lambda_{HS} g_{HS}}{M_S^4}|H|^4 + \frac{g_{HS}}{M_S^4}\Box|H|^2 + \cdots \end{aligned} \tag{C.4}$$

Plugging this expression into $\Delta\mathcal{L}$, Eq. C.1,

$$\begin{aligned}
\Delta\mathcal{L} \;\rightarrow\; & \frac{g_{HS}^2}{2M_S^4}\partial^\mu|H|^2\partial_\mu|H|^2 \\
& -\frac{g_{HS}^2}{2M_S^2}|H|^4+\frac{\lambda_{HS}g_{HS}^2}{M_S^4}|H|^6+\frac{g_{HS}^2}{M_S^4}|H|^2\Box|H|^2 \\
& +\frac{gg_{HS}^3}{3M_S^6}|H|^6 \\
& +\frac{g_{HS}^2}{M_S^2}|H|^4-\frac{\lambda_{HS}g_{HS}^2}{M_S^4}|H|^6-\frac{g_{HS}^2}{M_S^4}|H|^2\Box|H|^2 \\
& -\frac{\lambda_{HS}g_{HS}^2}{2M_S^4}|H|^6 \\
= \;& \frac{g_{HS}^2}{2M_S^2}|H|^4-\frac{(3\lambda_{HS}M_S^2-2gg_{HS})g_{HS}^2}{6M_S^6}|H|^6+\frac{g_{HS}^2}{2M_S^4}\partial^\mu|H|^2\partial_\mu|H|^2 \\
= \;& \frac{g_{HS}^2}{2M_S^2}|H|^4-\frac{(3\lambda_{HS}M_S^2-2gg_{HS})g_{HS}^2}{6M_S^6}Q_H-\frac{g_{HS}^2}{2M_S^4}Q_{H\Box} \qquad \text{(C.5)}
\end{aligned}$$

C.2 Complex Singlet

Taking the Lagrangian with *the same normalizations as in the real case*, but standard normalization for the kinetic terms:

$$\begin{aligned}
\Delta\mathcal{L} \;=\; & (\partial^\mu\Phi)^\dagger(\partial_\mu\Phi)-M^2|\Phi|^2-\frac{(M')^2}{2}\left(\Phi^2+h.c.\right) \\
& -\left(g_{HS}|H|^2\Phi+h.c.\right)-\left(\frac{g}{3}\Phi^3+h.c.\right)-\left(\frac{g'}{3}\Phi(\Phi^\dagger)^2+h.c.\right) \\
& -\left(\frac{\lambda_{H\Phi}}{2}|H|^2\Phi^2+h.c.\right)-\frac{\lambda'_{H\Phi}}{2}|H|^2|\Phi|^2-\left(\frac{\lambda}{4}\Phi^4+h.c.\right)-\frac{\lambda'}{4}|\Phi|^4-\left(\frac{\lambda_1}{4}\Phi(\Phi^\dagger)^3+h.c.\right) \qquad \text{(C.6)}
\end{aligned}$$

The classical EOM are:

$$
\begin{aligned}
\Box\Phi &= -M^2\Phi - (M')^2\Phi^\dagger - g^*_{HS}|H|^2 - g^*(\Phi^\dagger)^2 - \frac{2g'}{3}\Phi\Phi^\dagger - \frac{(g')^*}{3}\Phi^2 \\
&\quad -\lambda^*_{H\Phi}|H|^2\Phi^\dagger - \frac{\lambda'_{H\Phi}}{2}|H|^2\Phi - \lambda^*(\Phi^\dagger)^3 - \frac{\lambda'}{2}|\Phi|^2\Phi - \frac{3\lambda_1}{4}\Phi(\Phi^\dagger)^2 - \frac{\lambda^*_1}{4}\Phi^3 \\
\Box\Phi^\dagger &= -M^2\Phi^\dagger - (M')^2\Phi - g_{HS}|H|^2 - g\Phi^2 - \frac{g'}{3}(\Phi^\dagger)^2 + \frac{2(g')^*}{3}\Phi\Phi^\dagger \\
&\quad -\lambda_{H\Phi}|H|^2\Phi - \frac{\lambda'_{H\Phi}}{2}|H|^2\Phi^\dagger - \lambda\Phi^3 - \frac{\lambda'}{2}|\Phi|^2\Phi^\dagger - \frac{\lambda_1}{4}(\Phi^\dagger)^3 - \frac{3\lambda_1}{4}\Phi^\dagger\Phi^2
\end{aligned}
\tag{C.7}
$$

Linearizing the EOM,

$$
\left(\Box + M^2 + \frac{\lambda'_{H\Phi}}{2}|H|^2\right)\Phi^\dagger = -(M')^2\Phi - g_{HS}|H|^2 - \lambda_{H\Phi}|H|^2\Phi \tag{C.8}
$$

Solving for $\Phi^\dagger$ and taking the series to dimension–4 in fields/derivatives,

$$
\begin{aligned}
\Phi^\dagger_c &\sim \frac{1}{\Box + M^2 + \frac{\lambda'_{H\Phi}}{2}|H|^2}\left[-(M')^2\Phi - g_{H\Phi}|H|^2 - \lambda_{H\Phi}|H|^2\Phi\right] \\
&\sim \frac{(M')^2}{M^4}\Box\Phi - \frac{(M')^2}{M^2}\Phi - \frac{\lambda_{HS}}{M^2}|H|^2\Phi + \frac{\lambda'_{HS}(M')^2}{2M^4}|H|^2\Phi \\
&+ \frac{g_{HS}}{M^4}\Box|H|^2 - \frac{g_{HS}}{M^2}|H|^2 + \frac{g_{HS}\lambda'_{HS}}{2M^4}|H|^4 + \cdots
\end{aligned}
\tag{C.9}
$$

Plugging into the EOM for Φ yields,

$$
\begin{aligned}
\left[\left(1 - \tfrac{(M')^2}{M^4}\right)\Box\right. &+ \left.\left(M^2 + \tfrac{(M')^2}{M^2} + \tfrac{\lambda_{HS}}{M^2}|H|^2 + \tfrac{\lambda'_{HS}(M')^2}{2M^4}|H|^2\right)\right]\Phi \\
&= -\tfrac{g_{HS}(M')^2}{M^4}\Box|H|^2 + \tfrac{g_{HS}(M')^2}{M^2}|H|^2 - g^*_{HS}|H|^2 + \tfrac{g_{HS}\lambda^*_{HS}}{M^2}|H|^4
\end{aligned}
\tag{C.10}
$$

Solving for Φ_c to operator dimension–4,

$$
\begin{aligned}
\Phi_c &= -\frac{1}{M^2}\left(g^*_{HS} - \frac{g_{HS}(M')^2}{M^2} + \frac{g^*_{HS}(M')^4}{M^4} + \cdots\right)|H|^2 \\
&\quad + \frac{1}{2M^4}\left(g_{HS}\lambda^*_{HS} + \lambda'_{HS}g^*_{HS} - (g_{HS}\lambda'_{HS} - g^*_{HS}\lambda'_{HS} + g^*_{HS}\lambda^*_{HS})\frac{(M')^2}{M^2} + \cdots\right)|H|^4 \\
&\quad + \frac{1}{M^4}\left(g^*_{HS} - \frac{2(M')^2}{M^2}g_{HS} + 3\frac{(M')^4}{M^4}g^*_{HS} + \cdots\right)\Box|H|^2 \qquad \text{(C.11)}
\end{aligned}
$$

Where the $\cdots$ represent terms of higher powers of M'/M.

Plugging Φ_c and $\Phi_c^\dagger$ into the original $\Delta\mathcal{L}$ gives,

$$
\begin{aligned}
\Delta\mathcal{L} &\to \frac{1}{M^2}\left(|g_{HS}|^2 - \frac{(M')^2}{2M^2}[g^2_{HS} + (g^*_{HS})^2] + \frac{(M')^4}{M^4}|g_{HS}|^2\right)|H|^4 \\
&\quad - \frac{|H|^6}{M^4}\left[\frac{1}{2}|g_{HS}|^2\lambda'_{HS} + \frac{1}{2}(g^2_{HS}\lambda_{HS} + c.c.) - \frac{1}{3M^2}(g^3_{HS}g^* + c.c.) - \frac{1}{3M^2}(g^2_{HS}g'g^*_{HS} + c.c.)\right] \\
&\quad - \frac{1}{M^4}\left(|g_{HS}|^2 - \frac{(M')^2}{M^2}(g^2_{HS} + c.c.) + \cdots\right)|H|^2\Box|H|^2 \\
&\sim \frac{|g_{HS}|^2}{M^2}|H|^4 - \frac{M^2|g_{HS}|^2\lambda'_{HS}/2 + M^2\mathrm{Re}[g^2_{HS}\lambda_{HS}] - 2\mathrm{Re}[g^3_{HS}g^* + g^2_{HS}g'g^*_{HS}]/3)}{M^6}Q_H \\
&- \frac{|g_{HS}|^2}{M^4}Q_{H\Box} \qquad \text{(C.12)}
\end{aligned}
$$

Again $\cdots$ represents higher powers of M'/M and I've only shown to a convenient order for each operator, not necessarily the same order for each operator.

C.3 2HDMs

$$
\begin{aligned}
\mathcal{L} &= |D^\mu\Phi_1|^2 + |D^\mu\Phi_2|^2 - m^2_{11}\Phi_1^\dagger\Phi_1 - m^2_{22}\Phi_2^\dagger\Phi_2 + m^2_{12}(\Phi_1^\dagger\Phi_2 + h.c.) \\
&\quad + \frac{1}{2}\lambda_1(\Phi_1^\dagger\Phi_1)^2 + \frac{1}{2}\lambda_2(\Phi_2^\dagger\Phi_2)^2 + \lambda_3(\Phi_1^\dagger\Phi_1)(\Phi_2^\dagger\Phi_2) + \lambda_4(\Phi_1^\dagger\Phi_2)(\Phi_2^\dagger\Phi_1) \\
&\quad + \left[\frac{1}{2}\lambda_5(\Phi_1^\dagger\Phi_2)^2 + \lambda_6(\Phi_1^\dagger\Phi_1)(\Phi_1^\dagger\Phi_2) + \lambda_7(\Phi_2^\dagger\Phi_2)(\Phi_1^\dagger\Phi_2) + h.c.\right] \qquad \text{(C.13)}
\end{aligned}
$$

Which is rotated into the Higgs basis via [48]:

$$\begin{aligned} H_1 &= \cos\beta\Phi_1 + \sin\beta\Phi_2 \\ H_2 &= -\sin\beta\Phi_1 + \cos\beta\Phi_2 \end{aligned} \tag{C.14}$$

Recently in the literature we have Bélusca-Maïto et al. [41], with the potential in the Higgs basis,

$$\begin{aligned} V(H_1,H_2) &= Y_1|H_1|^2 + Y_2|H_2|^2 + (Y_3 H_1^\dagger H_2 + h.c.) + \frac{Z_1}{2}|H_1|^4 + \frac{Z_2}{2}|H_2|^4 \\ &\quad + Z_3|H_1|^2|H_2|^2 + Z_4(H_1^\dagger H_2)(H_2^\dagger H_1) \\ &\quad + \left(\frac{Z_5}{2}(H_1^\dagger H_2)^2 + (Z_6|H_1|^2 + Z_7|H_2|^2)(H_1^\dagger H_2) + h.c.\right) \end{aligned} \tag{C.15}$$

they claim all Y_i and Z_i are real. They integrate out to find the EFT, and can be used as a reference. Additionally the tree level D6 EFT is discussed in [49], and the 1–loop D6 EFT in [125]. Taking the Lagrangian with normalizations such that the EOM are nicely normalized and we have trivialized the couplings to fermions, we need to turn on/off various Yukawas here as well as scale them for the Higgs basis dependent on the 'Type' of 2HDM:

$$\begin{aligned} \Delta\mathcal{L} &= (D^\mu H_2)^\dagger (D_\mu H_2) - M^2|H_2|^2 - Y_3(H_1^\dagger H_2 + h.c.) - \frac{Z_2}{2}|H_2|^4 - Z_3|H_1|^2|H_2|^2 \\ &\quad - Z_4(H_1^\dagger H_2)(H_2^\dagger H_1) - \frac{Z_5}{2}(H_1^\dagger H_2)(H_1^\dagger H_2) - \frac{Z_5^*}{2}(H_2^\dagger H_1)(H_2^\dagger H_1) - Z_6|H_1|^2(H_1^\dagger H_2) \\ &\quad - Z_6^*|H_1|^2(H_2^\dagger H_1) - Z_7|H_2|^2(H_1^\dagger H_2) - Z_7^*|H_2|^2(H_2^\dagger H_1) \\ &\quad - \left(H_{2,i}\bar{Q}_j Y_u u \epsilon_{ij} + H_{2,i}\bar{Q}_i Y_d d + H_{2,i}\bar{L}_i Y_l e + h.c.\right) \end{aligned} \tag{C.16}$$

The classical EOM are:

$$
\begin{aligned}
D^2 H_{2,i} &= -M^2 H_{2,i} - Y_3 H_{1,i} - Z_2 H_{2,i}|H_2|^2 - Z_3 H_{2,i}|H_1|^2 - Z_4 H_{1,i}(H_1^\dagger H_2) \\
&\quad - Z_5^* H_{1,i}(H_2^\dagger H_1) - Z_6^* H_{1,i}|H_1|^2 - Z_7 H_{2,i}(H_1^\dagger H_2) - Z_7^* H_{2,i}(H_2^\dagger H_1) \\
&\quad - Z_7^* H_{1,i}|H_2|^2 - \bar{e} Y^\dagger L_i - \bar{d} Y_d^\dagger Q_i - \bar{u} Y_u^\dagger Q_j \epsilon_{ij} \\
\\
D^2 H_{2,i}^\dagger &= -M^2 H_{2,i}^\dagger - Y_3 H_{1,i}^\dagger - Z_2 |H_2|^2 H_{2,i}^\dagger - Z_3 |H_1|^2 H_{2,i}^\dagger - Z_4 (H_2^\dagger H_1) H_{1,i}^\dagger \\
&\quad - Z_5 (H_1^\dagger H_2) H_{1,i}^\dagger - Z_6 |H_1|^2 H_{1,i}^\dagger - Z_7 (H_1^\dagger H_2) H_{2,i}^\dagger - Z_7 |H_2|^2 H_{1,i}^\dagger \\
&\quad - Z_7^* (H_2^\dagger H_1) H_{2,i}^\dagger - \bar{L}_i Y_l e - \bar{Q}_i Y_d d - \bar{Q}_j Y_u u \epsilon_{ij}
\end{aligned}
\tag{C.17}
$$

Linearizing,

$$
\begin{aligned}
&(D^2 \delta_{ij} + M^2 \delta_{ij} + Z_3 |H_1|^2 \delta_{ij} + Z_4 H_{1,i} H_{1,j}^\dagger) H_{2,j} \\
&= -Y_3 H_{1,i} - Z_5^* H_{1,i}(H_2^\dagger H_1) - Z_6^* H_{1,i}|H_1|^2 - \bar{e} Y_l^\dagger L_i - \bar{d} Y_d^\dagger Q_i - \bar{u} Y_u^\dagger Q_j \epsilon_{ij} \\
\\
&H_{2,j}^\dagger (\overleftarrow{D}^2 \delta_{ij} + M^2 \delta_{ij} + Z_3 |H_1|^2 \delta_{ij} + Z_4 H_{1,j} H_{1,i}^\dagger) \\
&= -Y_3 H_{1,i}^\dagger - Z_5 (H_1^\dagger H_2) H_{1,i}^\dagger - Z_6 |H_1|^2 H_{1,i}^\dagger - \bar{L}_i Y_l e - \bar{Q}_i Y_d d - \bar{Q}_j Y_u u \epsilon_{ij}
\end{aligned}
\tag{C.18}
$$

Solving for $H_2^\dagger$,

$$
\begin{aligned}
(H_{2,i}^\dagger)_c &= -\frac{Y_3}{M^2} H_{1,i}^\dagger - \frac{1}{M^2} \bar{L}_i Y_l e - \frac{1}{M^2} \bar{Q}_i Y_d d - \frac{1}{M^2} \bar{Q}_j Y_u u \epsilon_{ij} \\
&\quad + \frac{Y_3(Z_3+Z_4) - M^2 Z_6}{M^4} (H_1^\dagger H_1) H_{1,i}^\dagger - \frac{(Z_3+Z_4)(Y_3(Z_3+Z_4) - M^2 Z_6)}{M^6} (H_1^\dagger H_1)^2 H_{1,i}^\dagger \\
&\quad + \frac{Y_3}{M^4} (D^2 H_{1,i})^\dagger + \frac{Z_6 M^2 - Y_3(2Z_3+Z_4)}{M^6} (H_1^\dagger H_1)(D^2 H_{1,i})^\dagger - \frac{Y_3}{M^6} (D^4 H_{1,i})^\dagger \\
&\quad - \frac{Z_5}{M^2} (H_1^\dagger H_2) H_{1,i}^\dagger + \frac{(Z_3+Z_4) Z_5}{M^4} (H_1^\dagger H_1)(H_1^\dagger H_2) H_{1,i}^\dagger + \frac{Z_5}{M^4} (H_1^\dagger H_2)(D^2 H_{1,i})^\dagger
\end{aligned}
\tag{C.19}
$$

Plugging this expression into the classical EOM for H2 (i.e. Eq. C.17), linearizing, and again solving for $(H_2)_c$ gives,

$$\begin{aligned}
(H_{2,i})_c \;=\; & -\frac{Y_3}{M^2}H_{1,i} - \frac{1}{M^2}\bar{e}Y_l^\dagger L_i - \frac{1}{M^2}\bar{d}Y_d Q_i - \frac{1}{M^2}\bar{u}Y_u Q_j \epsilon_{ij} \\
& + \frac{M^2 Y_3(Z_3+Z_4+Z_5^*) - M^4 Z_6^* - 2Y_3^2 Z_7^*}{M^6} H_{1,i}|H_1|^2 \\
& + \frac{M^4(Z_5^* Z_6 + (Z_3+Z_4)Z_6^*) + 2Y_3^2(3(Z_3+Z_4)+Z_5^*)Z_7^*}{M^8} H_{1,i}|H_1|^4 \\
& + \frac{-4Y_3^3(Z_7^*)^2 - M^4 Y_3((Z_3+Z_4)^2 + 2(Z_3+Z_4)Z_5^* + |Z_5|^2 + 2(Z_6+Z_6^*)Z_7^*}{M^{10}} H_{1,i}|H_1|^4 \\
& + \frac{Y_3}{M^4}D^2 H_{1,i} - \frac{Y_3}{M^6}(D^4 H_{1,i}) - \frac{M^2 Y_3(Z_3+Z_5^*) - M^4 Z_6^* - Y_3^2 Z_7^*}{M^8}(D^2 H_{1,i})|H_1|^2 \\
& + \frac{Y_3(-M^2 Z_4 + Y_3 Z_7^*)}{M^8} H_{1,i}(H_1^\dagger D^2 H_1) + \frac{Y_3(-M^2 Z_5^* + 2Y_3 Z_7^*)}{M^8} H_{1,i}(D^2 H_1)^\dagger H_1
\end{aligned} \tag{C.20}$$

Taking this expression and its *h.c.* and plugging it into the Lagrangian (less the kinetic term), Eq. C.16, we find the effective Lagrangian:

$$\begin{aligned}
& \Delta\mathcal{L} - (D^\mu H_2)^\dagger (D_\mu H_2) = \frac{Y_3^2}{M^2}|H_1|^2 \\
& - \left(2\mathrm{Re}[Z_6]\frac{Y_3}{M^2} - (2Z_3 + 2Z_4 + 2\mathrm{Re}[Z_5])\frac{Y_3^2}{2M^4} + \mathcal{O}(Y_3^3/M^6)\right)|H_1|^4 \\
& + \left(|Z_6|^2 - (Z_5^* Z_6 + Z_5 Z_6^* + 2(Z_3+Z_4)\mathrm{Re}[Z_6]\frac{Y_3}{M^2} + \mathcal{O}(Y_3^2/M^4)\right)\frac{1}{M^2}|H_1|^6 \\
& - \frac{Y_3^2}{M^6}(D^2 H_1)^\dagger (D^2 H_1) \\
& + \frac{Y_3 Z_2 - M^2 Z_7}{M^4}\frac{Y_3^3}{M^6}(H_1^\dagger H_1)[(D^2 H_1)^\dagger H_1 + h.c.] \\
& + \frac{Y_3}{M^2}\,(\text{Yukawa}) \\
& + \frac{1}{M^2}\,(4-\text{Fermi}) \\
& + \left(\frac{Z_6}{M^2} - (Z_3+Z_4+Z_5)\frac{Y_3}{M^4} + \mathcal{O}(Y_3^2/M^6)\right)|H_1|^2 H_{1,i}\left(\bar{d}Y_d^\dagger Q_i + \bar{u}Y_u^\dagger Q_j \epsilon_{ij} + \bar{e}Y^\dagger L_i\right) + h.c.
\end{aligned} \tag{C.21}$$

The kinetic term gives,

$$
\begin{aligned}
(D^\mu H_2)^\dagger (D_\mu H_2) &= -\frac{Y_3^2}{M^6}[(D^2 D^\mu H_1)^\dagger (D_\mu H_1) + h.c.] \\
&\quad + \frac{Y_3^2}{M^4}(D^\mu H_1)^\dagger (D_\mu H_1) \\
&\quad + \left(2Y_3 \mathrm{Re}[Z_6]\frac{Y_3}{M^2} - (2Z_3 + 2Z_4 + 2\mathrm{Re}[Z_5])\frac{Y_3^2}{M^4}\right)\frac{1}{M^2}|H_1|^2 (D^\mu H_1)^\dagger (D_\mu H_1) \\
&\quad + \frac{Y_3}{M^4}\left[(D^\mu H_{1,i}) D_\mu (\bar{L}_i Y_l e + \bar{Q}_i Y_d d + \bar{Q}_j Y_u u \epsilon_{ij}) + h.c.\right] \\
&\sim 0 \text{ (for sufficiently small } Y_3) \qquad \text{(C.22)}
\end{aligned}
$$

This is a good argument for at least neglecting terms $\mathcal{O}(Y_3^2/M^6)$. The last term can be traded via the EOM for 4–fermi interactions and rescaling of the Yukawas, via the EOM:

$$
(D^\mu D_\mu H)_i = m^2 H_i - \lambda |H|^2 H_i - \bar{e} Y_l^\dagger L_i - \bar{Q}_j Y_u u \epsilon_{ij} - \bar{d} Y_d^\dagger Q_i \qquad \text{(C.23)}
$$

So for sufficiently small Y_3 we have,

$$
\Delta\mathcal{L} = \frac{|Z_6|^2}{M^2} Q_H + \sum_i \frac{Z_6}{M^2} Y_{ii}(Q_{eH,ii} + Q_{uH,ii} + Q_{dH,ii}) + h.c. + \frac{1}{M^2}\,(4-\text{Fermi}) \qquad \text{(C.24)}
$$

C.4 Real Triplet

Taking the Lagrangian with normalizations such that the EOM are nicely normalized,

$$
\Delta\mathcal{L} = \frac{1}{2}(D_\mu \Phi^a)^2 - \frac{1}{2}M^2 \Phi^a \Phi^a + g H^\dagger \tau^a H \Phi^a - \frac{\lambda_{H\Phi}}{2}|H|^2 \Phi^a \Phi^a - \frac{1}{4}\lambda_\Phi (\Phi^a \Phi^a)^2 \qquad \text{(C.25)}
$$

The classical EOM are:

$$
D^2 \Phi^a = -M^2 \Phi^a - \lambda_{H\Phi}|H|^2 \Phi^a + g H^\dagger \tau^a H - \lambda_\Phi (\Phi^b \Phi^b)\Phi^a \qquad \text{(C.26)}
$$

Linearizing the EOM in Φ^a,

$$(D^2 + M^2 + \lambda_{H\Phi} H^2)\Phi^a = g H^\dagger \tau^k H \tag{C.27}$$

For M sufficiently larger than the momenta and the excitations of the field H this gives the approximation,

$$\begin{aligned}
\Phi_c^a &= \frac{1}{D^2 + M^2 + \lambda_{H\Phi}|H|^2} g H^\dagger \tau^a H \\
&= \frac{1}{M^2} g H^\dagger \tau^a H - \frac{D^2 + \lambda_{H\Phi}|H|^2}{M^4} g H^\dagger \tau^a H \\
&= \frac{g}{M^2} H^\dagger \tau^a H - \frac{g}{M^4} D^2 (H^\dagger \tau^a H) - \frac{\lambda_{H\Phi} g}{M^4} |H|^2 (H^\dagger \tau^a H)
\end{aligned} \tag{C.28}$$

Plugging this expression into $\Delta\mathcal{L}$, Eq. C.25,

$$\begin{aligned}
\Delta\mathcal{L} &= \frac{g^2}{2M^4}[D_\mu (H^\dagger \tau^a H)]^2 \\
&\quad - \frac{g^2}{2M^2}(H^\dagger \tau^a H)^2 + \frac{g^2}{M^4}(H^\dagger \tau^a H) D^2 (H^\dagger \tau^a H) + \frac{\lambda_{H\Phi} g^2}{M^4}|H|^2 (H^\dagger \tau^a H)^2 \\
&\quad + \frac{g^2}{M^2}(H^\dagger \tau^a H)^2 - \frac{g^2}{M^4}(H^\dagger \tau^a H) D^2 (H^\dagger \tau^a H) - \frac{g^2 \lambda_{H\Phi}}{M^4}|H|^2 (H^\dagger \tau^a H)^2 \\
&\quad - \frac{\lambda_{H\Phi} g^2}{2M^4}|H|^2 (H^\dagger \tau^a H)^2 \\
&= \frac{g^2}{2M^4}[D_\mu (H^\dagger \tau^a H)] + \frac{g^2}{2M^2}(H^\dagger \tau^a H)^2 - \frac{g^2 \lambda_{H\Phi}}{2M^4}|H|^2 (H^\dagger \tau^a H)^2
\end{aligned} \tag{C.29}$$

Noting that,

$$\tau^a_{ij} \tau^a_{kl} = \frac{1}{2}\delta_{il}\delta_{jk} - \frac{1}{4}\delta_{ij}\delta_{kl}, \tag{C.30}$$

we see,

$$(H^\dagger \tau^a H)(H^\dagger \tau^a H) = \frac{1}{4}(H^\dagger H)^2. \tag{C.31}$$

Considering the derivative term we have,

$$\begin{aligned} D^\mu(H^\dagger\tau^a H) &= [(D^\mu H)^\dagger\tau^a H + H^\dagger(D^\mu\tau^a H)] \\ &= (D^\mu H)^\dagger\tau^a H + H^\dagger\tau^a(D^\mu H) - H^\dagger[\tau^a, D^\mu]H \end{aligned} \tag{C.32}$$

Performing the commutator:

$$\begin{aligned} [\tau^a, D^\mu] &= [\tau^a, \partial^\mu] + [\tau^a, ig\tau^b A^{b\mu}] \\ &= -2gA^b_\mu\epsilon^{abc}\tau^c \end{aligned} \tag{C.33}$$

Because this is multiplied by $D_\mu(H^\dagger\tau^a H)$ this term is symmetric in $a \leftrightarrow c$ for the pauli matrices but antisymmetric in the Levi-Civita symbol, therefore this term vanishes. Then the derivative term becomes,

$$\begin{aligned} & D_\mu(H^\dagger\tau^a H)D^\mu(H^\dagger\tau^a H) \\ = \;& [(D_\mu H)^\dagger\tau^a H + H^\dagger\tau^a(D_\mu H)][(D_\mu H)^\dagger\tau^a H + H^\dagger\tau^a(D_\mu H)] \\ = \;& [(D_\mu H)^\dagger\tau^a H][(D^\mu H)^\dagger\tau^a H] + [H^\dagger\tau^a(D_\mu H)][H^\dagger\tau^a(D^\mu H)] + 2[H^\dagger\tau^a(D_\mu H)][(D^\mu H)^\dagger\tau^a H] \\ = \;& \frac{1}{4}\left((D_\mu H)^\dagger H(D^\mu H)^\dagger H + 4(D_\mu H)^\dagger(D_\mu H)H^\dagger H\right) \\ & -\frac{1}{4}\left(2(D_\mu H)^\dagger H H^\dagger(D_\mu H) + 2H^\dagger(D_\mu H)H^\dagger(D^\mu H)\right) \\ = \;& \frac{1}{4}\left[\partial^\mu(H^\dagger H)\partial_\mu(H^\dagger H) - 4(D^\mu H)^\dagger H H^\dagger(D_\mu H) + 4(D_\mu H)^\dagger(D_\mu H)H^\dagger H\right] \end{aligned} \tag{C.34}$$

Finally the full EFT at tree level to dimension–six is:

$$
\begin{aligned}
\Delta\mathcal{L} &= \frac{g^2}{2M^4}\left[-(D^\mu H)^\dagger H H^\dagger (D_\mu H) + \frac{1}{4}\partial^\mu (H^\dagger H)\partial_\mu (H^\dagger H) + (D_\mu H)^\dagger (D^\mu H)(H^\dagger H)\right] \\
&\quad + \frac{g^2}{8M^2}|H|^4 - \frac{g^2\lambda_{H\Phi}}{8M^4}|H|^6 \\
&= + \frac{g^2}{8M^2}|H|^4 - \frac{g^2}{2M^4}(D^\mu H)^\dagger H H^\dagger (D_\mu H) + \frac{g^2}{4M^4}\frac{1}{2}\partial^\mu |H|^2 \partial_\mu |H|^2 \\
&\quad + \frac{g^2}{2M^4}|H|^2 (D_\mu H)^\dagger (D^\mu H) - \frac{g^2\lambda_{H\Phi}}{8M^4}|H|^6 \\
&= \frac{g^2}{8M^2}|H|^4 - \frac{g^2}{2M^2}Q_{HD} - \frac{g^2}{8M^4}Q_{H\Box} + \frac{g^2}{2M^4}\left(\frac{1}{2}Q_{H\Box} + 2\lambda Q_H\right) - \frac{g^2\lambda_{H\Phi}}{8M^4}Q_H
\end{aligned}
\tag{C.35}
$$

Note here that $\lambda = \lambda_{SM} + \frac{g^2}{8M^2}$.

C.5 Complex Triplet

Taking the Lagrangian with *the same normalizations as in the real case*, but standard normalization for the kinetic terms:

$$
\Delta\mathcal{L} = |D_\mu \Phi^a|^2 - M^2|\Phi^a|^2 + (gH^T i\sigma_2 \tau^a H\Phi^a + h.c.) - \frac{\lambda_{H\Phi}}{2}|H|^2|\Phi^a|^2 - \frac{1}{4}\lambda_\Phi |\Phi^a|^4 - \frac{\lambda'}{4}(H^\dagger \tau^a \tau^b H)\Phi^a (\Phi^b)^\dagger
\tag{C.36}
$$

The classical EOM are:

$$
\begin{aligned}
D^2\Phi^a &= -M^2\Phi^a - g^* H^\dagger \tau^a i\sigma_2 H^* - \frac{\lambda_{H\Phi}}{2}|H|^2\Phi^a - \frac{1}{2}\lambda_\Phi |\Phi^b|^2 \Phi^a - \frac{\lambda'}{4}(H^\dagger \tau^b \tau^a H)\Phi^b \\
D^2(\Phi^a)^\dagger &= -M^2(\Phi^a)^\dagger + gH^T i\sigma_2 \tau^a H - \frac{\lambda_{H\Phi}}{2}|H|^2(\Phi^a)^\dagger - \frac{1}{2}\lambda_\Phi |\Phi^b|^2 (\Phi^a)^\dagger - \frac{\lambda'}{4}(H^\dagger \tau^a \tau^b H)(\Phi^b)^\dagger
\end{aligned}
\tag{C.37}
$$

Linearizing the EOM in Φ^a and $(\Phi^a)^\dagger$ and solving for Φ^a_c and $(\Phi^a_c)^\dagger$:

$$\begin{aligned}
\Phi_c^a &\sim \frac{1}{D^2+M^2+(\lambda_{H\Phi}/2+\lambda'/4)|H|^2}\left(-g^* H^\dagger \tau^a i\sigma_2 H^* - \frac{\lambda'}{4} H^\dagger i\epsilon^{abc}\sigma^c H\Phi^b\right) \\
&= -\frac{g^*}{M^2} H^\dagger \tau^a i\sigma_2 H^* + \frac{g^*}{M^4} D^2(H^\dagger \tau^a i\sigma_2 H^*) + \frac{g^*}{M^4}\left(\frac{\lambda_{H\Phi}}{2}+\frac{\lambda'}{4}\right)|H|^2(H^\dagger \tau^a i\sigma_2 H^*) \\
&\quad -\frac{\lambda'}{4M^2} H^\dagger i\epsilon^{abc}\sigma^c H\Phi^b + \frac{\lambda'}{4M^4} D^2(H^\dagger i\epsilon^{abc}\sigma^c H\Phi^b) + \frac{\lambda'}{4M^4}\left(\frac{\lambda_{H\Phi}}{2}+\frac{\lambda'}{4}\right)|H|^2(H^\dagger i\epsilon^{abc}\sigma^c H\Phi^b)
\end{aligned} \tag{C.38}$$

Iterating this solution to remove the dependence on Φ^b and removing terms with operator dimension ≥ 5 we find:

$$\begin{aligned}
\Phi_c^a &\sim -\frac{g^*}{M^2} H^\dagger \tau^a i\sigma_2 H^* + \frac{g^*}{M^4} D^2(H^\dagger \tau^a i\sigma_2 H^*) + \frac{g^*}{M^4}\left(\frac{\lambda_{H\Phi}}{2}+\frac{\lambda'}{4}\right)|H|^2(H^\dagger \tau^a i\sigma_2 H^*) \\
&\quad + \frac{\lambda' g^*}{4M^4}(H^\dagger i\epsilon^{abc}\sigma^c H)(H^\dagger \tau^b i\sigma_2 H^*)
\end{aligned}$$

$$\begin{aligned}
(\Phi_c^a)^\dagger &\sim \frac{g}{M^2} H^T \tau^a i\sigma_2 H - \frac{g}{M^4} D^2(H^T \tau^a i\sigma_2 H) - \frac{g}{M^4}\left(\frac{\lambda_{H\Phi}}{2}+\frac{\lambda'}{4}\right)|H|^2(H^T \tau^a i\sigma_2 H) \\
&\quad + \frac{\lambda' g}{4M^4}(H^\dagger i\epsilon^{abc}\sigma^c H)(H^T i\sigma_2 \tau^b H)
\end{aligned} \tag{C.39}$$

Plugging in to Eq. C.36,

$$\begin{aligned}
\Delta\mathcal{L} &= -\frac{|g|^2}{M^4}\left[D_\mu(H^T i\sigma_2 \tau^a H)\right]\left[D^\mu(H^\dagger \tau^a i\sigma_2 H^*)\right] - \frac{|g|^2}{M^2}(H^T i\sigma_2 \tau^a H)(H^\dagger \tau^a i\sigma_2 H^*) \\
&\quad + \frac{|g|^2}{M^4}\left(\frac{\lambda_{H\Phi}}{2}+\frac{\lambda'}{4}\right)|H|^2(H^\dagger \tau^a i\sigma_2 H)(H^T i\sigma_2 \tau^a H) \\
&\quad + \frac{|g|^2\lambda'}{4M^4}(H^\dagger \tau^a \tau^b H)(H^\dagger \tau^a i\sigma_2 H^*)(H^T \tau^b i\sigma_2 H)
\end{aligned} \tag{C.40}$$

Applying the identity,

$$\begin{aligned}
(H^T i\sigma_2 \tau^a H)(H^\dagger \tau^a i\sigma_2 H^*) &= \frac{1}{4}\left[2(H^T i\sigma_2 i\sigma_2 H^*)(H^\dagger H) - (H^T i\sigma_2 H)(H^\dagger i\sigma_2 H^*)\right] \\
&= -\frac{1}{2}(H^\dagger H)^2 + \emptyset
\end{aligned} \tag{C.41}$$

Similar to the derivative term for the real scalar triplet we find,

$$D^\mu(H^\dagger\tau^a i\sigma_2 H^*) = (D^\mu H)^\dagger\tau^a i\sigma_2 H^* + H^\dagger\tau^a i\sigma_2(D^\mu H^*) - H^\dagger[\tau^a i\sigma_2, D^\mu]H^* \tag{C.42}$$

C.6 Quadruplet $Y = 1/2$

$$\begin{aligned}\Delta\mathcal{L} &= (D^\mu\Phi^{*ijk})(D_\mu\Phi_{ijk}) - M^2\Phi^{*ijk}\Phi_{ijk} - (\lambda_{H3\Phi}H^{*i}\Phi_{ijk}H^{*j}\epsilon^{kl}H_l + h.c.)\\ &\quad -\lambda_{H2\Phi2}H^{*i}H_i\Phi^{*lmn}\Phi_{lmn} - \lambda'_{H2\Phi2}H^{*i}\Phi_{ijk}\Phi^{*jkl}H_l - \lambda_\Phi(\Phi^{*ijk}\Phi_{ijk})^2\\ &\quad -\lambda'_\Phi(\Phi^{*ijk}\Phi_{ilm}\Phi^{*lmn}\Phi_{jkn})\end{aligned} \tag{C.43}$$

From the EOM we have (neglecting terms cubic or higher in Φ, denoted: $\cdots$):

$$(D^2\delta_{lk} + M^2\delta_{lk} + \lambda_{H2\Phi2}H^{*m}H_m\delta_{lk} + \lambda'_{H2\Phi2}\delta_{ml}H_kH^{*m})\Phi_{ijl} = -\lambda^*_{H3\Phi}H_iH_j\epsilon_{kn}H^{*n} + \cdots \tag{C.44}$$

We solve for Φ, neglecting terms of mass dimension above 3, EXCEPT the terms involving D^2. The linearizing procedure above is a problem for dimension 8 operators, but will work for the terms proportional to D^2 because they cannot be formed by the Φ^3 or Φ^4 couplings we are neglecting.

$$\begin{aligned}\Phi_{ijl} &= -\frac{\lambda^*_{H3\Phi}}{M^2}H_iH_j\epsilon_{ln}H^{*n} + \frac{\lambda^*_{H3\Phi}}{M^4}D^2H_iH_j\epsilon_{ln}H^{*n} + \cdots\\ \Phi^{*ijl} &= -\frac{\lambda_{H3\Phi}}{M^2}H^{*i}H^{*j}\epsilon^{ln}H_n + \frac{\lambda_{H3\Phi}}{M^4}D^2H^{*i}H^{*j}\epsilon^{ln}H_n + \cdots\end{aligned} \tag{C.45}$$

Plugging this in we find (neglecting $d \geq 6$),

$$\begin{aligned}\Delta\mathcal{L} &= -\frac{|\lambda_{H3\Phi}|^2}{M^2}(H_iH_j\epsilon_{lm}H^{*m})(H^{*i}H^{*j}\epsilon^{ln}H_n)+\frac{2|\lambda_{H3\Phi}|^2}{M^2}(H^{*i}H^{*j}\epsilon^{kl}H_l)(H_iH_j\epsilon_{km}H^{*m})\\ &= \frac{|\lambda_{H3\Phi}|^2}{M^2}(H^{*i}H^{*j}\epsilon^{kl}H_l)(H_iH_j\epsilon_{km}H^{*m})\\ &= \frac{|\lambda_{H3\Phi}|^2}{M^2}(H^\dagger H)^3 \qquad \text{(C.46)}\end{aligned}$$

Where we have used,

$$\begin{aligned}(H^{*i}H^{*j}\epsilon^{kl}H_l)(H_iH_j\epsilon_{km}H^{*m}) &= (H^\dagger H)^2H_l\epsilon^{kl}\epsilon_{km}H^{*m}\\ &= (H^\dagger H)^2H_l\delta^l_mH^{*m}\\ &= (H^\dagger H)^3 \qquad \text{(C.47)}\end{aligned}$$

For the dimension 8 operators involving D^2 we have,

$$\begin{aligned}\Delta\mathcal{L}_8 &= \frac{|\lambda_{H3\Phi}|^2}{M^4}(D^\mu H^{*i}H^{*j}\epsilon^{ln}H_n)(D_\mu H_iH_j\epsilon_{lm}H^{*m})+\frac{|\lambda_{H3\Phi}|^2}{M^4}(H_iH_j\epsilon_{ln}H^{*n})(D^2H^{*i}H^{*j}\epsilon^{ln'}H_{n'})\\ &\quad+\frac{|\lambda_{H3\Phi}|^2}{M^4}(H^{*i}H^{*j}\epsilon^{ln}H_n)(D^2H^{*i}H^{*j}\epsilon^{ln'}H_{n'})-\frac{|\lambda_{H3\Phi}|^2}{M^4}(H^{*i}H^{*j}\epsilon^{kl}H_l)(D^2H_iH_j\epsilon_{kn}H^{*n})\\ &\quad-\frac{|\lambda_{H3\Phi}|^2}{M^4}(H_iH_j\epsilon_{kl}H^{*l})(D^2H^{*i}H^{*j}\epsilon^{kn}H_n)\\ &= \frac{|\lambda_{H3\Phi}|^2}{M^4}(D^\mu H^{*i}H^{*j}H_n)(D_\mu H_iH_jH^{*n}) \qquad \text{(C.48)}\end{aligned}$$

Then the T parameter part is given by:

$$\begin{aligned}\mathcal{L}_8^T &= \tfrac{2|\lambda_{H3\Phi}|^2}{M^4}|H^\dagger D^\mu H|^2|H|^2+\cdots\\ &= -\tfrac{1}{4}\tfrac{2|\lambda_{H3\Phi}|^2}{M^4}|H|^2(H^\dagger\overleftrightarrow{D}^\mu H)^2+\cdots\end{aligned} \qquad \text{(C.49)}$$

Where the second line is rewriting in terms of the operator used by Dawson et al. ($\cdots$ stands for non T parameter operators)

C.7 Quadruplet $Y = 3/2$

$$\begin{aligned}\Delta\mathcal{L} &= (D^\mu \Phi^{*ijk})(D_\mu \Phi_{ijk}) - M^2 \Phi^{*ijk}\Phi_{ijk} - (\lambda_{H3\Phi} H^{*i} H^{*j} H^{*k} \Phi_{ijk} + h.c.) \\ &\quad -\lambda_{H2\Phi 2} H^{*i} H_i \Phi^{*lmn}\Phi_{lmn} - \lambda'_{H2\Phi 2} H^{*i}\Phi_{ijk}\Phi^{*jkl} H_l - \lambda_\Phi (\Phi^{*ijk}\Phi_{ijk})^2 \\ &\quad -\lambda'_\Phi (\Phi^{*ijk}\Phi_{ilm}\Phi^{*lmn}\Phi_{jkn}) \end{aligned} \tag{C.50}$$

From the EOM we have (neglecting terms cubic or higher in Φ, denoted: $\cdots$):

$$(D^2\delta_{kl} + M^2\delta_{kl} + \lambda_{H2\Phi 2} H^{*m} H_m \delta_{kl} + \lambda'_{H2\Phi 2} H^{*i} H_k \delta_{kl})\Phi_{ijl} = -\lambda^*_{H3\Phi} H_i H_j H_k \tag{C.51}$$

Solving for Φ we find (neglecting terms of mass dimension above 3, denoted $\cdots$), EXCEPT the terms involving D^2. The linearizing procedure above is a problem for dimension 8 operators, but will work for the terms proportional to D^2 because they cannot be formed by the Φ^3 or Φ^4 couplings we are neglecting.

$$\begin{aligned}\Phi_{ijl} &= -\frac{\lambda^*_{H3\Phi}}{M^2} H_i H_j H_k + \frac{D^2}{M^4}\lambda^*_{H3\Phi} H_i H_j H_k + \cdots \\ \Phi^{*ijl} &= -\frac{\lambda_{H3\Phi}}{M^2} H^{*i} H^{*j} H^{*k} + \frac{D^2}{M^4}\lambda_{H3\Phi} H^{*i} H^{*j} H^{*k} + \cdots \end{aligned} \tag{C.52}$$

Plugging this in we find (neglecting $d \geq 6$),

$$\begin{aligned}\Delta\mathcal{L} &= -\frac{|\lambda_{H3\Phi}|^2}{M^2}(H^\dagger H)^3 + \frac{2|\lambda_{H3\Phi}|^2}{M^2}(H^\dagger H)^3 + \cdots \\ &= \frac{|\lambda_{H3\Phi}|^2}{M^2}(H^\dagger H)^3 + \cdots \end{aligned} \tag{C.53}$$

For the dimension 8 operators involving D^2 we have,

$$
\begin{aligned}
\Delta\mathcal{L}_8 &= \frac{|\lambda_{H3\Phi}|^2}{M^4}(D^\mu H^{*i}H^{*j}H^{*k})(D_\mu H_i H_j H_k) + \frac{|\lambda_{H3\Phi}|^2}{M^4}(H^{*i}H^{*j}H^{*k})D^2(H_iH_jH_k) \\
&\quad + \frac{|\lambda_{H3\Phi}|^2}{M^4}D^2(H^{*i}H^{*j}H^{*k})(H_iH_jH_k) \\
&\quad - \frac{|\lambda_{H3\Phi}|^2}{M^4}[H^{*i}H^{*j}H^{*k}D^2(H_iH_jH_k) + D^2(H^{*i}H^{*j}H^{*k})H_iH_jH_k] \\
&= \frac{|\lambda_{H3\Phi}|^2}{M^4}(D^\mu H^{*i}H^{*j}H^{*k})(D_\mu H_i H_j H_k) \qquad \text{(C.54)}
\end{aligned}
$$

Then the T parameter part is given by:

$$
\begin{aligned}
\mathcal{L}_8^T &= \tfrac{6|\lambda_{H3\Phi}|^2}{M^4}|H^\dagger D^\mu H|^2|H|^2 + \cdots \\
&= -\tfrac{1}{4}\tfrac{6|\lambda_{H3\Phi}|^2}{M^4}|H|^2(H^\dagger \overleftrightarrow{D}^\mu H)^2 + \cdots
\end{aligned} \qquad \text{(C.55)}
$$

BIBLIOGRAPHY

[1] Gfitter global result for oblique parameters. `http://project-gfitter.web.cern.ch/project-gfitter/Oblique_Parameters/`. Accessed: 2018-05-18.

[2] Lhc higgs cross section working group (2012-2013). `https://twiki.cern.ch/twiki/bin/view/LHCPhysics/CrossSections`. Accessed: 2015-09-30.

[3] Measurement of the total ZZ production cross section in proton-proton collisions at s = 8 TeV in 20 fb1 with the ATLAS detector.

[4] Measurements of the properties of the Higgs-like boson in the four lepton decay channel with the ATLAS detector using 25 fb1 of proton-proton collision data.

[5] Study of the double Higgs production channel $H(\rightarrow b\bar{b})H(\rightarrow \gamma\gamma)$ with the ATLAS experiment at the HL-LHC. Tech. Rep. ATL-PHYS-PUB-2017-001, CERN, Geneva, Jan 2017.

[6] Aaboud, Morad, et al. Search for pair production of Higgs bosons in the $b\bar{b}b\bar{b}$ final state using proton–proton collisions at $\sqrt{s} = 13$ TeV with the ATLAS detector. *Phys. Rev. D94*, 5 (2016), 052002.

[7] Aaboud, Morad, et al. Search for doubly charged Higgs boson production in multi-lepton final states with the ATLAS detector using protonproton collisions at $\sqrt{s} = 13\,\text{TeV}$. *Eur. Phys. J. C78*, 3 (2018), 199.

[8] Aad, Georges, et al. Observation of a new particle in the search for the Standard Model Higgs boson with the ATLAS detector at the LHC. *Phys. Lett. B716* (2012), 1–29.

[9] Aad, Georges, et al. Constraints on new phenomena via Higgs boson couplings and invisible decays with the ATLAS detector. *JHEP 11* (2015), 206.

[10] Aad, Georges, et al. Search for a CP-odd Higgs boson decaying to Zh in pp collisions at $\sqrt{s} = 8$TeV with the ATLAS detector. *Phys. Lett. B744* (2015), 163–183.

[11] Aad, Georges, et al. Searches for Higgs boson pair production in the $hh \rightarrow bb\tau\tau, \gamma\gamma WW^*, \gamma\gamma bb, bbbb$ channels with the ATLAS detector. *Phys. Rev. D92* (2015), 092004.

[12] Aad, Georges, et al. Combination of searches for WW, WZ, and ZZ resonances in pp collisions at $\sqrt{s} = 8$ TeV with the ATLAS detector. *Phys. Lett. B755* (2016), 285–305.

[13] Aad, Georges, et al. Measurements of the Higgs boson production and decay rates and constraints on its couplings from a combined ATLAS and CMS analysis of the LHC pp collision data at $\sqrt{s} = 7$ and 8 TeV. *JHEP 08* (2016), 045.

[14] Aad, Georges, et al. Performance of b-Jet Identification in the ATLAS Experiment. *JINST 11*, 04 (2016), P04008.

[15] Aad, Georges, et al. Search for an additional, heavy Higgs boson in the $H \to ZZ$ decay channel at $\sqrt{s} = 8$ TeV in pp collision data with the ATLAS detector. *Eur. Phys. J. C76*, 1 (2016), 45.

[16] Ade, P. A. R., et al. Planck 2015 results. XIII. Cosmological parameters. *Astron. Astrophys. 594* (2016), A13.

[17] Ahmad, Q. R., et al. Measurement of the rate of $\nu_e + d \to p + p + e^-$ interactions produced by ^8B solar neutrinos at the Sudbury Neutrino Observatory. *Phys. Rev. Lett. 87* (2001), 071301.

[18] Ahmad, Q. R., et al. Direct evidence for neutrino flavor transformation from neutral current interactions in the Sudbury Neutrino Observatory. *Phys. Rev. Lett. 89* (2002), 011301.

[19] Akeroyd, A. G., et al. Prospects for charged Higgs searches at the LHC. *Eur. Phys. J. C77*, 5 (2017), 276.

[20] Alam, S., Dawson, S., and Szalapski, R. Low-energy constraints on new physics revisited. *Phys. Rev. D57* (1998), 1577–1590.

[21] Alloul, Adam, Christensen, Neil D., Degrande, Cline, Duhr, Claude, and Fuks, Benjamin. FeynRules 2.0 - A complete toolbox for tree-level phenomenology. *Comput. Phys. Commun. 185* (2014), 2250–2300.

[22] Alonso, Rodrigo, Jenkins, Elizabeth E., Manohar, Aneesh V., and Trott, Michael. Renormalization Group Evolution of the Standard Model Dimension Six Operators III: Gauge Coupling Dependence and Phenomenology. *JHEP 04* (2014), 159.

[23] Altarelli, Guido, and Maiani, L. Octet Enhancement of Nonleptonic Weak Interactions in Asymptotically Free Gauge Theories. *Phys. Lett. 52B* (1974), 351–354.

[24] Alwall, J., Frederix, R., Frixione, S., Hirschi, V., Maltoni, F., Mattelaer, O., Shao, H. S., Stelzer, T., Torrielli, P., and Zaro, M. The automated computation of tree-level and next-to-leading order differential cross sections, and their matching to parton shower simulations. *JHEP 07* (2014), 079.

[25] Andersen, J R, et al. Handbook of LHC Higgs Cross Sections: 3. Higgs Properties.

[26] Arbelaz, Carolina, Dib, Claudio, Schmidt, Ivn, and Vasquez, Juan Carlos. Probing the Dirac or Majorana nature of the Heavy Neutrinos in pure leptonic decays at the LHC. *Phys. Rev. D97*, 5 (2018), 055011.

[27] Arkani-Hamed, Nima, Han, Tao, Mangano, Michelangelo, and Wang, Lian-Tao. Physics opportunities of a 100 TeV protonproton collider. *Phys. Rept. 652* (2016), 1–49.

[28] Arzt, Christopher. Reduced effective Lagrangians. *Phys. Lett. B342* (1995), 189–195.

[29] Azatov, Aleksandr, Contino, Roberto, Panico, Giuliano, and Son, Minho. Effective field theory analysis of double Higgs boson production via gluon fusion. *Phys. Rev. D92*, 3 (2015), 035001.

[30] Baak, M., Cth, J., Haller, J., Hoecker, A., Kogler, R., Mnig, K., Schott, M., and Stelzer, J. The global electroweak fit at NNLO and prospects for the LHC and ILC. *Eur. Phys. J. C74* (2014), 3046.

[31] Baak, M., Goebel, M., Haller, J., Hoecker, A., Kennedy, D., Kogler, R., Moenig, K., Schott, M., and Stelzer, J. The Electroweak Fit of the Standard Model after the Discovery of a New Boson at the LHC. *Eur. Phys. J. C72* (2012), 2205.

[32] Baglio, J., Djouadi, A., Grber, R., Mhlleitner, M. M., Quevillon, J., and Spira, M. The measurement of the Higgs self-coupling at the LHC: theoretical status. *JHEP 04* (2013), 151.

[33] Baker, C. A., et al. An Improved experimental limit on the electric dipole moment of the neutron. *Phys. Rev. Lett. 97* (2006), 131801.

[34] Barger, Vernon D., Hewett, J. L., and Phillips, R. J. N. New Constraints on the Charged Higgs Sector in Two Higgs Doublet Models. *Phys. Rev. D41* (1990), 3421–3441.

[35] Barger, Vernon, Everett, Lisa L., Jackson, C. B., and Shaughnessy, Gabe. Higgs-Pair Production and Measurement of the Triscalar Coupling at LHC(8,14). *Phys. Lett. B728* (2014), 433–436.

[36] Barger, Vernon, Langacker, Paul, McCaskey, Mathew, Ramsey-Musolf, Michael J., and Shaughnessy, Gabe. LHC Phenomenology of an Extended Standard Model with a Real Scalar Singlet. *Phys. Rev. D77* (2008), 035005.

[37] Barger, Vernon, Langacker, Paul, McCaskey, Mathew, Ramsey-Musolf, Michael, and Shaughnessy, Gabe. Complex Singlet Extension of the Standard Model. *Phys. Rev. D79* (2009), 015018.

[38] Baron, Jacob, et al. Order of Magnitude Smaller Limit on the Electric Dipole Moment of the Electron. *Science 343* (2014), 269–272.

[39] Barr, Alan J., Dolan, Matthew J., Englert, Christoph, Ferreira de Lima, Danilo Enoque, and Spannowsky, Michael. Higgs Self-Coupling Measurements at a 100 TeV Hadron Collider. *JHEP 02* (2015), 016.

[40] Baur, U., Plehn, T., and Rainwater, David L. Probing the Higgs selfcoupling at hadron colliders using rare decays. *Phys. Rev. D69* (2004), 053004.

[41] Belusca-Maito, Herms, Falkowski, Adam, Fontes, Duarte, Romo, Jorge C., and Silva, Joo P. Higgs EFT for 2HDM and beyond.

[42] Bernon, Jeremy, and Dumont, Beranger. Lilith: a tool for constraining new physics from Higgs measurements. *Eur. Phys. J. C75*, 9 (2015), 440.

[43] Bian, Ligong, Chen, Ning, and Zhang, Yongchao. CP violation effects in the diphoton spectrum of heavy scalars. *Phys. Rev. D96*, 9 (2017), 095008.

[44] Bian, Ligong, Liu, Tao, and Shu, Jing. Cancellations Between Two-Loop Contributions to the Electron Electric Dipole Moment with a CP-Violating Higgs Sector. *Phys. Rev. Lett. 115* (2015), 021801.

[45] Bizon, Wojciech, Gorbahn, Martin, Haisch, Ulrich, and Zanderighi, Giulia. Constraints on the trilinear Higgs coupling from vector boson fusion and associated Higgs production at the LHC.

[46] Blank, T., and Hollik, W. Precision observables in SU(2) x U(1) models with an additional Higgs triplet. *Nucl. Phys. B514* (1998), 113–134.

[47] Bochkarev, A. I., and Shaposhnikov, M. E. Electroweak Production of Baryon Asymmetry and Upper Bounds on the Higgs and Top Masses. *Mod. Phys. Lett. A2* (1987), 417.

[48] Branco, G. C., Ferreira, P. M., Lavoura, L., Rebelo, M. N., Sher, Marc, and Silva, Joao P. Theory and phenomenology of two-Higgs-doublet models. *Phys. Rept. 516* (2012), 1–102.

[49] Brehmer, Johann, Freitas, Ayres, Lopez-Val, David, and Plehn, Tilman. Pushing Higgs Effective Theory to its Limits. *Phys. Rev. D93*, 7 (2016), 075014.

[50] Brivio, I., Corbett, T., Eboli, O. J. P., Gavela, M. B., Gonzalez-Fraile, J., Gonzalez-Garcia, M. C., Merlo, L., and Rigolin, S. Disentangling a dynamical Higgs. *JHEP 03* (2014), 024.

[51] Brivio, I., Gonzalez-Fraile, J., Gonzalez-Garcia, M. C., and Merlo, L. The complete HEFT Lagrangian after the LHC Run I. *Eur. Phys. J. C76*, 7 (2016), 416.

[52] Buchmuller, W., and Wyler, D. Effective Lagrangian Analysis of New Interactions and Flavor Conservation. *Nucl. Phys. B268* (1986), 621–653.

[53] Burgess, C. P., Pospelov, Maxim, and ter Veldhuis, Tonnis. The Minimal model of nonbaryonic dark matter: A Singlet scalar. *Nucl. Phys. B619* (2001), 709–728.

[54] Butter, Anja, Eboli, Oscar J. P., Gonzalez-Fraile, J., Gonzalez-Garcia, M. C., Plehn, Tilman, and Rauch, Michael. The Gauge-Higgs Legacy of the LHC Run I. *JHEP 07* (2016), 152.

[55] Campos, Miguel D., Cogollo, D., Lindner, Manfred, Melo, T., Queiroz, Farinaldo S., and Rodejohann, Werner. Neutrino Masses and Absence of Flavor Changing Interactions in the 2HDM from Gauge Principles. *JHEP 08* (2017), 092.

[56] Casas, J. A., and Ibarra, A. Oscillating neutrinos and muon —¿ e, gamma. *Nucl. Phys. B618* (2001), 171–204.

[57] Celis, Alejandro, Jung, Martin, Li, Xin-Qiang, and Pich, Antonio. Scalar contributions to $b \to c(u)\tau\nu$ transitions. *Phys. Lett. B771* (2017), 168–179.

[58] Chatrchyan, Serguei, et al. Observation of a new boson at a mass of 125 GeV with the CMS experiment at the LHC. *Phys. Lett. B716* (2012), 30–61.

[59] Chatrchyan, Serguei, et al. Search for new physics in events with same-sign dileptons and b-tagged jets in pp collisions at $\sqrt{s} = 7$ TeV. *JHEP 08* (2012), 110.

[60] Chatrchyan, Serguei, et al. Search for a standard-model-like Higgs boson with a mass in the range 145 to 1000 GeV at the LHC. *Eur. Phys. J. C73* (2013), 2469.

[61] Chen, Chien-Yi, Dawson, S., and Zhang, Yue. Complementarity of LHC and EDMs for Exploring Higgs CP Violation. *JHEP 06* (2015), 056.

[62] Chen, Mu-Chun, Dawson, Sally, and Krupovnickas, Tadas. Higgs triplets and limits from precision measurements. *Phys. Rev. D74* (2006), 035001.

[63] Chen, Ning, Li, Jinmian, Liu, Yandong, and Liu, Zuowei. LHC searches for the CP-odd Higgs by the jet substructure analysis. *Phys. Rev. D91*, 7 (2015), 075002.

[64] Cheng, T. P., and Li, Ling-Fong. Neutrino Masses, Mixings and Oscillations in SU(2) x U(1) Models of Electroweak Interactions. *Phys. Rev. D22* (1980), 2860.

[65] Cheng, Wei, and Bian, Ligong. From inflation to cosmological electroweak phase transition with a complex scalar singlet.

[66] Chiang, Cheng-Wei, Ramsey-Musolf, Michael J., and Senaha, Eibun. Standard Model with a Complex Scalar Singlet: Cosmological Implications and Theoretical Considerations. *Phys. Rev. D97*, 1 (2018), 015005.

[67] Chivukula, R. Sekhar, Christensen, Neil D., and Simmons, Elizabeth H. Low-energy effective theory, unitarity, and non-decoupling behavior in a model with heavy Higgs-triplet fields. *Phys. Rev. D77* (2008), 035001.

[68] Cline, James M. Baryogenesis. In *Les Houches Summer School - Session 86: Particle Physics and Cosmology: The Fabric of Spacetime Les Houches, France, July 31-August 25, 2006* (2006).

[69] Cline, James M., and Lemieux, Pierre-Anthony. Electroweak phase transition in two Higgs doublet models. *Phys. Rev. D55* (1997), 3873–3881.

[70] Coleppa, Baradhwaj, Kling, Felix, and Su, Shufang. Exotic Decays Of A Heavy Neutral Higgs Through HZ/AZ Channel. *JHEP 09* (2014), 161.

[71] Collaboration, CMS. Summary results of high mass BSM Higgs searches using CMS run-I data.

[72] collaboration, The ATLAS. Constraints on New Phenomena via Higgs Coupling Measurements with the ATLAS Detector.

[73] collaboration, The ATLAS. Search for pair production of Higgs bosons in the $b\bar{b}b\bar{b}$ final state using proton−proton collisions at $\sqrt{s} = 13$ TeV with the ATLAS detector.

[74] Contino, R., et al. Physics at a 100 TeV pp collider: Higgs and EW symmetry breaking studies.

[75] Corbett, Tyler, Eboli, O. J. P., Gonzalez-Fraile, J., and Gonzalez-Garcia, M. C. Constraining anomalous Higgs interactions. *Phys. Rev. D86* (2012), 075013.

[76] Corbett, Tyler, Eboli, O. J. P., Gonzalez-Fraile, J., and Gonzalez-Garcia, M. C. Determining Triple Gauge Boson Couplings from Higgs Data. *Phys. Rev. Lett. 111* (2013), 011801.

[77] Corbett, Tyler, Eboli, O. J. P., Gonzalez-Fraile, J., and Gonzalez-Garcia, M. C. Robust Determination of the Higgs Couplings: Power to the Data. *Phys. Rev. D87* (2013), 015022.

[78] Corbett, Tyler, Eboli, O. J. P., and Gonzalez-Garcia, M. C. Unitarity Constraints on Dimension-Six Operators. *Phys. Rev. D91*, 3 (2015), 035014.

[79] Corbett, Tyler, Eboli, O. J. P., and Gonzalez-Garcia, M. C. Inverse amplitude method for the perturbative electroweak symmetry breaking sector: The singlet Higgs portal as a study case. *Phys. Rev. D93*, 1 (2016), 015005.

[80] Corbett, Tyler, Eboli, Oscar J. P., Goncalves, Dorival, Gonzalez-Fraile, J., Plehn, Tilman, and Rauch, Michael. The Higgs Legacy of the LHC Run I. *JHEP 08* (2015), 156.

[81] Corbett, Tyler, Eboli, Oscar J. P., Goncalves, Dorival, Gonzalez-Fraile, J., Plehn, Tilman, and Rauch, Michael. The Non-Linear Higgs Legacy of the LHC Run I.

[82] Cowan, Glen. Statistics for Searches at the LHC. In *Proceedings, 69th Scottish Universities Summer School in Physics : LHC Phenomenology (SUSSP69): St.Andrews, Scotland, August 19-September 1, 2012* (2013), pp. 321–355.

[83] Cowan, Glen, Cranmer, Kyle, Gross, Eilam, and Vitells, Ofer. Asymptotic formulae for likelihood-based tests of new physics. *Eur. Phys. J. C71* (2011), 1554. [Erratum: Eur. Phys. J.C73,2501(2013)].

[84] Csikor, F., Fodor, Z., and Heitger, J. Endpoint of the hot electroweak phase transition. *Phys. Rev. Lett. 82* (1999), 21–24.

[85] Cuesta, Antonio J., Niro, Viviana, and Verde, Licia. Neutrino mass limits: robust information from the power spectrum of galaxy surveys. *Phys. Dark Univ. 13* (2016), 77–86.

[86] Curtin, David, Galloway, Jamison, and Wacker, Jay G. Measuring the $t\bar{t}h$ coupling from same-sign dilepton $+2b$ measurements. *Phys. Rev. D88*, 9 (2013), 093006.

[87] Czakon, Michael, Krmer, Michael, and Worek, Malgorzata. Automated NLO/NLL Monte Carlo programs for the LHC. *Nucl. Part. Phys. Proc. 261-262* (2015), 93–114.

[88] Czakon, Micha, Fiedler, Paul, and Mitov, Alexander. Total Top-Quark Pair-Production Cross Section at Hadron Colliders Through $O(\frac{4}{S})$. *Phys. Rev. Lett. 110* (2013), 252004.

[89] Dawson, S., and Sullivan, M. Enhanced di-Higgs boson production in the complex Higgs singlet model. *Phys. Rev. D97*, 1 (2018), 015022.

[90] Dawson, Sally, and Murphy, Christopher W. Standard Model EFT and Extended Scalar Sectors.

[91] de Blas, Jorge, Chala, Mikael, Perez-Victoria, Manuel, and Santiago, Jose. Observable Effects of General New Scalar Particles. *JHEP 04* (2015), 078.

[92] de Favereau, J., Delaere, C., Demin, P., Giammanco, A., Lematre, V., Mertens, A., and Selvaggi, M. DELPHES 3, A modular framework for fast simulation of a generic collider experiment. *JHEP 02* (2014), 057.

[93] de Florian, D., et al. Handbook of LHC Higgs Cross Sections: 4. Deciphering the Nature of the Higgs Sector.

[94] de Florian, Daniel, and Mazzitelli, Javier. Two-loop virtual corrections to Higgs pair production. *Phys. Lett. B724* (2013), 306–309.

[95] Degrassi, Giuseppe, Fedele, Marco, and Giardino, Pier Paolo. Constraints on the trilinear Higgs self coupling from precision observables.

[96] Degrassi, Giuseppe, Giardino, Pier Paolo, Maltoni, Fabio, and Pagani, Davide. Probing the Higgs self coupling via single Higgs production at the LHC. *JHEP 12* (2016), 080.

[97] Dell'Oro, Stefano, Marcocci, Simone, Viel, Matteo, and Vissani, Francesco. Neutrinoless double beta decay: 2015 review. *Adv. High Energy Phys. 2016* (2016), 2162659.

[98] Di Valentino, Eleonora, Giusarma, Elena, Lattanzi, Massimiliano, Mena, Olga, Melchiorri, Alessandro, and Silk, Joseph. Cosmological Axion and neutrino mass constraints from Planck 2015 temperature and polarization data. *Phys. Lett. B752* (2016), 182–185.

[99] Di Valentino, Eleonora, Giusarma, Elena, Mena, Olga, Melchiorri, Alessandro, and Silk, Joseph. Cosmological limits on neutrino unknowns versus low redshift priors. *Phys. Rev. D93*, 8 (2016), 083527.

[100] Di Vita, Stefano, Grojean, Christophe, Panico, Giuliano, Riembau, Marc, and Vantalon, Thibaud. A global view on the Higgs self-coupling. *JHEP 09* (2017), 069.

[101] Dittmaier, S., et al. Handbook of LHC Higgs Cross Sections: 1. Inclusive Observables.

[102] Djouadi, Abdelhak. The Anatomy of electro-weak symmetry breaking. I: The Higgs boson in the standard model. *Phys. Rept. 457* (2008), 1–216.

[103] Djouadi, Abdelhak. The Anatomy of electro-weak symmetry breaking. II. The Higgs bosons in the minimal supersymmetric model. *Phys. Rept. 459* (2008), 1–241.

[104] Dolan, Matthew J., Englert, Christoph, and Spannowsky, Michael. New Physics in LHC Higgs boson pair production. *Phys. Rev. D87*, 5 (2013), 055002.

[105] Dorsch, G. C., Huber, S. J., Konstandin, T., and No, J. M. A Second Higgs Doublet in the Early Universe: Baryogenesis and Gravitational Waves. *JCAP 1705*, 05 (2017), 052.

[106] Dorsch, G. C., Huber, S. J., Mimasu, K., and No, J. M. Echoes of the Electroweak Phase Transition: Discovering a second Higgs doublet through $A_0 \to ZH_0$. *Phys. Rev. Lett. 113*, 21 (2014), 211802.

[107] Dorsch, G. C., Huber, S. J., and No, J. M. A strong electroweak phase transition in the 2HDM after LHC8. *JHEP 10* (2013), 029.

[108] Eguchi, K., et al. First results from KamLAND: Evidence for reactor anti-neutrino disappearance. *Phys. Rev. Lett. 90* (2003), 021802.

[109] Elias-Miro, J., Espinosa, J. R., Masso, E., and Pomarol, A. Higgs windows to new physics through d=6 operators: constraints and one-loop anomalous dimensions. *JHEP 11* (2013), 066.

[110] Elias-Mir, Joan, Grojean, Christophe, Gupta, Rick S., and Marzocca, David. Scaling and tuning of EW and Higgs observables. *JHEP 05* (2014), 019.

[111] Ellis, John, and Sakurai, Kazuki. Search for Sphalerons in Proton-Proton Collisions. *JHEP 04* (2016), 086.

[112] Englert, F., and Brout, R. Broken Symmetry and the Mass of Gauge Vector Mesons. *Phys. Rev. Lett. 13* (1964), 321–323. [,157(1964)].

[113] Enomoto, Tetsuya, and Watanabe, Ryoutaro. Flavor constraints on the Two Higgs Doublet Models of Z_2 symmetric and aligned types. *JHEP 05* (2016), 002.

[114] Espinosa, Jose R., Konstandin, Thomas, and Riva, Francesco. Strong Electroweak Phase Transitions in the Standard Model with a Singlet. *Nucl. Phys. B854* (2012), 592–630.

[115] Falkowski, Adam, Fuks, Benjamin, Mawatari, Kentarou, Mimasu, Ken, Riva, Francesco, and sanz, Vernica. Rosetta: an operator basis translator for Standard Model effective field theory. *Eur. Phys. J. C75*, 12 (2015), 583.

[116] Falkowski, Adam, and Riva, Francesco. Model-independent precision constraints on dimension-6 operators. *JHEP 02* (2015), 039.

[117] Febres Cordero, Fernando, Reina, L., and Wackeroth, D. W- and Z-boson production with a massive bottom-quark pair at the Large Hadron Collider. *Phys. Rev. D80* (2009), 034015.

[118] Ferrari, A., Collot, Johann, Andrieux, M-L., Belhorma, B., de Saintignon, P., Hostachy, J-Y., Martin, Ph., and Wielers, M. Sensitivity study for new gauge bosons and right-handed Majorana neutrinos in pp collisions at s = 14-TeV. *Phys. Rev. D62* (2000), 013001.

[119] Ferreira de Lima, Danilo Enoque, Papaefstathiou, Andreas, and Spannowsky, Michael. Standard model Higgs boson pair production in the ($b\bar{b}$)($b\bar{b}$) final state. *JHEP 08* (2014), 030.

[120] Ferreira, P. M. The vacuum structure of the Higgs complex singlet-doublet model. *Phys. Rev. D94*, 9 (2016), 096011.

[121] Fileviez Perez, Pavel, Han, Tao, Huang, Gui-yu, Li, Tong, and Wang, Kai. Neutrino Masses and the CERN LHC: Testing Type II Seesaw. *Phys. Rev. D78* (2008), 015018.

[122] Fileviez Perez, Pavel, Patel, Hiren H., Ramsey-Musolf, Michael.J., and Wang, Kai. Triplet Scalars and Dark Matter at the LHC. *Phys. Rev. D79* (2009), 055024.

[123] Foot, Robert, Lew, H., He, X. G., and Joshi, Girish C. Seesaw Neutrino Masses Induced by a Triplet of Leptons. *Z. Phys. C44* (1989), 441.

[124] Frederix, R., Frixione, S., Hirschi, V., Maltoni, F., Mattelaer, O., Torrielli, P., Vryonidou, E., and Zaro, M. Higgs pair production at the LHC with NLO and parton-shower effects. *Phys. Lett. B732* (2014), 142–149.

[125] Freitas, Ayres, Lpez-Val, David, and Plehn, Tilman. When matching matters: Loop effects in Higgs effective theory. *Phys. Rev. D94*, 9 (2016), 095007.

[126] Freund, Yoav, and Schapire, Robert E. Experiments with a new boosting algorithm. In *Proceedings of the Thirteenth International Conference on International Conference on Machine Learning* (San Francisco, CA, USA, 1996), ICML'96, Morgan Kaufmann Publishers Inc., pp. 148–156.

[127] Fromme, Lars, Huber, Stephan J., and Seniuch, Michael. Baryogenesis in the two-Higgs doublet model. *JHEP 11* (2006), 038.

[128] Fukuda, Y., et al. Evidence for oscillation of atmospheric neutrinos. *Phys. Rev. Lett. 81* (1998), 1562–1567.

[129] Furry, W. H. On transition probabilities in double beta-disintegration. *Phys. Rev. 56* (1939), 1184–1193.

[130] Gaillard, M. K., and Lee, Benjamin W. Δ I = 1/2 Rule for Nonleptonic Decays in Asymptotically Free Field Theories. *Phys. Rev. Lett. 33* (1974), 108.

[131] Garayoa, Julia, and Schwetz, Thomas. Neutrino mass hierarchy and Majorana CP phases within the Higgs triplet model at the LHC. *JHEP 03* (2008), 009.

[132] Gavela, M. B., Hernandez, P., Orloff, J., and Pene, O. Standard model CP violation and baryon asymmetry. *Mod. Phys. Lett. A9* (1994), 795–810.

[133] Gavela, M. B., Hernandez, P., Orloff, J., Pene, O., and Quimbay, C. Standard model CP violation and baryon asymmetry. Part 2: Finite temperature. *Nucl. Phys. B430* (1994), 382–426.

[134] Gell-Mann, Murray, Ramond, Pierre, and Slansky, Richard. Complex Spinors and Unified Theories. *Conf. Proc. C790927* (1979), 315–321.

[135] Georgi, Howard. On-shell effective field theory. *Nucl. Phys. B361* (1991), 339–350.

[136] Gilman, Frederick J., and Wise, Mark B. Effective Hamiltonian for Delta s = 1 Weak Nonleptonic Decays in the Six Quark Model. *Phys. Rev. D20* (1979), 2392.

[137] Giudice, G. F., Grojean, C., Pomarol, A., and Rattazzi, R. The Strongly-Interacting Light Higgs. *JHEP 06* (2007), 045.

[138] Giusarma, Elena, Gerbino, Martina, Mena, Olga, Vagnozzi, Sunny, Ho, Shirley, and Freese, Katherine. Improvement of cosmological neutrino mass bounds. *Phys. Rev. D94*, 8 (2016), 083522.

[139] Glashow, Sheldon L., and Weinberg, Steven. Natural Conservation Laws for Neutral Currents. *Phys. Rev. D15* (1977), 1958.

[140] Goertz, Florian, Papaefstathiou, Andreas, Yang, Li Lin, and Zurita, Jose. Higgs Boson self-coupling measurements using ratios of cross sections. *JHEP 06* (2013), 016.

[141] Gorbahn, Martin, and Haisch, Ulrich. Indirect probes of the trilinear Higgs coupling: $gg \to h$ and $h \to \gamma\gamma$. *JHEP 10* (2016), 094.

[142] Gorbahn, Martin, No, Jose Miguel, and Sanz, Veronica. Benchmarks for Higgs Effective Theory: Extended Higgs Sectors. *JHEP 10* (2015), 036.

[143] Graner, B., Chen, Y., Lindahl, E. G., and Heckel, B. R. Reduced Limit on the Permanent Electric Dipole Moment of Hg199. *Phys. Rev. Lett. 116*, 16 (2016), 161601. [Erratum: Phys. Rev. Lett.119,no.11,119901(2017)].

[144] Griffith, W. C., Swallows, M. D., Loftus, T. H., Romalis, M. V., Heckel, B. R., and Fortson, E. N. Improved Limit on the Permanent Electric Dipole Moment of Hg-199. *Phys. Rev. Lett. 102* (2009), 101601.

[145] Grzadkowski, B., Iskrzynski, M., Misiak, M., and Rosiek, J. Dimension-Six Terms in the Standard Model Lagrangian. *JHEP 10* (2010), 085.

[146] Gunion, John F., and Haber, Howard E. The CP conserving two Higgs doublet model: The Approach to the decoupling limit. *Phys. Rev. D67* (2003), 075019.

[147] Hagiwara, Kaoru, Hatsukano, T., Ishihara, S., and Szalapski, R. Probing non-standard bosonic interactions via W boson pair production at lepton colliders. *Nucl. Phys. B496* (1997), 66–102.

[148] Hagiwara, Kaoru, Ishihara, S., Szalapski, R., and Zeppenfeld, D. Low-energy effects of new interactions in the electroweak boson sector. *Phys. Rev. D48* (1993), 2182–2203.

[149] Hagiwara, Kaoru, Matsumoto, S., Haidt, D., and Kim, C. S. A Novel approach to confront electroweak data and theory. *Z. Phys. C64* (1994), 559–620. [Erratum: Z. Phys.C68,352(1995)].

[150] Han, Tao, Lewis, Ian, Ruiz, Richard, and Si, Zong-guo. Lepton Number Violation and W' Chiral Couplings at the LHC. *Phys. Rev. D87*, 3 (2013), 035011. [Erratum: Phys. Rev.D87,no.3,039906(2013)].

[151] Henning, Brian, Lu, Xiaochuan, and Murayama, Hitoshi. How to use the Standard Model effective field theory. *JHEP 01* (2016), 023.

[152] Henning, Brian, Lu, Xiaochuan, and Murayama, Hitoshi. One-loop Matching and Running with Covariant Derivative Expansion.

[153] Hernandez, P. Neutrino Physics. In *Proceedings, 8th CERNLatin-American School of High-Energy Physics (CLASHEP2015): Ibarra, Ecuador, March 05-17, 2015* (2016), pp. 85–142.

[154] Hespel, B., Maltoni, F., and Vryonidou, E. Higgs and Z boson associated production via gluon fusion in the SM and the 2HDM. *JHEP 06* (2015), 065.

[155] Higgs, Peter W. Broken Symmetries and the Masses of Gauge Bosons. *Phys. Rev. Lett. 13* (1964), 508–509. [,160(1964)].

[156] Higgs, Peter W. Broken symmetries, massless particles and gauge fields. *Phys. Lett. 12* (1964), 132–133.

[157] Higgs, Peter W. Spontaneous Symmetry Breakdown without Massless Bosons. *Phys. Rev. 145* (1966), 1156–1163.

[158] Hisano, Junji, and Tsumura, Koji. Higgs boson mixes with an SU(2) septet representation. *Phys. Rev. D87* (2013), 053004.

[159] Hocker, Andreas, et al. TMVA - Toolkit for Multivariate Data Analysis. *PoS ACAT* (2007), 040.

[160] Huang, T., No, J. M., Perni, L., Ramsey-Musolf, M., Safonov, A., Spannowsky, M., and Winslow, P. Resonant di-Higgs boson production in the $b\bar{b}WW$ channel: Probing the electroweak phase transition at the LHC. *Phys. Rev. D96*, 3 (2017), 035007.

[161] Huet, Patrick, and Sather, Eric. Electroweak baryogenesis and standard model CP violation. *Phys. Rev. D51* (1995), 379–394.

[162] Inoue, Satoru, Ovanesyan, Grigory, and Ramsey-Musolf, Michael J. Two-Step Electroweak Baryogenesis. *Phys. Rev. D93* (2016), 015013.

[163] Inoue, Satoru, Ramsey-Musolf, Michael J., and Zhang, Yue. CP-violating phenomenology of flavor conserving two Higgs doublet models. *Phys. Rev. D89*, 11 (2014), 115023.

[164] Izaguirre, Eder, and Shuve, Brian. Multilepton and Lepton Jet Probes of Sub-Weak-Scale Right-Handed Neutrinos. *Phys. Rev. D91*, 9 (2015), 093010.

[165] Jenkins, Elizabeth E., Manohar, Aneesh V., and Trott, Michael. Renormalization Group Evolution of the Standard Model Dimension Six Operators I: Formalism and lambda Dependence. *JHEP 10* (2013), 087.

[166] Jenkins, Elizabeth E., Manohar, Aneesh V., and Trott, Michael. Renormalization Group Evolution of the Standard Model Dimension Six Operators II: Yukawa Dependence. *JHEP 01* (2014), 035.

[167] Joshipura, Anjan S., Paschos, Emmanuel A., and Rodejohann, Werner. Leptogenesis in left-right symmetric theories. *Nucl. Phys. B611* (2001), 227–238.

[168] Jung, Martin, and Pich, Antonio. Electric Dipole Moments in Two-Higgs-Doublet Models. *JHEP 04* (2014), 076.

[169] Kajantie, K., Laine, M., Rummukainen, K., and Shaposhnikov, Mikhail E. Is there a hot electroweak phase transition at m(H) larger or equal to m(W)? *Phys. Rev. Lett. 77* (1996), 2887–2890.

[170] Kajantie, K., Laine, M., Rummukainen, K., and Shaposhnikov, Mikhail E. The Electroweak phase transition: A Nonperturbative analysis. *Nucl. Phys. B466* (1996), 189–258.

[171] Keung, Wai-Yee, and Senjanovic, Goran. Majorana Neutrinos and the Production of the Right-handed Charged Gauge Boson. *Phys. Rev. Lett. 50* (1983), 1427.

[172] Khachatryan, Vardan, et al. Constraints on the spin-parity and anomalous HVV couplings of the Higgs boson in proton collisions at 7 and 8TeV. *Phys. Rev. D92*, 1 (2015), 012004.

[173] Khachatryan, Vardan, et al. Precise determination of the mass of the Higgs boson and tests of compatibility of its couplings with the standard model predictions using proton collisions at 7 and 8 TeV. *Eur. Phys. J. C75*, 5 (2015), 212.

[174] Khachatryan, Vardan, et al. Search for a Higgs boson in the mass range from 145 to 1000 GeV decaying to a pair of W or Z bosons. *JHEP 10* (2015), 144.

[175] Khachatryan, Vardan, et al. Search for heavy resonances decaying to two Higgs bosons in final states containing four b quarks. *Eur. Phys. J. C76*, 7 (2016), 371.

[176] Khachatryan, Vardan, et al. Search for two Higgs bosons in final states containing two photons and two bottom quarks in proton-proton collisions at 8TeV. *Phys. Rev. D94*, 5 (2016), 052012.

[177] Khandker, Zuhair U., Li, Daliang, and Skiba, Witold. Electroweak Corrections from Triplet Scalars. *Phys. Rev. D86* (2012), 015006.

[178] Kibble, T. W. B. Symmetry breaking in nonAbelian gauge theories. *Phys. Rev. 155* (1967), 1554–1561. [,165(1967)].

[179] Klinkhamer, Frans R., and Manton, N. S. A Saddle Point Solution in the Weinberg-Salam Theory. *Phys. Rev. D30* (1984), 2212.

[180] Konetschny, W., and Kummer, W. Nonconservation of Total Lepton Number with Scalar Bosons. *Phys. Lett. B70* (1977), 433–435.

[181] Kotwal, Ashutosh V., Ramsey-Musolf, Michael J., No, Jose Miguel, and Winslow, Peter. Singlet-catalyzed electroweak phase transitions in the 100TeV frontier. *Phys. Rev. D94*, 3 (2016), 035022.

[182] Kribs, Graham D., Maier, Andreas, Rzehak, Heidi, Spannowsky, Michael, and Waite, Philip. Electroweak oblique parameters as a probe of the trilinear Higgs self-interaction.

[183] Kribs, Graham D., and Martin, Adam. Enhanced di-Higgs Production through Light Colored Scalars. *Phys. Rev. D86* (2012), 095023.

[184] Kumar, Krishna, Lu, Zheng-Tian, and Ramsey-Musolf, Michael J. Working Group Report: Nucleons, Nuclei, and Atoms. In *Fundamental Physics at the Intensity Frontier* (2013), pp. 159–214.

[185] Lazarides, George, Shafi, Q., and Wetterich, C. Proton Lifetime and Fermion Masses in an SO(10) Model. *Nucl. Phys. B181* (1981), 287–300.

[186] Lee, T. D. A Theory of Spontaneous T Violation. *Phys. Rev. D8* (1973), 1226–1239. [,516(1973)].

[187] Ma, Ernest. Pathways to naturally small neutrino masses. *Phys. Rev. Lett. 81* (1998), 1171–1174.

[188] Ma, Ernest. Neutrino Mass: Mechanisms and Models.

[189] Magg, M., and Wetterich, C. Neutrino Mass Problem and Gauge Hierarchy. *Phys. Lett. 94B* (1980), 61–64.

[190] Majorana, Ettore. Teoria simmetrica dellelettrone e del positrone. *Nuovo Cim. 14* (1937), 171–184.

[191] Maki, Ziro, Nakagawa, Masami, and Sakata, Shoichi. Remarks on the unified model of elementary particles. *Prog. Theor. Phys. 28* (1962), 870–880. [,34(1962)].

[192] Maltoni, Fabio, Pagani, Davide, Shivaji, Ambresh, and Zhao, Xiaoran. Trilinear Higgs coupling determination via single-Higgs differential measurements at the LHC. *Eur. Phys. J. C77*, 12 (2017), 887.

[193] Mangano, M. L., et al. Physics at a 100 TeV pp Collider: Standard Model Processes. *CERN Yellow Report*, 3 (2017), 1–254.

[194] Manohar, Aneesh V. Effective field theories. In *Quarks and colliders. Proceedings, 10th Winter Institute, Lake Louise, Canada, February 19-25, 1995* (1995), pp. 274–315.

[195] Manton, N. S. Topology in the Weinberg-Salam Theory. *Phys. Rev. D28* (1983), 2019.

[196] Masso, Eduard. An Effective Guide to Beyond the Standard Model Physics. *JHEP 10* (2014), 128.

[197] McDonald, John. Gauge singlet scalars as cold dark matter. *Phys. Rev. D50* (1994), 3637–3649.

[198] Minkowski, Peter. $\mu \to e\gamma$ at a Rate of One Out of 10^9 Muon Decays? *Phys. Lett. 67B* (1977), 421–428.

[199] Mohapatra, R. N., and Valle, J. W. F. Neutrino Mass and Baryon Number Nonconservation in Superstring Models. *Phys. Rev. D34* (1986), 1642. [,235(1986)].

[200] Mohapatra, Rabindra N., and Senjanovic, Goran. Neutrino Mass and Spontaneous Parity Violation. *Phys. Rev. Lett. 44* (1980), 912. [,231(1979)].

[201] Mohapatra, Rabindra N., and Senjanovic, Goran. Neutrino Masses and Mixings in Gauge Models with Spontaneous Parity Violation. *Phys. Rev. D23* (1981), 165.

[202] Morrissey, David E., and Ramsey-Musolf, Michael J. Electroweak baryogenesis. *New J. Phys. 14* (2012), 125003.

[203] Morse, David M. Latest results on di-Higgs boson production with CMS.

[204] Muselli, Claudio, Bonvini, Marco, Forte, Stefano, Marzani, Simone, and Ridolfi, Giovanni. Top Quark Pair Production beyond NNLO. *JHEP 08* (2015), 076.

[205] Nemevsek, Miha, Senjanovic, Goran, and Tello, Vladimir. Connecting Dirac and Majorana Neutrino Mass Matrices in the Minimal Left-Right Symmetric Model. *Phys. Rev. Lett. 110*, 15 (2013), 151802.

[206] Nemevek, Miha, Nesti, Fabrizio, and Popara, Goran. Keung-Senjanović process at LHC: from LNV to displaced vertices to invisible decays.

[207] Nemevek, Miha, Nesti, Fabrizio, and Vasquez, Juan Carlos. Majorana Higgses at colliders. *JHEP 04* (2017), 114.

[208] No, Jose M., and Ramsey-Musolf, Michael. Probing the Higgs Portal at the LHC Through Resonant di-Higgs Production. *Phys. Rev. D89*, 9 (2014), 095031.

[209] O'Connell, Donal, Ramsey-Musolf, Michael J., and Wise, Mark B. Minimal Extension of the Standard Model Scalar Sector. *Phys. Rev. D75* (2007), 037701.

[210] Palanque-Delabrouille, Nathalie, et al. Neutrino masses and cosmology with Lyman-alpha forest power spectrum. *JCAP 1511*, 11 (2015), 011.

[211] Papaefstathiou, Andreas, Yang, Li Lin, and Zurita, Jose. Higgs boson pair production at the LHC in the $b\bar{b}W^+W^-$ channel. *Phys. Rev. D87*, 1 (2013), 011301.

[212] Passarino, Giampiero. Field reparametrization in effective field theories. *Eur. Phys. J. Plus 132*, 1 (2017), 16.

[213] Patrignani, C., et al. Review of Particle Physics. *Chin. Phys. C40*, 10 (2016), 100001.

[214] Peskin, Michael E., and Takeuchi, Tatsu. Estimation of oblique electroweak corrections. *Phys. Rev. D46* (1992), 381–409.

[215] Plehn, T., Spira, M., and Zerwas, P. M. Pair production of neutral Higgs particles in gluon-gluon collisions. *Nucl. Phys. B479* (1996), 46–64. [Erratum: Nucl. Phys.B531,655(1998)].

[216] Politzer, H. David. Power Corrections at Short Distances. *Nucl. Phys. B172* (1980), 349–382.

[217] Pontecorvo, B. Inverse beta processes and nonconservation of lepton charge. *Sov. Phys. JETP 7* (1958), 172–173. [Zh. Eksp. Teor. Fiz.34,247(1957)].

[218] Profumo, Stefano, Ramsey-Musolf, Michael J., and Shaughnessy, Gabe. Singlet Higgs phenomenology and the electroweak phase transition. *JHEP 08* (2007), 010.

[219] Profumo, Stefano, Ramsey-Musolf, Michael J., Wainwright, Carroll L., and Winslow, Peter. Singlet-catalyzed electroweak phase transitions and precision Higgs boson studies. *Phys. Rev. D91*, 3 (2015), 035018.

[220] Pumplin, J., Stump, D. R., Huston, J., Lai, H. L., Nadolsky, Pavel M., and Tung, W. K. New generation of parton distributions with uncertainties from global QCD analysis. *JHEP 07* (2002), 012.

[221] Ps, Heinrich, and Rodejohann, Werner. Neutrinoless Double Beta Decay. *New J. Phys. 17*, 11 (2015), 115010.

[222] Quigg, Chris. LHC Physics Potential versus Energy.

[223] Quiros, M. Field theory at finite temperature and phase transitions. *Helv. Phys. Acta 67* (1994), 451–583.

[224] Robens, Tania, and Stefaniak, Tim. Status of the Higgs Singlet Extension of the Standard Model after LHC Run 1. *Eur. Phys. J. C75* (2015), 104.

[225] Robens, Tania, and Stefaniak, Tim. LHC Benchmark Scenarios for the Real Higgs Singlet Extension of the Standard Model. *Eur. Phys. J. C76*, 5 (2016), 268.

[226] Roitgrund, Aviad, Eilam, Gad, and Bar-Shalom, Shaouly. Implementation of the left-right symmetric model in FeynRules. *Comput. Phys. Commun. 203* (2016), 18–44.

[227] Rummukainen, K., Tsypin, M., Kajantie, K., Laine, M., and Shaposhnikov, Mikhail E. The Universality class of the electroweak theory. *Nucl. Phys. B532* (1998), 283–314.

[228] Sakharov, A. D. Violation of CP Invariance, C asymmetry, and baryon asymmetry of the universe. *Pisma Zh. Eksp. Teor. Fiz. 5* (1967), 32–35. [Usp. Fiz. Nauk161,no.5,61(1991)].

[229] Schechter, J., and Valle, J. W. F. Neutrino Masses in SU(2) x U(1) Theories. *Phys. Rev. D22* (1980), 2227.

[230] Selvaggi, Michele. DELPHES 3: A modular framework for fast-simulation of generic collider experiments. *J. Phys. Conf. Ser. 523* (2014), 012033.

[231] Selvaggi, Michele, and Ortona, Giacomo. .

[232] Senjanovic, Goran. Spontaneous Breakdown of Parity in a Class of Gauge Theories. *Nucl. Phys. B153* (1979), 334–364.

[233] Senjanović, Goran, and Tello, Vladimir. Probing Seesaw with Parity Restoration. *Phys. Rev. Lett. 119*, 20 (2017), 201803.

[234] Shu, Jing, and Zhang, Yue. Impact of a CP Violating Higgs Sector: From LHC to Baryogenesis. *Phys. Rev. Lett. 111*, 9 (2013), 091801.

[235] Simma, H. Equations of motion for effective Lagrangians and penguins in rare B decays. *Z. Phys. C61* (1994), 67–82.

[236] Sirunyan, Albert M, et al. Search for heavy neutral leptons in events with three charged leptons in proton-proton collisions at $\sqrt{s} = 13$ TeV. *Phys. Rev. Lett. 120*, 22 (2018), 221801.

[237] Sjostrand, Torbjorn, Mrenna, Stephen, and Skands, Peter Z. PYTHIA 6.4 Physics and Manual. *JHEP 05* (2006), 026.

[238] Sugiyama, Hiroaki. Radiative Neutrino Mass Models. In *2nd Toyama International Workshop on Higgs as a Probe of New Physics (HPNP2015) Toyama, Japan, February 11-15, 2015* (2015).

[239] Trodden, Mark. Electroweak baryogenesis. *Rev. Mod. Phys. 71* (1999), 1463–1500.

[240] Weinberg, Steven. Baryon and Lepton Nonconserving Processes. *Phys. Rev. Lett. 43* (1979), 1566–1570.

[241] Wudka, Jose. Electroweak effective Lagrangians. *Int. J. Mod. Phys. A9* (1994), 2301–2362.

[242] Yamanaka, N., Sahoo, B. K., Yoshinaga, N., Sato, T., Asahi, K., and Das, B. P. Probing exotic phenomena at the interface of nuclear and particle physics with the electric dipole moments of diamagnetic atoms: A unique window to hadronic and semi-leptonic CP violation. *Eur. Phys. J. A53*, 3 (2017), 54.

[243] Yanagida, Tsutomu. HORIZONTAL SYMMETRY AND MASSES OF NEUTRINOS. *Conf. Proc. C7902131* (1979), 95–99.

[244] Zee, A. A Theory of Lepton Number Violation, Neutrino Majorana Mass, and Oscillation. *Phys. Lett. 93B* (1980), 389. [Erratum: Phys. Lett.95B,461(1980)].

[245] Zurita, Jose. Di-Higgs production at the LHC and beyond. In *5th Large Hadron Collider Physics Conference (LHCP 2017) Shanghai, China, May 15-20, 2017* (2017).